



# Experimental investigation and numerical simulation of thermal debinding and sintering processes in powder injection moulding.

Belgacem Mamen

## ► To cite this version:

Belgacem Mamen. Experimental investigation and numerical simulation of thermal debinding and sintering processes in powder injection moulding.. Other. Université de Franche-Comté, 2013. English. NNT : 2013BESA2033 . tel-01124328

**HAL Id: tel-01124328**

**<https://theses.hal.science/tel-01124328>**

Submitted on 6 Mar 2015

**HAL** is a multi-disciplinary open access archive for the deposit and dissemination of scientific research documents, whether they are published or not. The documents may come from teaching and research institutions in France or abroad, or from public or private research centers.

L'archive ouverte pluridisciplinaire **HAL**, est destinée au dépôt et à la diffusion de documents scientifiques de niveau recherche, publiés ou non, émanant des établissements d'enseignement et de recherche français ou étrangers, des laboratoires publics ou privés.

# SPIM

## Thèse de Doctorat



École doctorale sciences pour l'ingénieur et microtechniques  
UNIVERSITÉ DE FRANCHE-COMTÉ

**Prepared and presented at**

L'U.F.R. DES SCIENCES ET TECHNIQUES  
DE L'UNIVERSITÉ DE FRANCHE-COMTE

**In order to obtain the**

**GRADE DE DOCTEUR DE L'UNIVERSITÉ  
DE FRANCHE-COMTE**

**Spécialité: Sciences pour l'Ingénieur**

**Experimental investigation and numerical  
simulation of thermal debinding and sintering  
processes in powder injection moulding**

**Expérimentation et simulation numérique du  
déliantage thermique et de la densification  
des composants obtenus par moulage par  
injection de poudres**

**Belgacem MAMEN**

**Defence on 10 December 2013, defence committee:**

**Chairman**

**Advisor**

**Co-Advisor**

**Reviewers**

**Examinators**

A. LERICHE

Professor, Université de Valenciennes

T. BARRIERE

Professor, Université de Franche-Comté

J-C. GELIN

Professor, Ecole Nationale Supérieure de Mécanique et des  
Microtechniques, Besançon

P. GUIGON

Professor, Université de Technologie Compiègne

J-M. CHAIX

Professor, Grenoble INP

F. VALDIVIESO

HDR, Ecole Nationale Supérieure des Mines de St-Etienne

C. GATUMEL

Assistant Professor, Ecole des Mines d'Albi-Carmaux





## **Acknowledgments**

These three years in FEMTO-ST institute (Applied Mechanics Department) have really been very rich for me. Now that my Thesis project arrives at its end, I have many people to thank for having made my stay and work here so lively.

I would like to express my deepest gratitude to my advisors Pr. Thierry Barriere and Pr. Jean-Claude Gelin for supporting me during these past three years. They have provided me many scientific advices and insightful discussions about my research project.

I am very grateful to the members of my dissertation committee: Pr. Anne Leriche (université de Valenciennes), Pr Jean-Marc Chaix (INP de Grenoble), Pr. Pierre Guigon (Université de Compiègne), Dr. Francois Valdivieso (HDR, Ecole Nationale Supérieure des Mines de St-Etienne) and Dr Cendrine Gatumel (Assistant Professor, Ecole des Mines d'Albi-Carmaux), who gave me some very constructive comments about my work to improve the quality of this manuscript.

I need to thank Dr. Farid Hammoud (Assistant Professor at the University of Batna, Algeria) and Dr. Evariste Ouedraogo (Assistant Professor at Grenoble INP) for encouraging me to pursue PhD studies.

I would like to appreciate the technical staff of (FEMTO-ST/Applied Mechanics Department) for their help and preparation of metallic components. I would like to thank Dr Jiupeng Song (China) for sending me prepared tungsten components. Still many thanks to my colleagues for their company: Hamza Djoudi, Edouard Falconnet, Elie Gibeau, Xiangji Kong, Gang Cheng, Alexandra Mitbauerova, Diala Bitar, Chang Wu, Mohamed Krifa and Oussama Dadi. I would like to thank my friends Amine Mechraoui and Moussa Cherraben for their encouragements during my studies at Grenoble University.

No acknowledgments would be complete without giving thanks to my parents. They have taught me about hard work and self-respect, about persistence and how to be independent. Many thanks to my sisters and brothers for their continuous encouragements. Acknowledgments to my second families: Lahouel and Salem, i had a great time with them during my stay here in Besançon.

Besançon, December 2013.

Belgacem MAMEN

## **Abstract**

Powder Injection Moulding (PIM) is one of the most efficient technologies for manufacturing of near net shape components. The PIM processing includes four stages: mixing of very fine metallic or ceramic powders and thermoplastic binders to elaborate a feedstock, injection of powder/binder mixtures in the die mould cavity, thermal/catalytic or solvent debinding stage and finally thermal sintering by solid state diffusion.

Thermal debinding is one of the most important steps in Powder Injection Moulding process. Thermogravimetric analyses (TGA) are employed to analyze the physics and kinetics of thermal debinding behaviour under argon atmosphere. Thermal debinding kinetics with different heating rates have been compared using 316L stainless steel feedstocks loaded typically at 60, 62, 64 and 66 vol% for fine metallic powders  $D_{50}=3.4\text{ }\mu\text{m}$ . The Kissinger and Ozawa methods have been used to estimate the kinetic parameters from thermogravimetric experiments. To set up the numerical simulations of thermal debinding stage using finite element method, a coupled mathematical has been developed. The basic steps of the proposed model consist to solve the following sequences of coupled problems: thermal degradation of binder coupled with heat transfer and deformation phenomena by finite element method using Comsol Multiphysics<sup>®</sup> software. The proposed numerical simulations allow the determination of remaining binder distribution, temperature distribution and strain fields in the component during the whole thermal debinding process at any time.

In the second part of this thesis, sintering behaviour of tungsten powders injection moulded components, under pure hydrogen atmosphere at temperature up to 1700°C by varying the initial grain size in the range 0.4–1 $\mu\text{m}$  for fine powders and 5.0-7.0  $\mu\text{m}$  for coarse powders. Sintering behaviour is investigated by means of the bending and dilatometric tests in the Setaram<sup>®</sup> analyser. The experimental tests are used to determine the material parameters in the viscoplastic constitutive law, which is important for modeling of the sintering behaviour. The sintering model is implemented in ABAQUS software as user subroutine UMAT. The model is incorporated with the identified parameters in order to simulate the final shrinkages and densities of tungsten injection moulded components during the sintering process. The results reveal that initial particle size had no effect on the shrinkage evolution using coarse powders. For

the fine powders, the evolution of shrinkage more strongly depends on initial particle size and increases with decreasing the initial particle size. Relative density was found to increase sharply for fine tungsten powders and reached up to 90-94 % in the case of 0.4 $\mu$ m. Comparison between the numerical simulations results and experimental ones, in term of shrinkages and sintered densities, shows a good agreement between the two.

**Keywords:** powder injection moulding, thermal debinding, kinetic parameters, porous media, binder distribution, sintering by solid state diffusion, viscoplastic, finite element method.

## Résumé

Le Moulage par Injection de Poudres (PIM) est l'une des technologies les plus efficaces pour la production de composants de géométries complexes. Le procédé PIM comporte quatre étapes: mélangeage, injection, déliantage et enfin la densification par diffusion à l'état solide pour obtenir la cohésion du composant et ainsi une densité élevée.

L'étape de déliantage est une étape importante et parfois critique pour le procédé. A cet effet, des analyses thermogravimétriques (TGA) ont été réalisées pour bien comprendre les mécanismes du déliantage thermique sous atmosphère imposée (Argon). Les variations de la quantité du liant restante à l'intérieur du composant, en utilisant différentes cinétiques du chauffage, ont été comparées pour différents taux de charge en poudre 60, 60, 64 et 66%. La poudre utilisée est l'inox 316L avec  $D_{50}=3.4 \mu\text{m}$ . Les méthodes de Kissinger et Ozawa ont été utilisées, en se basant sur les résultats des analyses thermogravimétriques, afin d'estimer les paramètres cinétiques nécessaires pour la simulation numérique. Quant à la simulation numérique, notre modèle se propose de décrire les phénomènes physiques liés à la dégradation du polymère, le transfert de chaleur et la déformation du composant pendant le déliantage thermique. Les différentes équations, régissant les phénomènes concernés, ont été résolues à l'aide d'un code éléments finis, Comsol®. Les résultats de la simulation numérique sont capables de nous donner des renseignements sur la nature des distributions spatio-temporelles de la masse du liant conservée, les champs de température et de déformation dans le composant délianté.

La deuxième partie de la thèse est dédiée à la compréhension des mécanismes et du comportement du frittage des composants en tungstène sous une atmosphère d'hydrogène jusqu'à une température de 1700°C. Deux types de poudres de tungstène, fines (0.4-3 $\mu\text{m}$ ) et grosses (5.0-7.0  $\mu\text{m}$ ), ont été considérées dans cette partie des travaux de thèse. Des appareils expérimentaux, ont été mis en place afin de constituer une base de données physiques nécessaire pour la simulation et l'optimisation de l'étape de densification, à partir des résultats fournis par l'analyseur thermique modulaire à multiple fonctions (TMA, Setaram®). Le but de ce type d'essais est de quantifier l'évolution du retrait et de la déflexion pendant la densification. L'identification de l'ensemble des lois de comportement a été réalisée en prenant en

compte les spécificités physiques des deux types de poudres (énergie d'activation pour la densification et taille initiale des grains). Les lois de comportement identifiées sont implémentées dans le code de calcul éléments finis (ABAQUS) afin de valider les simulations numériques. Un modèle de comportement de type thermo-élasto-viscoplastique est formulé pour représenter la loi de densification par diffusion solide, puis appliqué pour les différentes tailles de poudres de tungstène. La dernière étape consiste à valider des simulations numériques avec ABAQUS pour une meilleure détermination des densités et des retraits finaux des composants injectés.

**Mots clés :** moulage par injection de poudres, déliantage thermique, paramètres cinétiques, milieux poreux, distribution du polymère, densification par diffusion solide, viscoplastique, méthode des éléments finis.

# Table of Contents

|   |           |
|---|-----------|
| Liste of figures .....  | X         |
| Liste of tables .....   | XVI       |
| List of Symbols .....   | XVIII     |
| <hr/>   |           |
| <b>General Introduction</b>   | <b>1</b>  |
| <hr/>   |           |
| <b>1 Context and Research Motivation</b> .....                                    | <b>2</b>  |
| <b>2 Research Problem and Objectives</b> .....                                    | <b>4</b>  |
| <b>3 Thesis Organization and Strategy</b> .....                                   | <b>6</b>  |
| <hr/>   |           |
| <b>Chapter 1: State of the Art of Powder Injection Moulding Technology</b>        | <b>7</b>  |
| <hr/>   |           |
| <b>1.1 Introduction</b> .....   | <b>8</b>  |
| <b>1.2 Powder Injection Moulding (PIM)</b> .....                                  | <b>13</b> |
| 1.2.1 Brief history of Powder injection moulding.....                             | 13        |
| 1.2.2 Principal powder injection moulding steps.....                              | 14        |
| 1.2.2.1 Feedstock elaboration stage.....  | 15        |
| 1.2.2.2 Injection moulding stage.....   | 23        |
| 1.2.2.3 Debinding step.....   | 25        |
| 1.2.2.4 Sintering step.....   | 30        |
| <b>1.3 Raw material and Market of PIM</b> .....                                   | <b>32</b> |
| 1.3.1 Raw material for metal Powder Injection Moulding technology .....           | 32        |
| 1.3.1.1 Metal powders.....  | 32        |
| 1.3.1.2 Binder system.....  | 32        |
| 1.3.2 Powder Injection Moulding Market.....                                       | 33        |
| <b>1.4 Summary</b> .....  | <b>34</b> |
| <hr/>   |           |
| <b>Chapter 2: Literature Review on Thermal Debinding and Sintering Behaviours</b> | <b>35</b> |
| <hr/>   |           |
| <b>2.1 Introduction</b> .....   | <b>36</b> |
| <b>2.2 Thermal debinding of PIM components</b> .....                              | <b>36</b> |
| 2.2.1 Physics of thermal debinding .....  | 37        |
| 2.2.1.1 Diffusion controlled debinding.....                                       | 38        |

|   |           |
|---|-----------|
| 2.2.1.2 Permeation controlled debinding.....                  | 39        |
| 2.2.1.3 Wicking controlled debinding.....                     | 40        |
| 2.2.1.4 Thermal debinding based on kinetic model.....         | 43        |
| 2.2.1.5 Master Decomposition Curve for Thermal Debinding..... | 44        |
| 2.2.2 Factors affecting thermal debinding .....               | 47        |
| 2.2.3 Current defects in thermal debinding process .....      | 49        |
| <b>2.3 Sintering of PIM components .....</b>                  | <b>50</b> |
| 2.3.1 Sintering mechanisms .....                              | 50        |
| 2.3.2 Driving force of sintering phenomenon.....              | 51        |
| 2.3.3 Stages in solid state sintering.....                    | 52        |
| 2.3.4 Modeling of solid state sintering.....                  | 53        |
| <b>2.4 Summary.....</b>                                       | <b>58</b> |

---

## **Chapter 3: Thermal and Solvent Debinding Investigation for PIM Components**

---

|   |           |
|---|-----------|
| <b>3.1 Introduction.....</b>  | <b>61</b> |
| <b>3.2 Experimental investigation in thermal debinding.....</b>     | <b>63</b> |
| 3.2.1 Materials .....   | 63        |
| 3.2.1.1 Powder properties.....                                      | 63        |
| 3.2.1.2 Binder components properties .....                          | 64        |
| 3.2.1.3 Feedstocks preparation.....                                 | 64        |
| 3.2.2 Weight loss during thermal debinding.....                     | 67        |
| 3.2.3 Thermal characterisation of binders and feedstocks.....       | 68        |
| 3.2.3.1 Differential scanning calorimetry (DSC).....                | 69        |
| 3.2.3.2 Thermogravimetric analysis (TGA).....                       | 70        |
| 3.2.4 Estimation of kinetic parameters.....                         | 73        |
| 3.2.4.1 Ozawa method.....   | 73        |
| 3.2.4.2 Kissinger method.....                                       | 74        |
| 3.2.5 Effect of heating rate and powder volume loading energy.....  | 76        |
| 3.2.6 Effect of powder volume loading on the activation energy..... | 78        |
| 3.2.7 Evolution of activation energy during thermal debinding.....  | 80        |
| <b>3.3 Experimental investigation in solvent debinding .....</b>    | <b>82</b> |
| 3.3.1 Material.....   | 83        |
| 3.3.2 Evolution of remaining binder content.....                    | 84        |
| <b>3.4 Summary.....</b>   | <b>85</b> |

---



|   |            |
|---|------------|
| <b>Chapter 4: Numerical simulation of Thermal and Solvent Debinding</b>                   | <b>86</b>  |
| <b>4.1 Introduction.....</b>  | <b>87</b>  |
| <b>4.2 Numerical simulation of thermal debinding process .....</b>                        | <b>87</b>  |
| 4.2.1 Kinetic model for multi reaction steps .....  | 87         |
| 4.2.2 Identification of kinetic parameters.....   | 89         |
| 4.2.3 Numerical simulation using identified kinetic parameters.....                       | 91         |
| 4.2.4 Material and process numerical implementation.....                                  | 95         |
| 4.2.5 Results of numerical simulation.....  | 98         |
| 4.2.5.1 Mass transport mechanisms related to thermal debinding .....                      | 98         |
| 4.2.5.2 Temperature variation inside the PIM components.....                              | 100        |
| 4.2.5.3 Geometrical deformation in the PIM components.....                                | 101        |
| <b>4.3 Numerical simulation of solvent debinding process .....</b>                        | <b>103</b> |
| 4.3.1 Physical model.....   | 103        |
| 4.3.2 Mathematical modelling.....   | 104        |
| 4.3.3 Process numerical implementation.....   | 106        |
| 4.3.4 Numerical simulation results.....   | 106        |
| 4.3.4.1 Evolution of remaining soluble binder content.....                                | 106        |
| 4.3.4.2 Effect of component thickness.....  | 109        |
| 4.3.4.3 Comparison between 1D and 2D numerical simulations.....                           | 111        |
| <b>4.4 Summary.....</b>   | <b>112</b> |
| <b>Chapter 5: Experimental and Numerical Study of Sintering Process</b>                   | <b>115</b> |
| <b>5.1 Introduction.....</b>  | <b>116</b> |
| <b>5.2 Experimental investigation in sintering process.....</b>                           | <b>118</b> |
| 5.2.1 Materials .....   | 118        |
| 5.2.1.1 Powder properties.....  | 118        |
| 5.2.1.2 Binder properties .....   | 119        |
| 5.2.1.3 Samples preparation .....   | 120        |
| 5.2.2 Thermo-mechanical characterisation of W parts under H <sub>2</sub> atmosphere ..... | 121        |
| 5.2.2.1 Dilatometric tests during sintering process.....                                  | 121        |
| 5.2.2.2 Beam bending tests during sintering process.....                                  | 124        |
| 5.2.3 Determination of sintering activation energy.....                                   | 126        |
| 5.2.3.1 Dorn's method.....  | 126        |

|  |                  |
|--|------------------|
| 5.2.3.2 Constant heating rate method.....  | 127              |
| 5.2.4 Densification of tungsten components.....                                    | 128              |
| 5.2.5 Microstructure change and grain growth.....                                  | 130              |
| 5.2.6 Variation of activation energy during sintering process.....                 | 132              |
| <b>5.3 Finite element modeling and identification of sintering parameters.....</b> | <b>135</b>       |
| 5.3.1 Constitutive model for sintering process.....                                | 135              |
| 5.3.2 Identification of sintering parameters.....                                  | 138              |
| 5.3.2.1 Identification of material constants for W components.....                 | 138              |
| 5.3.2.2 Determination of maximum sintering stress.....                             | 142              |
| 5.3.2.3 Determination of uniaxial viscosity.....                                   | 143              |
| 5.3.2.3 Determination of activation energy for grain growth.....                   | 143              |
| <b>5.4 Numerical simulation results .....</b>                                      | <b>146</b>       |
| 5.4.1 Material and process numerical implementation.....                           | 146              |
| 5.4.2 Final shrinkages and relative densities of sintered bars.....                | 148              |
| 5.4.3 Comparison between the simulation and experimental results .....             | 151              |
| 5.4.3.1 Relative density.....  | 151              |
| 5.4.3.2 Final shrinkages.....  | 151              |
| <b>5.5 Summary.....</b>  | <b>153</b>       |
| <hr/> <b>Chapter 6: Conclusions and Perspectives</b>                               | <hr/> <b>154</b> |
| <hr/> <b>References</b>  | <hr/> <b>158</b> |

## List of Figures

- Figure 1.1:** Major processing steps of Powder Metallurgy Technology.
- Figure 1.2:** Components made by PIM process: a) Air injector components are made from stainless steel by MIM [KIN 13], b) Rado watches made by CIM [CON 13] c) W, Mo tungsten alloy products made by MIM [MAD 13], d) Micro-components [MIC 12].
- Figure 1.3:** Schematic diagram of whole PIM process, showing the basic steps from feedstock elaboration stage to sintered component [MAT 13].
- Figure 1.4:** PIM feedstock ready for use in the injection moulding equipments.
- Figure 1.5:** Schematic diagram showing three possible situations in a powder–binder mixture: (a) excess of binder, (b) critical and (c) excess of powder [GER 97, LI 07].
- Figure 1.6:** a) Evolution of mixture apparent density versus powder volume loading of a PIM feedstock and b) Evolution of relative feedstock viscosity versus powder volume loading. Line curve represents a model fitting for the estimation of critical powder volume loading.
- Figure 1.7:** Mixing torque versus mixing time at several levels of powder volume loading, by adding progressively the powder into the mixing chamber.
- Figure 1.8:** Determination of critical powder volume loading through feedstock viscosity model (316L stainless steel,  $D_{50} = 3.4 \mu\text{m}$ , powder loadings varying from 64 to 72%, measured at 160 °C) [KON 12].
- Figure 1.9:** Instruments used to measure the viscosity in our laboratory: a) capillary rheometer and b) rotational rheometer.
- Figure 1.10:** Mixer W 50 EHT with two mixing screws used in our laboratory.
- Figure 1.11:** Hydraulic injection molding equipment, a) Arburg 220-S<sup>®</sup> micro injection molding equipment ( $\phi 15\text{mm}$ , maximum temperature 350°C, maximum volume 10.8 cm<sup>3</sup>, maximum pressure 2000 bar) used in our laboratory and b) detailed sketch of the injection molding equipment.
- Figure 1.12:** Schematic illustration of catalytic debinding process [ATT2 12].
- Figure 1.13:** Schematic illustration of solvent debinding process.
- Figure 1.14:** Used laboratory oven for thermal debinding process with maximum temperature of 300 °C.
- Figure 1.15:** Furnace used in our laboratory for conventional sintering: a) external view; b) internal view.
- Figure 1.16:** Survey of the global sales of the firms according to geographical regions (1990 to 2010). [KON 11].
- Figure 2.1:** Diagram identifying the different debinding techniques based on thermal concept [GER 87].
- Figure 2.2:** Sketch of the pore model for debinding by permeation or diffusion, where the binder–vapor interface is a distance L from the component surface, adapted from [GER 87].
- Figure 2.3:** Porosity dependence of the debinding time as function of the fractional density to illustrate the significant debinding penalty associated with high packing densities [GER 87].

- Figure 2.4:** Schematic of wick debinding mechanism proposed by German [GER 87].
- Figure 2.5:** Schematic of wick debinding mechanism proposed by Vetter et al. [VER2 94], based on German model [GER 87].
- Figure 2.6:** Comparing calculated conversion, conversion rate (- - -) with experimental data (—) at different heating rates 2 and 10 K/min, [ZHA 09].
- Figure 2.7:** Evolution of remaining weight fraction of polymer: comparison between the TGA analysis and MDC with a single step for polypropylene PP, [AGG 07].
- Figure 2.8:** Evolution of remaining weight fraction of multi component binder system (PP+PW+SA): comparison between the TGA analysis and the model (MDC multireaction steps), [AGG 07].
- Figure 2.9:** Failed ceramic components by cracks and distortion after thermal debinding process, (a, b) components heated with a 10 °C/min ramp to 600 °C with a 1 h hold [ABE 11], (c, d) components heated with 7.5 and 5 °C/min, respectively, [SAC 11].
- Figure 2.10:** Mechanisms of mass transport during sintering: 1) surface diffusion, 2) grain boundary diffusion, 3) volume diffusion, 4) evaporation and condensation.
- Figure 2.11:** Basic phenomena occurring during sintering under the driving force for sintering.
- Figure 2.12:** Microstructure evolution during sintering stages, [RIV 11].
- Figure 2.13:** Two-particle geometric model for the initial stage of sintering, [CAL 05].
- Figure 2.14:** Neck evolution during the first stage of sintering through the use of cerium oxide (CeO<sub>2</sub>) powders, [CLA 13].
- Figure 2.15:** Representative unit cell for intermediate -stage solid -state sintering: (a) Original model of Coble [COB 61] and (b) modification by Beere [BEE 75], adapted from [BAN 12].
- Figure 2.16:** Closed pores located at grain corners during the final stage of sintering [GER 96], adapted from [SON 07].
- Figure 3.1:** Scanning electron micrographs of fine 316L stainless steel powders (D50=3.4 µm) used in the proposed investigations with magnification equals to a) 2000 and b) 10000.
- Figure 3.2:** Mixing torques vs. time for 316L stainless steel powder with different powder volume loadings at maximal mixing temperature of 160 °C during 30 min.
- Figure 3.3:** Scanning electron micrographs of feedstock loaded at 60, 62, 64 and 66% after mixing stage.
- Figure 3.4:** Heating cycles of the thermal debinding process using three heating rates of 2, 5 and 10° C/min with same cooling rate of 20°C/min.
- Figure 3.5:** Differential Scanning Calorimetry apparatus, DSC92.
- Figure 3.6:** DSC curves related to 316L stainless steel feedstock loaded at 60 % at different heating rates.
- Figure 3.7:** Remaining binder content vs. temperature, corresponding to different powder volume loadings at different heating rates for 316L stainless steel in argon atmosphere.
- Figure 3.8:** Weight binder loss rate vs. temperature, corresponding to different powder volume loadings at different heating rates for 316L stainless steel in argon atmosphere.

- Figure 3.9:** Curves related to the Ozawa method used for the determination of activation energy related to the thermal decomposition of steel 316L stainless steel feedstock loaded at 60, 62, 64 and 66%.
- Figure 3.10:** Curves related to the Kissinger method used for the determination of activation energy related to the thermal decomposition of steel 316L stainless steel feedstock loaded at 60, 62, 64 and 66%.
- Figure 3.11:** Maximal binder decomposition temperature versus powder volume loading: (a) first step corresponding to degradation of PW+SA, (b) second step corresponding to degradation of PP.
- Figure 3.12:** Remaining binder content vs. temperature, corresponding to different powder volume loadings at different heating rates for 316L stainless steel in argon atmosphere.
- Figure 3.13:** Apparent activation energy of 316L stainless steel feedstocks (elaborated at the same mixing conditions 160°C, 30 rpm and 30 min) as a function of powder volume loading: (a) first step corresponding to degradation of PW+SA, (b) second step corresponding to degradation of PP.
- Figure 3.14:** SEM images of debinded tensile specimen after thermal debinding process for feedstock loaded at 66% of powder volume loading, debound at 300°C with the same heating rate and the same atmosphere.
- Figure 3.15:** SEM images of debinded tensile specimen after thermal debinding process for feedstock loaded at 62% of powder volume loading, debound at 300°C with the same heating rate and the same atmosphere.
- Figure 3.16:** Curves related to the Flynn-Wall-Ozawa (FWO) method used for the determination of activation energy related to the thermal decomposition of steel 316L stainless steel feedstock loaded at 60%.
- Figure 3.17:** Apparent activation energy of 316L stainless steel feedstocks as a function of fraction weight loss at different powder volume loadings from 60 to 66% elaborated at the same mixing conditions 160°C, 30 rpm and 30 min.
- Figure 3.18:** Pellets of granulated feedstock based on copper powders ready for use in the injection moulding machine.
- Figure 3.19:** Square specimens (5.6×5.6×0.92mm) injection moulded at 175°C using Arburg machine.
- Figure 3.20:** Binder remaining content inside 0.92-mm-thick square sample at different debinding temperatures 40, 50 and 60 °C.
- Figure 4.1:** Evolution of remaining binder content versus temperature, comparison between experimental and identified kinetic model results for a fine 316L stainless steel feedstock loaded at 60, 62, 64, and 66% of powder volume loading with heating rate eq. 2 °C/min.
- Figure 4.2:** Description of geometry used for FEM simulations (a) Three-dimensional component with boundaries and (b) two-dimensional cross section of the component, [MAN 13].
- Figure 4.3:** Interaction diagram between partial differential equations (PDE), Heat transfer and Structural mechanics module, [MAN 13].
- Figure 4.4:** Finite element discretization used for FEM simulations (a) Three-dimensional component (b) two-dimensional cross section of the component.

- Figure 4.5:** Remaining polypropylene binder content distribution in (%) for fine 316L stainless steel feedstock loaded at 60% with a heating rate equals 2°C/min at debinding temperature of 385 and 420 °C (a) 2D, (b) 3D, respectively.
- Figure 4.6:** Calculated distributions of binder content inside the component at different debinding temperatures for fine 316L stainless steel feedstocks loaded at 60 and 62% of powder volume loading.
- Figure 4.7:** Temperature distribution in°C at the end of debinding process for fine 316L stainless steel feedstocks loaded at 60 and 62 % of powder volume loading, (a)-(c) along the length direction and (b)-(d) along the width direction.
- Figure 4.8:** Temperature distribution in°C at the end of debinding process for fine 316L stainless steel feedstocks loaded at 60 powder volume loading, (a) 2D and (b) 3D.
- Figure 4.9:** Normal strains evolution in the PIM component for fine 316L stainless steel feedstocks loaded at 60%, [MAN 13].
- Figure 4.10:** Contours of strains inside the component for fine 316L stainless steel feedstocks loaded at 60%.
- Figure 4.11:** Volumetric strains in the PIM components with same heating rate of 2°C/min for different powder volume loadings.
- Figure 4.12:** Schematic of the diffusion model used in numerical simulation.
- Figure 4.13:** Finite element discretization.
- Figure 4.14:** Temperature dependence of binder remaining after 30 min solvent debinding by linear regression fitting of equation (4-22).
- Figure 4.15:** Steps in the solution procedure using finite element method for solvent debinding process.
- Figure 4.16:** Comparison between experimental and numerical remaining soluble binder content inside 0.92-mm-thick square sample at different debinding temperatures from 40 to 60 °C.
- Figure 4.17:** Contours of soluble binder content inside 0.92-mm-thick square sample, (a) after 15 minutes solvent debinding and (b) after 30 minutes solvent debinding.
- Figure 4.18:** Debinding time needed to reach 95 % for components with different thicknesses at different temperatures.
- Figure 4.19:** Contours of soluble binder content inside square samples with different thickness after 30 minutes solvent debinding.
- Figure 4.20:** Contours of soluble binder content inside 0.92-mm-thick square sample after 10 minutes solvent debinding, (a) results for simulation 1D and (b) 2D.
- Figure 4.21:** Binder remaining content inside 0.92-mm-thick square sample using 1D and 2D numerical simulations at 50°C

- Figure 5.1:** (a, b) SEM (secondary electron) image of fine (0.4 $\mu$ m) and coarse (7.0 $\mu$ m) W powders, Particle size distribution of fine W powder (with cumulative size in the range of 0.4  $\mu$ m) and (d) Particle size distribution of coarse W powder (with cumulative size in range of 7–70  $\mu$ m).
- Figure 5.2:** Tungsten components: (a) molded; (b) solvent debinded in heptane at 37°C for 140 min; (c) thermal debinded at 450 °C for 120 min with a heating rate of 1.5°C/min, followed by heating to 900 °C at 2 °C/min and holding for 30 min under N<sub>2</sub> atmosphere and (d) sintered at 1700°C under H<sub>2</sub> atmosphere.
- Figure 5.3:** (a) Configurations of sintered components of fine and coarse W powders in dilatometer after sintering test at maximal temperature of 1700°C and H<sub>2</sub> atmosphere , (b) vertical dilatometer used in the experiments using Setaram<sup>®</sup> analyser.
- Figure 5.4:** Evolution of shrinkage components vs. time for (a) fine W powders and (b) coarse W powders heated up to 1700°C using a heating rate of 5 °C/min and pure hydrogen atmosphere.
- Figure 5.5:** Evolution of shrinkage rates vs. time (a) fine W powders and (b) coarse W powders heated up to 1700°C using a heating rate of 5 °C/min.
- Figure 5.6:** (a) Components configurations after beam bending tests at 1700°C and 100% hydrogen atmosphere for fine and coarse W powders, (b) vertical dilatometer used in the experiments using Setaram© analyser.
- Figure 5.7:** Deflections of W beam bending components vs. temperature during sintering with heating of 5°C/min in pure hydrogen atmosphere (a) fine grain sizes, (b) coarse grain sizes.
- Figure 5.8:** Deflection rates of W beam bending components vs. temperatures during sintering with heating of 5°C/min in pure hydrogen atmosphere, (a) fine grain sizes, (b) coarse grain sizes.
- Figure 5.9:** Sintering activation energy plots of  $\ln[T\beta(d\lambda/dT)]$  vs.  $1/T$  at different shrinkages and  $Q/R$  is the slope of the plot, (a) 0.4  $\mu$ m, (b) 7.0  $\mu$ m.
- Figure 5.10:** Final relative density of W vs. initial grain size before and after sintering process for components heated up to 1500 and 1700°C with 5°C/min for 5 minutes holding time under pure hydrogen atmosphere.
- Figure 5.11:** Microstructures variation of the sintered W samples after the thermal cycles of heating up to 1700 °C at 5 °C/min under pure hydrogen atmosphere for different holding time, (a) initial powders of 0.4 $\mu$ m, (b) 5, (c) 30, (d) 60, (e) 90 and (f) 120 minutes.
- Figure 5.12:** Change in sintering activation energy values with increasing temperature observed for Dorn's method and constant heating rate method, (a) 0.4  $\mu$ m, (b) 7.0 $\mu$ m using pure hydrogen atmosphere.
- Figure 5.13:** Sintering activation energy vs. initial grain size calculated based on constant heating rate and Dorm's method at 1500 °C using pure hydrogen atmosphere.
- Figure 5.14:** Thermo-elasto-viscoplastic constitutive model used for the sintering process.

- Figure 5.15:** Evolution of uniaxial shrinkage versus sintering time, comparison between experimental and identified model results for: (a) fine W powders and (b) coarse W powders with heating rate eq. 5 °C/min in pure hydrogen atmosphere.
- Figure 5.16:** Maximum sintering stress plotted against initial grain size using pure hydrogen atmosphere.
- Figure 5.17:** Determined uniaxial viscosity vs. sintering temperature, (a) fine powders, (b) coarse powders.
- Figure 5.18:** Grain growth during sintering process up to 1700 °C for 5min holding time and heating rate 5°C/min, (a) fine powders and (b) coarse powders.
- Figure 5.19:** (a) Green component and the support plate before sintering, (b) finite element mesh of the assembly.
- Figure 5.20:** Numerical simulation results-final relative density values of sintered components at 1700 °C.
- Figure 5.21:** Numerical simulation results- shrinkage values of sintered components at 1700 °C.
- Figure 5.22:** Comparison between the experimental and the numerical densities of tungsten components sintered at 1700°C.
- Figure 5.23:** Comparison between the experimental and the numerical shrinkages: (a) fine W powders and (b) coarse W powders with heating rate eq. 5 °C/min.



## List of Tables

|                    |  |
|--------------------|--|
| <b>Table 1.1:</b>  | Brief History related to the development of Powder Metallurgy [ANG 09].  |
| <b>Table 1.2:</b>  | Some proposed mathematical models describing the dependence of the feedstock's relative viscosity on powder loading.                                     |
| <b>Table 1.3:</b>  | Comparison between four major debinding techniques [GON 12].   |
| <b>Table 3.1:</b>  | Particle size distribution of the gas atomized 316L stainless steel powders.   |
| <b>Table 3.2:</b>  | Chemical composition of the gas atomized 316L stainless steel powders.   |
| <b>Table 3.3:</b>  | Characteristics of the polymer ingredients used in the binder system.  |
| <b>Table 3.4:</b>  | Components and contents used for the proposed feedstock formulations with different powder volume loadings.  |
| <b>Table 3.5:</b>  | Weight loss after thermal debinding process for elaborated feedstocks at different heating rates and maximal temperature of 500°C.                       |
| <b>Table 3.6:</b>  | Maximal temperatures for which degradation rate is maximal at the first step for different feedstocks using different heating rates 2, 5 and 10 °C/min.  |
| <b>Table 3.7:</b>  | Maximal temperatures for which degradation rate is maximal at the second step for different feedstocks using different heating rates 2, 5 and 10 °C/min. |
| <b>Table 3.8:</b>  | Activation energy values using Ozawa method for the first and second step of different feedstocks.   |
| <b>Table 3.9:</b>  | Activation energy values using Kissinger method for the first and second step of different feedstocks.   |
| <b>Table 3.10:</b> | Chemical and physical characteristics of the Copper powders.   |
| <b>Table 4.1:</b>  | Content of ingredients used in the binder system for feedstock loaded at 60%.  |
| <b>Table 4.2:</b>  | Identified pre-exponential factors for fine 316L stainless steel feedstocks loaded from 60 to 66%.   |
| <b>Table 4.3:</b>  | Conditions for the numerical simulation of thermal debinding process used for a feedstock loaded at 60%, [MAN 13].                                       |
| <b>Table 5.1:</b>  | Chemical composition of the fine and coarse tungsten powders.  |
| <b>Table 5.2:</b>  | Binder system components used in feedstock preparation.  |
| <b>Table 5.3:</b>  | Relative density after presintering using coarse and fine tungsten powders under H <sub>2</sub> with 4°C/min of heating rate and 120 min holding time.   |
| <b>Table 5.4:</b>  | Shrinkages in different directions and final densities of the sintered components (using different grain size of tungsten powders).                      |
| <b>Table 5.5</b>   | Identified material constants for fine and coarse W powders with heating rate eq. 5 °C/min in hydrogen atmosphere.                                       |

**Table 5.6:** Identified values of grain growth activation energy.

**Table 5.7:** Conditions for the numerical simulation of sintering process used for fine powders 0.4  $\mu\text{m}$ .

## List of Symbols

|                      |   |
|----------------------|---|
| $H$ :                | component thickness   |
| $M$ :                | molecular weight of the vapor   |
| $k$ :                | Boltzmann's constant  |
| $T$ :                | absolute temperature  |
| $D$ :                | particle diameter   |
| $p$ :                | pressure at the binder-vapor interface  |
| $P_0$ :              | external component surface pressure   |
| $\theta$ :           | total porosity  |
| $U$ :                | molecular volume for the solid binder   |
| $G$ :                | fluid viscosity   |
| $A$ :                | pre-exponential factor  |
| $E_a$ :              | apparent activation energy  |
| $R$ :                | universal gas constant  |
| $\beta$ :            | non-isothermal reaction rate  |
| $\Theta$ :           | work of decomposition   |
| $dE_f$ :             | change of system free energy  |
| $X$ :                | diameter of the neck  |
| $T_{\max}$ :         | temperature at which the maximum rate of weight binder loss occurs                                    |
| $C_b$ :              | remaining weight fraction of a polymer  |
| $k$ :                | rate constant for thermal degradation   |
| $C_{b1}$ :           | mass ratio to initial mass of the low molecular weight polymer  |
| $C_{b2}$ :           | mass ratio to the initial mass of the high molecular weight polymer                                   |
| $C_0$ :              | initial mass of the two polymers  |
| $w$ :                | ratio of the initial mass of the low molecular weight polymer to the initial mass of the two polymers |
| $C_{01}$ :           | initial mass of low molecular weight polymer  |
| $C_{02}$ :           | initial mass of high molecular weight polymer   |
| $G(x)$ :             | mean residual squares of the tolerance objective function   |
| $C_b^{\text{exp}}$ : | experimental remaining binder content obtained from the TGA test                                      |

|                      |   |
|----------------------|---|
| $C_b^{num}$ :        | numerical remaining binder content obtained by using the optimization procedure |
| $\phi$ :             | powder volume loading   |
| $\rho_p$ :           | density of powder skeleton  |
| $\rho_b$ :           | density of polypropylene  |
| $C_{pp}$ :           | specific heat coefficient of powder skeleton                                    |
| $C_{pb}$ :           | specific heat coefficient of polypropylene                                      |
| $\vec{q}$ :          | Heat flow   |
| $\lambda_p$ :        | thermal conduction coefficients of the powder skeleton                          |
| $\lambda_b$ :        | thermal conduction coefficients of polypropylene                                |
| $\varepsilon_b$ :    | deformation caused by polymer-content change                                    |
| $\varepsilon_T$ :    | deformation caused by temperature change  |
| $\varepsilon_p$ :    | deformation associated to gas pressure  |
| $\nu$ :              | Poisson's ratio of the powder skeleton  |
| $\alpha_p$ :         | linear-expansion coefficient of powder skeleton                                 |
| $\alpha_b$ :         | linear-expansion coefficient of polypropylene                                   |
| $D$ :                | elasticity matrix   |
| $\sigma$ :           | stress tensor   |
| $\sigma_0$ :         | initial residual stress   |
| $\sigma_x$ :         | stress in the x   |
| $\sigma_y$ :         | stress in the y   |
| $\sigma_z$ :         | stress in the z   |
| $\tau_{xy}$ :        | shear stress in the xy plane  |
| $\Omega$ :           | material domaine  |
| $\partial\Omega_i$ : | boundaries  |
| $\vec{n}$ :          | denotes the normal to the boundaries  |
| $t$ :                | time  |
| $t_f$ :              | final processing time   |

|                       |   |
|-----------------------|---|
| $C_i$                 | initial soluble binder content                                      |
| $C_{rm}$              | average concentration of the remaining binder in the component      |
| $\lambda$             | shrinkage during sintering  |
| $\Delta l$            | change in length  |
| $l_0$                 | original length of presintered components                           |
| $l$                   | length at any time during sintering process                         |
| $\dot{\delta}$        | deflection rate at the middle position of the bending test specimen |
| $\Delta\delta$        | change in deflection  |
| $\Delta T$            | change in sintering temperature                                     |
| $\nu_1$               | isothermal shrinkage rate at first recorded temperature             |
| $\nu_2$               | isothermal shrinkage rate at second temperature                     |
| $K(T)$                | Arrhenius constant  |
| $n$                   | constant whose value depends on the sintering mechanism             |
| $\gamma$              | free surface energy   |
| $G_c$                 | size of the crystallite   |
| $Q$                   | sintering activation energy   |
| $D_0$                 | pre-exponential term of the diffusion coefficient                   |
| $\rho$                | relative density  |
| $\rho_{ap}$           | apparent density  |
| $\rho_{th}$           | theoretical density   |
| $V_{ap}$              | apparent volume (surface $\times$ depth)                            |
| $V_{py}$              | measured volume using the pycnometer                                |
| $\dot{\epsilon}$      | total strain rate   |
| $\dot{\epsilon}_e$    | elastic strain rate   |
| $\dot{\epsilon}_{th}$ | thermal strain rate   |
| $\dot{\epsilon}_{vp}$ | viscoplastic strain rate.   |
| $D_e$                 | elastic stiffness matrix for the isotropic materials                |
| $\alpha$              | thermal expansion coefficient                                       |

|                                  |   |
|----------------------------------|---|
| $\dot{T}$ :                      | incremental temperature                 |
| $I$ :                            | second order identity tensor            |
| $\sigma'$ :                      | deviatoric stress tensor                |
| $\text{tr}(\sigma)$ :            | stress tensor trace                     |
| $G_p$ :                          | shear viscosity of the porous material  |
| $K_p$ :                          | bulk viscosity of the porous material   |
| $\sigma_s$ :                     | sintering stress                        |
| $B$ :                            | material constants of sintering stress  |
| $C$ :                            | material constants of sintering stress  |
| $\dot{\epsilon}_z^{\text{vp}}$ : | vertical strain rate                    |
| $\sigma_z$ :                     | applied external stress on the specimen |
| $\eta_p$ :                       | uniaxial viscosity                      |
| $V_a$ :                          | atomic volume                           |
| $D_{b0}$ :                       | grain boundary diffusion frequency      |
| $\delta_b$ :                     | thickness of grain boundary             |
| $\sigma_m$ :                     | mean stress                             |

# General Introduction

## Contents

---

|          |   |          |
|----------|---|----------|
| <b>1</b> | <b>Context and Research Motivation .....</b>  | <b>2</b> |
| <b>2</b> | <b>Research Problem and Objectives .....</b>  | <b>4</b> |
| <b>3</b> | <b>Thesis Organization and Strategy .....</b> | <b>6</b> |

---

# General Introduction

## 1 Context and Research Motivation

Many industries are constantly faced with the selection of the efficient manufacturing technologies in order to reduce costs, improve performance and increase productivity. Using conventional powder metallurgy technology, produced components require assembly and secondary manufacturing operations in order to get good finished surfaces. To avoid such operations, one of the most efficient technologies is powder injection moulding (PIM). Powder injection moulding (PIM) is an established, net or near-net shape process which is used for the cost-effective mass production of metallic and/or ceramic components. It combines the design flexibility of plastic injection moulding and the advantage of powder metallurgy [HAU 11]. The PIM process includes mixing of either metal or ceramic powders with a binder to produce a feedstock, injection moulding to form a green part with the desired shape by making the feedstock flow into and fill a mold under pressure, debinding to form a brown part by removing the binder components and sintering to near full density [GER 97]. Despite its technical and economic benefits, powder injection moulding technology is still little used in Europe. In fact, the European industry is facing an increasing demand for production of complex shaped functional metallic or ceramic components such as: watch cases, cutting tools, dental implants, surgical instruments, advanced aircraft equipments, and so on.

My research work has been carried out through the FUI NewPIM project (Fonds Unique Interministériel) led by Alliance Company (Saint-Vit, Besançon). This project brings together 13 industrial companies and research laboratories: INSA (Lyon), PEP (Ain), CEA (Grenoble) and FEMTO-ST (Besançon). NewPIM project aims to create a full independent French Industry by developing the PIM process through its processing stages including feedstock elaboration, mixing, moulding, debinding and sintering. Also, to develop a real integrated numerical simulation of PIM process based on physical material parameters resulting from the identification experiments in order to produce complex shaped components in high quantity and quality that will be later used in different fields like automotive by A. Rymond Company and aeronautics by Radiall Company.



So, the FEMTO-ST contribution, in terms of research, to NewPIM project is to carry out different experimental investigations, by determining the required parameters and properties of raw materials (e.g. grain size of powders, powder volume loading, quantity and type of binders) and also the proper condition tests (e.g. mixing time, injection pressure, heating rate, maximal debinding and sintering temperature, atmosphere), in order to get components with high mechanical properties and without any defect. The second contribution is to develop physical models that properly account the main PIM process parameters. Then, numerical simulations, based on the developed physical models, are performed using finite element codes to obtain qualitative informations about debinded and sintered components. Other experimental investigations and numerical simulations of mixing and injection processes are proposed by a Ph.D student in our research team H. Djoudi.

The present research work is performed at the Applied Mechanics Department of FEMTO-ST Institute within the research group “Polymers and Polymers Loaded with Micro and Nano-particles”, directed by Professor Jean-Claude GELIN. This group has more than 15 years of research experience focused on the experimental investigation, optimization, modeling and numerical simulations of PIM processes through many Ph.D theses : M. Dutilly [DUT 98] proposed, for injection process, a physical model to improve the experimental results by varying the main process parameters. For T. Barriere, a biphasic flow formulation has been used and developed to account the segregation effects during injection moulding [BAR 00]. G. Ayad [AYA 06] proposed an optimisation procedure for reducing the powder segregation arising from the injection of feedstocks in a cavity mould. The works of J. Song [SON 07] were devoted to identify the material parameters, used in the implemented sintering constitutive equations, and set up the numerical simulation of sintering process for stainless steel components. Within the three last Ph.D theses [QUI 08], [KON 11], [BRI 12], several rheological tests and physical characterization of new elaborated feedstocks (Nickel iron, actinide powders, TiAl based superalloy, TiNi shape-memory alloy and Tungsten Carbide Cobalt WC/Co) have been carried out.

## 2 Research Problem and Objectives

At the present time, problems related to: thermal debinding and sintering stages have not been enough studied for some increasingly used materials in powder injection moulding process such as Tungsten (W) and molybdenum (Mo). However, for the common powders used in PIM process like 316L steel stainless and copper, thermal debinding process should be more investigated to avoid shape distortions caused by the component failure during this crucial stage.

In the first section of the present Ph.D thesis, debinding process for fine 316L stainless steel and copper feedstocks is investigated. The popularity of this type of powders results from its capabilities to be sintered to high densities and its corrosion resistance [QUI 09]. Nevertheless, large quantities of PIM components made of 316L stainless steel and/or copper powders still have problems like shape distortions and cracks during debinding stage. These problems are principally due to an incomplete binder removal, where the trapped polymeric residues will be a contamination source and may affect the final physical or electrical properties of the component [MAS 89]. If the binder removal is too fast, defects such as cracks and large voids may appear and will affect the micro-structural characteristics of the component during sintering [DON 89].

So, the main goal of this section is to investigate the influence of powder volume loading on thermal debinding behaviour of the feedstocks based on 316L fine stainless steel powders ( $D_{50}=3.4 \mu\text{m}$ ) and a multi-component binder system. Thermogravimetric analyses (TGA) are employed to analyze the kinetics and physical of thermal debinding behaviour under argon atmosphere. X. Kong reported in his Ph.D thesis [KON11] that feedstocks loaded at 60, 62, 64 and 66% could be well injected without external defects on the injected components. Therefore, evolution of remaining binder with different heating rates is analysed using different feedstocks loaded typically at 60, 62, 64 and 66 vol% in order to estimate the kinetic parameters: thermal activation energy ( $E$ ) and pre-exponential factor ( $A$ ) using Kissinger and Ozawa method. Based on the identified kinetic parameters, one should set up a physical model of thermal debinding stage using finite element method. To do this, a coupled mathematical model for mass diffusion and heat transfer in deformable porous media is developed.

The second part of the Ph.D thesis is focused principally on the investigation of the solid state sintering of tungsten (W) powders injection moulded components under pure hydrogen atmosphere. High density of sintered tungsten components is hard to be achieved. Owing to the very high fusion point, the consolidation of a conventional microcrystalline W powder is difficult and generally requires a temperature in excess of 1700°C through solid-state sintering in density electrical resistance sintering furnace under hydrogen atmosphere [AVI 10]. The low as-sintered density is an obstacle to the production of pure W components by PIM for applications concerned by high temperature such as electrodes of high intensity discharge lamps, plasma facing components for fusion reactors, furnace parts, etc. Many efforts have been reported to improve the sinterability of W and reduce the sintering temperature. Recently, among theses researches, Chanthapan et al. [CHA 12] carried out an experimental investigation using W powder (0.6-0.9  $\mu\text{m}$ ) sintered by field assisted sintering technology (FAST) at various processing conditions. The sample sintered with in-situ hydrogen ( $\text{H}_2$ ) reduction pretreatment and pulsed electric current during heating showed the lowest amount of oxygen. For the sample sintered at 2000°C for 30 min holding time, the maximum achieved relative density is 98.5%.

In this second part of my Ph.D researches, the aim goal is to carry out conventional sintering experiments, using dilatometer, in order to understand the densification behaviour of tungsten material and determine the different physical parameters like sintering activation energy and grain growth energy. In another way, we try to decrease the sintering temperature of tungsten from 2300 to 1700°C by using different particle sizes and sintering atmospheres. The obtained results reveal that the W components, made of fine powders 0.4  $\mu\text{m}$ , are successfully manufactured with a relative density of (90-94%) at the end of sintering process. Based on the experimental data, one has to identify the material parameters for viscoplastic sintering model and then set up the associated numerical simulation. Therefore, our final goal is to provide a fruitful numerical simulation for powder injection moulding process to predict final shrinkages and densities of tungsten injection moulded components during sintering stage.

### **3 Thesis organization and Strategy**

This thesis is organized into five chapters describing the existing literature and the results of this work. Firstly, a general introduction into the research topic provides a statement of the research motivation, problem and objectives of the present Ph.D thesis. In the chapter 1, the state of the art of powder metallurgy and powder injection moulding is briefly introduced. The chapter 2 consists in literature review including thermal debinding and sintering mechanisms with previous works on modeling and numerical simulations for both mechanisms.

For chapter 3, thermogravimetric analyses (TGA) are performed to analyze thermal debinding behaviour under argon atmosphere for 316L feedstocks, loaded at different powder volume loadings, by measuring the reaming binder during the thermal debinding stage using different heating rates. Also, experimental investigations are carried out for water solvent debinding by measuring the remaining quantity of soluble binder at different temperatures in order to estimate the diffusion coefficient.

In chapter 4, based on the experimental debinding characterization, kinetic parameters are identified using an inverse method implemented in Matlab<sup>®</sup> software. A coupled mathematical model, based on the previous kinetic parameters, is implemented in Comsol software in order to predict the spatio-temporal distribution of reaming binder content, debinding temperature inside the debinded component and its deformation during thermal debinding. Numerical simulations of solvent debinding are also presented.

Chapter 5 treats principally the sintering behaviour of tungsten components under high temperature and pure hydrogen atmosphere. The experimental characterization has been performed by using dilatometric and bending tests. The adopted phenomenological model for sintering based on continuum mechanics is implemented in Abaqus software for the numerical simulation of sintering process.

Finally, we present conclusions as well as lines of future work which can complete the present work for both processes: thermal debinding and sintering.

# **Chapter 1: State of the Art of Powder Injection Moulding Technology**

---

## **Contents**

---

|   |           |
|---|-----------|
| <b>1.1 Introduction.....</b>  | <b>08</b> |
| <b>1.2 Powder Injection Moulding (PIM).....</b>                         | <b>13</b> |
| 1.2.1 Brief history of Powder injection moulding.....                   | 13        |
| 1.2.2 Principal powder injection moulding steps.....                    | 14        |
| 1.2.2.1 Feedstock elaboration stage.....                                | 15        |
| 1.2.2.2 Injection moulding stage.....                                   | 23        |
| 1.2.2.3 Debinding step.....   | 25        |
| 1.2.2.4 Sintering step.....   | 30        |
| <b>1.3 Raw material and Market of PIM.....</b>                          | <b>32</b> |
| 1.3.1 Raw material for metal Powder Injection Moulding technology ..... | 32        |
| 1.3.1.1 Metal powders.....  | 32        |
| 1.3.1.2 Binder system.....  | 32        |
| 1.3.2 Powder Injection Moulding Market.....                             | 33        |
| <b>1.4 Summary.....</b>   | <b>34</b> |

---

## **1.1 Introduction**

Metallic materials play an important role in our daily life. Such type of materials always generated curiosity and interest all over the world due to their large applications. They provide us with innumerable and invaluable services that make our existence easier or more enjoyable: from transport, defense, security, information and communication technology to advanced manufacturing. Metallic materials as exactly powders are generally used in manufacturing of metallic components which can be produced with simple or complex shapes depending on the used technique. The art and science of producing metal powders is called Powder Metallurgy (PM). The time when powder metallurgy was first used dates back to ancient time, 3000 BC. Examples are gold powder by the Incas, iron powder by the Egyptians and the Delhi column in India [GER 94]. These civilizations forged ornamental pieces, daggers, and other weapons from metal without the process of melting.

The importance of Powder Metallurgy as an important manufacturing process became evident as early as 19<sup>th</sup> century when tungsten powders were produced and strengthened with thoria for use in electric lamp filaments [ANG 09]. Since the end of the 20<sup>th</sup> century, people during the 1920s were overwhelmed by the rise of a modern consumer and began civilian automobile manufacturing. The emergence of the civilian automobile market caused a large increase in demand for metal components, especially for chain self-lubricating and oilless bearings that were popular automotive parts. In the 1970s, manufacturers began using metal parts in TVs, radios, electric fans, refrigerators and heating appliances and many more applications that still see use today. About the 1980s, companies had begun using powdered metals for airplane parts as well as an increasing number of automobile components.

In particular, the growth of Powder Metallurgy was phenomenal during the last quarter of the 20<sup>th</sup> century with the development of novel material processing techniques such as Atomization, Mechanical Alloying (MA), Rapid Solidification Process (RSP) for powder production, Cold Isostatic Pressing (CIP) and Hot Isostatic Pressing (HIP) for component fabrication. A brief history related to the development of Powder Metallurgy is given in **Table 1.1** [ANG 09].

**Table 1.1:** Brief History related to the development of Powder Metallurgy [ANG 09].

| Date        | Description  | Origin                     |
|-------------|--|----------------------------|
| 3000 BC     | “Sponge iron” for tools and other implements   | India, Egypt               |
| 1200 AD     | Cementing of noble metals (platinum)   | South America              |
| 1781        | Fusible platinum-arsenic alloy   | France, Germany            |
| 1790        | Production of platinum-arsenic chemical vessels  | France                     |
| 1822        | Platinum ingot making from powders   | France                     |
| 1826        | High-temperature sintering of platinum powder compacts   | Russia                     |
| 1829        | Wollaston method producing compact platinum from sponge  | England                    |
| 1830        | Sintering of different metals and alloy powders  | Europe                     |
| 1870        | Patent for bearing materials made from metal powders   | United states              |
| 1878-1900   | Incandescent lamp filaments  | United states              |
| Early 1900s | Porous metals and metallic filters   | United states              |
| 1915s-1930s | Cemented carbides  | Germany                    |
| 1940s       | Iron powder metallurgy   | Central Europe             |
| 1950s-1960s | P/M wrought and dispersion-strengthened products, including P/M forgings, mechanical alloying, oxide dispersion strengthened nickel and iron base alloys | United states              |
| 1970s       | Hot Isostatic, Pressing, P/M tool steels and superplastic superalloys  | United states              |
| 1980s       | Rapid solidification and powder injection moulding   | United states              |
| 1990s       | Intermetallics, metal-matrix composition, spray forming, nanoscale powders and warm compaction   | United states and England  |
| 1990s-2000s | Micro Powder Injection Moulding ( $\mu$ PIM)   | Japan, Europe              |
| 2000s-2012s | Two-component Micro Powder Injection Molding (2C- $\mu$ PIM), Inmold-labelling Micro Powder Injection Molding (IML- $\mu$ PIM)                           | Germany and United kingdom |

[PIO 12, ATT1 12 ]

Too high melting point for some materials (W, Mo) makes Powder Metallurgy competitive with the other processes such as casting, forging, and machining. Before the metallic powders are produced and classified, the conventional powder metallurgy process generally consists of four major processing steps: (1) production of metal powder (2) mixing of powders, (3) compaction, (4) sintering and a number of secondary manufacturing and finishing operations, **Figure 1.1**.

Several production methods are available for making powders. Most common is atomization, which produces nearly 80% of the total volume of powders. This method produces of both ferrous and nonferrous metals; speciality powder like stainless steel, superalloy (nickel base) as well as titanium alloy powders are also

made by this technique. Reduction of compounds is another widely used process used for the production of iron, copper as well as tungsten and molybdenum [NAG 06]. Powders having the desired size range, shape and other characteristics are chosen to obtain the properties required for the end use, **Figure 1.1-a**. Powders along additives are mixed thoroughly using mixers. Lubricants (0.5-2% by weight of the charge) may be added prior to mixing to facilitate easy ejection of the component and minimize the wear of compaction tool. Typical lubricants include waxes or metallic stearates, graphite, stearates, **Figure 1.1-a**. Powders are then characterized for properties like size, flow, density and compressibility before being compacted. Powder characterisation is very important since powder characteristics influence both the compaction behaviour as well as the properties of green and sintered components [NAG 06].

The desired quantities of different types of powder to be mixed are put inside a cylindrical drum closed from both the ends, **Figure 1.1-b**. The cylinder is then rotated to mix the powder. To ensure uniform mixing, time and speed of rotation are controlled. It should be noted that if the mixing is not properly carried out, the ingredients will not be distributed uniformly and the desired properties in the product will not be obtained. On the other hand, excessive mixing can work-harden the metallic powders making the compaction difficult [NAG 06].

A component is produced from powdered metal by filling a rigid die, which gives the final shape to the product, with metal powder, and applying pressure from top and bottom by movable punches. The fine particles of the powder are forced together so intimately that they interlock and form mechanical bonds [NAG 06]. The pressure required to compact depends upon the desired porosity, the type of metallic powders used, and the size of the product. This step is known as compaction and is illustrated in **Figure 1.1-c**.

Sintering of the green component is carried out in a furnace under a controlled atmosphere to bond the particles metallurgically, **Figure 1.1-d**. Sintering is carried out at temperatures about 70% of the absolute melting point of the material. Bonding occurs by diffusion of atoms, giving integrity to the component. Shrinkage occurs during sintering resulting in densification of the component. This densification enables significant improvements in the physical and mechanical properties of the component [ANG 09].



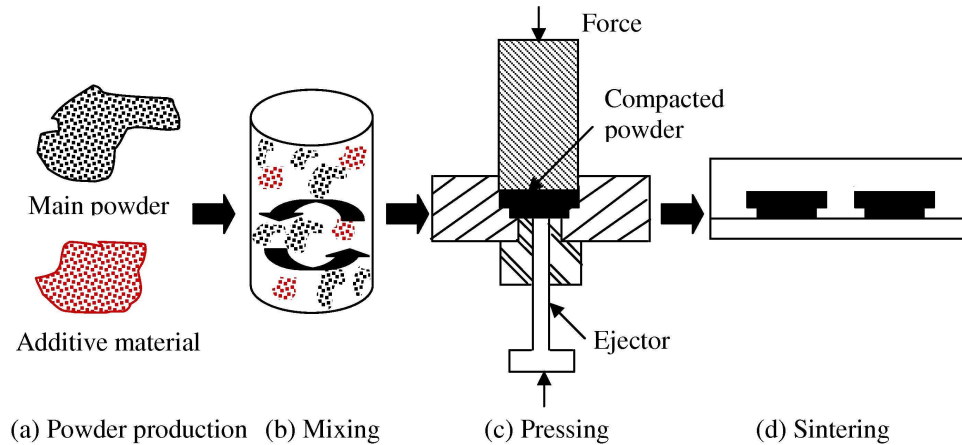


**Figure 1.1:** Major processing steps of Powder Metallurgy Technology.

Many sintered components are machined prior to final assembly, as certain features such as finish dimensions and precision, high densities and smoother surface finish must be introduced by secondary manufacturing operations [MAD 95, SAN 97]. It is estimated that over 50% of all Powder Metallurgy components require machining [BER 01].

Nevertheless, Powder Metallurgy is a relatively new technology that had the potential to enhance the production of metal components and has also provided a good source of revenue for many companies over the world. To highlight the contribution of powder metallurgy for industry, the following advantages and limitations of this technology, compared with the other conventional processes such as (casting, extrusion and forging), are given as follow [ANG 09]:

Powder Metallurgy offers the following specific advantages:

1. Powder Metallurgy consumes only around 45% of the energy and number of process is greatly reduced compared with forging process,
2. Reducing unnecessary cost encountered during the machining process,
3. Powder metallurgy steps are simple and automated that make the PM as a mass production process with around 60000 components per hour for small and simple shapes,
4. Wide variety of materials is possible,
5. Refractory materials as tungsten and molybdenum can be used to produce components that are difficult to manufacture.

Powder Metallurgy has the following limitations [ANG 09]:

1. Poor mechanical proprieties including low fracture resistance which is due principally to the residual porosity. The use of such components can be limited when high stresses are required,
2. The cost of required equipments is so expensive, the used dies in powder metallurgy must be manufactured with expensive materials and be relatively soft to applied pressures during pressing step,
3. Pressing step is generally accompanied by nonuniform density which leads to large variations in the property of produced components,
4. Components with complex shapes can not be produced using this type of technology because they can not be ejected from the dies,
5. Secondary manufacturing operations are needed in order to obtain good finished surfaces,
6. Health and safety hazards: the smaller the particle size, the greater the potential health hazard,
7. It is economical for only mass production.

At the present time, main challenges in Powder Metallurgy research field are design complexity and flexibility of the elaboration process, with quality production and lower manufacturing cost. There have been a lot of developments in which researchers have always tried to propose their best solution to fulfill the innovative industries and their growing requirements. One of the new invented methods is to combine the recent and innovative powder metallurgy technology with the plastic injection moulding process. Such new technology is called Powder Injection Moulding (PIM).

Principally, Powder Injection Moulding process is more complicated compared to the plastic injection moulding process. The process is based on the use of fine and/or coarse powder particles mixed with the small quantity of wax binders and/or thermoplastic polymer to form the feedstock that can be moulded [GER 97]. This new process allows us to produce functional components with high quality and complex shapes, which were and still the main limitations for conventional powder metallurgy.

## **1.2 Powder Injection Moulding Process (PIM)**

### **1.2.1 Brief history of powder injection moulding**

In recent years, industry was able to produce complex shaped components using injection moulding technology. Nevertheless, these components have been only made of typical materials as polymers or binders and especially those with thermoplastic behaviour. Metals and ceramics often have advantages over other materials such as polymers. They are widely used in various technical applications because of their property advantages such as: high mechanical properties, high operating temperatures and their special magnetic and thermal properties which are not possible with polymers. On the other hand, polymers have light weight and low viscosity which make the injection process comfortable and easy for them.

A new process has been recently developed by regrouping the advantages of both powders and polymers; this method is called Powder Injection Moulding (PIM). Powder injection moulding process is an economical manufacturing process which enables the use of shaping advantage of injection moulding to produce large amounts of small and complex metal or ceramic components which can not be made by conventional powder metallurgy process [SCH 00, JOR 08]. The PIM process is principally related to the used powders; it is always called Ceramic Injection Moulding (CIM) in the case of ceramic powders and Metal Injection Moulding (MIM) when the metallic ones are used. The PIM process consists in a small quantity of a polymer binder with an inorganic powder to form a feedstock that can be injected and moulded in injection equipments [GER 97]. After moulding, the polymeric binder is extracted and the powder is sintered to near-theoretical densities.

PIM technology was developed at the beginning of the twentieth century, exactly in November 1940; Klinger et al. got a German patent claiming, a method of producing spark plugs by injecting a ceramic component with addition of organic binders into a mould by application of pressure [KLI 40]. However at that time, ceramic injection moulding was of minor interest to the ceramic industry [MUT 89]. Development efforts performed during the 1970's and 1980's had given more attention and significant progression to PIM technology [GER 07]. In 1984 Carborundum carried out a considerable work on injection moulding to produce turbocharger rotors. Injection moulding had enabled General Motors Company to

produce such components as axial turbine blades and pre-combustion chambers [MAC 84]. Among net-shaping techniques, powder injection moulding (PIM) is considered to be well-suited for mass production of dimensionally precise, 3D complex part geometries from metals or ceramics [ONB 10]. Some examples of components made by Powder Injection Moulding process are shown in **Figure 1.2**.

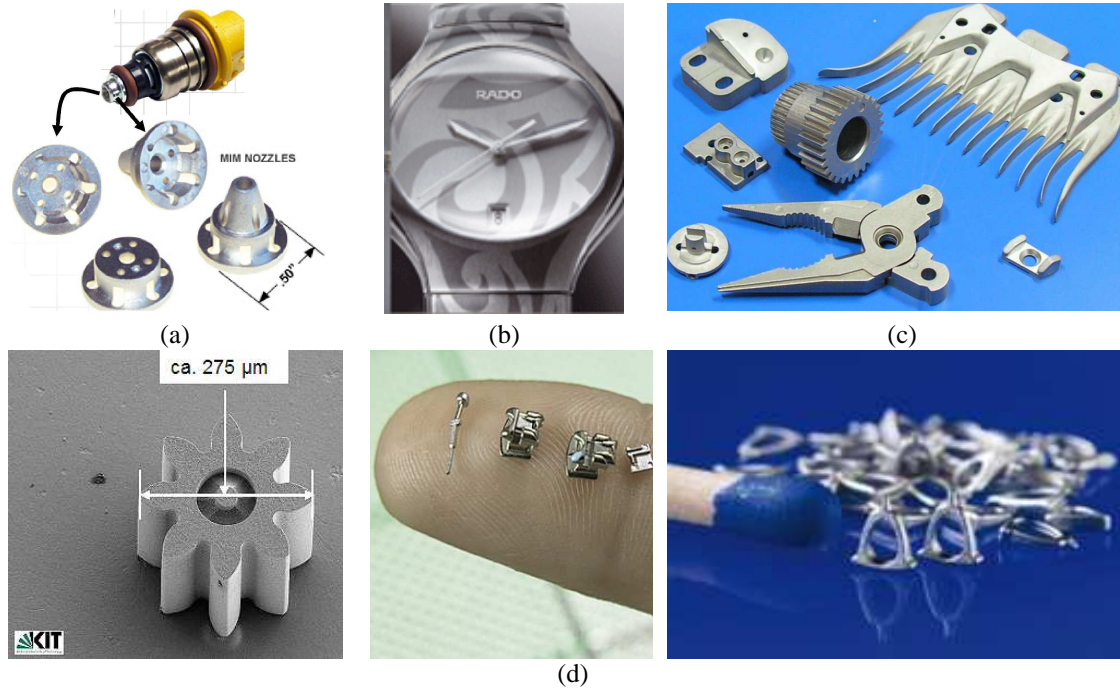


**Figure 1.2:** Components made by PIM process: a) Air injector components are made from stainless steel by MIM [KIN 13], b) Rado watches made by CIM [CON 13] c) W, Mo tungsten alloy products made by MIM [MAD 13], d) Micro-components [MIC 12].

### 1.2.2 Principal powder injection moulding steps

A schematic diagram of the whole powder injection moulding process is shown in **Figure 1.3**. The process begins by mixing metallic or ceramic powders with binder system in order to produce a feedstock.

The feedstock is heated and then injected under pressure into the tool cavity in order to get the desired shape. During the debinding step, the binder is partially removed from the component. At the final step, the debinded component is heated at high temperature in such a way that particles bond together and create one solid coherent component.

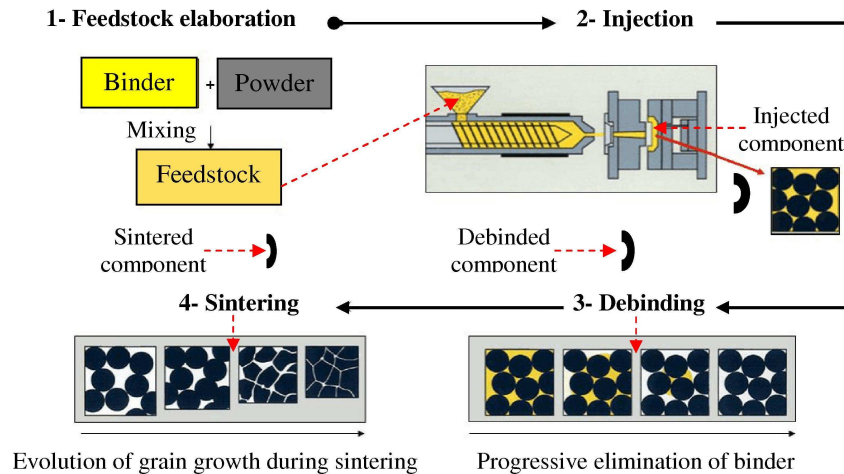


**Figure 1.3:** Schematic diagram of whole PIM process, showing the basic steps from feedstock elaboration stage to sintered component [MAT 13].

#### 1.2.2.1 Feedstock elaboration stage

The procedure of feedstock preparation consists of mixing a small amount of polymer, known as a binder, with small-sized metal or ceramic powder. The obtained product is called “feedstock”, as shown in **Figure 1.4**.

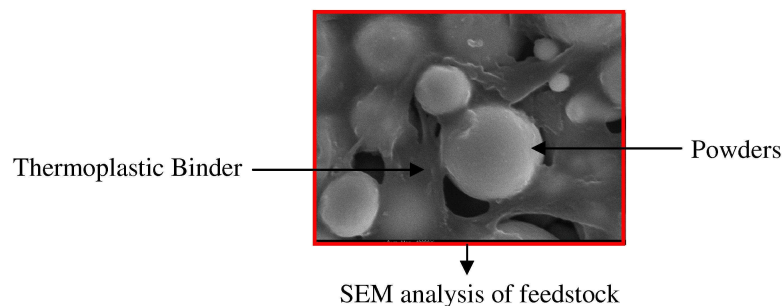


**Figure 1.4:** PIM feedstock ready for use in the injection moulding equipments.

The feedstock is then injected using an injection moulding equipments, as that are used for polymer, to produce a component of defined geometry. In powder injection moulding, the feedstock preparation is one of the crucial steps. All the other steps, injection, debinding and sintering, depend largely to this step and any mistake made during the feedstock elaboration will induce later several problems such as porosity that causes distortions and deformations in the final component. From literature, one can resume the following factors that should be considered and taken into account before the feedstock elaboration step:

The first factor is the powder characteristics, in the most common technology of MIM, powders must be of small particle size, typically less than 20  $\mu\text{m}$ , to accomplish sintering to nearly full density. Also, spherical powders give desirably low viscosity mixtures as well as isotropic shrinkage and high full density, while slightly irregular powders are less prone to slumping during debinding and early stages of sintering. Slightly irregular powders also provide the so-called brown strength or the compact strength subsequent to debinding, which is desirable in many situations [KLA 07]. These and other opposing requirements suggest that a spheroidal powder, that is, a nearly but not fully spherical powder, the particles of which have an aspect ratio of approximately 1:1.2 and a packing density of approximately 60% of theoretical, is considered most desirable [GER 97]. Another way can be used to improve the feedstock quality, Pascoli et al. used blends of gas- and water- atomized powders to obtain an optimal combination of injection moulding and mechanical properties [PAS 02]. Basically, a feedstock should contain the maximum powder content to minimize shrinkage during sintering, and at the same time, without sacrificing its ease of moulding. A feedstock with the optimal powder fraction will have proper rheological properties for moulding, small distortion and good mechanical properties after debinding and sintering [LI 07].

The second controlled factor is the binder system composition. Generally, a binder system is composed of different components with low molecular weight (stearic acid and paraffin wax...etc) as primary binder component and high molecular weight (polypropylene...etc) as secondary binder component. The primary binder component is removed first to partially open the pores. The secondary binder component remains in the green moulded component and retains the shape of the component after debinding step. Waxes are often used as primary binder components. They have low melting point, good wetting behaviour, short molecular chain, low viscosity and decompose with small volume change. However, its disadvantage is poor mechanical properties. Ethylene Vinyl Acetate (EVA), polypropylene (PP) and High Density Polyethylene (HDPE) are good secondary binder components since they have high strength and can serve as backbone polymers during debinding [YAN 99, LIU 01]. The used debinding method (catalytic, thermal, solvent, etc.) should be also taken into account during the elaboration of the binder system components.



The ratio powder / binder system is a relevant factor and must be slightly less than the critical value. Several problems are encountered when this ratio is too low or too high. The excess binder will separate from the powder during debinding and cause slumping and inhomogeneities in the brown component, **Figure 1.5-a**.

On the other hand, too much powder increases the feedstock viscosity which results difficulties in moulding operation. Trapped voids are also created and cause cracks in the brown component during debinding step, **Figure 1.5-c**. Critical powder concentration occurs when all the powder particles are packed as closely as possible with enough binder to occupy all the voids, **Figure 1.5-b**. Powder loading is usually measured in terms of the volumetric ratio of powder to binder, according to the following mixture law [JOR 08]:

$$\frac{w_p / \rho_p}{w_p / \rho_p + w_b / \rho_b} \quad (1-1)$$

where  $w_p$  and  $w_b$  are the weight fraction of powder and binder.  $\rho_p$  and  $\rho_b$  are the densities of the powder and binder respectively.

Among the three situations shown in **Figure 1.5**, the second one gives the ideal example for a feedstock with a proper homogeneity. The importance of feedstock homogeneity has been pointed out by several researchers and all agree that the inhomogeneity of the feedstock can lead to powder/binder separation and therefore defects in the final PIM components. In order to prevent the agglomeration of powder or binder system components, several research works have been focused on the determination of the critical powder volume loading [LIU 00, KON 12], studying the effects of binder system, powder composition [AHN 09] and other parameters related to the mixing operation such as: mixing equipments, mixing temperature, mixing time and shear rate [GER 90, GER 97, SUP 00]. The principal aim of these investigations is to elaborate homogenous feedstocks that can be injected and moulded without any problems.

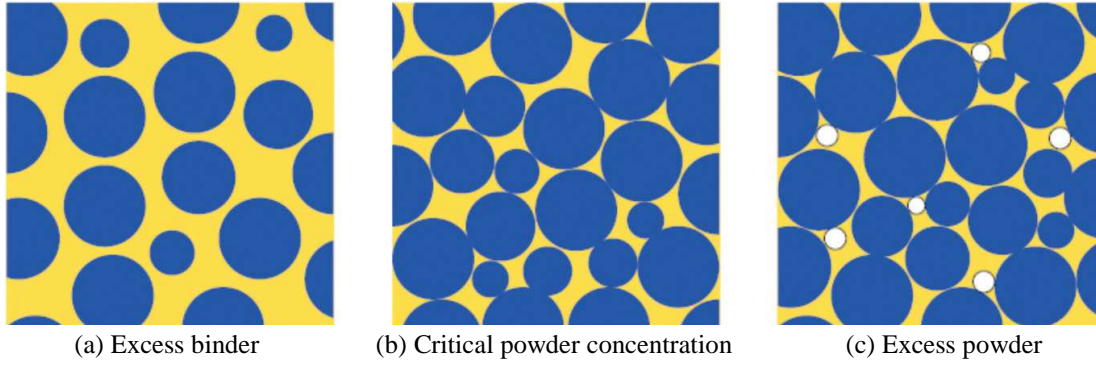


**Figure 1.5:** Schematic diagram showing three possible situations in a powder–binder mixture: (a) excess of binder, (b) critical and (c) excess of powder [GER 97, LI 07].

### Methods for the determination of the critical powder volume loading

Determination of the optimal solid loading for feedstock elaboration is an important parameter for PIM industry. Any given feedstock has an optimal powder volume loading which is just slightly below the critical one. The critical powder volume loading can be determined using different methods by representing: feedstock apparent density versus powder loading, feedstock viscosity versus powder loading, mixing torque versus mixing time at several levels of powder loading and finally feedstock viscosity model versus powder loading.

Density of feedstock versus composition (powders and binders) allows determination of the critical powder volume loading [SHI 06]. **Figure 1.6-a** illustrates a typical curve of the feedstock apparent density versus solids fraction. The feedstock density depends on the powder volume loading. At low powder volume loading, the feedstock density follows along the theoretical density line, calculated by the following equation:

$$\rho_{mix} = \phi \rho_p + (1 - \phi) \rho_b \quad (1-2)$$

where  $\rho_{mix}$  is the density of the feedstock,  $\phi$  is the powder volume loading,  $\rho_p$  is the density of the powder and  $\rho_b$  is the density of the binder.

At a certain composition, the mixture density breaks away from the theoretical line which means that the powders are in their closest packing condition and just enough binder exists to fill the voids between the particles. The powder volume loading for which the density breaks away from the theoretical line corresponds to the critical powder volume loading as shown in **Figure 1.6-a**.



Feedstock viscosity vs. powder loading consists of the analysis of the feedstock viscosity dependence on the powder loading. Viscosity of a PIM feedstock has a great dependence on the solids loading. Increasing the powder loading, the feedstock becomes difficult to flow and viscosity increases. As the powder loading approaches to the critical value, the viscosity increases faster and becomes unacceptable for powder injection moulding process, as shown in **Figure 1.6-b**. **Table 1.2** shows some proposed mathematical models describing the dependence of the feedstock's relative viscosity on powder loading.

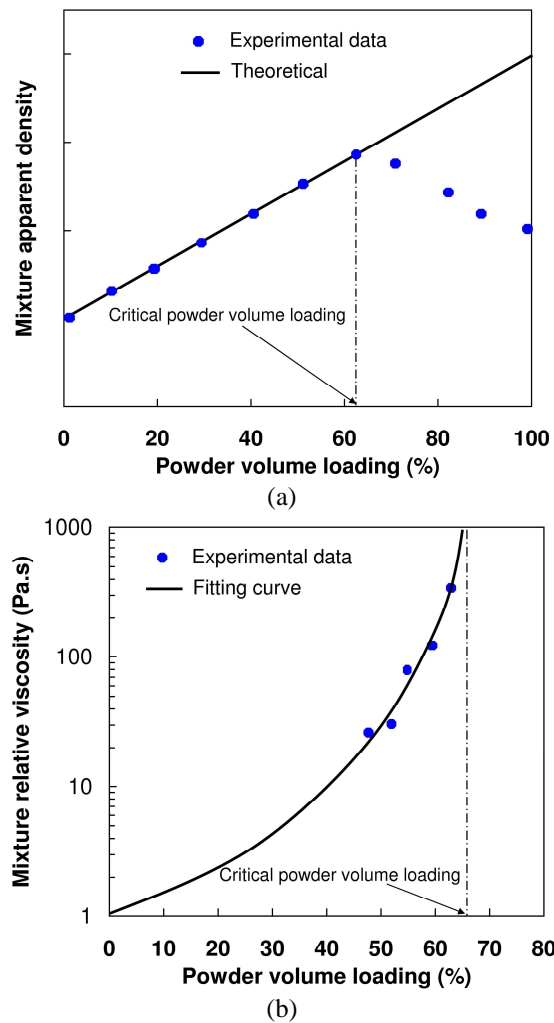


**Figure 1.6:** a) Evolution of mixture apparent density versus powder volume loading of a PIM feedstock and b) Evolution of mixture relative viscosity versus powder volume loading. Line curve represents a model fitting for the estimation of critical powder volume loading.

**Table 1.2:** Some proposed mathematical models describing the dependence of the feedstock's relative viscosity on powder loading.

| Author                  | Formulation  | Remarks                                   |
|-------------------------|--|---|
| Eilers (1941)           | $\eta_r = \left( 1 + \frac{1.25\phi}{1 - \frac{\phi}{\phi_m}} \right)^2$                 | Spherical particles                       |
| Mooney (1951)           | $\eta_r = \exp \left( \frac{2.5\phi}{1 - \frac{\phi}{\phi_m}} \right)$                   | Spherical particles                       |
| Chong et al. (1971)     | $\eta_r = \left( 1 + 0.75 \frac{\frac{\phi}{\phi_c}}{1 - \frac{\phi}{\phi_m}} \right)^2$ | Spherical particles                       |
| Mills (1985)            | $\eta_r = \frac{1 - \phi}{\left( 1 - \frac{\phi}{\phi_m} \right)^2}$                     | Spherical particles                       |
| Koda and Fruruse (2006) | $\eta_r = \frac{1 + 0.5k\phi - \phi}{(1 - k\phi)^2(1 - \phi)}$                           | $k = 1 + 0.6\phi$ for spherical particles |

where  $\eta_r$  is the relative viscosity,  $\phi$  is the powder loading and  $\phi_m$  the maximal compact stacking.

Another method to determine the critical powder volume loading is mixing torque by continuously increasing powder loading. The powder loading is increased gradually by adding the powders with an increment equals generally to 2% for each level [JAR 08]. The mixing torque according to mixing time is related in **Figure 1.7**. Two aspects indicate the overcome of the critical solid loading: a sudden increase in the mixing torque with irregular and unstable values [AGG 06]. This method can provide a way to get the critical solid loading in a simple way just using one testing cycle and its application takes the shortest time of all methods.

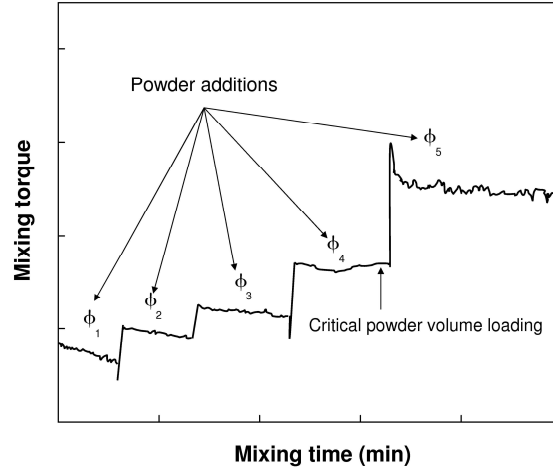


**Figure 1.7:** Mixing torque versus mixing time at several levels of powder volume loading, by adding progressively the powder into the mixing chamber.

The last method, feedstock viscosity model versus powder loading, is based on the model proposed by [AGG 06]. The viscosity of the non-Newtonian binder has been expressed vs. shear rate and temperature, as mentioned by Chen et al. (2004) [CHE 04] during the determination of phenomenological constant in shear-induced particle migration model, see the following equation:

$$\eta(\dot{\gamma}, T) = K \dot{\gamma}^{n-1} \quad (1-3)$$

where  $\eta$ ,  $\dot{\gamma}$ ,  $n-1$  and  $K$  correspond to the viscosity, the shear rate, the powder-law exponent and the consistency coefficient described as:

$$K = B \exp\left[\frac{E}{RT}\right] \quad (1-4)$$

where  $B$  is the specific material reference factor (some authors call this factor the reference viscosity),  $E$  is the flow activation energy for the Arrhenius temperature dependence of the viscosity and  $R$  is the gas constant. The absolute value of  $(n-1)$  indicates the shear rate exponent. The lower the  $n$  value is, the more sensitive the viscosity vs. shear rate is [SOT 10].

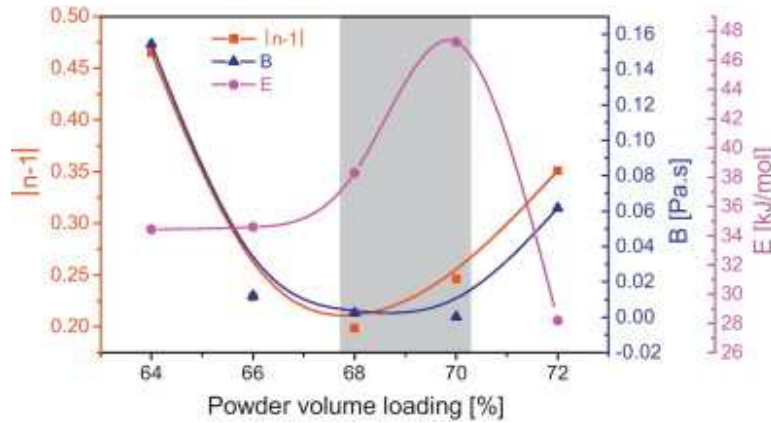


**Figure 1.8:** Determination of critical powder volume loading through feedstock viscosity model (316L stainless steel,  $D_{50} = 3.4 \mu\text{m}$ , powder loadings varying from 64 to 72%, measured at 160 °C) [KON 12].

The variation of  $(n-1)$ ,  $B$  and  $E$  versus powder volume loading is shown in **Figure 1.8**. It is possible to determine a typical zone for powder volume loading through the variation of these three parameters vs. the different powder volume loadings that indicate an inflection zone around 68–70% where a sudden change appears. This zone can be called the critical powder volume loading zone corresponding to the minimal value of  $n$ , so the range of 68–70% has been retained for the critical powder volume loading through the viscosity power law tests based on a power law shear viscosity.

For this purpose, capillary rheometry is one the most accurate and sensitive method for the homogeneity assessment. German reported that the minimum viscosity for a particular mixture occurs with the most homogeneous feedstock [GER2 94]. The evaluation of feedstock homogeneity by this method is carried at a determined shear rate, varying from study to study. Some examples of shear rates are given in the literature  $3.543 \text{ s}^{-1}$  [CAO 92],  $294.5 \text{ s}^{-1}$  [SUR 03] and  $1180 \text{ s}^{-1}$  [ZAU 04]. Liu et al. reported that if a shear rate is varying from 100 to  $10000 \text{ s}^{-1}$  and the corresponding feedstock viscosity is below 1000 Pa.s, the feedstock is suitable for injection moulding [LIU 03].

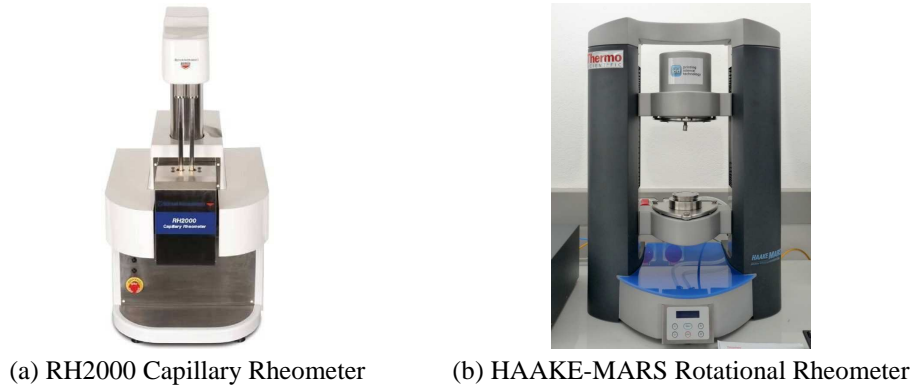


**Figure 1.9:** Instruments used to measure the viscosity in our laboratory: a) capillary rheometer and b) rotational rheometer.

The mixer design is another important parameter to prevent the agglomeration of powder or binder system components. The proper mixing is achieved with high shear rate. Nevertheless, too high shear rate during mixing can damage the particles or overheats the binder [MUT 95]. The shear level could have a space variation in a mixing chamber and good mixing operation requires all regions be equally sheared. Several high shear mixer designs are used for PIM feedstock, Mixer W 50 EHT with two mixing screws is one of the successful for research laboratory, since it combines high shear rate with elevated temperatures up to 500°C, **Figure 1.10**.

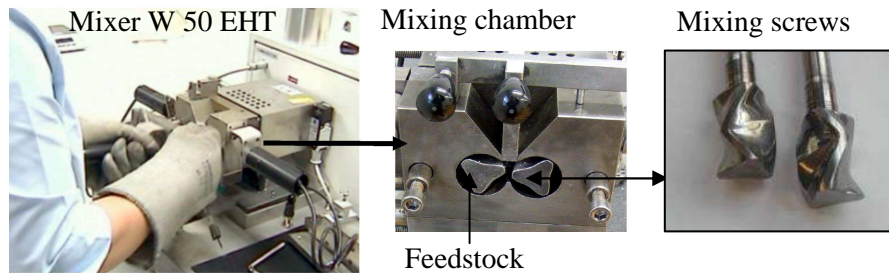


**Figure 1.10:** Mixer W 50 EHT with two mixing screws used in our laboratory.

### 1.2.2.2 Injection moulding stage

The next step in PIM process is injection moulding step, just like plastic injection moulding. The injection moulding equipment used in our laboratory is an Arburg 220-S<sup>®</sup>, **Figure 1.11-a**. The feedstock pellets are gravity fed from a hopper into the equipment's barrel where heaters melt the binder and then the feedstock is pushed through the injection nozzle using reciprocating screw that acts as a mixer to ensure uniform heating during melting, **Figure 1.11-b**.

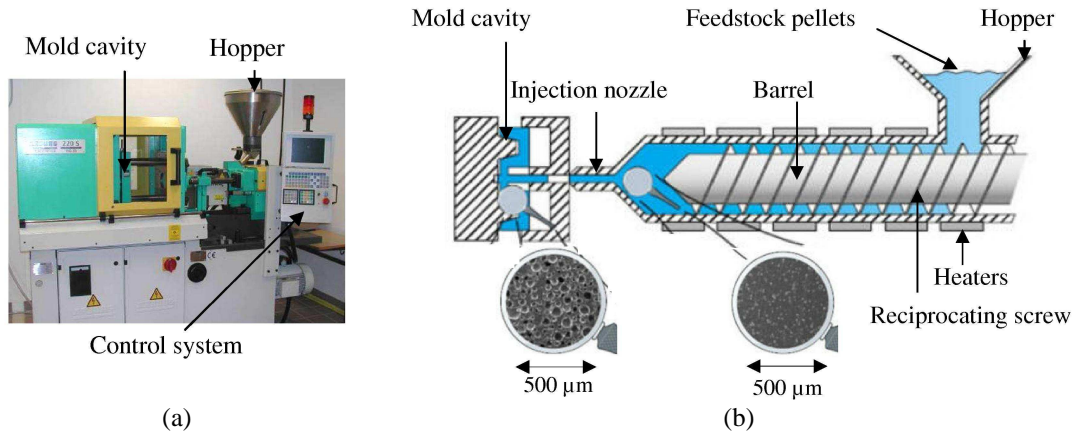


**Figure 1.11:** Hydraulic injection moulding equipment, a) Arburg 220-S<sup>®</sup> micro injection moulding equipment ( $\phi 15\text{mm}$ , maximum temperature  $350^\circ\text{C}$ , maximum volume  $10.8\text{ cm}^3$ , maximum pressure 2000 bar) used in our laboratory and b) detailed sketch of the injection moulding equipment.

Once the mould is filled, it cools down the component quickly and the produced component is removed out of the mould. The moulded component is often called green component and it is preferably to be handled by robots to prevent damage during the handling process to the next step.

However, the moulding stage is a critical step for forming a desired shape. This step requires specific rheological behaviour and thermal properties of the PIM feedstocks. The injection pressure is the driving force for making flow of PIM feedstock during filling stage. The viscosity of PIM feedstock is the most important property to flow behaviour. In addition, the thermal properties of PIM feedstock such as thermal conductivity and heat capacity are more important in PIM than in plastic injection moulding, because of faster heat transfer from PIM feedstock than from plastic resin [AHN 08].

Based on the existed literature, defective components are often due to binder separation and powder segregation during injection and filling processes. Their principal causes can be summarized as follow: jetting, layered flow, nonuniform pressure, thermal interactions and inhomogeneity of the feedstock.

The binder separation is due to the formation of a layer of neat binder near the surface of the mold, which results in the acceleration of the feedstock because of the lubricating action of the low viscosity layer near the wall. In this occurrence, the high velocity feedstock hits the surface of the mold bouncing back creating voids and weld

lines during freezing [ADA 07]. One can conclude that the binder separation problem is due to the low adhesion between binder and particles.

The powder segregation occurs simultaneously with the binder separation, this phenomenon is also called phase segregation. Phase segregation happens during the high speed and high pressure injection moulding process due to the different densities associated to powder and binders. Powder segregation can induce large inhomogeneities in the green components and makes them soft [JEN 08].

In order to eliminate such problems, one of the best ways is numerical simulation tool which offers significant help in optimizing the injection moulding parameters. Binder separation and powder segregation effects in MIM process, using numerical simulation tool, have been incorporated into mathematical models developed by several researchers such as: Dutilly [DUT 98], T. Barriere [BAR 00], G. Ayad [AYA 05], Hwang et al. [HWA 02], Barriere et al. [BAR 03], Ayad [AYA 04] and Cheng et al [CHE 12].

### **1.2.2.3 Debinding step**

Binders are widely used in powder injection moulding technology to produce components with complex shapes. Such binders need to be removed, without producing defects, from the PIM components before the sintering process. The polymer extraction process is called debinding and it can be carried out by different methods, as it will be explained below. In the case of incomplete binder removal, the trapped polymeric residues may affect the final mechanical properties which make defects more susceptible to be produced during the sintering process. The successful removal of binder occurs without disrupting the integrity of the moulded green component. Basically, binder removal often put limits on the size and shape complexity of injection moulded components since large and/or thick components make binder removal very difficult in an acceptable period of time and induces therefore more defects after debinding steps [TRU 02].

As mention before, a number of advanced methods have been developed for binder extraction: catalytic debinding, supercritical debinding, solvent debinding and thermal decomposition or thermal debinding [GER 97, SAN 05]. Solvent and thermal debinding are the most commonly used methods of binder removal process [SAN 05].



After debinding process, the moulded components must be strong enough to retain their shape during sintering process.

Catalytic debinding is used for binders that decompose exclusively, at relative low temperatures, into smaller molecules (monomers) under a nitrogen atmosphere containing a small amount of gaseous nitric acid (catalyst). Low temperature prevents the component from softening. Binder based on POM (sometimes also referred as polyacetal) is highly recommended for such type of debinding. This polymer depolymerises completely under the influence of an acid, **Figure 1.12**. By using a catalyst, the polymer at the surface of the green component is broken down into monomers and evaporates. As the monomers evaporate, pores are created and the depolymerization process continues deeper into the moulded component [GON 12].

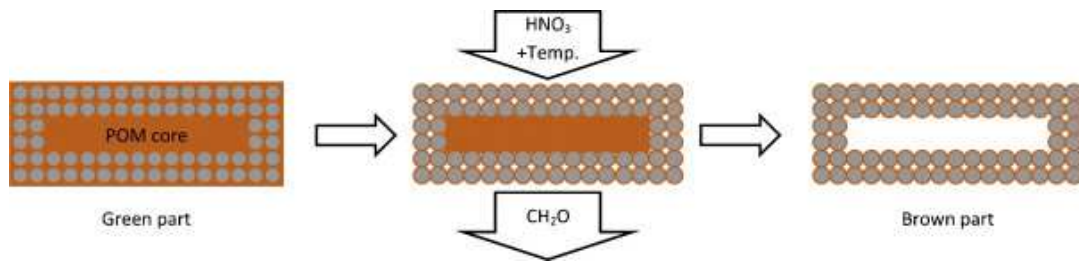


**Figure 1.12:** Schematic illustration of catalytic debinding process [ATT2 12].

In addition, shorter debinding times are achieved with the use of catalysts, as the diffusion rate of the monomer with smaller-sized molecules is much higher [GUI13]. Catalytic debinding is around ten times faster than the other conventional techniques (solvent and thermal debinding). The debinding time depends on the quantity and concentration of catalyst and also temperature. An increase of the mentioned parameters increases the rate of debinding. Other parameters could also affect the catalytic debinding process such as: particle size of the powder and geometry of the moulded component. This type of debinding is performed below the melting temperature of polyacetal binder, basically between 110 and 140 °C. These relative low temperatures prevent the formation of a liquid phase and thus prevent deformation of the green component caused by gravitational distortion or stress relaxation [FU 05]. Also, the internal gas pressure is low in order to minimize the danger of cracks and their propagation. However, there are some limitations with regard to the use of catalysts and their contents, due to health concerns. Polyacetal



binder decomposes into toxic elements known as formaldehyde which must be controlled under certain concentration limit. The catalytic debinding has an appreciate consumables cost of catalyst and inert gas [CFI 06].

In the case of supercritical debinding, the extraction is carried out by using supercritical fluids (carbon dioxide or propane) which allow the removal of organic additives without creation of defects in PIM components. Binder extraction by supercritical fluids involves different mechanisms such as solubilisation, diffusion and capillary migration (when organic components are in liquid state). The operative pressure is controlled around 10 MPa and temperatures are less than 100 °C. Supercritical debinding is not widely employed in commercial operations due to the long processing times and elevated cost of the necessary equipment. Supercritical debinding requires high precision control in temperature and pressure [SAN 04].

In solvent debinding, the moulded components are immersed in a gaseous or liquid solvent such as ethanol, hexane, heptanes and acetone at low temperature basically 50 to 60 °C [TOR 11], **Figure 1.13**. Once the components are immersed, the solvent (liquid or gaz) starts to diffuse inside the component and dissolve progressively the binder system or one of its components. In fact, the solvent debinding temperature varies from study to study depending on the used binder system. Some examples of solvent debinding temperatures are given in the literature 30-60 °C [LIN 98], 80-130 °C [YAN 03] and 40-60 °C [ONB 13].

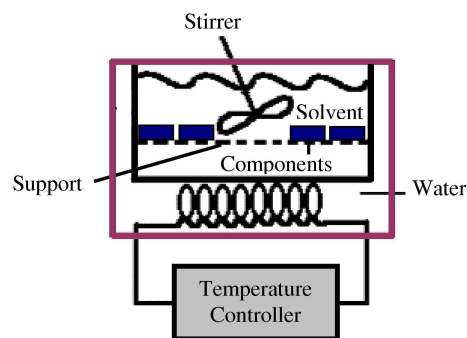


**Figure 1.13:** Schematic illustration of solvent debinding process.

Solvent debinding process is completely related to the geometry of the green component, in particular, to the surface/volume ratio, since the solvent needs to penetrate into the component through its external surfaces. Other factors that influence solvent debinding include temperature and porosity variation. The temperature effect is related to an increase in interaction between soluble binders and

solvents as temperature increases, in other words temperature changes the solubility and diffusion coefficient of the binder [OLI 05]. In general, the solvent debinding time is a function of the powder material, particle size, component geometry, solvent temperature, binder system components. After debinding, components are usually air dried at ambient temperature and then placed in a vacuum furnace at 40 to 50°C for 2 to 3 hours in order to remove the solvent trapped in the pores [HOW 05, FAN 09].

Thermal debinding uses the mechanisms of thermal polymers degradation which is commonly referred as thermal debinding. During thermal debinding step, PIM components are slowly heated in an oven to give progressive degradation of organic binders, **Figure 1.14**. The binder is removed in an oxidizing, inert atmosphere or in a vacuum atmosphere. The choice of atmosphere, under which thermal debinding is performed, influences some characteristics of the final component such as density, carbon or oxygen content [QUI 11]. Thermal debinding technique is still widely used in PIM industry for the low investment equipment [TAS 11]. However, the process is time-consuming because the thermal debinding is often carried out very slowly under protective atmosphere in order to avoid internal pressure build up from decomposed gas. Internal pressures could cause cracking and defects during thermal debinding step [TASS 09]. Burning residues, which are mainly carbon monoxide, can strongly affect mechanical and physical properties of the final sintered components.



**Figure 1.14:** Used laboratory oven for thermal debinding process with maximum temperature of 300 °C.

However, the more advanced debinding techniques require sequential debinding process. A typical sequence is solvent debinding followed by thermal decomposition [RAJ 12]. The major differences, advantages and disadvantages between the four types of debinding techniques are summarized in **Table 1.3**.

**Table 1.3:** Comparison between four major debinding techniques [GON 12]

| Debinding technique  | Key features   | Advantages  | Disadvantages   |
|----------------------|--|---|---|
| <b>Catalytic</b>     | <ul style="list-style-type: none"> <li>- Heat green part in Atmosphere containing catalyst to depolymerize binder and sweep away monomers.</li> <li>- Binder goes from solid to gas.</li> </ul>                    | <ul style="list-style-type: none"> <li>- Rapid process (4 to 6 hours) that works well on thick and thin sections with excellent shape retention.</li> </ul>   | <ul style="list-style-type: none"> <li>- Possible hazards with acid catalysts and decomposition products.</li> <li>- Exhaust products must be treated properly to prevent health and environmental hazards.</li> </ul>  |
| <b>Supercritical</b> | <ul style="list-style-type: none"> <li>- Extraction of organic additives by supercritical fluids CO<sub>2</sub> (SC-CO<sub>2</sub>)</li> <li>- Temperature less than 100°C and pressures around 10 Mpa.</li> </ul> | <ul style="list-style-type: none"> <li>- Environmentally friendly: no VOC emissions, no prohibition by the environmental treaties, and no increase in greenhouse gases.</li> </ul>  | <ul style="list-style-type: none"> <li>- The use of low temperatures results in slow diffusion of the binder to the surface of the green part, resulting in long processing times.</li> </ul>   |
| <b>Solvent</b>       | <ul style="list-style-type: none"> <li>- Green component is placed in a solvent (gaseous or liquid state) to extract binder via dissolution</li> </ul>   | <ul style="list-style-type: none"> <li>- Component remains rigid without chemical reactions.</li> <li>- Lower temperatures minimize defects and distortions.</li> <li>- Faster than thermal debinding (around 6 hours)</li> </ul> | <ul style="list-style-type: none"> <li>- Solvent hazard, chemical handling and environmental concern (unless water soluble binder is used).</li> <li>- Expensive equipment if using supercritical extraction.</li> <li>- Drying before sintering required if using liquid solvent.</li> </ul> |
| <b>Thermal</b>       | <ul style="list-style-type: none"> <li>- Slowly heat green part to melting or degradation temperatures with a continuous sweep gas to remove binder.</li> </ul>  | <ul style="list-style-type: none"> <li>- One step process, no need to handle product between debinding and sintering.</li> <li>- Low cost installation.</li> <li>- Applicable to a wide range of binders.</li> </ul>              | <ul style="list-style-type: none"> <li>- Soft binder allows warpage, poor dimensional control and relatively slow process (up to 60 hours).</li> <li>- If a wick is used, problems to separate part from it.</li> </ul>   |

#### 1.2.2.4 Sintering step

Sintering is the last stage of the powder injection moulding process. The first form of sintering has been used in the fabrication of bricks and pottery by heating clays in fire to high temperature [GER 03]. Nowadays, sintering is used for the manufacturing of complex shape components in different materials (ceramic, Tungsten Carbide Cobalt) [KAN 05]. Sintering is a thermal treatment (within 70 to 90% of the melting temperature of the major constituent, so that the particles remain unmelted) that transforms metallic or ceramic powders into a bulk material containing, in most cases, residual porosity. However, the mechanical strength of the sintered component is much improved [LAM 03]. At such temperatures as mentioned above, the particles recrystallize into each other causing them to fuse together [BOL 10].

Sintering time can also vary depending upon the material and the size of the prepared component. Large and complex shape components require a longer sintering time to ensure that component is completely sintered. In this case, the sintering time can be around 3 hours or more. On the other hand, small and non-complex components require less sintering time that varies from 1 to 1.5 hours. For specific materials such as tungsten, the sintering time may go up to 8 hours [BOL 10]. Sintering stage depends on many factors which can be divided into two categories. The first one concern operating conditions such as temperature, heating rate, atmosphere and the second one is related to the physical characteristics of the material to be sintered for example: particle shape, particle structure and particle composition.

*Sintering Temperature:* An increase in the sintering temperature greatly increases the rate and magnitude of any changes occurring during sintering. At higher temperature, translation of vacancies increases which helps in increase of density and/or volume shrinkage [DJO 09]. However, the sintering temperature depends greatly on material used, as an example: coppers are often sintered near 1050 °C, stainless steel near 1250 °C, alumina near 1600 °C and tungsten near 2300 °C.

*Atmosphere:* During sintering process some gases can be used as a protective atmosphere in order to prevent oxidation of sintered components. Nitrogen and argon atmospheres are commonly used. However, vacuum atmosphere can be also used for stainless steel and hydrogen atmosphere in the case of tungsten components.

Bergman et al. [BER 10] reported that the hydrogen atmosphere reduces Fe oxide layers on the powder surfaces during the heating stage of the sintering process which facilitates the sinter neck formation.

*Heating rate:* heating rate affects directly the sintered density of components. Very fast heating rates reduce the sintering cycle time, therefore low sintered density and poor mechanical properties are expected [BOL 10].

*Particle Shape:* decreasing sphericity and increasing roughness lead to greater intimate contact between particles and largely promote the sintering process [UPA 97].

*Particle Structure:* Fine grain particles can promote sintering because of its favourable effect on several material transport mechanisms [UPA 97].

*Particle Composition:* Alloying additions or impurities within a metal can affect the sintering kinetics. The effect can either be deleterious or beneficial depending upon the distribution and reaction of the impurity [UPA 97].

There are many typical sintering methods to produce metal or ceramic components such as: conventional sintering (CS), microwave sintering (MWS), electrical sintering (ES), laser sintering (LS) and spark plasma sintering (SPS). For conventional sintering method, energy is transferred to the component through conduction, radiation and convection mechanisms, it means that the external surface of the component is first heated followed by the heat moving inward [MOR 10]. The heat transfer rate from the external surface to the centre depends on the thermal conductivity of the material used. **Figure 1.15** shows furnace laboratory used for conventional sintering; its maximal temperature is 1850 °C with possibility to use primary and secondary vacuum.

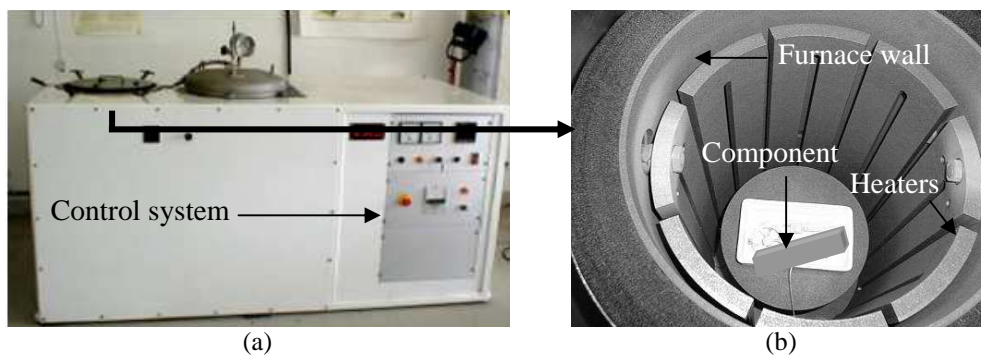


**Figure 1.15:** Furnace used in our laboratory for conventional sintering: a) external view; b) internal view.

### **1.3 Raw material and Market of PIM**

In recent years, powder injection moulding has become one of the powder metallurgy processes which is still gradually developing. This development is mainly due to the increased demand for high performance materials (stainless, copper, ceramic...etc and hard materials as tungsten and molybdenum) and the miniaturization of complex shaped components in various fields. PIM market has exceeded the \$ 1 billion mark in 2007, becoming approximately six times larger than 15 years before [GER 08]. World metal and ceramic PIM market is forecast to reach \$ 3.7 billion by the year 2017, [GIA 11].

#### **1.3.1 Raw material for metal Powder Injection Moulding technology**

For powder injection moulding, two main categories of materials (powders and binders) are required for this process. Among them, the most popular ones are described in the following subsections:

##### **1.3.1.1 Metal powders**

The most common metals available in powder form are iron and steel, tin, nickel, copper, aluminum and titanium, as well as refractory metals such as tungsten, molybdenum and tantalum. Alloys such as bronze, brass and nickel cobalt superalloys are also available in powder form. Fine powders are required for PIM to increase sinterability, particle size is basically between 0.5 and 20  $\mu\text{m}$ . Major methods for making metal powders are atomization of molten metal, reduction of oxides, electrolysis and chemical reduction. Gas and water atomization methods are often used to produce 316L stainless steel powder [APMI 12].

These different powders have many different properties that should be analyzed. The most important are the particle size, packing density and particle shape [KAR 04]. Ideal powders should also have the following characteristics: No agglomeration, dense particles free of internal voids, clean particle surface for appropriate interaction with the binder [ZLA 08].

##### **1.3.1.2 Binder system**

The binder has a major influence on the successful production of injection moulded components, although the binder should be not in the final composition of the moulded material. The role of the binder is to provide flowability during injection moulding step, to connect the metal particles after injection of the moulded parts and

to provide sufficient strength at room temperature conditions [GER 97]. Binder system with different components is necessary to fulfill the following requirements [BEN 07]:

Binder system must wet the powder particles, be melted at a suitably low temperature for injection moulding, has to be easily removed by using chemical or thermal methods without leaving residues, provide sufficient green strength and must be environmentally friendly.

### 1.3.2 Powder Injection Moulding Market

Considering the sales of the firms identified in PIM, a survey from 1990 to 2010 is related in **Figure 1.16** according to the geographical origin. The company number has grown from about 50 to about 350. It can be clearly observed that China and India have experienced impressive growth in the last decades and this tendency will continue in the coming years [BAL 05].

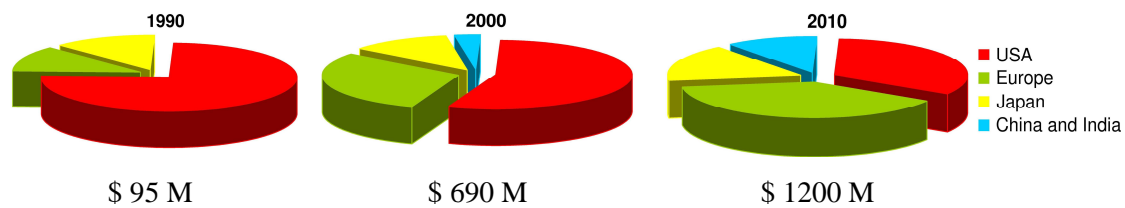


**Figure 1.16:** Survey of the global sales of the firms according to geographical regions (1990 to 2010), [KON 11].

## **1.4 Summary**

Powder injection moulding, by combining the advantages of both powders and polymers, becomes a competitive technology that enables to produce quantities of small and complex metal or ceramic components that can not be made using other technologies like conventional powder metallurgy. Nevertheless, this process is still unable to overcome some problems like limited thickness and weight of produced components. Literature has related that four countries in the world (China, USA, Japan and Europe) are still conducting extensive research by publishing several papers about PIM technology. As previously reported for the four main stages of PIM processes, many factors could influence the production quality including processing variables such as speed and time of mixing, thermal and sintering temperatures, atmospheres and material variables such as powder characteristics, powder volume loading and binder composition.

Regarding to the debinding stage, the more advanced debinding techniques require sequential debinding process. A typical sequence is solvent debinding followed by thermal decomposition [RAJ 12]. When a fraction of the binder is removed by solvent extraction, pores are created inside the components and therefore, migration of decomposed products during thermal debinding between 200 and 600 °C will be easier for such components [TAN 08].

Conventional sintering is still a more attractive sintering method to produce metallic and/or ceramic components, mainly due to its simplicity and cost compared to other sintering methods. The next chapter continues the literature review, but has a very different goal. Mechanisms, physical and mathematical models related to thermal debinding and sintering stages will be described.



## Chapter 2: Literature Review on Thermal Debinding and Sintering Behaviours

---

### Contents

---

|            |   |           |
|------------|---|-----------|
| <b>2.1</b> | <b>Introduction.....</b>                              | <b>36</b> |
| <b>2.2</b> | <b>Thermal debinding of PIM components .....</b>      | <b>36</b> |
| 2.2.1      | Physics of thermal debinding .....                    | 37        |
| 2.2.1.1    | Diffusion controlled debinding.....                   | 38        |
| 2.2.1.2    | Permeation controlled debinding.....                  | 39        |
| 2.2.1.3    | Wicking controlled debinding.....                     | 40        |
| 2.2.1.4    | Thermal debinding based on kinetic model.....         | 43        |
| 2.2.1.5    | Master Decomposition Curve for Thermal Debinding..... | 44        |
| 2.2.2      | Factors affecting thermal debinding .....             | 47        |
| 2.2.3      | Current defects in thermal debinding process .....    | 49        |
| <b>2.3</b> | <b>Sintering of PIM components .....</b>              | <b>50</b> |
| 2.3.1      | Sintering mechanisms .....                            | 50        |
| 2.3.2      | Driving force of sintering phenomenon.....            | 51        |
| 2.3.3      | Stages in solid state sintering.....                  | 52        |
| 2.3.4      | Modeling of solid state sintering.....                | 53        |
| <b>2.4</b> | <b>Summary.....</b>                                   | <b>58</b> |

---

## **2.1 Introduction**

For the successful manufacturing of components by powder injection moulding, the binder system must be safely removed from the injection moulded component during thermal debinding to avoid distortion or defects. Basically, the binder system is composed by various components: low molecular mass binder like paraffin wax as the first component and high molecular mass polymeric like polypropylene as the second one. These components have different melting points, viscosities and behave differently during thermal decomposition for fulfilling some goals. The debinding is the most critical step in the powder injection moulding process. This process can typically be a long process and takes often many hours or even days, depending on component thickness and powder grain size. Long time is a major obstacle for the economic success of powder injection technology [OSS 08].

The next stage after debinding one is the sintering stage where the final mechanical properties are strongly affected by many factors such as heating rate, maximal sintering temperature, holding time, sintering atmosphere and other material characteristics like particle size. This stage is commonly considered as one of the important step among the four MIM processing steps. To understand the sintering behaviour, various models have been established and developed. For modeling sintering process, three major approaches could be distinguished: (i) microscopic model, (ii) mesoscopic model and (iii) macroscopic model [ZHA 05]. In the present chapter, we will focus on the microscopic model in which sintering process is investigated through the study of two spherical particles that are placed in contact. Macroscopic model will be used in numerical simulation of solid state sintering for tungsten components in chapter 5.

## **2.2 Thermal debinding of PIM components**

The process of binder removal from green PIM components is not just a problem of capillary flux in a porous medium. Complex chemical reactions take place between the binder system components, also between them and the ceramic/metallic particles surface, making it very difficult to describe the concurrent reactions and the whole debinding process in detail. The difficulties are even greater when dealing with the debinding of large cross-section components made with submicrometer-sized ceramic/metallic powder [TRU 97, ZOR 02].

### 2.2.1 Physics of thermal debinding

Successful debinding occurs without contamination and distortion. Thermal debinding involves the removal of the binder from the component at slightly elevated temperatures. One variant of thermal debinding occurs at a temperature where the binder softens and flows out of the component via capillary action. A wicking material (porous substrate) in contact with the compact provides for capillary flow as the binder viscosity decreases with increasing temperature. Alternatively, the binder may be thermally decomposed into low molecular weight species (such as methane, carbon dioxide or carbon monoxide) and subsequently removed by diffusion and permeation depends on the mean free path of the gas species. In turn, the mean free path varies with the pressure, molecular weight of the gas and pore dimensions. Generally, diffusion will be dominant at low pressures, where laminar flow controls the rate of gas exit from the component [GER 87].

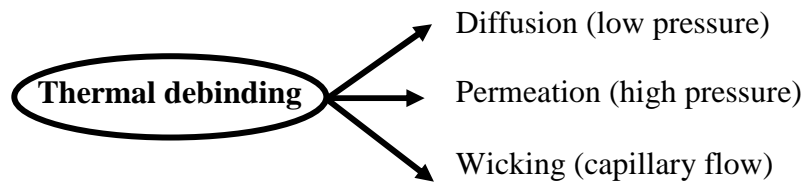


**Figure 2.1:** Diagram identifying the different debinding techniques based on thermal concept [GER 87].

Theses three thermal debinding techniques and the calculation of debinding time will be presented in the following paragraphs. The calculated debinding times will be approximations because of the several assumptions involved in the analysis. German proposed three different mechanisms for binder transport: diffusion, permeation, and wicking. These mass transport models of binder removal were simulated with simple 1D model. The following German's models are frequently used as the basis for research specially in wick debinding.

### 2.2.1.1 Diffusion controlled debinding

Under conditions where the mean free path is much greater than the pore dimension, diffusion controlled debinding is anticipated. The diffusivity of gas will improve with higher porosities and large pore sizes since there is less molecular scattering. Additionally, a low molecular weight vapor, higher temperature and higher vapor pressure will be beneficial to diffusion. The model assumed for the diffusion and permeation calculations is shown in **Figure 2.2** [GER 87].

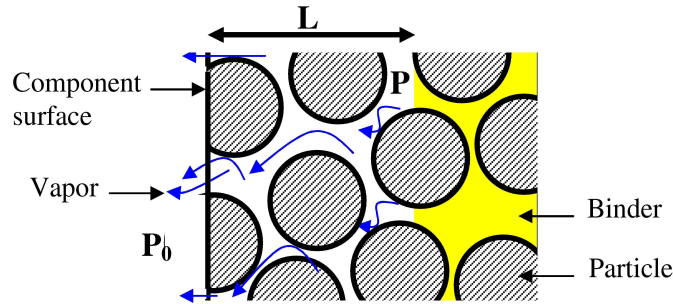


**Figure 2.2:** sketch of the pore model for debinding by permeation or diffusion, where the binder-vapor interface is a distance  $L$  from the component surface, adapted from [GER 87].

This sketch shows a partially open pore channel between spherical particles with a flux of vapor exiting at external surface. As vapor is thermally generated at the binder-vapor interface the transport distance increases. It is also assumed debinding occurs under isothermal conditions involving a single component, low molecular weight vapor. In practice debinding is not isothermal, nor is the binder a single component. The resulting debinding time  $t$  for a diffusion controlled process is given approximately as follows [GER 87]:

$$t = H^2 (MkT)^{1/2} / [2D(P - P_0)\theta^2 U] \quad (2-1)$$

where  $H$  is the component thickness,  $M$  is the molecular weight of the vapor,  $k$  is Boltzmann's constant,  $T$  is absolute temperature,  $D$  is the particle diameter,  $P - P_0$  is the pressure difference between the pressure  $P$  at the binder-vapor interface and the external component surface pressure  $P_0$ ,  $\theta$  is the total porosity and  $U$  is molecular volume for the solid binder.

The solution for binder diffusion controlled debinding as represented by equation (2-1) says debinding time depends on the square of the maximum section

thickness, and varies inversely with particle diameter, pressure drop and porosity squared. The temperature effects the debinding time in a more complex manner since there is square-root temperature term in the numerator and an exponential temperature term for the binder vaporization in the denominator:

$$P = P_e \exp(-E/kT) \quad (2-2)$$

where  $P_e$  is preexponential pressure term and  $E$  represents the activation energy. The exponential form dominates; thus, higher temperatures give shorter debinding times. For short debinding times by diffusion the guiding principals are to use thin sections, large particles, high pressure gradients (with low external pressures such vacuum), high porosity components and high debinding temperatures. Unfortunately, all of these parameters are not independently adjustable. Particle size is selected for rheology, sintering and packing density concerns. Indeed, high packing densities are desired to minimize dimensional change in sintering, with a concomitant penalty in debinding time. Also, the low strength of the component as the binder is removed limits the internal vapor pressure at the binder-vapor interface. Too high pressure will create an internal pressure which will damage the component.

### 2.2.1.2 Permeation controlled debinding

At higher gas pressure the collisions between molecules will limit the debinding rate. Assuming viscous flow of the vapor through the pore structure with no initial effects allows use of Darcy's law, the debinding time under permeation control is given as follows [GER 87]:

$$t = 22.5H^2(1-\theta)^2 PG / [\theta^3 D^2 F(P^2 - P_0^2)] \quad (2-3)$$

Equation (2-3) indicates the debinding time varies with the vapor viscosity, square of the section thickness, inversely with particle size squared and inversely since porosity appears in both the numerator and denominator. **Figure 2.3** plots the porosity function  $(1-\theta)^2/\theta$  versus fractional density to indicate the strong sensitivity to porosity at the high densities. The shape of this function indicates considerable difficulty in debinding components with packing densities over approximately 75% of theoretical. Thus, for rapid debinding the choice would be thin sections, large particles, high porosity, large pressure gradients (with a low surface pressure) and again high temperatures. Note both the vapor viscosity  $G$  and binder-vapor interface

pressure  $P$  increase with temperature. It is expected that the latter will exhibit the dominant effect, giving shorter debinding times at higher temperatures, as long as the component is not damaged in the process.

It appears that the permeation control is the typical case for thermal debinding. The estimated error on debinding times by this model 50%. Even so, the model provides a first guide to efficient debinding [GER 87].

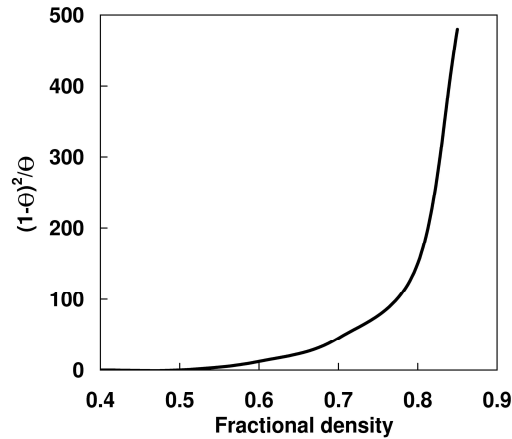


**Figure 2.3:** Porosity dependence of the debinding time as function of the fractional density to illustrate the significant debinding penalty associated with high packing densities [GER 87].

### 2.2.1.3 Wicking controlled debinding

The third form of thermal debinding involves unidirectional capillary wicking as shown in **Figure 2.4**. The powder compact placed on substrate (the wick) and heated to a temperature where the binder viscosity is sufficiently low that capillary flow will occur [GER 87].

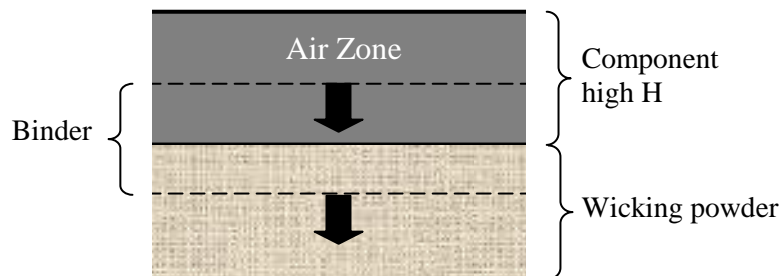


**Figure 2.4:** Schematic of wick debinding mechanism proposed by German [GER 87].

The binder may be stored in the wick or may further evaporate from the more open pore structure of the wick. Also wick material can be a packed powder with helps support the fragile component after the binder has been removed. Binder flow

will occur because of capillary attraction. A successful wick must satisfy criteria including nonreactivity, no sintering, small pore size and high porosity. There are two possible cases for wicking; 1) component with controlled permeability and 2) wick controlled permeability. The resulting debinding time  $t$  for a wick controlled process is given approximately as follows [GER 87]:

$$t = 4.5(1 - \theta_c)^2 GH^2 D_w / [\theta_c^3 W D_c (D_c - D_w)] \quad (2-4)$$

where  $\theta_c$  is the component porosity,  $G$  is the fluid viscosity,  $H$  is the component thickness,  $D$  is the particle diameter with subscript  $w$  indicating the wick and subscript  $c$  indicating the component,  $W$  is the binder-vapor surface energy.

The form using equation (2-4) means that the debinding time will depend on the section thickness squared, similar to the previous two debinding models. Furthermore, the porosity effect is the same as seen in the vapor permeability model as shown in **Figure 2.2**. The debinding time is predicted to vary linearly with the fluid viscosity. Since liquids decrease in viscosity as temperature increases, this clearly indicates the benefit of high temperature debinding. The fluid surface energy appears in the denominator because higher surface energies contribute to higher capillary pressures in the wick, thereby increasing the flux. Also, the difference in the component and wick particle sizes appears in the denominator of equation (2-4), indicating faster debinding with larger particle size differences. Thus, for rapid debinding by wicking, the best practice would be have a small wick particle size, large component particle size, large component porosity, larger wick porosity, low fluid viscosity, low fluid surface energy, and thin component dimensions [GER 87].

Mechanism of wick debinding process is not well developed, and much of the published work in the literature builds on the model published by German (1987) with later evidence [VER1 94] indicating its limitations [SOM 08]. Its principal limitation is due to the non uniformity distribution of the binder inside the component during thermal debinding.

Vetter et al. [VER2 94] proposed an alternative model in which air enters the component through channels in the wicking powder, as shown in **Figure 2.5**. The binder is removed counter-current to the air flow and is fed from the bulk binder by arteries through to the wicking powder. They developed an appropriate relationship for the debinding time in a similar fashion to Equation (2-4) except that they included

the wicking powder permeability. Although their experimental results showed that there was less binder near the compact-wick interface than in the centre of the compact, the binder distribution was not described in any detail.

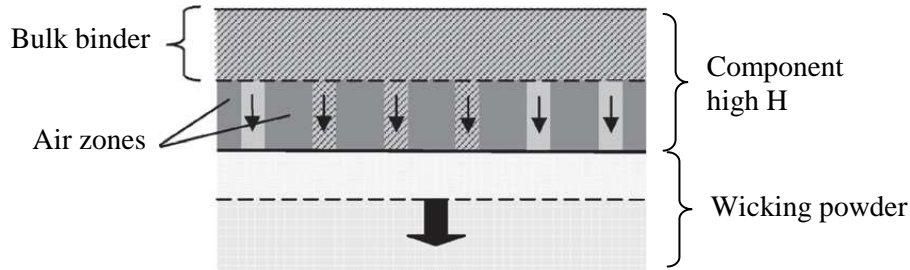


**Figure 2.5:** Schematic of wick debinding mechanism proposed by Vetter et al.

[VER2 94], based on German model [GER 87].

Chen and Hourng [CHE 99] set up finite element numerical simulations based on Equation (2-4) that agreed with the theory as expected. Their 2D simulations showed binder moving from a compact into wicking powder with both leading and trailing fronts as in **Figure 2.4**. However, their results were not validated experimentally. Lin and Hourng [LIN 05] simulated the movement of binder from a compact into wicking powder by German's binder removal mechanism using a pore network approach. They compared the predicted location of the binder front with corresponding experimental observation of the front in the wicking powder. Although their results demonstrated reasonably good agreement, they again assumed a trailing binder front leaving the compact on completion of debinding.

Somasundram et al. [SOM 08] has carried out an experimental investigation of wick debinding to dissect the governing mechanisms and develop a numerical simulation capable of predicting the process. The key parameters of the developed model were the permeability of the wicking powder and the relationship between the capillary pressure, saturation and relative permeability of the component. However, the permeability of the wicking powder can not be elucidated experimentally due to the complex proprietary structure. Thus, Somasundram et al. found this parameter by comparing simulation results to those of experiments. The proposed model 1D showed a good agreement with the experimental behaviour of binder distribution.



#### 2.2.1.4 Thermal debinding based on kinetic model

There are other attempts to model thermal debinding process based on differential thermal analysis, (DTA), differential scanning calorimetry (DSC), and thermo-gravimetric analysis (TGA). The models permit the determination of the weight loss of binder content inside the component at any time. The thermal decomposition of polymeric materials can be described by the following basic kinetic equation [SHI 02]:

$$\frac{dx}{dt} = k(T)f(x) \quad (2-5)$$

where  $x$  represents the extent of reaction (degree of conversion),  $t$  is the time and  $k$  is rate constant at temperature  $T$  and  $f(x)$  is a function which describes the mechanism reaction. The value of  $x$  is experimentally obtained from the weight loss using thermo-gravimetric analysis (TGA). The temperature dependence of the rate constant is given by the Arrhenius equation:

$$k = A \exp(-E_a/RT) \quad (2-6)$$

where  $A$  is the pre-exponential factor,  $E_a$  is the apparent activation energy and  $R$  is the universal gas constant.

Assuming a first order process ( $n = 1$ ) [ZHA 09] and considering  $k$  from equation (2-5), one obtains:

$$\frac{dx}{dt} = A \exp(-E_a/RT)(1-x) \quad (2-7)$$

Equation (2-7) can be rewritten for non-isothermal experiments using a linear heating rate,  $\beta = dT/dt$  as follows:

$$\frac{dx}{dT} = \frac{A}{\beta} \exp(-E_a/RT)(1-x) \quad (2-8)$$

where  $\beta$  is the non-isothermal reaction rate.

For our case, the main kinetic parameters of the thermal decomposition: apparent activation energy  $E_a$  and pre-exponential factor  $A$  will be determined later in the next chapter using Kissinger and Ozawa methods. The relationship between temperature and conversion ( $x$ ), for different heating rates using the kinetic model, can be plotted as shown in **Figure 2.6** [ZHA 09].

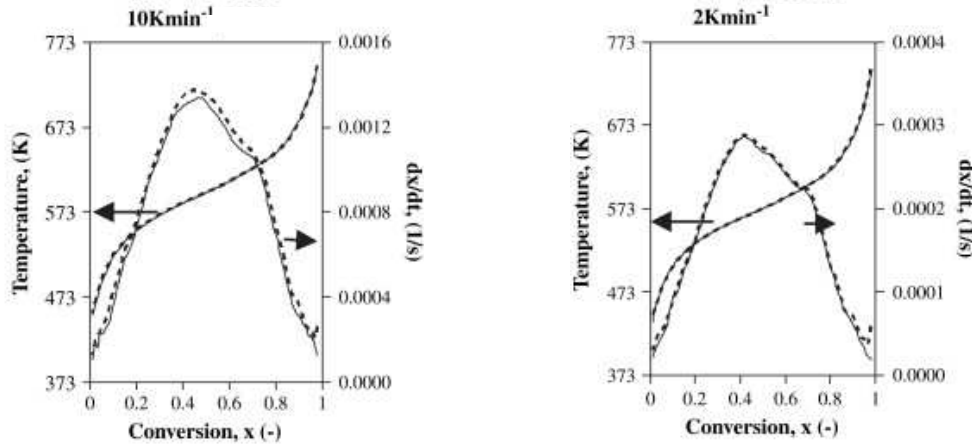


**Figure 2.6:** Comparing calculated conversion, conversion rate (---) with experimental data (—) at different heating rates 2 and 10 K/min, [ZHA 09].

### 2.2.1.5 Master Decomposition Curve for Thermal Debinding

Aggarwal et al. [AGG 07] and Park et al. [PAR 09] developed a master decomposition curve (MDC) to analyze the thermal debinding process; the master decomposition curve is based on the intrinsic kinetics of polymer pyrolysis. The kinetic parameter (activation energy) for this study has been estimated using the Kissinger method [KIS 57] based on the thermogravimetric investigations. Also, the effect of heat-transfer has been investigated for different powders with identification of the critical parameters of thermal decomposition during thermal debinding. Two approaches of master decomposition curve have been developed by Aggarwal et al., the first one for single reaction step and the second one for a multireaction steps.

#### *MDC for a Single Reaction Step*

Thermal decomposition of polymeric binders can be analysed by first-order reaction kinetics as presented previously by [SHI 02], remaining weight fraction of a polymer can be written as function of decomposition work as follows [AGG 07, PAR 09]:

$$-\int_1^x \frac{dx}{x} = -\ln x = \int_0^t A \exp\left[\frac{-E_a}{RT}\right] dt = A\Theta \quad (2-9)$$

where  $\Theta$  is the work of decomposition defined as follows:

$$\Theta(t, T; E_a) \equiv \int_0^t \left[ \frac{E_a}{RT} \right] dt \quad (2-10)$$

The remaining weight fraction of a polymer ( $x$ ) is related to the work of decomposition  $\Theta$  from equation (2-9) as follows:

$$x(\Theta; A) = \exp[-A\Theta] \quad (2-11)$$

Using equation (2-11), one can obtain the decomposition curve for a given polymer using the concept of work of decomposition as related in **Figure 2.7** in the case of polypropylene, [AGG 07].

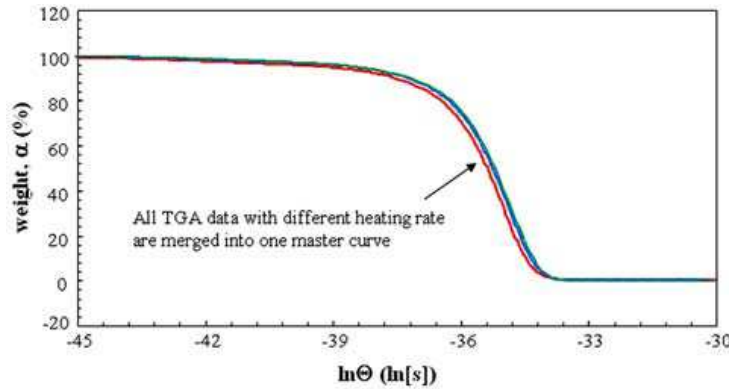


**Figure 2.7:** Evolution of remaining weight fraction of polymer: comparison between the TGA analysis and MDC with a single step for polypropylene PP, [AGG 07].

### MDC for Multireaction Steps

The mathematical form describing the remaining binder system components (two polymers pyrolysis) during thermal debinding process is given by the following expression [AGG 07, PAR 09]:

$$x = wx_1 + (1 - w)x_2 \quad (2-11)$$

where  $x$  is the mass ratio of the initial masses of two polymers,  $x_1$  is the mass ratio to initial mass of the low molecular weight polymer,  $x_2$  is the mass ratio to initial mass of the high molecular weight polymer and  $w$  is the ratio of the initial mass of the low molecular weight polymer to the initial mass of the two polymers. Aggarwal et al. [AGG 07, PAR 09] assumed that the kinetics are only controlled by the temperature:

$$-\frac{1}{A\beta} dx = \exp\left[-\frac{E_a}{R}\left(\frac{1}{T} - \frac{1}{T_i}\right)\right] dt$$

$$\text{If: } x \geq w, x = wx_1 + (1 - w), \beta = \frac{x + w - 1}{w}, A = A_1, E_a = E_1$$

$$\text{If: } x < w, x = (1-w)x_2, \beta = \frac{x}{1-w}, A = A_2, E_a = E_2 \quad (2-12)$$

where  $T_t$  is the transition temperature between the first and second sigmoids, subscripts 1 and 2 denote the first and second step, respectively.

The left and right side of equation (2-12) can be written as follows, respectively:

$$\phi(x; A) \equiv \int_1^x -\frac{1}{A\beta} dx \quad (2-12)$$

$$\Theta(t; T; E_a, T_t) \equiv \int_0^t \exp \left[ -\frac{E_a}{R} \left( \frac{1}{T} - \frac{1}{T_t} \right) \right] dt \quad (2-13)$$

The work of decomposition  $\Theta$  depends only on the apparent activation energy  $E_a$ , the transition temperature  $T_f$  and the time temperature profile  $T$ .  $\phi(x)$  is a characteristic that quantifies the effect of binder system components on the decomposition kinetics.

**Figure 2.8** relates two steps of thermal decomposition using a niobium feedstock where the lower molecular weight binder components (wax and SA) decompose first and then the higher molecular weight binder components (PP and PE) are later eliminated. The experimental results are in good agreement with ones obtained by the developed mathematical model of MDC multireaction steps [AGG 07].

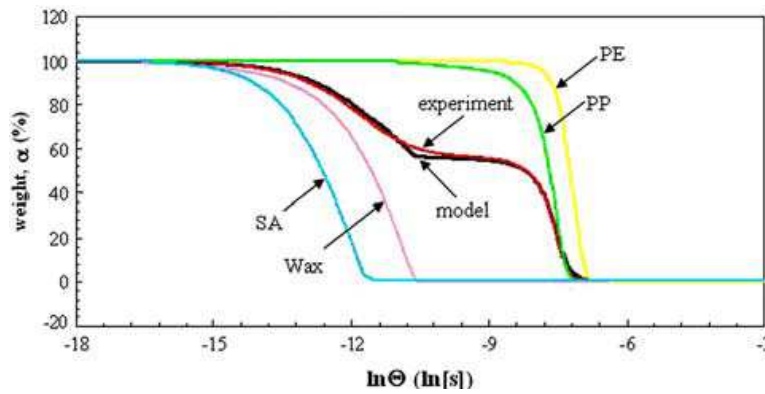


**Figure 2.8:** Evolution of remaining weight fraction of multi component binder system (PP+PW+SA): comparison between the TGA analysis and the model (MDC multireaction steps), [AGG 07].

### **2.2.2 Factors affecting thermal debinding**

The main factors affecting the thermal debinding process could be the heating rate, atmosphere in which debinding is carried out and binder amounts [YAK 00]. For an effective thermal debinding operation, the extraction must be fast with any trapped polymeric residues which could affect final mechanical properties of the sintered components.

Hu et al. [HU 00] investigated the dimensions changes and their causes during thermal debinding of injection moulded components made of iron powders. The binder system consisted of 40 wt-% low density polyethylene (LDPE), 55 wt-% paraffin wax (PW) and 5 wt-% stearic acid (SA). The purpose of this research was to study the effect of the following parameters: atmosphere, backbone binder content and heating rate during thermal debinding stage. The components in nitrogen and in vacuum atmosphere did not expand throughout the debinding process while an expansion has been taken place for the same components under hydrogen atmosphere. This expansion might be possibly caused by carburisation from the decomposed hydrocarbon gas. Also, researchers reported that the amount of expansion decreased when the amount of the LDPE decreased. The decrease in expansion is due to the decrease in carburising hydrocarbon gas (main cause of expansion) which is supplied by the backbone binder. In addition, when the heating rate of 1 °C/min is employed, the amount of expansion occurring at about 300°C is only 0.15%, much less than the amount of expansion occurring at higher heating rates such as 10 and 20 °C/min. Hu et al. concluded that to avoid abrupt expansion of the components during debinding, slower heating rates, smaller amounts of backbone binders and inert gases or vacuum should be employed in thermal debinding [HU 00].

As mentioned above, the type of atmosphere during debinding can directly affect the binder removal rate and quality of the extraction. Li et al. [LI 03] investigated the thermal debinding process of injection moulded water atomized 316L stainless steel powder (with a mean particle size of 24.65 µm) components under a vacuum and hydrogen atmosphere. The wax-based binder was composed of high-density polyethylene (HDPE) and low molecular weight components such as stearic acid (SA) and paraffin wax (PW). Thermogravimetric analysis method was used to measure the weight loss of binder, moulded injection components were taken out at

different stages of the debinding process and their pore structure evolution was analyzed using a mercury porosimeter. Li et al. concluded that the binder removal rate in vacuum was higher than that in the hydrogen atmosphere, with the same binder composition and the same temperature profile. In addition, the mercury porosimetry results indicated that the pore structure evolution in injection molded components during thermal debinding in vacuum was greatly different from that in hydrogen atmosphere. The difference in binder removal rate and pore structure evolution in these two atmospheres is due to the difference of the vapor pressure drop, which was the vapor pressure difference between that in the molded components and that in the ambient environment [LI 03].

Liu et al. [LIU 07] investigated the effects of debinding on the surface roughness of 316 L stainless steel (with mean size of 3  $\mu\text{m}$ ) microstructured components. The feedstocks have obtained after mixing the present powder with a multi-component binder system. The debinding has been carried out in a continuous flow of argon and hydrogen gas mixture at a flow rate of 150 cc/min in a tube furnace. The debound components were characterized by TGA and SEM. Liu et al. reported through this investigation that slower heating rates during debinding gave lower weight loss due to the introduction of oxides during debinding. After sintering, the debound parts with higher weight loss gave better surface finish. This improvement was more significant for increasing sintering temperature than increasing time [LIU 07].

Abeln and al. [ABE 11] used a combined debinding process to remove binder from green multilayer ceramic capacitors; it consists of a supercritical extraction method followed by a thermal debinding method. The binder system is composed of poly (vinyl butyral) plasticized with phthalates. The reason for using supercritical extraction as a first step was to increase the porosity (increasing the gas permeability inside the components) and at the same time decreasing the adhesion strength between layers. This increase in the porosity, during the supercritical extraction, led to a decrease in cycle time and defects during the thermal debinding process. This cycle time was much shorter than typical cycles of 50-150 h used in industry for samples of similar size and physical properties [ABE 11].

### 2.2.3 Current defects in thermal debinding process

The current defects that might be met during or after thermal debinding stage are the distortion of component and cracks or fissures propagation. Sometimes, a complete fracture can be extended completely through the debinded component. These problems are generally due to unadapted thermal debinding cycles, using a binder system with only one component, poor homogeneity of the injected component or incompatible thermal debinding method for the used binder system. In fact, a unadapted cycle of thermal debinding can influence the thermal degradation of the binder system and therefore cause excessive internal stress inside the debinded component. So, one should elaborate an homogeneous feedstock in order to prevent powder/binder separation and the agglomeration of powders. On the other hand, using a multi-component binder system, the thermal debinding process can be controlled at low and high debinding temperature. **Figure 2.9** shows images of failed ceramic components by cracks and distortion after thermal debinding process, [BRA 11, SAC 11].

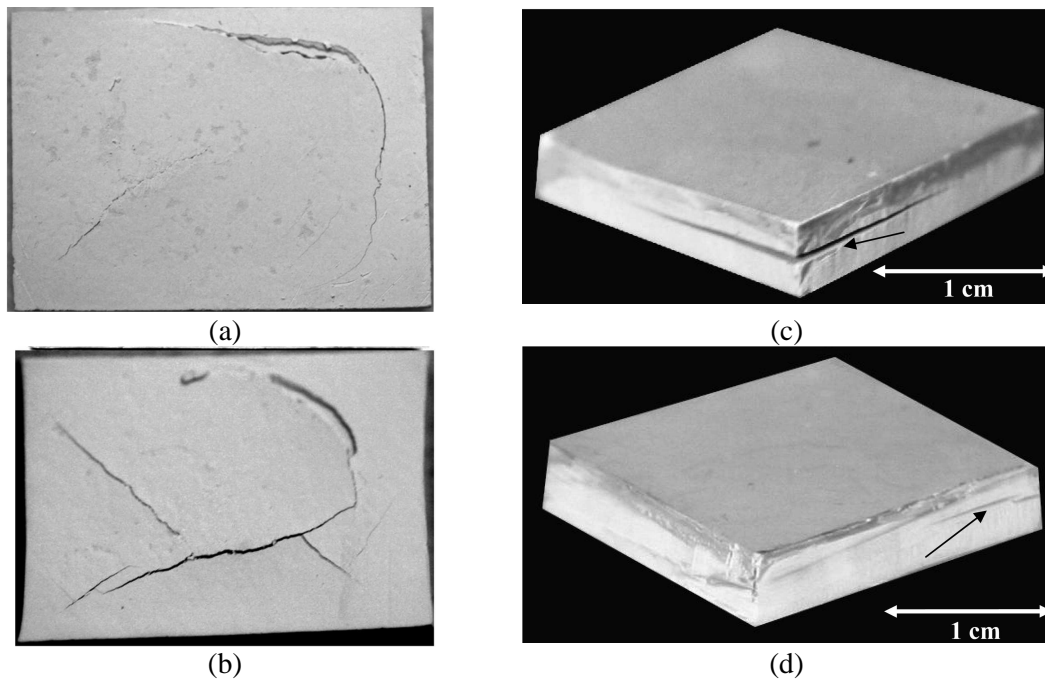


**Figure 2.9:** Failed ceramic components by cracks and distortion after thermal debinding process, (a, b) components heated with a 10 °C/min ramp to 600 °C with a 1 h hold [ABE 11], (c, d) components heated with 7.5 and 5 °C/min, respectively, [SAC 11].

## 2.3 Sintering of PIM components

The sintering process aims to produce solid components from metallic or ceramic powders. During this process, the injection moulded components are thermally treated at temperatures below the melting point of the main constituent to increase the strength of the components by bonding particles together. In addition, components undergo shrinkages in dimensions and final dense or full dense products are obtained [GER 97]. Therefore, sintering or densification is an irreversible thermodynamic phenomenon to convert unstable packed powder having excess free energy to stable sintered agglomerates. The sintering phenomenon involves the fusion of particles, volume reduction, decrease in porosity and increase in grain size [MAS 06].

### 2.3.1 Sintering mechanisms

Growth of the neck connections between grains during sintering is a result of mass transport by different mechanisms [HOS 06]. The main mass transport mechanisms during sintering process are as follow: surface diffusion for which vacancies and atoms move along the particle surfaces, grain boundary diffusion (along the grain boundaries), volume diffusion (through the lattice interior) as well as evaporation and condensation (across pore spaces). The different mechanisms for sintering process, in the case of two adjacent particles, are shown schematically in **Figure 2.10**.

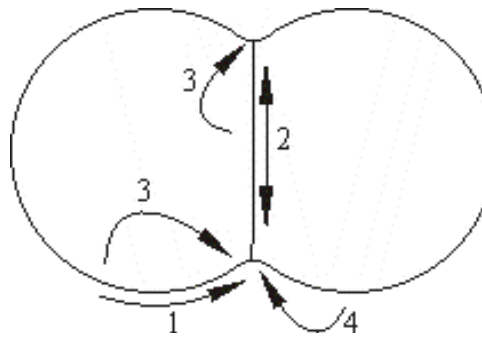


**Figure 2.10:** Mechanisms of mass transport during sintering: 1) surface diffusion, 2) grain boundary diffusion, 3) volume diffusion, 4) evaporation and condensation.

The densification occurs only when the atoms move along the grain boundaries in order to create the continual mass (neck). As a result of the stresses in the neck and the surface tension the particles are attracted to each other leading to macroscopic shrinkage of the system, **Figure 2.10**. The grain boundary diffusion and



volume diffusion from the grain boundaries contribute to densification. On the other hand, surface diffusion, evaporation-condensation and volume diffusion from the surfaces are the coarsening mechanisms and do not contribute to densification.

### 2.3.2 Driving force of sintering phenomenon

Sintering is accompanied by a reduction of the free energy of the system. The processes and other phenomena that provide the impetus for reducing the free energy are usually referred to as the driving forces for sintering and include the force associated with the curved surfaces of particles, externally applied pressure, and chemical reaction(s). In our case, sintering has been performed without the external pressure or chemical reaction. So, the reduction in total interfacial energy occurs via densification and grain growth which are the basic phenomena of sintering [MAS 06].

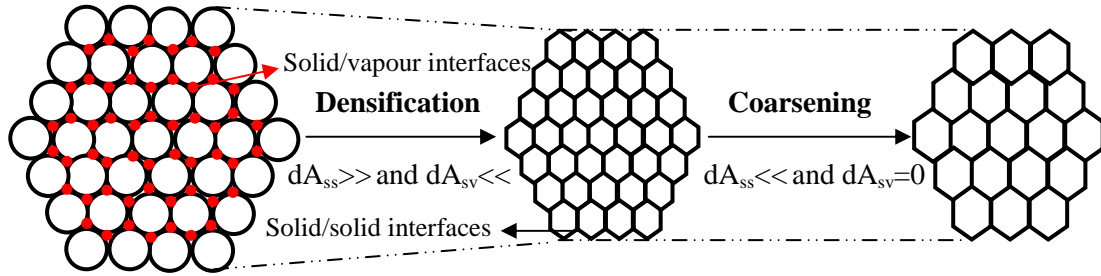


**Figure 2.11:** Basic phenomena occurring during sintering under the driving force for sintering.

The change of system free energy  $dE_f$  due to densification is therefore composed of the increase due to the creation of new grain boundary areas,  $dA_{ss} > 0$ , and due to the annihilation of vapour-solid interfaces,  $dA_{sv} < 0$  at the contact area between particles [BAN 12], **Figure 2.11**. The necessary global thermodynamic condition for the sintering to proceed is:

$$dE_f = \Gamma_{ss} dA_{ss} + \Gamma_{sv} dA_{sv} < 0 \quad (2-14)$$

where  $dE_f$  is the change of free energy,  $\Gamma$  is the surface energy,  $A$  is the interface area,  $dA$  is the change of the interface area. The subscripts sv and ss denote the solid-vapor interfaces and solid-solid interfaces (grain boundary) respectively.

Initially, the surface area of the compact represents the free surface area, since no grain boundaries have developed as yet and, therefore,  $A_{sv} = A_{sv0}$  and  $A_{ss} = 0$ .

As the sintering proceeds  $A_{SV}$  decreases and  $A_{SS}$  increases. The sintering process will stop when the overall change in the free energy of the system becomes zero,  $dE_f = 0$

$$\Gamma_{SS}/\Gamma_{SV} = -dA_{SV}/dA_{SS} \quad (2-15)$$

Grain coarsening or grain growth phenomena leads to a partial elimination of grain boundary and can also reduce the free energy of the sintered compact, as shown in **Figure 2.10**. In this case, grain growth reduces the solid-solid interface  $dA_{SS} < 0$  where the solid-vapor interface  $dA_{SV} = 0$ . It contributes nothing to densification, but reduces the free energy as follows [SON 07]:

$$dE_f = \Gamma_{SS} dA_{SS} < 0 \quad (2-16)$$

In practice, densification and coarsening are concurrent and competing processes since they both reduce the driving force for sintering [BAN 12]. The sintering process will stop when:  $dE_f = 0$ .

### 2.3.3 Stages in solid state sintering

The sintering process provides the energy to encourage the individual powder particles to bond together in order to eliminate the porosity present between the particles. The process of sintering (solid state) is divided in three stages that phenomenologically appear and can be identified, see **Figure 2.12**.

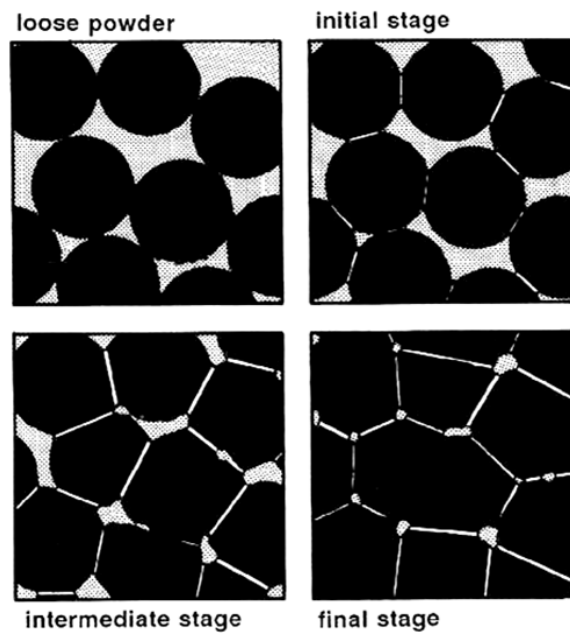


**Figure 2.12:** Microstructure evolution during sintering stages, [RIV 11].

At the initial stage, the sintering process starts with an aggregation of particles and the disappearance of the border began to produce a neck in the points of contact between the particles. Grain boundaries are formed between two adjacent particles in the contact plane. The centres of the particles are only slightly closer, which means very low shrinkage has happened [RIV 11]. Generally, the produced shrinkage at the end of this stage is around 4%.

In the intermediate stage the pores are reduced due to the growth of the neck of the initial stage [NAS 04]. At the same time, these pores are reorganized, rounding and interconnected like the cylindrical channel in order to maximize the contact between the particles. The grain growth takes place late in this stage.

Final stage sintering is much slower than the initial and intermediate stages. In this stage, pores are closed, isolated and located principally at the boundaries or within the grains. Also, the densification rate becomes slow and the grain growth is more evident. At the end of sintering process, the green component shrinks by around 40 vol % [GER 96].

#### 2.3.4 Modeling of solid state sintering

Numerical simulation of sintering stage is one of the most interesting research topics in powder injection moulding process. Research works related to sintering modeling started in the middle of the twentieth century. On the other hand, the last three decades have seen the emergence of numerical simulation as a new tool for the study of the microstructural evolution during sintering.

##### *a) Initial Stage - Solid State Sintering Models*

Several models for initial - stage solid - state sintering have been developed by many researchers [FRE 45] and [JOH 63]. These models predict the rate of neck growth and densification for simple geometries like spheres. Equations have been proposed to calculate the neck size, **Figure 2.13**, as a function of time for different transport mechanisms, for example, Equation (2-17):

$$\left(\frac{X}{R}\right)^n = \frac{Bt}{R^m} \quad (2-17)$$

where  $t$  is the sintering time at a specific isothermal sintering temperature,  $X$  is the diameter of the neck,  $R$  is the diameter of spherical particles and  $B$  is a coefficient

characteristic of the mechanism.  $n$  and  $m$  are the exponent values related to different mechanisms.

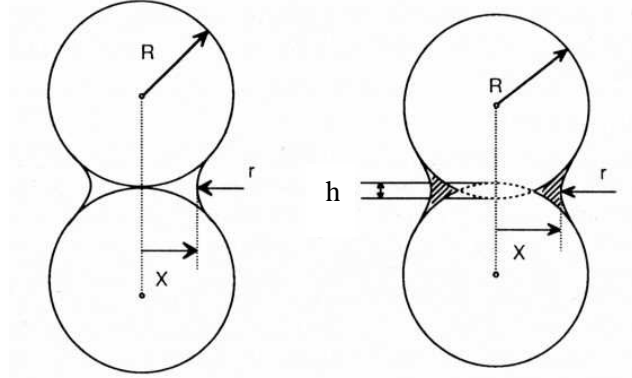


**Figure 2.13:** Two-particle geometric model for the initial stage of sintering, [CAL 05].

Clavier et al. tried [CLA 13] studied the first stage of sintering through the use of cerium oxide powders with controlled morphology. It was possible to observe the building bridges (the necks), **Figure 2.14**, similar to those frequently developed in the numerical models, **Figure 2.13**.

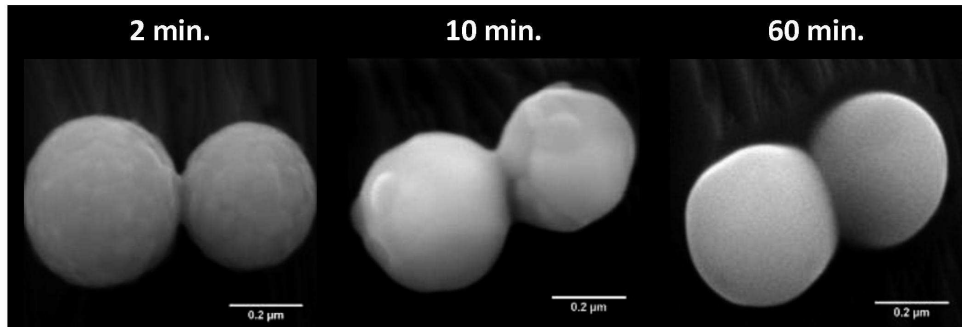


**Figure 2.14:** Neck evolution during the first stage of sintering through the use of cerium oxide ( $\text{CeO}_2$ ) powders, [CLA 13].

Based on the two- particle geometric model as shown in **Figure 2.13**, the shrinkage is determined by the ratio of the overlap distance  $h$  to the initial distance between the two sphere centers,  $R$  , as follows:

$$\frac{\Delta L}{L_0} = \frac{h}{R} \quad (2-18)$$

Another approximate geometric relationship is given as follows [SON 07]:

$$y = \frac{h}{2} = \frac{X^2}{8R} \quad (2-19)$$

By combining equations (2-18) and (2-19), the shrinkage related to the neck size is given as follows:

$$\frac{\Delta L}{L_0} = \left( \frac{X}{2R} \right)^2 \quad (2-20)$$

By combining equations (2-17) and (2-20), the shrinkage during the initial sintering stage can be given as follows:

$$\left( \frac{\Delta L}{L_0} \right)^{n/2} = \frac{Bt}{2^n R^m} \quad (2-21)$$

### ***b) Intermediate Stage - Solid State Sintering Models***

Coble [COB 61] adapted a representative model for the intermediate solid state sintering. Microstructure with porosity was modeled as cylinders around the edges of the grains, **Figure 2.15**. The densification rate is calculated for the case of matter transport by volume and grain boundary diffusions. For volume diffusion, the densification rate using equation (2-22) is:

$$\frac{1}{V} \frac{dV}{dt} = -457 \frac{D_v \gamma \Omega}{kTd^3} \quad (2-22)$$

In the case of grain boundary diffusion, the densification rate is given as follows:

$$\frac{1}{V} \frac{dV}{dt} = -40 \frac{\delta_b D_b \gamma \Omega}{kTd^4} \frac{1}{r} \quad (2-23)$$

where  $1/V dV/dt$  is the volumetric densification rate.  $D_v$  and  $D_b$  are the diffusion coefficients for volume and grain boundary diffusion, respectively.  $\Omega$  is the atomic volume,  $\gamma$  is the surface energy,  $\delta_b$  is the width for grain boundary diffusion,  $k$  is the Boltzmann constant, and  $T$  is the absolute sintering temperature. The parameters  $r$ ,  $l$  and  $d$  characterize the microstructure, and they are shown in **Figure 2.14**.

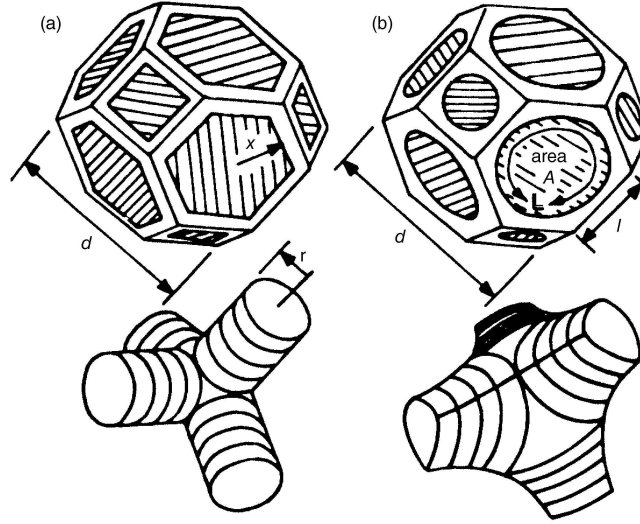


**Figure 2.15:** Representative unit cell for intermediate -stage solid -state sintering: (a) Original model of Coble [COB 61] and (b) modification by Beere [BEE 75], adapted from [BAN 12].

The densification rate for combined volume and grain boundary diffusions during intermediate stage, in terms of geometric parameters has been developed by Johnson [JOH 70]; its expression is given as follows:

$$\frac{1}{V} \frac{dV}{dt} = -8 \frac{\bar{H} \gamma \Omega}{\bar{x} k T} \{ D S_v + \delta_b D_b L_v \} \quad (2-24)$$

where  $\bar{H}$  and  $\bar{x}$  are the average value of the pore curvature and of the grain boundary radius, respectively.  $S_v$  is the pore surface area per unit volume and  $L_v$  is the length of the grain boundary/pore intersection per unit volume.

### c) Final - Stage Solid - State Sintering Models

This stage of sintering starts to take place when most of the pores, which during the intermediate stage form a network, are closed and isolated. One can say that final stage of sintering is geometrically the simplest one among the three stages. [COB 61] has proposed a model based on this geometry, **Figure 2.16**, to estimate the rate of densification during this stage. For this model, Coble suggested concentric spherical lattice diffusion of atoms from a distance of  $r_2$  to the surface of the pore with a radius of  $r_1$ . The total material flux  $J_{total}$  passing through the imaginary spherical surface towards a pore is expressed as:

$$J_{Total} = 4\pi \frac{D_L}{RT} \Delta\sigma \frac{r_1 r_2}{r_2 - r_1} \quad (2-25)$$

where  $D_L$  is the lattice diffusion coefficient,  $\sigma$  is the sintering stress,  $R$  is the gas constant and  $T$  is the absolute temperature.

If  $r_1 \ll r_2$ , the densification rate  $d\rho/dt$  is given as:

$$\frac{d\rho}{dt} = \frac{288D_L\gamma_s V_m}{RTG^3} \quad (2-26)$$

where  $\gamma_s$  is the specific surface energy,  $V_s$  is the molar volume and  $G$  is the grain size.

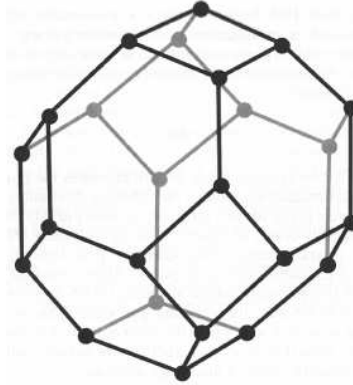


**Figure 2.16:** Closed pores located at grain corners during the final stage of sintering [GER 96], adapted from [SON 07].

Kang [KAN 04], Based on Coble's work, suggested the equations for calculating the densification rate of the sintered body in the final stage for volume diffusion from grain boundary, equation (2-27) and for grain boundary diffusion, equation (2-28) as follows:

$$\frac{d\rho}{dt} = \frac{441D_v\gamma_{sv}\Omega}{kTG^3}(1-\rho)^{1/3} \quad (2-27)$$

$$\frac{d\rho}{dt} = \frac{733D_b\gamma_{sv}\Omega}{kTG^4} \quad (2-28)$$

#### d) Combined - Stage Sintering Model

Hansen et al proposed a single equation that quantifies sintering as a continuous process including: initial, intermediate and final stages which are combined in one stage model [HAN 92] and [KUT 04]. They used two separate parameters representing geometry and scale in order to characterize the

microstructure. The instantaneous linear shrinkage rate using this model for grain boundary and volume diffusion is given as follows:

$$-\frac{dL}{Ldt} = \frac{\gamma\Omega_a}{k_B T} \left( \frac{\Gamma_v D_v}{G^3} + \frac{\Gamma_b \delta D_b}{G^4} \right) \quad (2-28)$$

where  $\gamma$  is the surface energy,  $k_B$  is Boltzmann's constant,  $D$  is the diffusivity,  $T$  is absolute temperature, and  $\Omega_a$  is the atomic volume,  $G$  is the mean grain diameter.

$\Gamma_v$  and  $\Gamma_b$  are the dimensionless geometric parameters which are expressed as follows:

$$\Gamma_b = \frac{aC_k C_b}{C_\lambda C_a C_h} \quad (2-29)$$

$$\Gamma_v = \frac{aC_k C_v}{C_\lambda C_a C_h} \quad (2-30)$$

The above dimensionless geometric parameters change continually to characterize the microstructural evolutions as the sintering proceeds.

## 2.4 Summary

The present chapter has provided a summary of the research studies (experimental and modeling analysis) carried out in thermal debinding and sintering process, over the past few decades, for injection moulded components.

Three principal analytical models for estimation of thermal debinding time have been developed by German [GER 87], these models help identify the options most appropriate for minimizing debinding times. The calculated debinding times are only for relative assessments, since the models represent ideal conditions with several simplifying assumptions. In all three models there is a time dependence on the section thickness squared. Component porosity clearly has a main effect on debinding for all the processes. In thermal debinding, a partial vacuum is most attractive since the diffusion and permeation rates will be reasonable and the gas will aid thermal transport. In addition, small particles sizes are detrimental to removing the binder. Small particles are usually selected for ease of densification during sintering. This provides a conflict between the desire for rapid debinding and high sintered properties. Another approach to describe thermal debinding that is called Master Decomposition Curve (MDC) has been recently developed by Aggarwal et al. [AGG



07, PAR 09]. This approach can describe the evolution of remaining binder for single reaction step (one component of polymer) or multireaction steps (two components of polymer). It is principally based on the work of decomposition  $\Theta$  that depends only on the apparent activation energy  $E_a$ .

Solid state sintering has been largely studied from the theoretical point of view by many researchers by developing microscopic models: J. Frenkel [FRE 45], D L. Johnson [JOH 63] and R L. Coble [COB 61]. Such models have described the evolution of sintering phenomenon for two particles in contact and provided a successful approach to predict the rate of neck growth as a function of time for different transport mechanisms. Since 1990s, many works have been focused on building of macroscopic models describing the evolution of shrinkage and distortions of PIM components during sintering process [GER 02]. In these works, macroscopic models were based on continuum mechanics by implementing proper constitutive law in finite element codes. The famous constitutive law that it was largely used in macroscopic models for sintering is the viscoplastic constitutive one: [BOR 88], [OLE 98], [KRA 04], [SON 07] and [WAK 13].

## Chapter 3: Thermal and Solvent Debinding Investigation for PIM Components

---

### Contents

---

|            |   |           |
|------------|---|-----------|
| <b>3.1</b> | <b>Introduction.....</b>                                      | <b>61</b> |
| <b>3.2</b> | <b>Experimental investigation in thermal debinding.....</b>   | <b>63</b> |
| 3.2.1      | Materials .....   | 63        |
| 3.2.1.1    | Powder properties.....  | 63        |
| 3.2.1.2    | Binder components properties .....                            | 64        |
| 3.2.1.3    | Feedstocks preparation.....                                   | 64        |
| 3.2.2      | Weight loss during thermal debinding.....                     | 67        |
| 3.2.3      | Thermal characterisation of binders and feedstocks.....       | 68        |
| 3.2.3.1    | Differential scanning calorimetry (DSC).....                  | 69        |
| 3.2.3.2    | Thermogravimetric analysis (TGA).....                         | 70        |
| 3.2.4      | Estimation of kinetic parameters.....                         | 73        |
| 3.2.4.1    | Ozawa method.....   | 73        |
| 3.2.4.2    | Kissinger method.....   | 74        |
| 3.2.5      | Effect of heating rate and powder volume loading energy.....  | 76        |
| 3.2.6      | Effect of powder volume loading on the activation energy..... | 78        |
| 3.2.7      | Evolution of activation energy during thermal debinding.....  | 80        |
| <b>3.3</b> | <b>Experimental investigation in solvent debinding .....</b>  | <b>82</b> |
| 3.3.1      | Material.....   | 83        |
| 3.3.2      | Evolution of remaining binder.....                            | 84        |
| <b>3.4</b> | <b>Summary.....</b>   | <b>85</b> |

---

### **3.1 Introduction**

As mentioned previously, the binder system usually consists of several components which have different functionalities. First binder paraffin wax (PW) has a low viscosity to allow an easy cavity filling during injection moulding. The second binder is polypropylene (PP) that keeps the component shape after injection moulding and then debinding. The third binder is an additive surfactant stearic acid (SA) that is added to facilitate powder wetting by decreasing the surface energy of the binder-powder.

Thermoplastic binders are widely used both in powder metallurgy or ceramic industries, such as in sensors manufacturing and medical devices [IMB 08]. Such binders need to be removed from the powder compact before the sintering stage at final functional component. The most commonly used method for binder removal is thermal debinding, which is the oxidation of the binder in air or the pyrolysis of binder in argon. If binder removal is incomplete, the trapped polymeric residues will be a contamination source and may affect the final physical or electrical properties of the component [MAS 89]. If the binder removal is too fast, defects such as cracks and large voids may appear and will affect the micro-structural characteristics of the component during sintering [DON 89]. The successful removal of binder occurs without disrupting the packing of the particles or producing any defects in the green components. Thus, the thermal debinding is a critical processing step in the powder injection moulding for processing microcomponents [LEW 96].

Thermal stability studies of different materials by differential thermal analysis (DTA) and thermogravimetric analysis (TGA) have been carried out during years [KOH 07]. Kinetic studies are a main aspect in thermal analysis, in which the purpose is to determine the pyrolysis reaction mechanism and to identify the parameters of the Arrhenius equation [POU 07]. Kissinger [KIS 57] and Ozawa [OZA 65] methods demonstrated that DTA, based on the linear relation between peak temperature and heating rate, can be used to determine the main kinetic parameters of the thermal decomposition: activation energy ( $E$ ) and pre-exponential factor ( $A$ ).

G. Aggarwal et al. proposed a mathematical model based on the characteristics of the polymeric binders used in PIM. The model can predict the decomposition behaviour for new binder formulations related to different powder

characteristics. It provides a tool to change the binder formulations with or without metal powder and to calculate the degradation temperature, the holding time and the heating rate for the debinding process. An earlier study has been proposed for degradation of binders used in powder injection moulding for the manufacturing of complex shape in titanium and Ti alloys [AGG 07]. A comprehensive approach based on intrinsic kinetics of polymers pyrolysis has been set-up to formulate a master decomposition curve (MDC) for each individual binder component and found to be very useful for systematic analyses of thermal debinding behaviour [PAR 09].

The purpose of this chapter is to investigate the influence of powder volume loading on thermal debinding behaviour of the feedstocks based on 316L fine stainless steel powders ( $D_{50}=3.4\text{ }\mu\text{m}$ ) and a multi-component binder system. On the other hand, solvent debinding tests for components made of copper will be also carried out in order to study the influence of debinding temperature.

## 3.2 Experimental investigation in thermal debinding

### 3.2.1 Materials

#### 3.2.1.1 Powder properties

During the last recent years, 316L stainless steel is one of the most common metals for injection moulding, either provided in gas atomized or water atomized. Its popularity results from its capabilities to be sintered to high densities and its corrosion resistance [QUI 09]. A large number of researchers investigated the different aspects of 316L stainless steel. Raza et al. related that the thermal debinding temperature, heating rate and thermal debinding time can considerably influence the final characteristics of PIM products [RAF 12]. Barriere et al. conclude that particle size, shape, solid loading, heating rate and atmosphere also affect the deformation defects [BAR 03]. Here in this study, stainless steel powders 316L with particle size of 5  $\mu\text{m}$  have been selected. The metallic powders used in this analysis consist in a gas atomized spherical stainless 316L steel powders with a density equals 7.9  $\text{g}/\text{cm}^3$  [KON 10].

**Figure 3.1** exhibits a scanning electron micrograph (SEM) of the used powders with magnification equals to 2000 and 10000, respectively. One can notice that most of particles are mainly spherical or elliptical, that is well appropriated for injection moulding. Powder size distribution and the chemical composition are related in **Table 3.1** and **Table 3.2**, respectively.

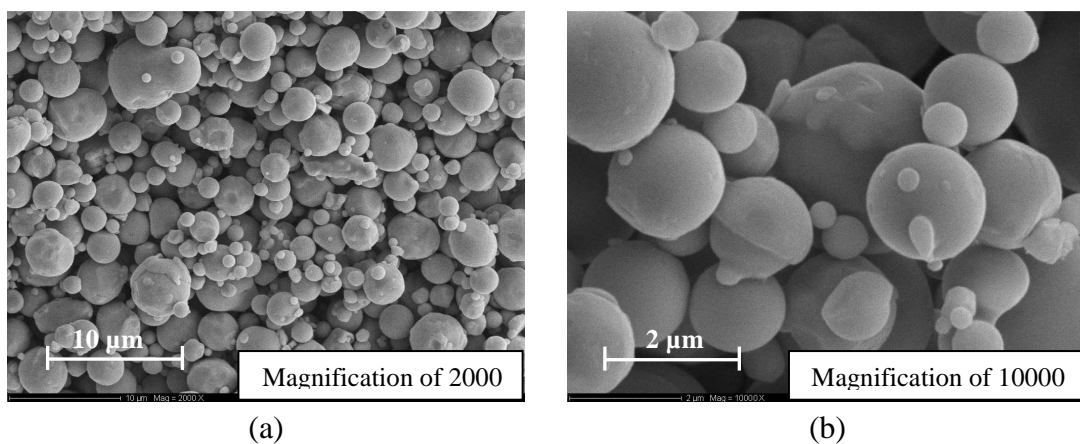


**Figure 3.1:** Scanning electron micrographs of fine 316L stainless steel powders ( $D_{50}=3.4 \mu\text{m}$ ) used in the proposed investigations with magnification equals to a) 2000 and b) 10000.

**Table 3.1:** Particle size distribution of the gas atomized 316L stainless steel powders.

| Powder 316L | Size | D <sub>10</sub> | D <sub>50</sub> | D <sub>90</sub> | density                |
|-------------|------|-----------------|-----------------|-----------------|------------------------|
|             | 5 µm | 1.8 µm          | 3.4 µm          | 6.0 µm          | 7.9 g.cm <sup>-3</sup> |

**Table 3.2:** Chemical composition of the gas atomized 316L stainless steel powders.

| Element    | Cr   | Ni   | Mo  | Mn  | Si   | C     | P     | S     | Fe   |
|------------|------|------|-----|-----|------|-------|-------|-------|------|
| 5µm (wt.%) | 17.4 | 10.9 | 2.5 | 1.2 | 0.64 | 0.021 | 0.015 | 0.006 | Bal. |

### 3.2.1.2 Binder components properties

A multi-component binder system based on paraffin wax has been prepared and used. The paraffin wax (PW) has been chosen as the primary binder in order to decrease the feedstock viscosity and allow an easy flow during injection moulding. The additive surfactant stearic acid (SA) has been added to facilitate powder wetting. The secondary binder polypropylene (PP) has been chosen to keep the component shape after injection moulding and then debinding. The characteristics of the binder components are summarised in **Table 3.3**.

**Table 3.3:** Characteristics of the polymer ingredients used in the binder system.

| Binder components  | Density [g.cm <sup>-3</sup> ] | Decomposition range (°C) | Linear formula  | Molecular weight                                |
|--------------------|-------------------------------|--------------------------|---|---|
| Primary binder     |                               |                          |   |   |
| Polypropylene (PP) | 0.90                          | 390 to 500               | [CH <sub>2</sub> CH(CH <sub>3</sub> )] <sub>n</sub>     | M <sub>w</sub> ≈304940<br>M <sub>n</sub> ≈46832 |
| Secondary binder   |                               |                          |   |   |
| Paraffin Wax (PW)  | 0.91                          | 260 to 380               | [C <sub>n</sub> H <sub>2n+2</sub> ] <sub>m</sub>        | M <sub>w</sub> ≈754<br>M <sub>n</sub> ≈721      |
| Surfactant         |                               |                          |   |   |
| Stearic Acid (SA)  | 0.86                          | 220 to 350               | [CH <sub>3</sub> (CH <sub>2</sub> ) <sub>16</sub> COOH] | M <sub>w</sub> ≈484<br>M <sub>n</sub> ≈475      |

### 3.2.1.3 Feedstocks preparation

A previous study has been carried out by Kong et al. [KON 11], where different formulations of feedstocks have been tested and characterized. Binder systems with three components were elaborated using the following polymers:

Polypropylene (PP), Polyethylene, Paraffin Wax (PW), Carnauba Wax (CW), Oleic Acid (OA) and Stearic Acid (SA). The powder volume loading varied from 50 to 78%. The formulation with binder system composed of Polypropylene (PP), Paraffin Wax (PW) and Stearic Acid (SA) with powder volume loadings of 60, 62, 64 and 66% has been chosen as the formulation the most proper for injection step. The critical powder volume loading was fixed at 68%.

In the present study, 316L stainless steel powders mixtures with different powder volume loadings varying from 60 to 66% with increment 2% are mixed with the polymeric binder system (Powder + PP + PW + SA) at a temperature equals 180°C during 30 minutes using twin screw mixing, **Table 3.4**. Then, the elaborated feedstocks have been used for thermal debinding step in order to choose the proper one for this step.

**Table 3.4:** Components and contents used for the proposed feedstock formulations with different powder volume loadings.

| Formulations       | Contents in volume (%) |                    |                   |                   |
|--------------------|------------------------|--------------------|-------------------|-------------------|
|                    | Powder volume loading  | Polypropylene (pp) | Paraffin Wax (PW) | Acid Stearic (SA) |
| <b>Feedstock 1</b> | 60                     | 16                 | 22                | 2                 |
| <b>Feedstock 2</b> | 62                     | 15                 | 21                | 2                 |
| <b>Feedstock 3</b> | 64                     | 14                 | 20                | 2                 |
| <b>Feedstock 4</b> | 66                     | 13                 | 19                | 2                 |

In mixing process, the binder and metallic powders are introduced in the heated mixing chamber where two rotating blades are turning reversely towards each other with different speeds in order to provide excellent compounding and mixing characteristics.

As shown in **Figure 3.2**, at the beginning of mixing operation, mixing torques increase progressively in values, this increasing is due to the presence of friction between the metallic powders and the partially melted binder system. Just after the torque peaks, the viscous effect of the melted binder appears and leads to a decreasing in the friction between the feedstocks components (powders + binder) and therefore a decreasing in the mixing torque values is obtained. At the end of the mixing process,

the mixing torques stabilize and reach low values which explains that the binder system is fully melted and the feedstocks are homogenously mixed, see **Figure 3.3**.

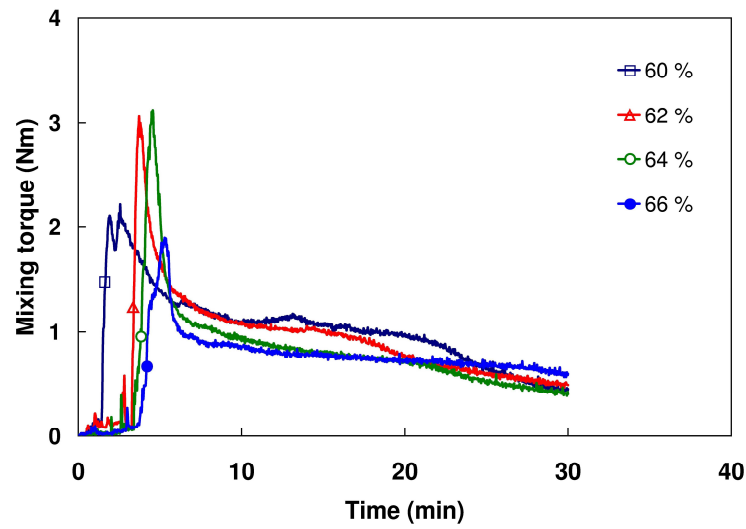


**Figure 3.2:** Mixing torques vs. time for 316L stainless steel powder with different powder volume loadings at maximal mixing temperature of 180 °C during 30 min.

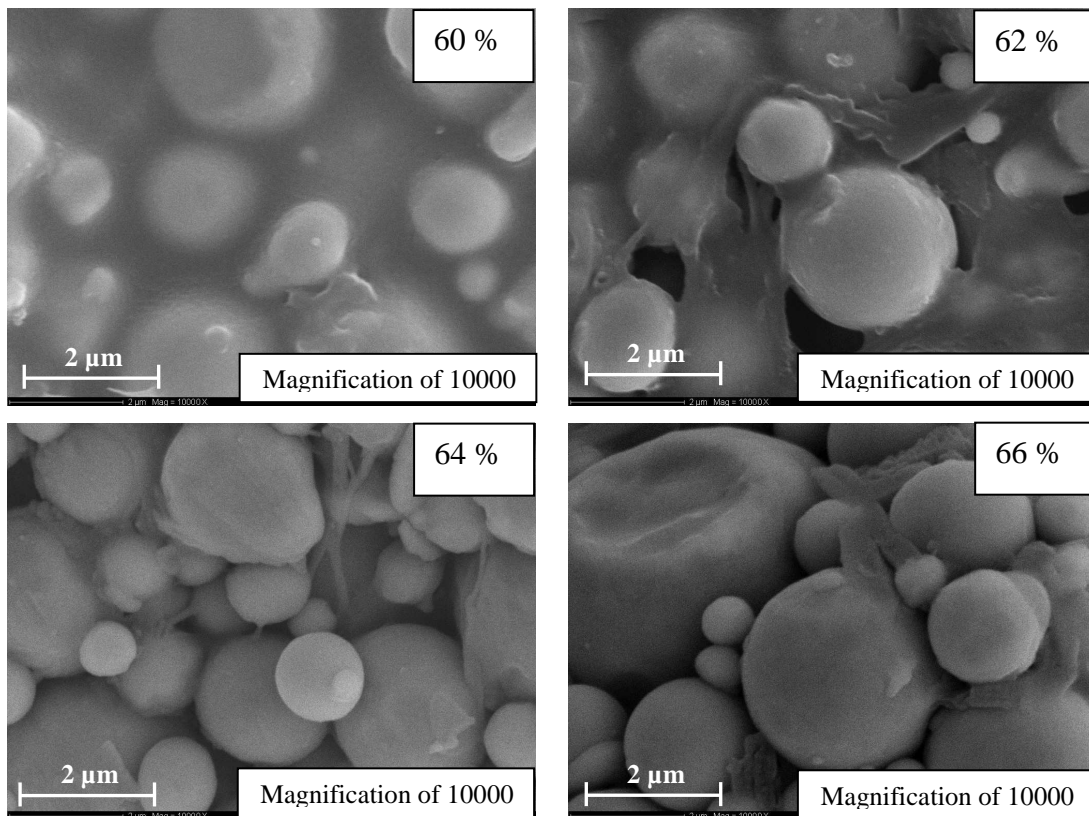


**Figure 3.3:** Scanning electron micrographs of feedstock loaded at 60, 62, 64 and 66% after mixing stage.



### 3.2.2 Weight loss during thermal debinding

Debinding process is generally employed to remove the binders from the moulded components and depends on the composition of the binder system in the feedstock. In the present study; the debinding process has been carried out by thermal debinding using SETSYS Evolution provided by Setaram<sup>®</sup>. The temperature test varied from 25 to 500°C at three different heating rates 2, 5 and 10°C/min for the elaborated feedstocks loaded at 60, 62, 64 and 66%. The same cooling rate of 20°C/min was used for our tests. The thermal debinding cycle using the different heating rates is shown in **Figure 3.4**. To maintain pyrolysis conditions and prevent oxidation of the metallic powder, non-reactive atmosphere (argon) with high purity and flow rate of 20 mL/min has been used as the carrier gas to maintain a stable environment. Sample weights were about 100 mg and all the samples have been put and heated in Platinum crucible.

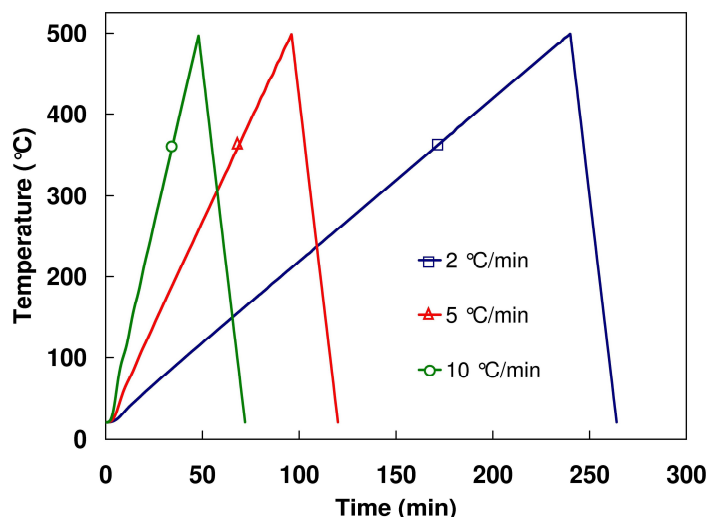


**Figure 3.4:** Heating cycles of the thermal debinding process using three heating rates of 2, 5 and 10° C/min with same cooling rate of 20°C/min.

After thermal debinding stage, measurements have been done in order to determine the final weight loss of system binder for different feedstocks. In fact, the removed quantity is due the total decomposition and evaporation of the binder components during the heating cycle. By comparing the different results as shown in **Table 3.5**, one can clearly notice that the maximal weight loss was obtained in most cases for heating rate of 2 °C/min. On the other hand, the maximal quantity of binder weight loss was obtained for the feedstock loaded at 64, 62 and 60 %, respectively.

**Table 3.5:** Weight loss after thermal debinding process for elaborated feedstocks at different heating rates and maximal temperature of 500°C.

| Heating rate<br>°C/min | Initial weight<br>(mg) | Weight loss<br>(mg) | Weight loss<br>(%) |
|------------------------|------------------------|---------------------|--------------------|
| <b>60%</b>             |                        |                     |                    |
| <b>2</b>               | 104.7                  | 7.102               | 6.78               |
| <b>5</b>               | 99.7                   | 6.922               | <b>7.01</b>        |
| <b>10</b>              | 114.9                  | 6.993               | 6.08               |
| <b>62%</b>             |                        |                     |                    |
| <b>2</b>               | 117.8                  | 8.566               | <b>7.27</b>        |
| <b>5</b>               | 101.7                  | 6.384               | 6.28               |
| <b>10</b>              | 110.6                  | 6.504               | 5.88               |
| <b>64%</b>             |                        |                     |                    |
| <b>2</b>               | 102.1                  | 7.047               | <b>6.90</b>        |
| <b>5</b>               | 125.3                  | 5.969               | 4.76               |
| <b>10</b>              | 145.2                  | 8.687               | 5.98               |
| <b>66%</b>             |                        |                     |                    |
| <b>2</b>               | 117.6                  | 6.42                | <b>5.46</b>        |
| <b>5</b>               | 132.8                  | 7.17                | 5.39               |
| <b>10</b>              | 96.6                   | 5.27                | 5.45               |

### 3.2.3 Thermal characterisation of feedstocks

Thermal characterisations aim to investigate the thermal stability of the binder components used previously in the elaboration of feedstocks. These thermal characterisations are generally carried out by means of Differential Scanning Calorimetry (DSC) and/or simultaneous thermogravimetry and differential thermal analysis (TG-DTA). Its principal goal is the determination of kinetic parameters of non-isothermal decomposition of binder components. Thermal stability studies of different materials by Differential Scanning Calorimetry (DSC), Differential Thermal Analysis (DTA) and Thermogravimetric Analysis (TGA) have been carried out for several years: Commercial rubbers using TG-ATG [KIM 00], feedstocks for Powder Injection Moulding [SHI 04] using TG-ATG. BMA [Benzyl Methyl Amino] and

BDA [Bis Dibenzyl Amino] using TG-ATG and DSC [HAJ 09]. To calculate the kinetic parameters of the Arrhenius equation, two methods have been used in this investigation: Ozawa and Kissinger methods and both methods will be presented in the next section. The term of kinetic was derived from the Greek language that means: action of moving. The kinetics of feedstocks decomposition is investigated in order to determine the appropriate binder system and powder volume loading for limiting cracks and distortion of the injected moulded components during thermal debinding.

### **3.2.3.1 Differential Scanning Calorimetry tests**

Differential Scanning Calorimetry (DSC) is one of the adaptive apparatus which is used for direct assessment of the heat energy uptake, which occurs in a sample within a regulated increase or decrease in temperature [POO 10]. It provides qualitative and quantitative information on the phase transitions and degradations of materials. Based on the mechanism of operation, DSC can be classified into two types: heat-flux DSC and power-compensated DSC [HAI 98].

In a heat flux DSC, the sample material is enclosed in a pan and an empty reference pan are then placed on a thermoelectric disk surrounded by a furnace. However, owing to the heat capacity ( $C_p$ ) of the sample, there would be a temperature difference between the sample and reference pans, which is measured by area thermocouples, and the consequent heat flow is determined by the thermal equivalent of Ohm's law [HAI 98, DAN 02]. The present (DSC) experiments were conducted in a Setaram (DSC92, **Figure 3.5**) instrument at different heating rates 2, 5 and 10 °C/min in the temperature range of 25 to 500 °C. The sample weight varied between 10 and 20 mg.



**Figure 3.5:** Differential Scanning Calorimetry apparatus, DSC92.

The DSC curves for the feedstock loaded at 60 % are displayed in **Figure 3.6**. The DSC curves exhibit a broad endothermic peak around 60°C which reflects the melting point of the combined stearic acid and paraffin wax. The extremely broad exothermic peak in the range from 200 to 500°C corresponds to the decomposition of stearic acid, Paraffin wax and polypropylene. However to analyse thermal debinding, it is important to get exact decomposition temperatures for different steps. For DSC results, the peak of maximal temperature in the first step of decomposition can't be determined. The same problem was encountered for the other feedstocks loaded at 62, 64 and 66%. So, all the tests will be carried out using a thermogravimetric analyser (TGA) provided also by Setaram<sup>®</sup>.

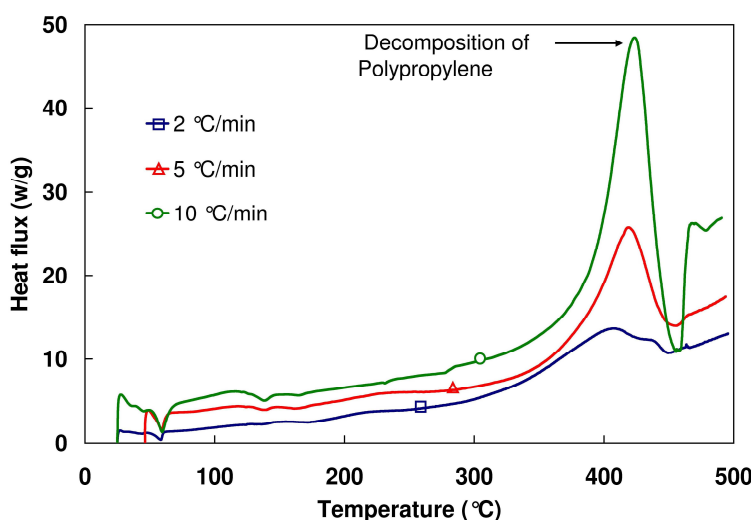


**Figure 3.6:** DSC curves related to 316L stainless steel feedstock loaded at 60 % at different heating rates.

### 3.2.3.2 Thermogravimetric Analysis TGA

Thermogravimetry (TG) test aims to study the relationship between the sample's weight loss and its temperature during thermal debinding. So, the sample weight loss can be measured at any temperature and/or time. From the literature, three modes thermogravimetry test have been distinguished as follows: (1) isothermal thermogravimetry, in which the sample mass is recorded as a function of time at constant temperature, (2) quasi-isothermal thermogravimetry, in which the sample is heated to some constant temperature, (3) dynamic thermogravimetry, in which the sample is exposed to the effect of some temperature programme, usually a linear rate. The TG curve giving the evolution of weight loss versus temperature can be called also: thermolysis curve, pyrolysis curve and thermogravimetric curve [ARO 05]. The

TG technique is largely limited to the study of decomposition and oxidation reactions and to such physical processes as vaporization, sublimation and desorption [PRI 00]. The thermogravimetry test provides crucial informations about mechanisms of materials degradation, composition of the possible residue and also can give ideas about its thermal stability.

The TGA curves presenting the remaining binder content for the feedstocks loaded at 60, 62, 64 and 64 % are displayed in **Figure 3.7**. The TGA curves exhibit two decomposition steps; the first step in the range from 180 to 350°C corresponds to the decomposition of stearic acid and paraffin wax according to their low molecular weight. The second one in the range from 350°C to 460°C corresponds to the decomposition of polypropylene with height molecular weight. However to analyse thermal debinding, it is important to get accurate maximal decomposition temperature for both steps. The TG analyses were repeated three to six times.

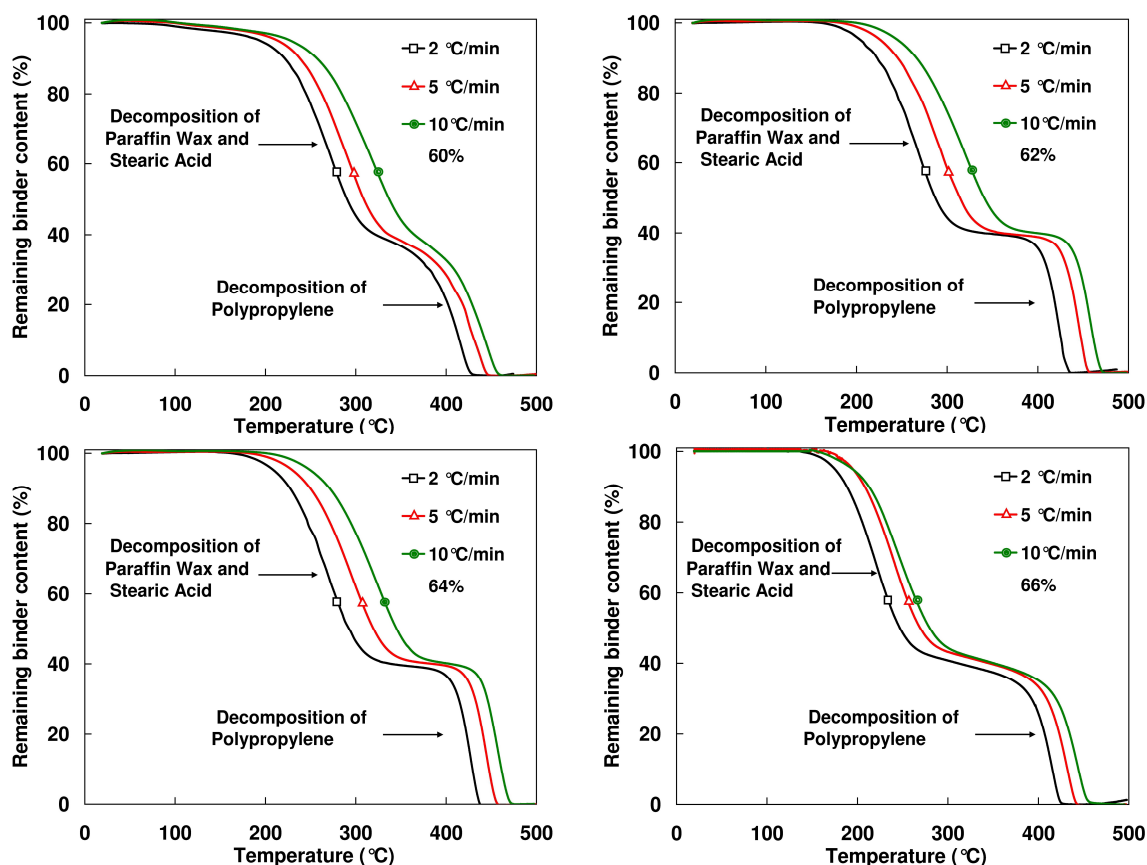


**Figure 3.7:** Remaining binder content vs. temperature, corresponding to different powder volume loadings at different heating rates for 316L stainless steel in argon atmosphere.

DTG results shown in **Figure 3.8** are used to obtain the derivative curve peaks in order to estimate the accurate maximal temperature for which degradation rate is maximal at the first step and the second one, see **Table 3.6** and **Table 3.7**, respectively.

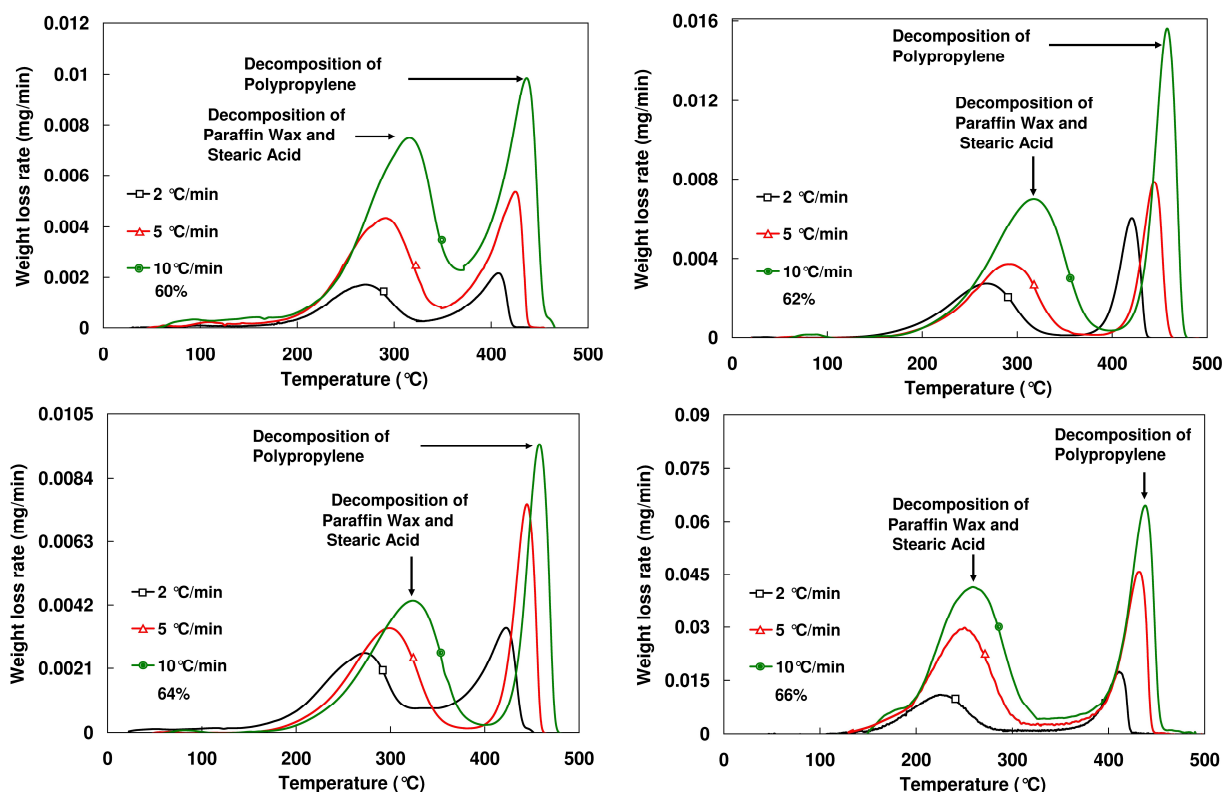


**Figure 3.8:** Weight binder loss rate vs. temperature, corresponding to different powder volume loadings at different heating rates for 316L stainless steel in argon atmosphere.

**Table 3.6:** Maximal temperatures for which degradation rate is maximal at the first step for different feedstocks using different heating rates 2, 5 and 10 °C/min.

| Powder volume loading                   |           | 60%    | 62%    | 64%    | 66%    |
|---|-----------|--------|--------|--------|--------|
| Maximal temperature of degradation (°C) | 2 °C/min  | 274 ±6 | 271 ±3 | 276 ±3 | 229 ±3 |
|   | 5 °C/min  | 293 ±6 | 297 ±3 | 302 ±3 | 252 ±3 |
|   | 10 °C/min | 319 ±6 | 323 ±4 | 328 ±4 | 262 ±4 |

**Table 3.7:** Maximal temperatures for which degradation rate is maximal at the second step for different feedstocks using different heating rates 2, 5 and 10 °C/min.

| Powder volume loading                   |           | 60%    | 62%    | 64%    | 66%    |
|---|-----------|--------|--------|--------|--------|
| Maximal temperature of degradation (°C) | 2 °C/min  | 410 ±4 | 422 ±2 | 426 ±2 | 413 ±2 |
|   | 5 °C/min  | 426 ±4 | 445 ±2 | 444 ±2 | 429 ±2 |
|   | 10 °C/min | 437 ±4 | 458 ±4 | 458 ±4 | 439 ±4 |

### 3.2.4 Estimation of kinetic parameters

In this work the activation energy has been obtained from non-isothermal TGA test. The methods used to calculate kinetic parameters, proposed by Kissinger [KIS 57] and Ozawa [OZA 65], are called model-free non-isothermal methods and require a set of experimental tests at different heating rates. The activation energy determined by applying these methods is the sum of activation energies associated to chemical reactions and physical processes in thermal decomposition and therefore it is called apparent activation energy [SUA 04]. As we said previously, kinetic parameters (Activation energy  $E$  and Pre-exponential factor  $A$ ) and heating temperature represent the main variables of Arrhenius equation. The activation energy describes quantitatively the energy barrier to reaction or degradation of the polymers in question. On the other hand, the Pre-exponential factor is then deduced from the measured activation energy value using a mathematical formula proposed in the literature. The Pre-exponential factor can be also identified using inverse method.

#### 3.2.4.1 Ozawa method

The Ozawa method [OZA 65] represents a relatively simple method for the determination of activation energy directly from weight loss versus temperature data, obtained for several heating rates.

The temperature at which the maximum rate of weight binder loss occurs ( $T_{\max}$ ) is used to calculate the kinetic parameters through the Ozawa method. These parameters are the activation energy ( $E$ ) and the pre-exponential factor ( $A$ ) related to the decomposition process. A linear relationship, **Figure 3.9**, between the heating rate ( $\text{Log}\beta$ ) and the reciprocal of the absolute temperature ( $1/T_{\max}$ ) may be found and the following linear equation can be established:

$$\text{Log}\beta = aT_{\max}^{-1} + b \quad (3-1)$$

where ( $a$ ) and ( $b$ ) are the parameters of the linear curve: ( $a$ ) is  $-0.4567 E/R$  (slope) and ( $b$ ) is a constant (linear coefficient).  $R$  is the gas constant.

Assuming that the rate constant follows the Arrhenius law, the maximum conversion rate for different heating rates is a linear curve. According for such assumptions, equation (3-1) may be applied at maximal temperature considering different heating rates. Thus carrying out several experiments at different heating



rates, the variation of  $\text{Log}\beta$  vs.  $1/T_{\text{max}}$  can be plotted and the activation energy can be estimated directly from the slope of the curve using the following equation derived from equation (3-1):

$$E = -2.19R(d \log \beta / dT_{\text{max}}^{-1}) \quad (3-2)$$

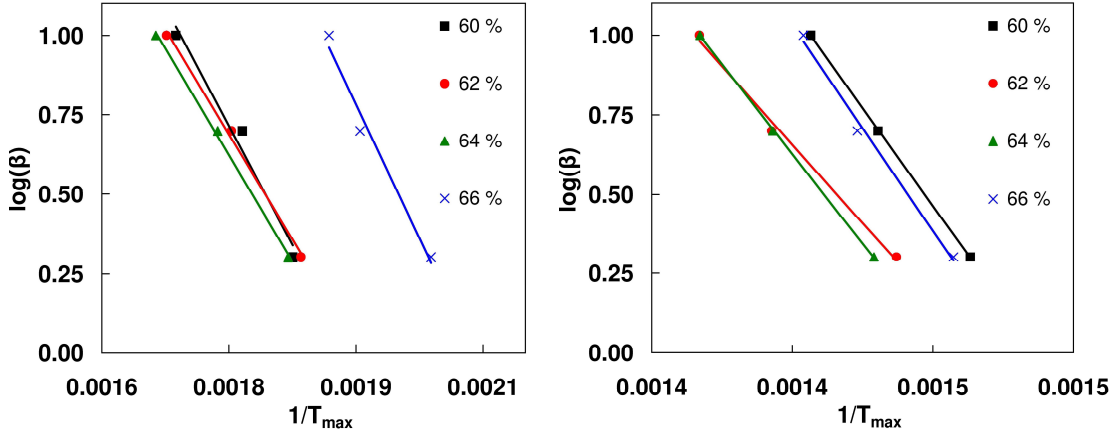


**Figure 3.9:** Curves related to the Ozawa method used for the determination of activation energy related to the thermal decomposition of steel 316L stainless steel feedstock loaded at 60, 62, 64 and 66%.

The **Table 3.8** relates the activation energy values, using Ozawa method, estimated for the elaborated feedstocks 60, 62, 64 and 66% with three different heating rates 2, 5, 10 °C/min as presented in **Figure 3.10**.

**Table 3.8:** Activation energy values using Ozawa method for the first and second step of different feedstocks.

| Powder volume loading      |             | 60%    | 62%    | 64%    | 66%    |
|----------------------------|-------------|--------|--------|--------|--------|
| Activation energy (kJ/mol) | First step  | 91 ±5  | 80 ±5  | 81 ±5  | 102 ±3 |
|                            | Second Step | 212 ±6 | 179 ±3 | 205 ±3 | 235 ±6 |

### 3.2.4.2 Kissinger method

With the above assumptions, the Kissinger method [KISS 57] allows to obtain the kinetic parameters of a solid-state reaction without knowing the reaction mechanism.



This method allows to obtain the value of activation energy from a plot of  $\ln(\beta/T_{\max}^2)$  against  $1/T_{\max}$ , see **Figure 3.10**.

$$E = -R[d \ln(\beta/T_{\max}^2)/dT_{\max}^{-1}] \quad (3-3)$$

Once ( $E$ ) is known, the values of pre-exponential factor,  $A$ , are calculated with equation (3-5):

$$A = \beta E e^{E/RT_{\max}} / RT_{\max}^2 \quad (3-5)$$

For both methods, the correlation between ( $E$ ) and ( $A$ ) observed by Seong-Jin et al. for titanium powder [PAR 09] is quite similar to the one observed in the present work.

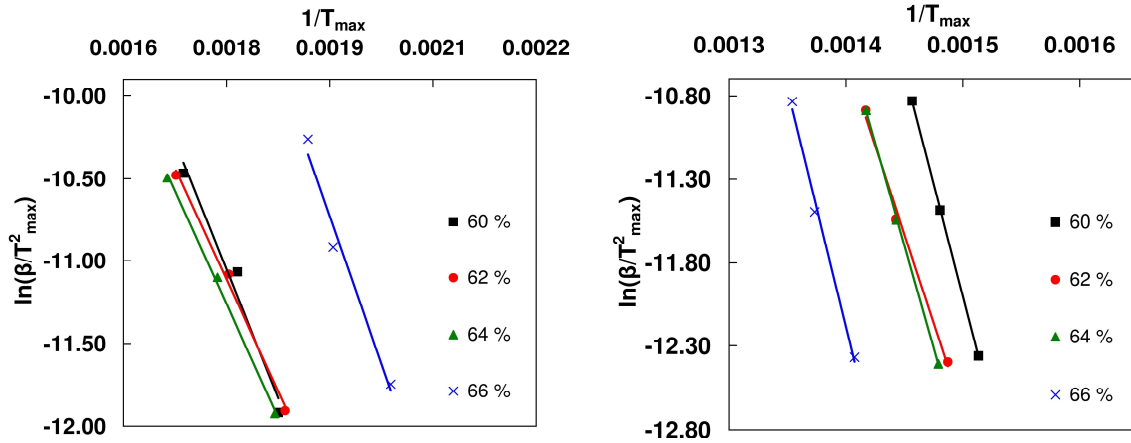


**Figure 3.10:** Curves related to the Kissinger method used for the determination of activation energy related to the thermal decomposition of steel 316L stainless steel feedstock loaded at 60, 62, 64 and 66%.

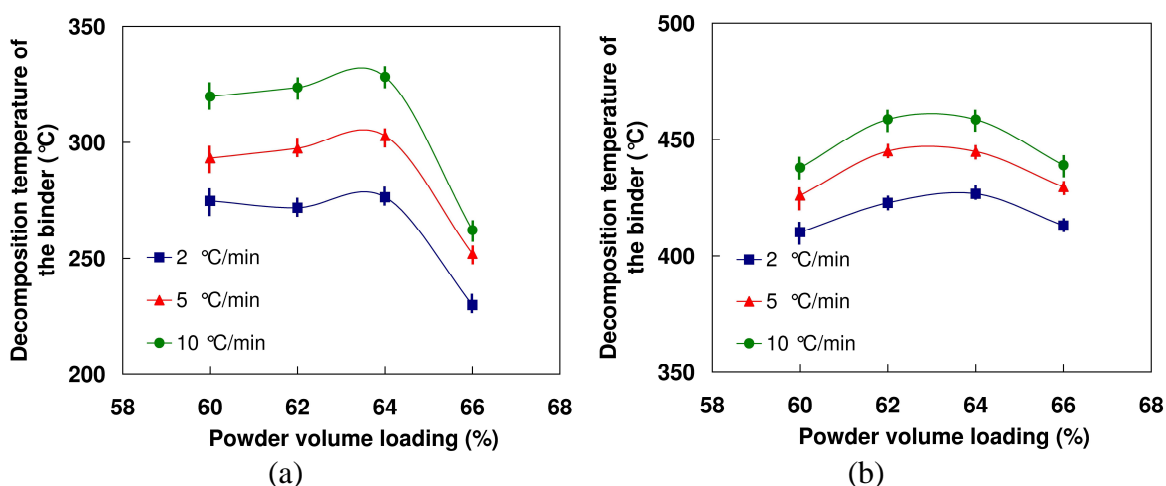
The **Table 3.9** relates the activation energy values, using Kissinger method, estimated for the elaborated feedstocks 60, 62, 64 and 64% with three different heating rates 2, 5, 10 °C/min as presented previously in **Figure 3.11**.

**Table 3.9:** Activation energy values using Kissinger method for the first and second step of different feedstocks.

| Powder volume loading      |             | 60%    | 62%    | 64%    | 66%    |
|----------------------------|-------------|--------|--------|--------|--------|
| Activation energy (kJ/mol) | First step  | 86 ±3  | 74 ±3  | 76 ±3  | 98 ±2  |
|                            | Second Step | 212 ±4 | 176 ±3 | 204 ±2 | 235 ±4 |

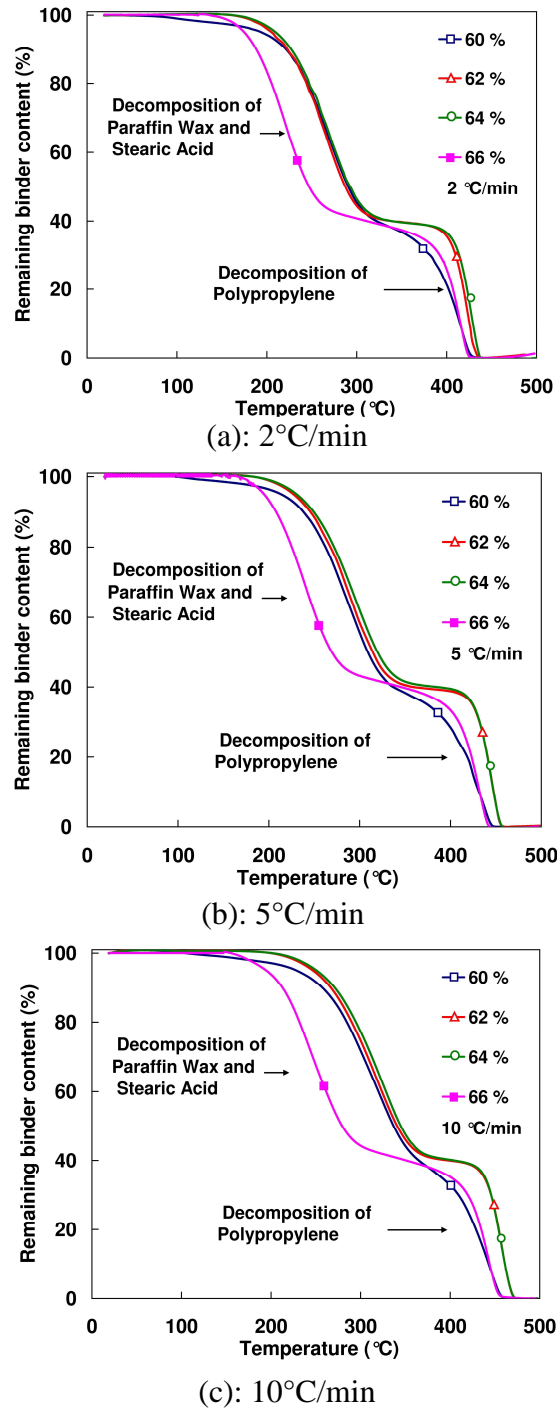
### 3.2.5 Effect of heating rate and powder volume loading

**Figure 3.11** relates the effect of powder volume loading on the decomposition temperature of the binder system at three different heating rates. The data presented in figure 3.11 shows two main stages in the variation of decomposition temperature whatever the heating rate, that as the powder volume loading is increased from 60 to 64 %, the decomposition temperature of the feedstocks is shifted to relatively higher temperatures for all heating rates 2, 5 and 10°C/min. The decomposition temperature is almost constant when the powder volume loading ranges between 62 and 64 %. As the powder volume loading increases from 64 to 66 %, the decomposition temperature of the feedstocks is decreased for all heating rates and especially for feedstock loaded at 66% in the first stage corresponding to the elimination of Acid stearic and Paraffin Wax.



**Figure 3.11:** Maximal binder decomposition temperature versus powder volume loading: (a) first step corresponding to degradation of PW+SA, (b) second step corresponding to degradation of PP.

In addition, the decomposition temperatures, obtained for feedstock loaded at 60%, are low but not as the ones corresponding to 66%. So, this feedstock may be not proper for thermal debinding. Therefore, the feedstock with powder volume loading of 66% seems the most sensitive to temperature; the thermal degradation of the binder system for this feedstock is quite fast which may lead to the distortion of components during thermal debinding stage. This fast degradation will look more clear in the **Figure 3.12**. On the other hand, the decomposition temperature of the binder system is strongly increased when the heating rate increases from 2 to 10°C/min.



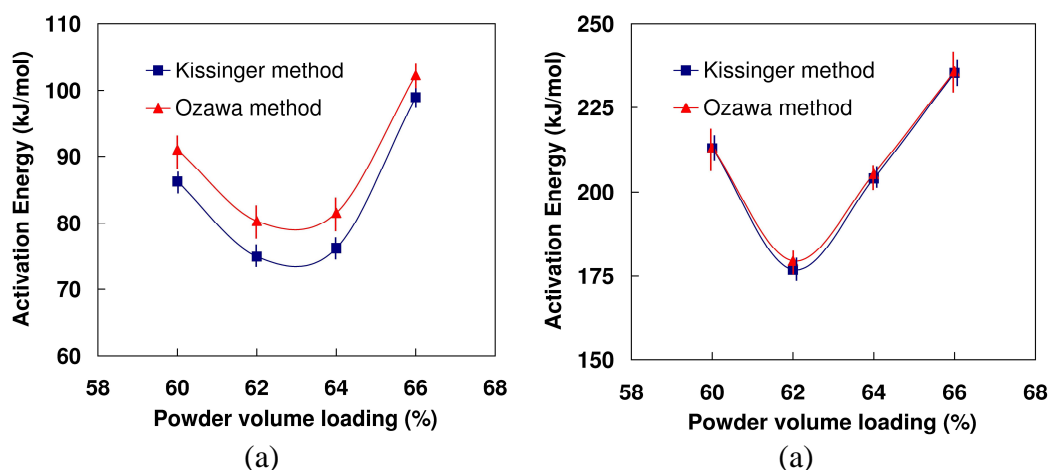
**Figure 3.12:** Remaining binder content vs. temperature, corresponding to different powder volume loadings at different heating rates for 316L stainless steel in argon atmosphere.

Figure 3.12 presents the remaining binder versus temperature for different powder volume loadings at different heating rates, it can be shown that the remaining binder content (%) for feedstock loaded at 66 % during the first step is the fast one comparing to other feedstocks and specially with the heating rate of 10 °C/min. This

high rate in binder decomposition could influence, later in the second step, on the component and leads to cracks.

### 3.2.6 Effect of powder volume loading on the activation energy

The apparent activation energy of elaborated feedstocks as a function of powder volume loading is shown in **Figure 3.13**. The values of activation energy obtained from the Kissinger method are consistent with the range of values obtained by the Ozawa method and their average values are very near to each other in both steps, **Figure 3.13**. The difference between the Kissinger and Ozawa method in first step is due to the fact that Ozawa method is more suitable for high decomposition temperatures. The results related to this investigation are in close agreement with the activation energy value of  $214 \text{ kJ mol}^{-1}$  for 316L stainless material determined by Was et al. in a temperature range from 400 to 500°C [WAS 06]. The relationship between activation energy and pre-exponential factor observed by Seong-Jin et al. for titanium powders [PAR 09] is quite similar to the one observed in the present work.



**Figure 3.13:** Apparent activation energy of 316L stainless steel feedstocks (elaborated at the same mixing conditions 180°C, 30 rpm and 30 min) as a function of powder volume loading: (a) first step corresponding to degradation of PW+SA, (b) second step corresponding to degradation of PP.

The use of different experimental methods for calculations causes that the derived kinetic parameters (even if it were calculated with the same method) may differ for the same type of feedstock. In the related analysis, kinetic parameters obtained from the Kissinger and Ozawa methods for different feedstocks indicate a proper correlation.

The activation energy decreases when powder volume loading ranges from 60% to 62%, then increases significantly in the range 62-66% as shown in **Figure 3.13-a** and **Figure 3.13-b**. High value of  $E$  indicates a strong sensitivity of feedstock vs. debinding temperature. Therefore, small temperature fluctuation during thermal debinding for feedstocks with high powder volume loading could cause defects in the debound parts. As debinding temperature increased up to 200°C, a major change has been noticed which is due to debinding rate increasing, as shown previously by the TGA curve in **Figure 3.8**. The binder decomposition usually gives an internal gas pressure, if the gas can not escape fast enough through the interconnected fine pore channels; the gas pressure could increase and build-up [SHE 02], particularly in the center of the part and tend to push the binder fluid out. If the feedstock is high loaded by powder, the internal gas pressure builds up significantly and leads to the formation of cracks and other defects, as related in the case for feedstock loaded at 66% **Figure 3.14**, such cracks and distortions are due to the stress concentration of internal gas pressure in the core of the sample during thermal debinding process.

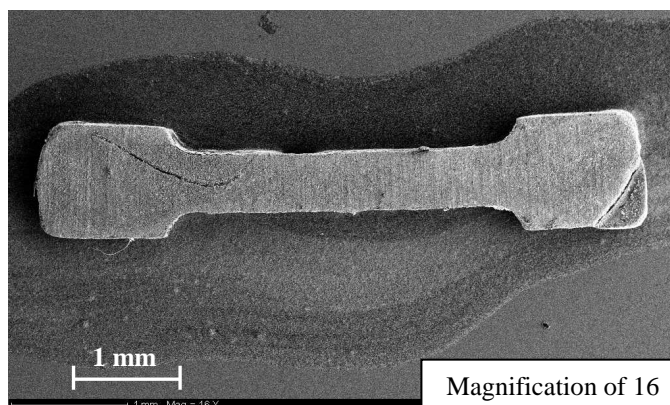


**Figure 3.14:** SEM images of debinded tensile specimen after thermal debinding process for feedstock loaded at 66% of powder volume loading, debound at 300°C with the same heating rate and the same atmosphere.

The small value of  $E$  obtained for feedstock loaded at 62% and relatively small for feedstocks loaded in the range 60-64% indicates a low sensitivity to debinding temperature. Consequently, it results that the debinding rate for these feedstocks (larger interconnected pores) becomes less sensitive to heating rates. This allowed a binder system to have a fast debinding rate without introducing high internal stresses from decomposed gas, thereby minimizing stress concentration, cracks and distortions in the debound parts as shown in **Figure 3.15**. One can say that

feedstock loaded at 62% is the best feedstock to be debound, as this feedstock is less sensitive to temperature.

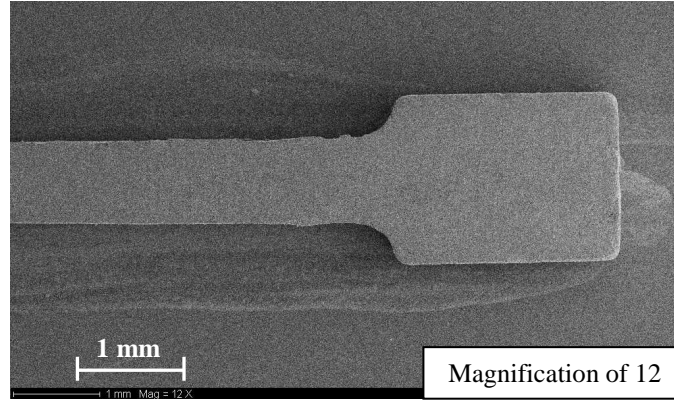


**Figure 3.15:** SEM images of debinded tensile specimen after thermal debinding process for feedstock loaded at 62% of powder volume loading, debound at 300°C with the same heating rate and the same atmosphere.

### 3.2.7 Evolution of activation energy during thermal debinding

The evolution of the apparent activation energy, during thermal debinding, is determined using the Flynn-Wall-Ozawa (FWO) method [OZA 65, FLY 66]. The basic assumption of this method is that the reaction rate at a constant weight loss depends only on the temperature. According to the Flynn-Wall-Ozawa (FWO) method, which involves measuring the temperatures corresponding to fixed values of weight loss from experiments at different heating rates (**Figure 3.7**), the activation energy at any particular value of weight loss is determined by the following equation:

$$\log \beta = \log \left[ \frac{AE}{R g(\alpha)} \right] - 2.315 - 0.4567 \left( \frac{E}{RT} \right) \quad (3-6)$$

Where  $\beta$  is the heating rate,  $A$  (the pre-exponential factor) and  $E$  (the activation energy) are the Arrhenius parameters,  $R$  is the gas constant and  $\alpha$  (10-90 %) is the weight loss.

$g(\alpha)$  is the integral conversion function which depends on the reaction model [JAN 08].

The plot  $\log \beta$  vs.  $1/T$ , obtained from a series of experiments performed at several heating rates, should be a straight line whose slope allows evaluation of the activation energy, **Figure 3.16**:

$$\text{Slope} = \frac{d(\log \beta)}{d(1/T)} = 0.4567 \left( \frac{E}{RT} \right) \quad (3-7)$$

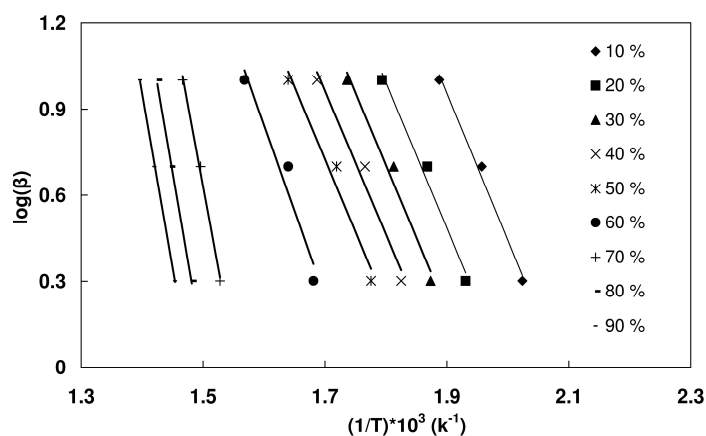


**Figure 3.16:** Curves related to the Flynn-Wall-Ozawa (FWO) method used for the determination of activation energy related to the thermal decomposition of steel 316L stainless steel feedstock loaded at 60%.

The same strategy for the other feedstocks was carried out. **Figure 3.17** shows the apparent activation energy  $E$  dependencies evaluated for the thermal degradation of different feedstocks loaded typically at 60 to 66% under argon. The initial activation energy required to start degradation is about 75 to 110 kJ mol<sup>-1</sup>. As the reaction approaches 70 % conversion, the activation energy increases to a maximum value of about 180 to 235 kJ mol<sup>-1</sup>. This increase falls in the transition region between the first and second step in the mass loss. One can notice that apparent activation energy for the pyrolysis of fine 316L stainless steel feedstocks was not similar for all conversions (weight loss) indicating the existence of a complex multistep mechanism that occurs in the solid state. This means that the thermo-physical mechanism is not the same in the whole degradation process and that activation energy is dependent on conversion and also powder volume loading. A complex dependence of the activation energy on the degree of conversion has been also reported by Budrugaec et al. [SEG 04]. Tomašić et al. explained this variation in apparent activation energy in the terms of the heterogeneous nature of solid sample and/or due to a complex reaction mechanism. It is known that degradation reactions are often very complex and can involve several processes with different activation energies and physical properties of the considered materials [TOM 11].



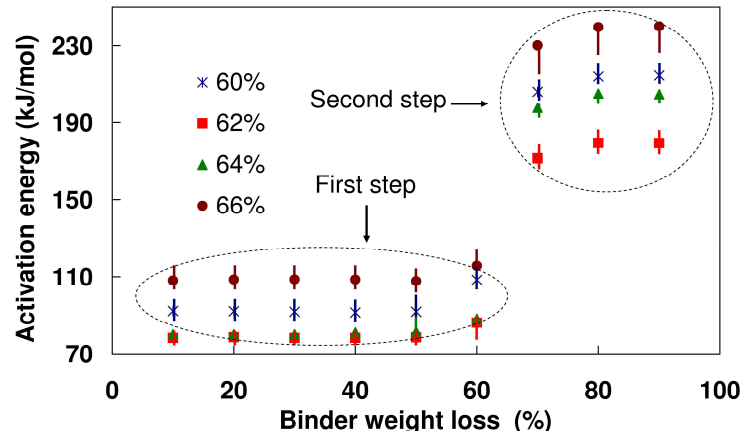


**Figure 3.17:** Apparent activation energy of 316L stainless steel feedstocks as a function of fraction weight loss at different powder volume loadings from 60 to 66% elaborated at the same mixing conditions 180°C, 30 rpm and 30 min.

### 3.3 Experimental investigation for solvent debinding

The binder systems are classified by their debinding techniques and the more advanced debinding techniques require a two-step process, solvent debinding and then thermal debinding process. During the first stage a lower molecular weight binder is dissolved into a fluid in order to create open pore channels within the metal powder assembly. These pore channels provide possibilities for the decomposed gas molecules of the remaining binders to escape to the compact surface during the second debinding step at high temperatures [FAN 09]. Solvent extraction, water debinding, and chemical degradation techniques are most common. A certain binder fraction remains rigid during the first step in order to provide mechanical strength during the chemical and physical removal of the main binder content. The amount of soluble binder removed during this step, should be great enough to form interconnected pores throughout the compact [MOH 11].

In the second processing step the remaining high molecular weight of binder system are removed using a properly adapted thermal treatment in a gas atmosphere (e.g., argon) well known as thermal debinding [QUI 11]. The advantage of the two-step binder systems is that the thermal binder fraction is greatly reduced, thus minimizing the risk of defects such as cracking and part deformation [ANG 95].



### 3.3.1 Material

Copper powders with a pycnometer density of  $8.5 \text{ g/cm}^3$  and an average oversize factor of 1.15 have been used as the base powder in this study. The feedstock shown in **Figure 3.18** has been prepared using copper powder and a multicomponent binder system [JOC 09]. The chemical and physical characteristics of the used powder [JOC 09] are listed in **Table 3.10**.



**Figure 3.18:** Pellets of granulated feedstock based on copper powders ready for use in the injection moulding machine.

**Table 3.10:** Chemical and physical characteristics of the copper powders.

| Composition                | Cu                     | Balance |
|----------------------------|------------------------|---------|
|                            | Fe                     | 0.1     |
|                            | O                      | 0.05    |
| <b>Density</b>             | 8.58 g/cm <sup>3</sup> |         |
| <b>Yield strength Rp02</b> | >50 Mpa                |         |
| <b>Tensile strength Rm</b> | >210 Mpa               |         |
| <b>Hardness</b>            | >40 HB                 |         |

After mixing, the feedstock has been injected using an injection moulding machine, in which square specimens ( $5.6 \times 5.6 \times 0.92 \text{ mm}$ ) have been moulded at  $175^\circ\text{C}$ . The square specimens are then debound at  $40\text{--}60^\circ\text{C}$  with water as solvent. For measuring the soluble binder extraction rate, the specimens have been debound for different periods of time (15 min–2 h) and then dried at  $40^\circ\text{C}$  for 24 h. The components have been sealed on four sides using nonsoluble resin in order to calculate the unidirectional coefficient of diffusion, **Figure 3.19**.

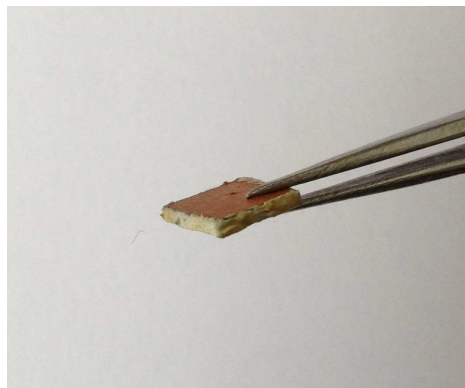


**Figure 3.19:** Square specimens (5.6×5.6×0.92mm) injection moulded at 175 °C using Arburg machine.

### 3.3.2 Evolution of remaining binder content

The influence on the solvent debinding process for the injection moulded components (5.6×5.6×0.92 mm) at three different debinding temperatures is related in **Figure 3.20**. An increase in debinding temperature leads to an efficient improvement in debinding process, due to an improvement in solubility and diffusivity of soluble binder in water as function of temperature [RIC 05].

An initially fast period followed by a progressively slower debinding rate can be observed for the different debinding temperatures, 40, 50 and 60 °C. During solvent debinding process, water diffuses into PIM components and then a chemical reaction occurs by dissolving the soluble binder.

The experimental results clearly show the influence of debinding temperature on the required debinding time. At 40 °C, the components reached 10 % of remaining binder after 1 hour in the water bath. Increasing the bath temperature to 50 °C, the debinding time decreased to 0.5 hour. At a bath temperature 60 °C, 10 % of remaining binder is reached after 0.25 hour, **Figure 3.20**. One can say that the molecular mobility at 60 °C is faster than 40 °C which explain the short time obtained at 60 °C and hence an increasing in water bath temperature leads automatically to an increase in removal rates. Nevertheless, high temperatures are not recommended because the parts will lose their mechanical strength and deformations could occur. For remaining bidder content less then 10%, problems in measurements have been encountered.

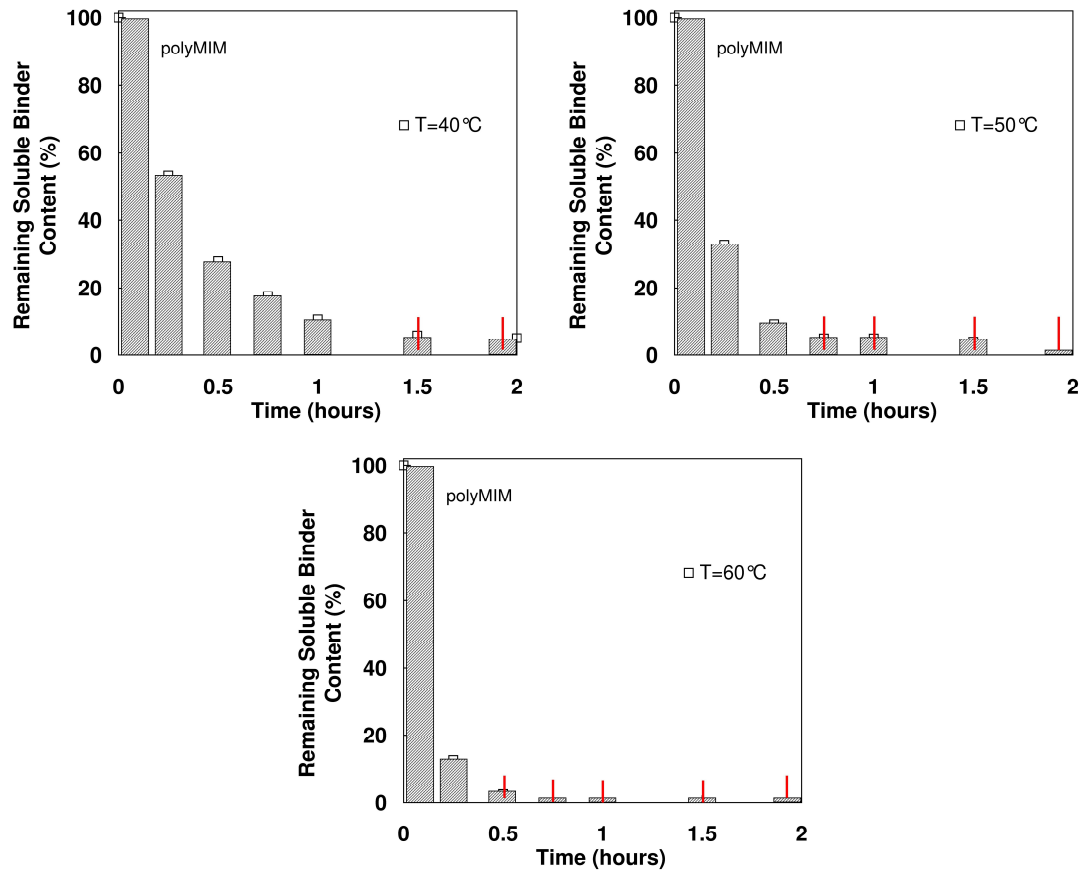


**Figure 3.20:** Binder remaining content inside 0.92-mm-thick square sample at different debinding temperatures 40, 50 and 60 °C.

### 3.4 Summary

Feedstocks made of 316L stainless steel powders have been investigated for PIM process in terms of their thermal debinding behaviour with different powder volume loadings (60, 62, 64 and 66%) and different heating rates (2, 5 and 10°C/min). It was clearly shown that the powder volume loading parameter has an effect on the thermal debinding behaviour. The thermal degradation of the binder system for feedstocks loaded at 62 and 64 % is nearly the same (low values of E); and these feedstocks are the ones less sensitive to temperature. One can also conclude that the feedstock loaded at 62% is the well adapted one for thermal debinding step. The values of the kinetic parameters that were obtained by the Kissinger and Ozawa methods for different feedstocks indicate a proper correlation.

On the other hand, water debinding process for green copper components has been also analysed. The debinding temperature plays a very important role in the water debinding process.

## Chapter 4: Numerical Simulation of Thermal and Solvent Debinding

---

### Contents

---

|            |  |            |
|------------|--|------------|
| <b>4.1</b> | <b>Introduction.....</b>                                       | <b>87</b>  |
| <b>4.2</b> | <b>Numerical simulation of thermal debinding process .....</b> | <b>87</b>  |
| 4.2.1      | Kinetic model for multi reaction steps .....                   | 87         |
| 4.2.2      | Identification of kinetic parameters.....                      | 89         |
| 4.2.3      | Numerical simulation using identified kinetic parameters.....  | 91         |
| 4.2.4      | Material and process numerical implementation.....             | 95         |
| 4.2.5      | Results of numerical simulation.....                           | 98         |
| 4.2.5.1    | Mass transport mechanisms related to thermal debinding .....   | 98         |
| 4.2.5.2    | Temperature variation inside the PIM component.....            | 100        |
| 4.2.5.3    | Geometrical deformation in the PIM component.....              | 101        |
| <b>4.3</b> | <b>Numerical simulation of solvent debinding process .....</b> | <b>103</b> |
| 4.3.1      | Physical model.....  | 103        |
| 4.3.2      | Mathematical modelling.....                                    | 104        |
| 4.3.3      | Process numerical implementation.....                          | 106        |
| 4.3.4      | Numerical simulation results.....                              | 106        |
| 4.3.4.1    | Evolution of remaining soluble binder content.....             | 106        |
| 4.3.4.2    | Effect of component thickness.....                             | 109        |
| 4.3.4.3    | Comparison between 1D and 2D numerical simulations.....        | 111        |
| <b>4.4</b> | <b>Summary.....</b>  | <b>112</b> |

---

## 4.1 Introduction

In this chapter numerical simulations related to thermal debinding and solvent debinding for metallic components obtained by powder injection moulding of fine 316L stainless steel (for thermal debinding) and copper (for solvent debinding) will be carried out based on the experimental results presented in the previous chapter.

For thermal debinding, a mathematical model, based on the kinetic parameters ( $E$ : activation energy and  $A$ : pre-exponential factor) of polymer pyrolysis, is proposed in our study for a multi-reaction steps. Therefore, the activation energy calculated previously from experiments will be used in order to identify the pre-exponential factor using an inverse identification strategy, by the mean of the quadratic error estimation. Then the kinetic parameters are used in an appropriate finite element model in order to perform the simulation of thermal debinding process for 2D and 3D components. The proposed numerical simulation allows the determination of remaining binder distribution, temperature distribution and deformation fields in the component during the whole thermal debinding process at any time.

In the second part of this chapter, numerical simulations based on the finite element method are also carried out for validation through determination of the remaining soluble binder content at different solvent debinding temperatures. The effect of solvent temperature and component thickness during water debinding process will be investigated. The proposed numerical simulation provides improved monitoring possibilities for solvent debinding techniques particularly to extract binder from the complicated molded components numerically without any experimentation.

## 4.2 Numerical simulation of thermal debinding

### 4.2.1 Kinetic model for multi reaction steps

This proposed model is developed for the purpose of describing the TGA curves which exhibit two decomposition steps. The first step corresponds to the decomposition of stearic acid and paraffin wax and the second one corresponds to the decomposition of polypropylene. All kinetic analyses assume that the isothermal rate of conversion is a linear function of a temperature-dependent rate constant ( $k$ ) and a

temperature-independent function of the conversion [SHI 02], the remaining weight fraction of a polymer ( $C_b$ ) can be expressed as:

$$dC_b/dt = -k \cdot f(C_b) \quad (4-1)$$

where  $k$  is the rate constant for thermal degradation ( $\text{min}^{-1}$ ) that follows an Arrhenius equation. The kinetic function of the thermal decomposition is defined in equation (4-2) in which ( $n$ ) is the apparent reaction order and is assumed to be constant during the greater part of the reaction [AHA 09].

$$f(C_b) = (C_b)^n = (C_b) \quad (4-2)$$

The Arrhenius equation is given as:

$$k = A e^{-E/RT} \quad (4-3)$$

where  $A$  is the pre-exponential factor assumed to be temperature independent ( $\text{min}^{-1}$ ),  $E$  is the activation energy for thermal degradation ( $\text{J mol}^{-1}$ ),  $R$  is the gas constant ( $\text{J mol}^{-1} \text{K}^{-1}$ ) and  $T$  is the absolute temperature.

Metal powders may have catalytic effects on the pyrolysis rate. However, the shape of the pyrolysis curve with powders is similar to that without powders [AGG 07]. Therefore, equation (4-3) of polymer pyrolysis can still be applied for feedstocks [PAR 09]:

$$C_b = w C_{b1} + (1 - w) C_{b2} \quad (4-4)$$

$$w = C_{01} / (C_{01} + C_{02}) \quad (4-5)$$

$$C_0 = C_{01} + C_{02} \quad (4-6)$$

where  $C_b$  is the mass ratio corresponding to the mass of both polymers where  $C_{b1}$  is the mass ratio to initial mass of the low molecular weight polymer and  $C_{b2}$  the mass ratio to the initial mass of the high molecular weight polymer,  $C_0$  is the initial mass of the two polymers  $w$  is the ratio of the initial mass of the low molecular weight polymer to the initial mass of the two polymers,  $C_{01}$  and  $C_{02}$  initial mass of low molecular and high molecular weight polymer, respectively. In our case, SA and PW have low molecular weight and PP has height molecular weight **Table 4.1**.

If the sample temperature is changed at a controlled and constant heating rate  $\beta$ , the variation in the conversion can be analyzed as a function of temperature, this temperature being dependent on the time of heating. Therefore, the reaction rate may be written as follows:

$$dT = \beta dt \quad (4-7)$$

$$dC_b/dt = \beta dC_b/dT \quad (4-8)$$

Substituting expressions (4-8), (4-3) and (4-2) into equation (4-1) gives the expression of reaction rate in the form:

$$dC_b/dT = (-A_i/\beta)e^{-E_i/RT}(C_b) \quad (4-9)$$

where  $A_i$  and  $E_i$  are the kinetic parameters for each step.

**Table 4.1:** Content of ingredients used in the binder system for feedstock loaded at 60%.

| Initial binder content |                         | PW+SA+PP=40%         |     |
|------------------------|-------------------------|----------------------|-----|
| Components             | $C_{01} = \text{PW+SA}$ | $C_{02} = \text{PP}$ | w   |
| Values                 | 24%                     | 16%                  | 0.6 |

#### 4.2.2 Identification of kinetic parameters for a fine 316L stainless steel feedstock

The activation energy values estimated in the previous chapter using Kissinger and Ozawa method will be used to identify the corresponding pre-exponential factors. So, the strategy to identify the pre-exponential factors  $A_1$  and  $A_2$  using Matlab<sup>®</sup> platform consists in fitting the numerical remaining binder content curve according to equation (4-10) to the one obtained from the TGA tests. The inverse identification procedure [LAG 98, SON 07, KON 11], by the mean of the squared estimation error, has been used as related in the algorithm summarised in the following expression:

$$\begin{cases} \min G(x) \\ G(x) = \sum_{i=1}^n |C_b^{\text{exp}}(T_i, x) - C_b^{\text{num}}(T_i, x)|^2 \\ x = [A_1, A_2] \end{cases} \quad (4-10)$$

where  $G(x)$  is the mean residual squares of the tolerance objective function where  $i=1, \dots, n$  indicates different values of the debinding temperature;  $x$  stands for the set of material parameters to be identified,  $C_b^{\text{exp}}$  is the experimental remaining binder content obtained from the TGA test and  $C_b^{\text{num}}$  is numerical remaining binder content obtained by using the optimization procedure.

The identified pre-exponential factors ( $A$ ) obtained for a fine 316L stainless steel feedstocks loaded at 60, 62, 64 and 66%, using both methods Ozawa and Kissinger, are related in **Table 4.2** for both steps.

**Table 4.2:** Identified pre-exponential factors for fine 316L stainless steel feedstocks loaded from 60 to 66%.

| Methods |                               |                         | Ozawa                 | Kissinger             |
|---------|-------------------------------|-------------------------|-----------------------|-----------------------|
| 60%     | Identified kinetic parameters | $A_1 (\text{min}^{-1})$ | $1.53 \times 10^4$    | $0.46 \times 10^4$    |
|         |                               | $A_2 (\text{min}^{-1})$ | $1.79 \times 10^{19}$ | $1.77 \times 10^{19}$ |
| 62%     | Identified kinetic parameters | $A_1 (\text{min}^{-1})$ | $1.47 \times 10^3$    | $0.48 \times 10^3$    |
|         |                               | $A_2 (\text{min}^{-1})$ | $2.70 \times 10^{15}$ | $1.64 \times 10^{15}$ |
| 64%     | Identified kinetic parameters | $A_1 (\text{min}^{-1})$ | $1.83 \times 10^3$    | $0.54 \times 10^3$    |
|         |                               | $A_2 (\text{min}^{-1})$ | $2.45 \times 10^{17}$ | $1.89 \times 10^{17}$ |
| 66%     | Identified kinetic parameters | $A_1 (\text{min}^{-1})$ | $1.85 \times 10^6$    | $0.81 \times 10^6$    |
|         |                               | $A_2 (\text{min}^{-1})$ | $1.52 \times 10^{20}$ | $1.49 \times 10^{20}$ |

The variation of remaining binder content obtained using the identified kinetic parameters ( $E$  and  $A$ ) with heating rate  $2^\circ\text{C}/\text{min}$  is related in **Figure 4.1** for different feedstocks. One can notice that the global average error is about 5%. The inverse method results are in a proper agreement with the experimental ones.



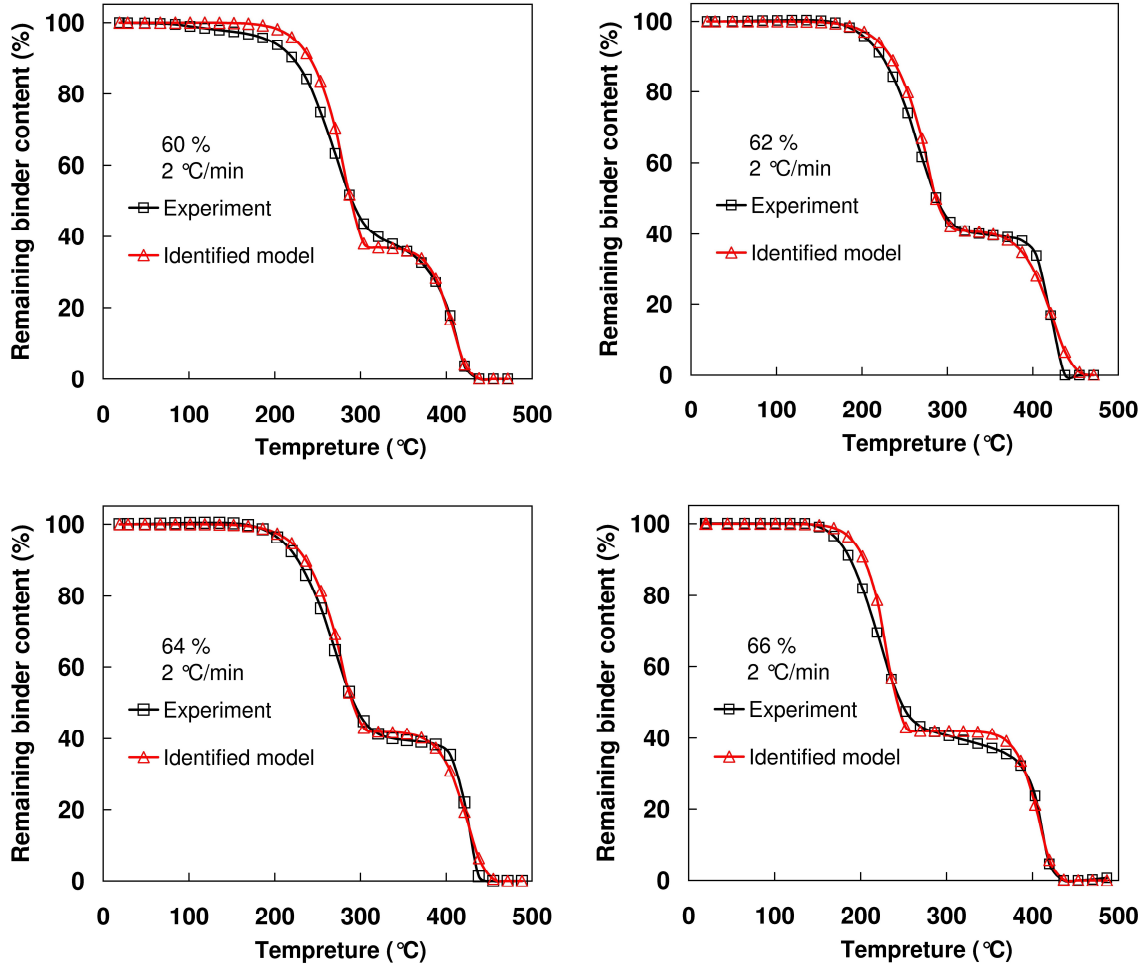


**Figure 4.1:** Evolution of remaining binder content versus temperature, comparison between experimental and identified kinetic model results for a fine 316L stainless steel feedstock loaded at 60, 62, 64, and 66% of powder volume loading with heating rate eq. 2 °C/min.

#### 4.2.3 Numerical simulation of thermal debinding

A 3D model of thermal debinding for which the component behaves as a porous media is assumed. The proposed numerical simulation will be focused on the second step of debinding process corresponding to degradation of polypropylene (PP). However, the considered deformation during the first debinding step only results from thermal expansion but not from the paraffin wax (PW) and stearic acid (SA) loss. Because even with 24% total loss of paraffin wax and stearic acid, polypropylene (PP) still acts as a backbone to keep the component shape during the first debinding step. So the component deformation during the first debinding step is

due only to temperature change. The state equations in the present model are discussed below:

In reality, during thermal debinding, the distribution of remaining weight binder content is not the same inside the component (there is a difference in the quantity between the external surface and the center of the component). The kinetic model given in (equation 4-1) can not describe the spatial evolution of the remaining binder inside the component. In order take into account this property; the identified kinetic parameters will be used to define the diffusion coefficient ( $k$ ) which is also considered as the rate constant for thermal degradation, equation (4-11):

$$dC_b/dt = \nabla \cdot (k \nabla C_b) \quad , (x, y, z, t) \in \Omega \times [0, t] \quad (4-11)$$

$$k = A e^{-E/RT}$$

where  $\Omega$  is the material domain and  $t$  is the time.

The temperature variation is governed by the heat equation, given by the equation (4-12):

$$\left( \frac{\phi \cdot \rho_p + C_{02} \cdot \rho_b}{\phi + C_0} \right) \left( \frac{\phi \cdot C_{pp} + C_{02} \cdot C_{pb}}{\phi + C_0} \right) \frac{\partial T(x, y, z, t)}{\partial t} + \text{div}(\vec{q}) = 0 \quad , (x, y, z, t) \in \Omega \quad (4-12)$$

where  $\phi$  is the powder volume loading,  $C_0$  is the initial volume fraction of the binder system,  $C_{02}$  is the volume fraction of the second binder ingredient (PP) polypropylene,  $\rho_p$  is the density of powder skeleton,  $\rho_b$  is the density of polypropylene,  $C_{pp}$  is the specific heat coefficient of powder skeleton and  $C_{pb}$  is the specific heat coefficient of polypropylene.

The Fourier's law gives the relation between the heat flow  $\vec{q}$  and the temperature  $T$ :

$$\vec{q} = -\lambda \text{grad}(T)$$

where  $\lambda_p, \lambda_b$  are the thermal conduction coefficients of the powder skeleton and polypropylene, respectively. Assuming this relation, the heat equation becomes:

$$\left( \frac{\phi \cdot \rho_p + C_{02} \cdot \rho_b}{\phi + C_0} \right) \left( \frac{\phi \cdot C_{pp} + C_{02} \cdot C_{pb}}{\phi + C_0} \right) \frac{\partial T(x, y, z, t)}{\partial t} - \left( \frac{\phi \cdot \lambda_p + C_{02} \cdot \lambda_b}{\phi + C_0} \right) \Delta T = 0 \quad , (x, y, z, t) \in \Omega$$

During the final removal of residual polymers from a PIM compact by thermal debinding, two principal mechanisms contributing to the deformation of the

component have been differentiated: polymer-content change and temperature change. Thus, the strain tensor,  $\varepsilon$  describing the deformation of the component is the sum of:

$$\varepsilon = \varepsilon_b + \varepsilon_T + \varepsilon_p \quad (4-13)$$

where  $\varepsilon_b$  is the deformation caused by polymer-content change,  $\varepsilon_T$  is the deformation caused by temperature change and  $\varepsilon_p$  is the deformation associated to gas pressure. During the polymer-removal process, the powder skeleton is subjected to a body force of distributed load that is equal to the total gas pressure,  $P$ . The partial pressures of polymer vapor effect are taken in account based on the identified kinetic parameters [SHE 02].

Using the same methodology as commonly adopted in drying technology [KOW 97], the strain caused by polymer-content change and temperature change is considered as follow:

$$\varepsilon = (1 + \nu) \left\{ \left( \frac{\phi \cdot \alpha_p + C_{02} \cdot \alpha_b}{\phi + C_0} \right) \cdot \Delta \frac{C_b}{C_0} \right\} \quad (4-14)$$

where  $\nu$  is the Poisson's ratio of the powder skeleton,  $\alpha_p$  is the linear-expansion coefficient of powder skeleton and  $\alpha_b$  is the linear-expansion coefficient of polypropylene.

The constitutive behaviour of the powder skeleton is considered to be elastic, as it is dominant for metal powder with a temperature of less than 873 K [SHE 02]. It is further assumed that small deformation and low deformation rate are applied. For plane-strain problems, the stress and strain relationship is well defined as [ZIE 77].

$$\varepsilon = D^{-1}(\sigma - \sigma_0) \quad (4-15)$$

$D$  is the elasticity matrix, considered to be equal to the sum of the strains caused by polymer-content change and temperature change,  $\sigma$  is the stress tensor and  $\sigma_0$  is the initial residual stress. The initial moulding residual stress has been neglected as the present investigation focuses only on the debinding stage.

The equivalent stress  $\sigma_i$  describes the distortion energy and is responsible for the yielding of a material according to the Huber–von Mises-Hencky criterion, expressed in the following form [MUS 96].

$$\sigma_i^2 = 1/6 [(\sigma_x - \sigma_y)^2 + (\sigma_y - \sigma_z)^2 + (\sigma_z - \sigma_x)^2] + \tau_{xy}^2 \quad (4-16)$$

where  $\sigma_x$ ,  $\sigma_y$ , and  $\sigma_z$  are the stresses in the x, y and z directions respectively and  $\tau_{xy}$  is the shear stress in the xy plane.

To illustrate the proposed model and associated numerical scheme, a three dimensional component with two-dimensional cross section is considered as shown respectively in **Figure 4.2-a** and **Figure 4.2-b**, OA=15 mm (long edge), OC=5 mm (short edge) and AD=0.5mm.

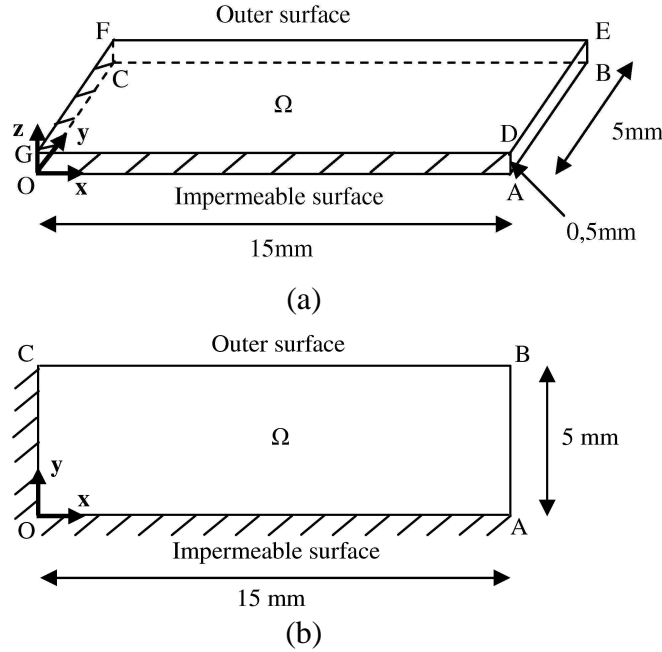


**Figure 4.2:** Description of geometry used for FEM simulations (a) Three-dimensional component with boundaries and (b) two-dimensional cross section of the component, [MAN 13].

#### a) Initial and boundary conditions

The solution of the problem requires initial and boundary conditions. Initially, the temperature of the compact is room temperature ( $T_0=25^\circ C$ ). The initial opened porosity is filled with atmospheric air and its pressure is equal to the ambient pressure 100000 Pa, [MAN 13].

$$C_b(x, y, z, 0) = C_{02} \quad (x, y, z) \in \Omega$$

$$P(x, y, z, 0) = P_0 = 1000000 \text{ Pa}, \quad (x, y, z) \in \Omega$$

$$T(x, y, z, 0) = T_0 = 25^\circ \text{C}, \quad (x, y, z) \in \Omega$$

#### b) Boundary conditions

During thermal debinding, two boundary conditions exist, **Figure 4.2-a**. One is the impermeable surfaces, i.e., surfaces OGDA, OCFG and OABC, which are considered to be impermeable and they could be planes of symmetry, where the normal components of heat flux and displacements are zero. The others are the outer surfaces which are exposed to an external field temperature ( $T$ ) as related in equation (4-17). The total gas pressure is equal to the ambient gas pressure.

$$T(x, y, z, t) = T_0 + \beta * t, \quad (x, y, z) \in \partial\Omega_i \quad (4-17)$$

$$\vec{n} \cdot (\nabla C_b) = 0, \quad (x, y, z) \in \partial\Omega_i$$

where  $\beta$  is the heating rate and  $\vec{n}$  denotes the normal to the boundaries  $\partial\Omega_i$ .

#### 4.2.4 Material and process numerical implementation

The above governing equations that describe the mass-degradation, thermal problem and deformation phenomena during thermal debinding are strongly coupled, implemented and then solved by finite element methods using Comsol<sup>®</sup> software. Comsol<sup>®</sup> is a modeling package for the simulation of any physical process described with partial differential equations (PDE). The coupled mathematical model has been implemented and can be considered as a multiphysic coupled problem between “PDE module” (for diffusion and degradation problem), “the heat transfer module” (for the thermal problem) and “the structural mechanics module” (for deformation problem), **Figure 4.3**.

The domain  $\Omega$  has been discretized using an automatic mesh generator, with 3560 triangular elements and 1072 quadrilateral elements, resulting in a total of 20303 degrees of freedom (DOF), **Figure 4.4-a**. An explicit time stepping scheme is used for the time dependant solver algorithm with an automatic time step adjustment. The diagram related in **Figure 4.3** shows the interaction between the three modules. The solution is given at each time step until  $t = t_f$  where  $t_f$  stand for the final processing

time. The material parameters and physical constants used in the present numerical simulation are summarized in **Table 4.3**.

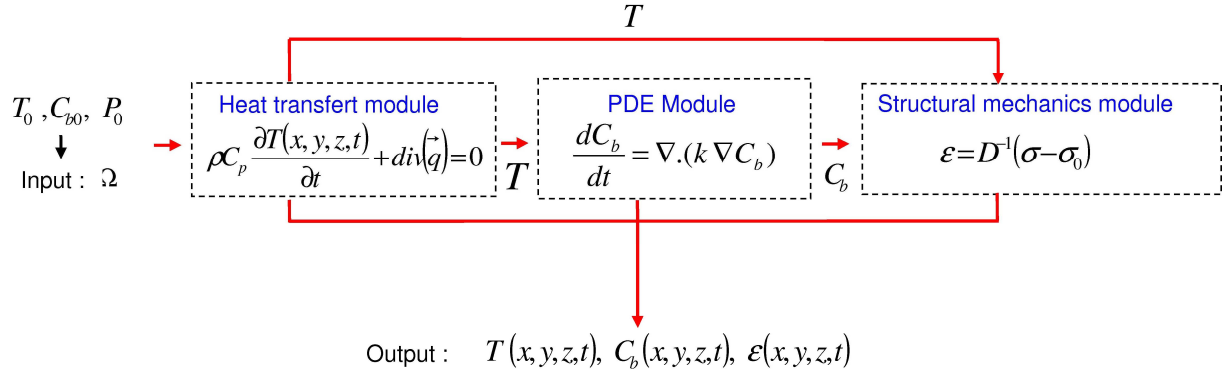
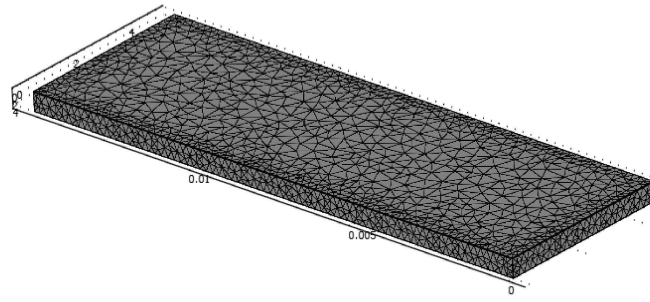
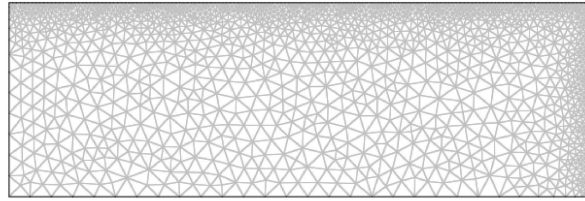


**Figure 4.3:** Interaction diagram between partial differential equations (PDE), Heat transfer and Structural mechanics module, [MAN 13].



(a)



(b)

**Figure 4.4:** Finite element discretization used for FEM simulations (a) Three-dimensional component (b) two-dimensional cross section of the component.

**Table 4.3:** Conditions for the numerical simulation of thermal debinding process used for a feedstock loaded at 60%, [MAN 13].

| Model parameters                                  |                | Value                                  |
|---|----------------|--|
| Binder  | PP             | Polypropylene                          |
| Pre-exponential factor                            | $A$            | $1.77 \times 10^{19} \text{ min}^{-1}$ |
| Activation energy                                 | $E$            | 212,98 kJ/mol                          |
| Universal gas constant                            | $R$            | 8.314 J/mol.K                          |
| Heating rate                                      | $\beta$        | 2°C/min                                |
| Ambient pressure                                  | $P_0$          | 100000 Pa                              |
| Initial temperature (t=0)                         | $T_0$          | 25°C                                   |
| Powder volume loading                             | $\phi$         | 60%                                    |
| Linear-expansion coefficient of powder skeleton   | $\alpha_p$     | $18.5 \times 10^{-6} \text{ 1/K}$      |
| Thermal conduction coefficient of powder skeleton | $\lambda_p$    | 14.6 W/m.K                             |
| Specific heat coefficient of powder skeleton      | $C_{pp}$       | 500 J/kg.K                             |
| Density of powder skeleton                        | $\rho_p$       | 7900 kg/m <sup>3</sup>                 |
| Poisson's ratio of the powder skeleton            | $\nu$          | 0.30                                   |
| Total volume fraction of polymer                  | $C_0$          | 40%                                    |
| Volume fraction of polypropylene                  | $C_{02}$       | 16%                                    |
| Linear-expansion coefficient of polypropylene     | $\alpha_b$     | $200 \times 10^{-6} \text{ 1/K}$       |
| Thermal conduction coefficient of polypropylene   | $\lambda_{pb}$ | 0.15 W/m.K                             |
| Specific heat coefficient of polypropylene        | $C_{pb}$       | 1800 J/kg.K                            |
| Density of polypropylene                          | $\rho_b$       | 900 kg/m <sup>3</sup>                  |

## 4.2.5 Results of numerical simulation

### 4.2.5.1 Mass transport mechanisms related to thermal debinding

**Figure 4.5-a** and **Figure 4.5-b** show the remaining polypropylene distribution along the width, length and thickness directions from the center to the outer surfaces of the component at the debinding temperature of 385 and 420 °C. The remaining polymer distribution varies continuously with the distance from the outer surfaces to the center of the component.

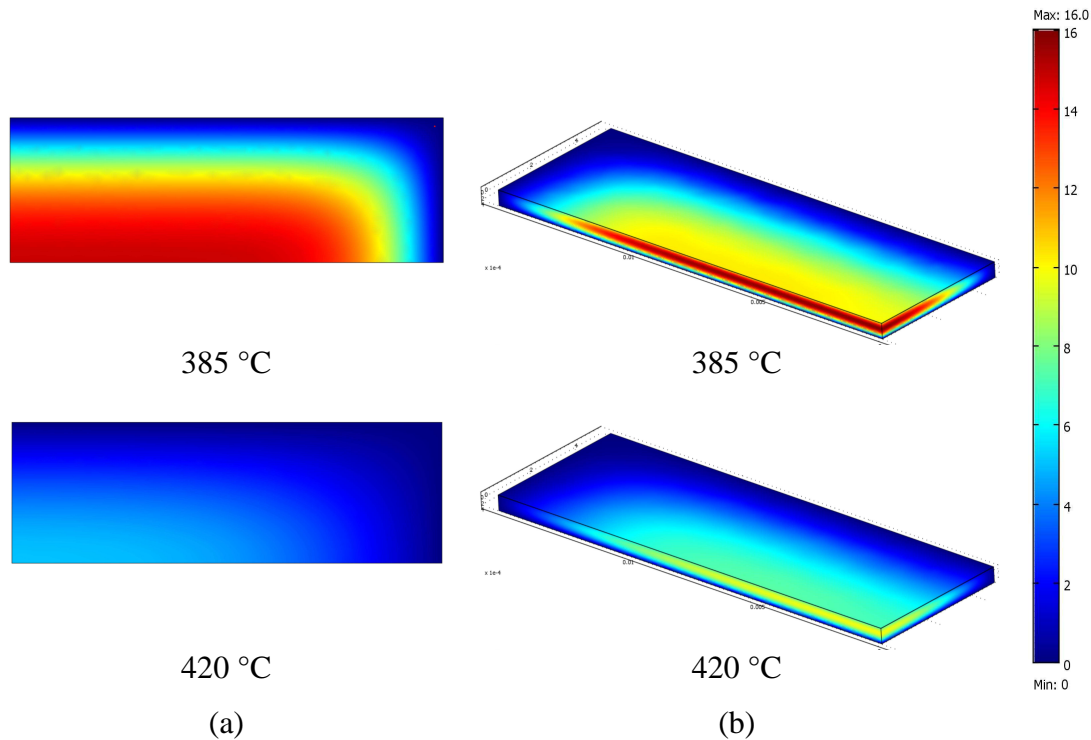


**Figure 4.5:** Remaining polypropylene binder content distribution in (%) for fine 316L stainless steel feedstock loaded at 60% with a heating rate equals 2°C/min at debinding temperature of 385 and 420 °C (a) 2D, (b) 3D, respectively.

**Figure 4.6 (a, b, c)** and **(d, e, f)** present clearly the remaining binder content profile of different cross sections along the length direction of the component at different debinding temperatures for feedstocks loaded at 60 and 62%, respectively. As can be shown in **Figure 4.6-a**, the remaining binder content in the component is equal to the initial binder content 16% that means there is no degradation of polypropylene at this temperature. Once the imposed temperature reaches the degradation polypropylene temperature as related in **Figure 4.6-b**, the remaining binder is rapidly eliminated at the component surface. The debinding process is



governed by diffusion controlled debinding (since the diffusion distance for the polymer is short, the debinding rate is quite fast near the component surface). At the center of the component, the remaining binder is not totally eliminated and debinding process is governed by permeation controlled debinding (collisions between molecules limit the debinding rate). At 425°C as can be shown in **Figure 4.6-c**, the binder content is almost disappeared inside the component.

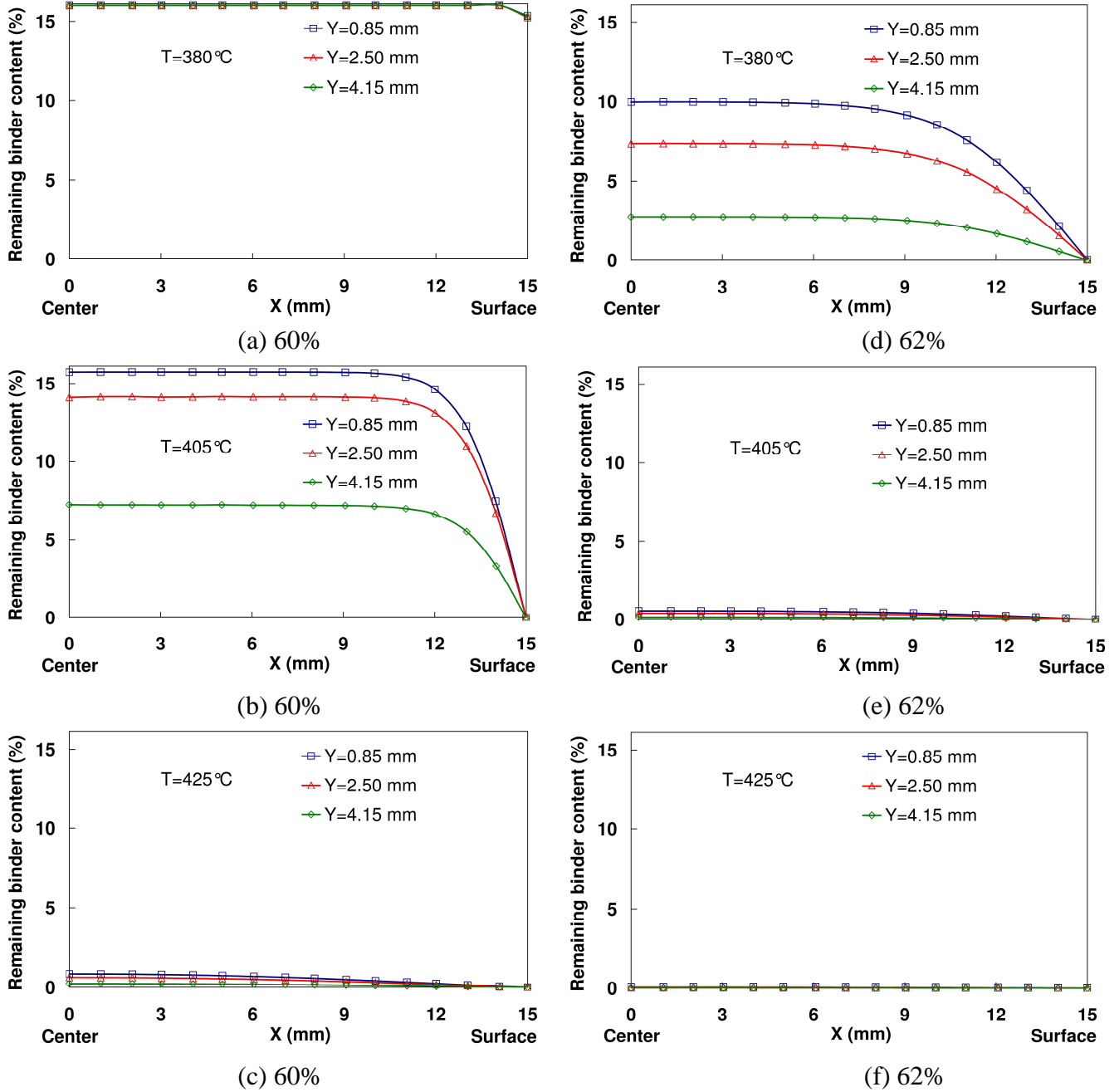


**Figure 4.6:** Calculated distributions of binder content inside the component at different debinding temperatures for fine 316L stainless steel feedstocks loaded at 60 and 62% of powder volume loading.

#### 4.2.5.2 Temperature variation inside the PIM components

The temperature evolution at the end of debinding process is shown in **Figure 4.7 (a, b) and (c, d)** along the length and the width directions from the center to the outer surface for feedstocks loaded at 60 and 62%, respectively. At the beginning of the simulation, the temperature inside the PIM component is equal to the ambient temperature of 25°C. During the simulation, the temperature inside the PIM component increases up to a limit value equal to 422°C, corresponding to the degradation temperature of polypropylene that is used. It is also shown in **Figure 4.7 (a, b, c, d)** that there is almost no difference between the temperature at the centre of the component and the outer surfaces where the temperature is practically equal to the imposed furnace one. The contours of debinding temperature inside the component for 2D and 3D numerical simulation are shown in **Figures 4.8-a** and **4.8-b** for feedstock loaded at 60%, respectively [MAN 13].

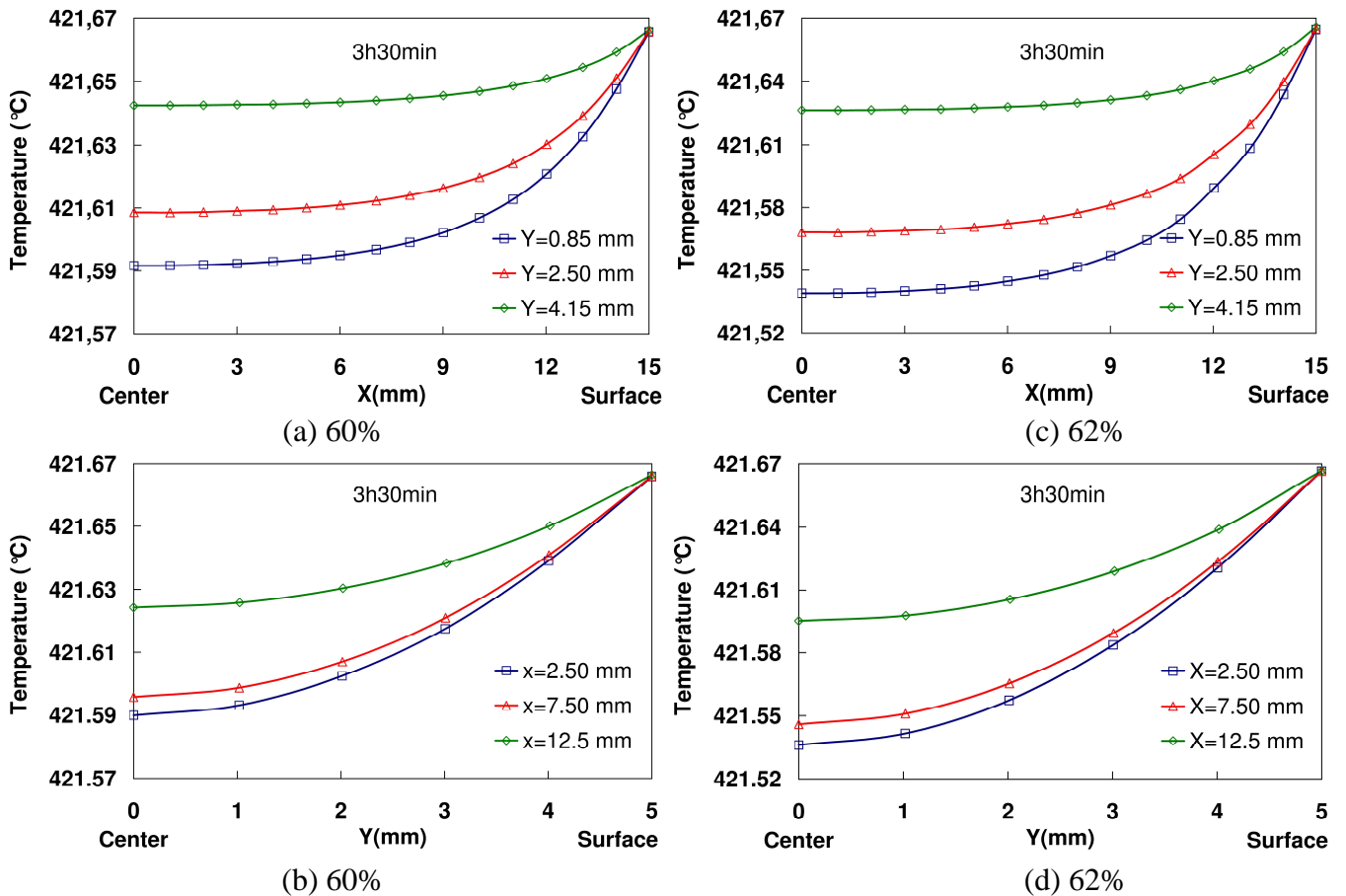


**Figure 4.7:** Temperature distribution in °C at the end of debinding process for fine 316L stainless steel feedstocks loaded at 60 and 62 % of powder volume loading, (a)-(c) along the length direction and (b)-(d) along the width direction.

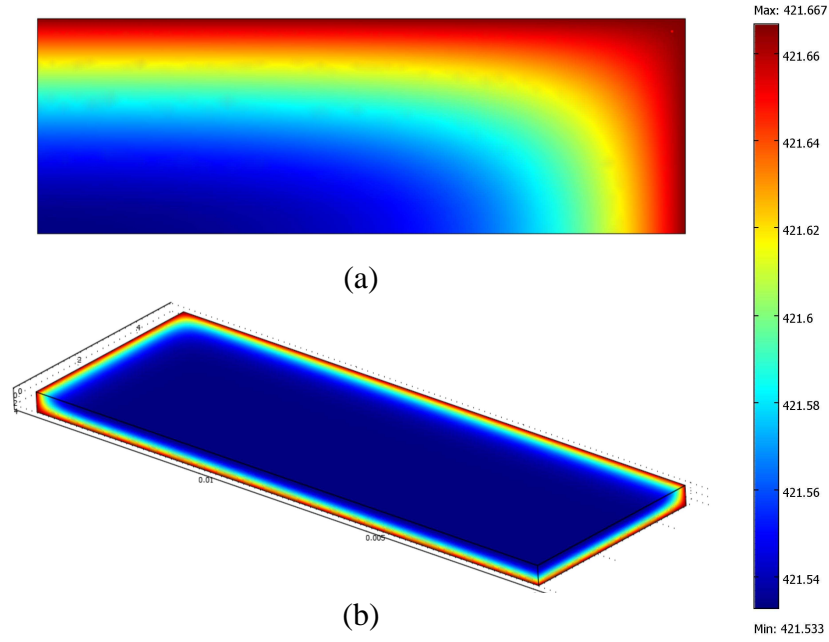


**Figure 4.8:** Temperature distribution in °C at the end of debinding process for fine 316L stainless steel feedstocks loaded at 60 powder volume loading, (a) 2D and (b) 3D.

#### 4.2.5.3 Geometrical deformation in the PIM component during debinding

Numerical simulations of geometrical deformations in thermal debinding of PIM components, based on the established model, have been carried out. The obtained results will show that deformations of the PIM component are principally due to temperature and binder content change.

**Figure 4.9** presents the normal strains in the PIM component for fine 316L stainless steel feedstocks loaded at 60%. When the temperature varies in the range 25-380°C, compact expands proportionally with temperature, indicating that the thermal expansion of the compact is nearly uniform, and there is almost no shear deformation in the specimen. During the high debinding-rate period from 380 to 420°C, the shrinkage caused by polymer removal dominates on the deformation of the compact and the entire specimen contracts as the polymer inside the part is removed rapidly. The contours of strains inside the component are shown in **Figures 4.10** for feedstock loaded at 60.

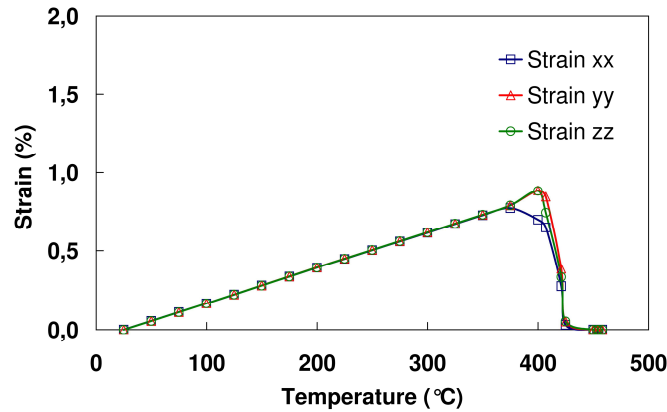


**Figure 4.9:** Normal strains evolution in the PIM component for fine 316L stainless steel feedstocks loaded at 60%, [MAN 13].

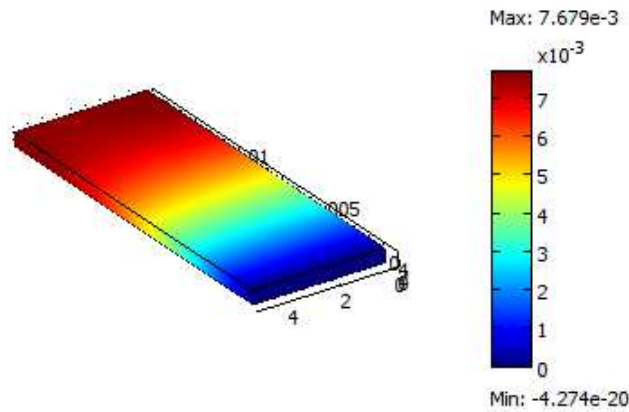


**Figure 4.10:** Contours of strains inside the component for fine 316L stainless steel feedstocks loaded at 60%.

Volumetric strains during the thermal debinding stage up to 500°C with same heating rate of 2°C/min have been compared for four powder volume loadings 60, 62, 64 and 66%. The maximal total deformations measured for debinded test components range from 2.41 to 2.96 % and are illustrated in **Figure 4.11**. In the proposal numerical simulation, a minimum deformation was observed in debinded test specimen loaded at 62%. The results related that deformation was increased considerably at the highest powder volume loading 66%. The difference in deformation is due to the lower volume loading of powders 60 and 62%. The related numerical results are in proper agreement with SEM micrograph results presented in **Figures 3.14** and **3.15**, in the previous chapter.

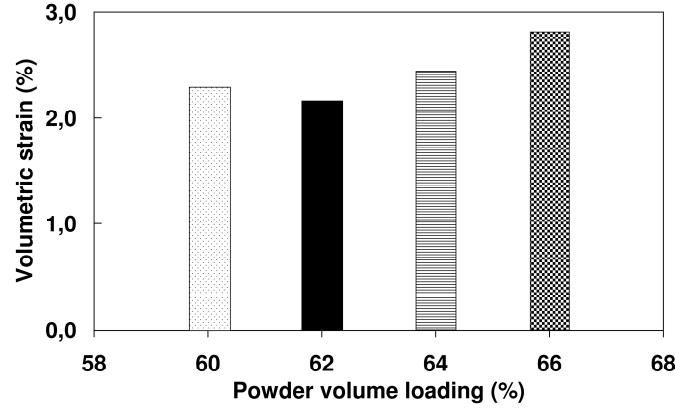


**Figure 4.11:** Volumetric strains in the PIM components with same heating rate of 2°C/min for different powder volume loadings.

### 4.3 Numerical simulation of solvent debinding

#### 4.3.1 Physical model

The solvent-debinding process can be considered as the interdiffusion of solvent and soluble binders within the specimen [YAN 03]. The distribution of the concentration ( $C$ ) of the remaining soluble binder inside the specimen (which has its four sides sealed) can be calculated by using second Fick's diffusion law, equation (4-18) [FAN 09]:

$$\frac{\partial C}{\partial t} = D \left( \frac{\partial^2 C}{\partial x^2} + \frac{\partial^2 C}{\partial y^2} \right) \quad (4-18)$$

With:

$$D = \begin{bmatrix} D_{11} & 0 \\ 0 & D_{22} \end{bmatrix}$$

**Initial conditions ( $t=0$ ):**

$$C(x,0) = C_i, \quad \text{and} \quad -b \leq x \leq b$$

$$C(x,0) = C_i, \quad \text{and} \quad -a \leq x \leq a$$

**Initial conditions ( $t=0$ ):**

$$C(x,y,t) = 0 \quad \text{for} \quad x = \pm b \quad \text{and} \quad y = \pm a$$

$$\frac{\partial C(x,t)}{\partial x} = 0 \quad \text{for} \quad x = 0$$

$$\frac{\partial C(y,t)}{\partial y} = 0 \quad \text{for} \quad y = 0$$

where  $t$  is the extraction time,  $D$  is the effective diffusion coefficient and  $C_i$  is the boundary condition,  $b$  is the distance from the center plane of the specimen and is along the width direction,  $a$  is the distance from the center plane of the specimen and is along the thickness direction, **Figure 4.12**. The domain has been discretized using an automatic mesh generator with 668 triangular elements, **Figure 4.13**.

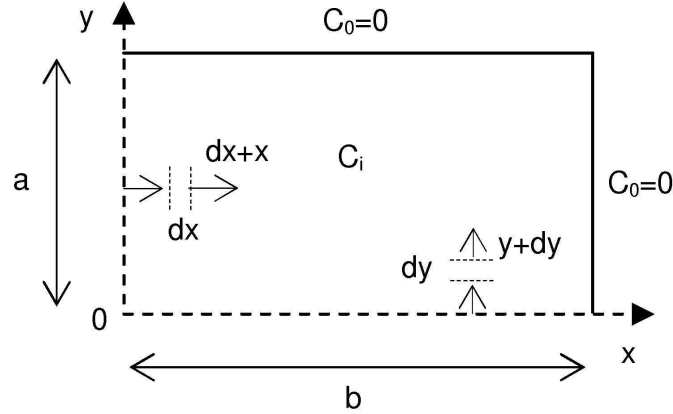


**Figure 4.12:** Schematic of the diffusion model used in numerical simulation.

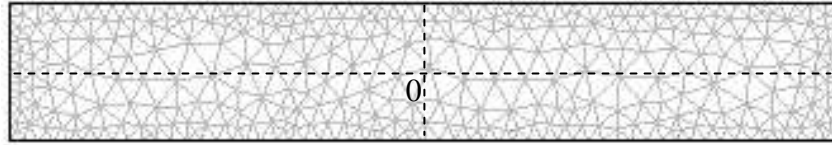


**Figure 4.13:** Finite element discretization.

### 4.3.2 Mathematical modelling

The effective diffusion coefficient  $D$  must be analytically calculated using experimental data. Once  $D$  calculated one can solve equation (4-18) numerically using finite element code COMSOL Multiphysics®.

The analytical solution for a 1D approximation has been provided by Crank as [CRA 75]:

$$\frac{C_{rm}}{C_i} = \frac{4}{\pi} \sum_{n=0}^{\infty} \frac{(-1)^n}{(2n+1)} \exp\left(-D \frac{(2n+1)^2 \pi^2}{4a^2} t\right) \times \left(\cos \frac{(2n+1)\pi y}{2a}\right) \quad (4-19)$$

where  $C_i$  is the initial soluble binder content,  $C_{rm}$  is the average concentration of the remaining binder in the component.

For a long time debinding operation, equation (4-19) can be simplified as:

$$\frac{C_m}{C_i} = \exp\left(-\frac{D\pi^2}{4a^2}t\right) \quad (4-20)$$

Assuming  $D$  is only temperature-dependent, but not concentration-dependent:

$$D = D_0 \exp\left(-\frac{E}{kT}\right) \quad (4-21)$$

where  $D_0$  is the pre-exponential frequency factor,  $E$  is the activation energy,  $k$  is the Boltzmann's constant and  $T$  is the temperature in K.

After a period of extraction, the binder concentration for the unidirectional diffusion could be approximated by substituting equation (4-21) into equation (4-20) that gives:

$$\ln\left(-\ln\frac{C_m}{C_i}\right) = \ln\left(\frac{D_0\pi^2}{4a^2}t\right) + \frac{-E}{k} \frac{1}{T} \quad (4-22)$$

A plot of  $\ln(-\ln(C_m/C_i))$  vs.  $1/T$  is related in **Figure 4.14**. From the linear regression analysis of this curve, the effective activation energy and then the diffusion coefficient for 0.92-mm-thick specimens can be obtained. For the specimen treated with a 30 minutes extraction, the amounts of remaining soluble binder at 40°C, 45°C, and 50°C were 27.8, 17.4 and 9.2 pct, respectively. For temperatures 55 and 60°C, problems in measurements have been encountered.

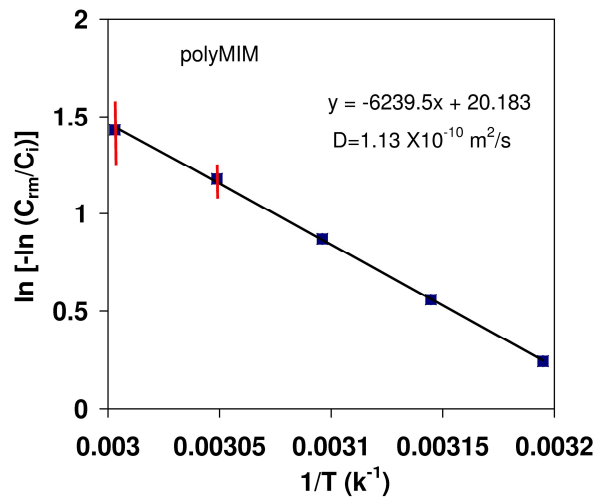


**Figure 4.14:** Temperature dependence of binder remaining after 30 min solvent debinding by linear regression fitting of equation (4-22).

From **Figure 4.14**, one can determine  $D_0$  and  $E$ :  $2.78 \times 10^{-2} \text{ m}^2/\text{s}$  and  $51.88 \text{ kJ/mol}$ , respectively. The diffusion coefficient at  $50^\circ\text{C}$ , calculated from Equation (4-21), is  $1.13 \times 10^{-10} \text{ m}^2/\text{s}$ .

### 4.3.3 Process numerical implementation

In this study, we implemented the second Fick equation using PDE (Partial Differential Equations) module, the PDE is an efficient solver for performing analysis on the mechanism of mass transport. The dependent variable is the amount of remaining soluble binder ( $C$ ). Using this module, one can define different diffusion coefficients for different directions. In our case, the same diffusion coefficient is taken for both directions. A flow chart, **Figure 4.15**, explains the followed steps to solve the problem described by (4-18).

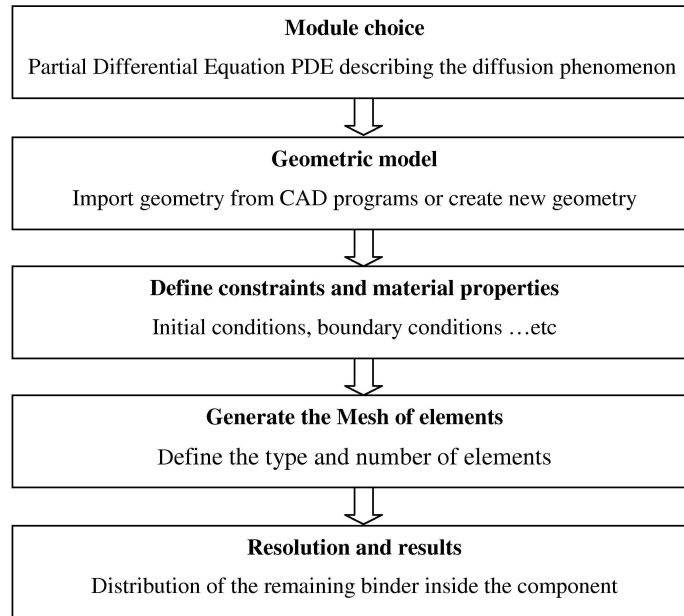


**Figure 4.15:** Steps in the solution procedure using finite element method for solvent debinding process.

### 4.3.4 Numerical simulation results

#### 4.3.4.1 Evolution of remaining soluble binder content

Comparison between experimental and numerical remaining soluble binder content inside 0.92-mm-thick square sample at different debinding temperatures is related in **Figure 4.16**.



It is shown that at the end of solvent debinding experiment, the amount of remaining soluble binder was slightly higher than the numerical value. This is due to a small amount of soluble binder which blended into the nonsoluble binder during mixing and could not be extracted during solvent debinding process. Other than these small differences, the experimental data are, in general, in proper agreement with the numerical simulation results. These results indicated that the model and numerical simulation are accurate and can provide improved monitoring possibilities for solvent debinding techniques particularly to extract binder from the complicated molded components numerically without any experimentation.

The experimental data related in **Figure 4.16** shows that the maximum amount of soluble binder removed at the end is about 95%. This amount may increase as the amount of soluble binder in the binder system decreases and vice versa.

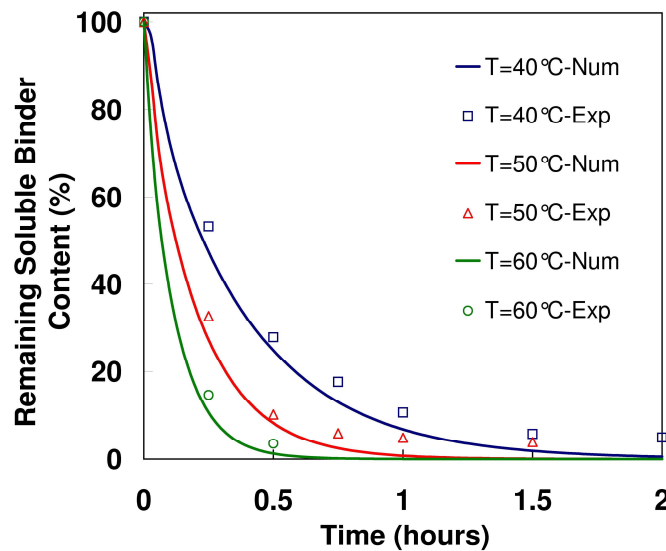


**Figure 4.16:** Comparison between experimental and numerical remaining soluble binder content inside 0.92-mm-thick square sample at different debinding temperatures from 40 to 60 °C.

**Figure 4.17** presents the evolution of remaining soluble binder content, inside 0.92-mm-thick square sample, versus time with different debinding temperatures. For solvent debinding temperature of 40°C, one can notice that the increasing in debinding time is very gainful (significant effect): after 15 minutes the remaining quantity of soluble binder is 60% and after 30 minutes the remaining quantity of soluble binder decreases drastically to about 30%. However, the

debinding time effect becomes insignificant when the debinding temperature increases to 60°C: after 15 and 30 minutes the remaining quantities of soluble binder are 15 and 5%, respectively.

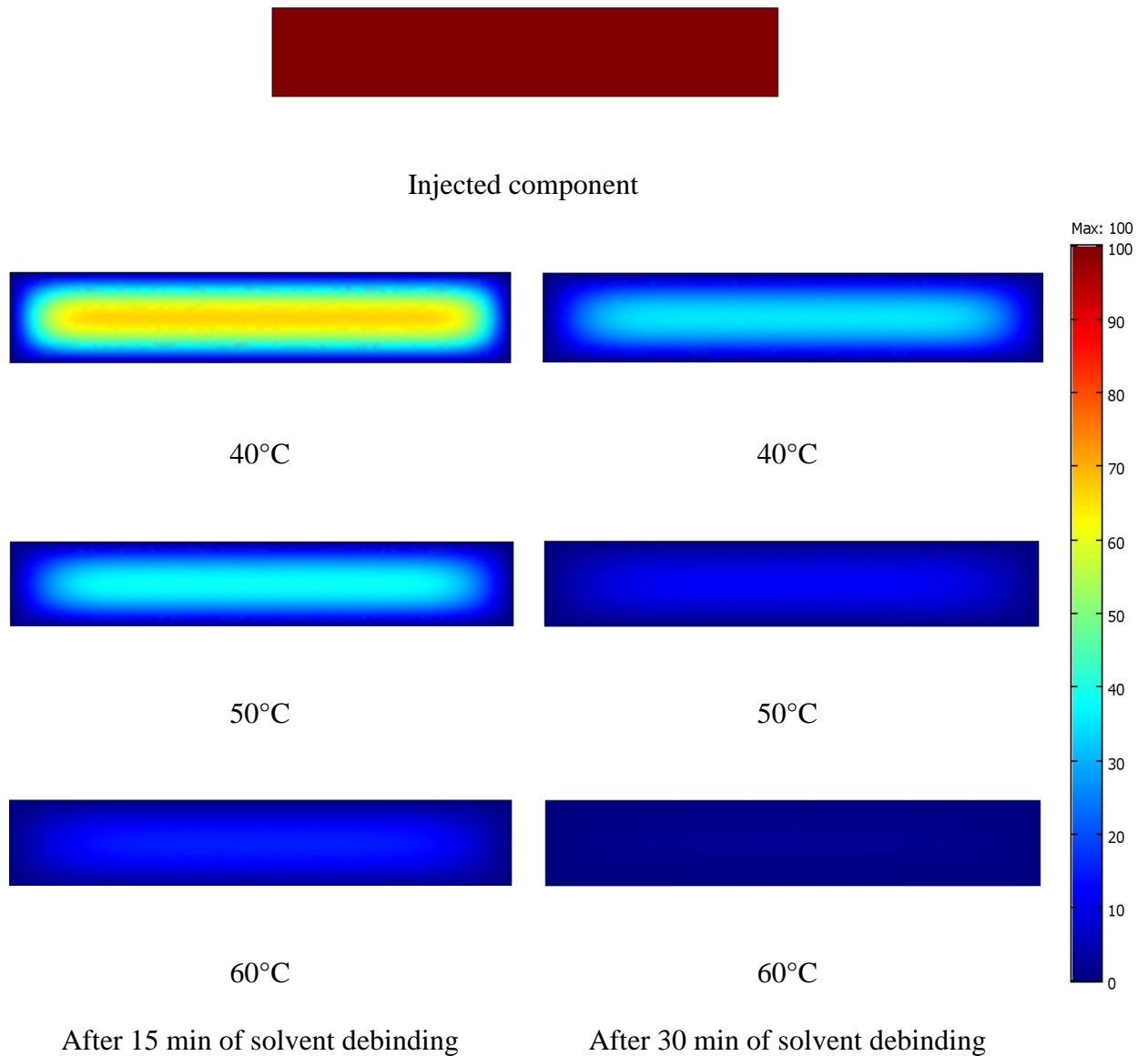


**Figure 4.17:** Contours of soluble binder content inside 0.92-mm-thick square sample, (a) after 15 minutes solvent debinding and (b) after 30 minutes solvent debinding.

#### 4.3.4.2 Effect of component thickness

As we conclude previously, the maximum amount of soluble binder removed at the end is about 95%. To reach this level of 95 pct, the required debinding time for parts with different thicknesses at different temperatures is related in **Figure 4.18**. One can notice that the debinding time increases with increased sample thickness and decreased debinding temperature. For example, when the thickness increases from 1.0 to 5.0 mm, the necessary debinding time will significantly increase, from 1.8 to 33.9 hours at 40°C and from 1.5 to 16 hours at 50°C. Based on **Figure 4.18**, one can provide an approximate model (eq. 4-23) in order to determine the minimum required debinding time.

$$t = \left( \frac{T_{\min}}{T} \right)^3 \cdot x^2 \quad (4-23)$$

where  $t$  is the minimum required depending time in hours,  $T_{\min}$  is the minimal debinding temperature that equals to 40°C,  $T$  is the used debinding temperature and  $x$  is the component thickness in millimetres.

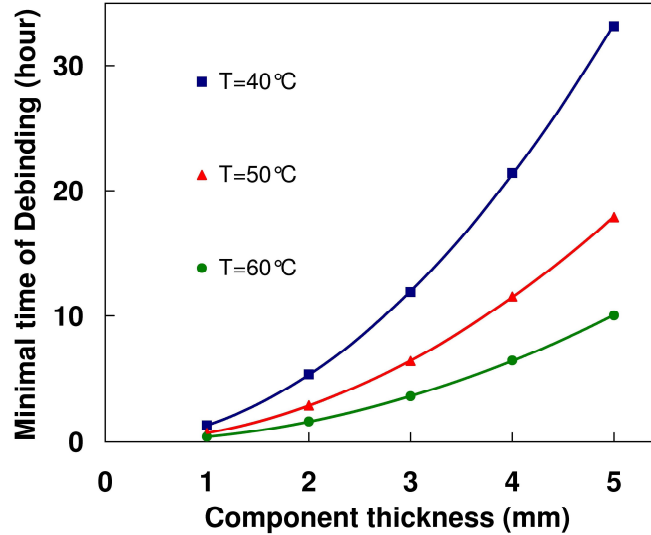


**Figure 4.18:** Debinding time needed to reach 95 % for components with different thicknesses at different temperatures.

The distribution of the remaining soluble binder content, inside square samples with different thickness (1, 2, 3 and 5 mm) after 30 minutes of solvent debinding, is shown in **Figure 4.19**. It is clearly shown for components with 1 and 5 mm thickness, the remaining soluble binder contents are 20 and 90 %, respectively.

This huge difference in remaining soluble binder contents leads us to conclude that the thickness of PIM components, during water solvent debinding, has an important effect.

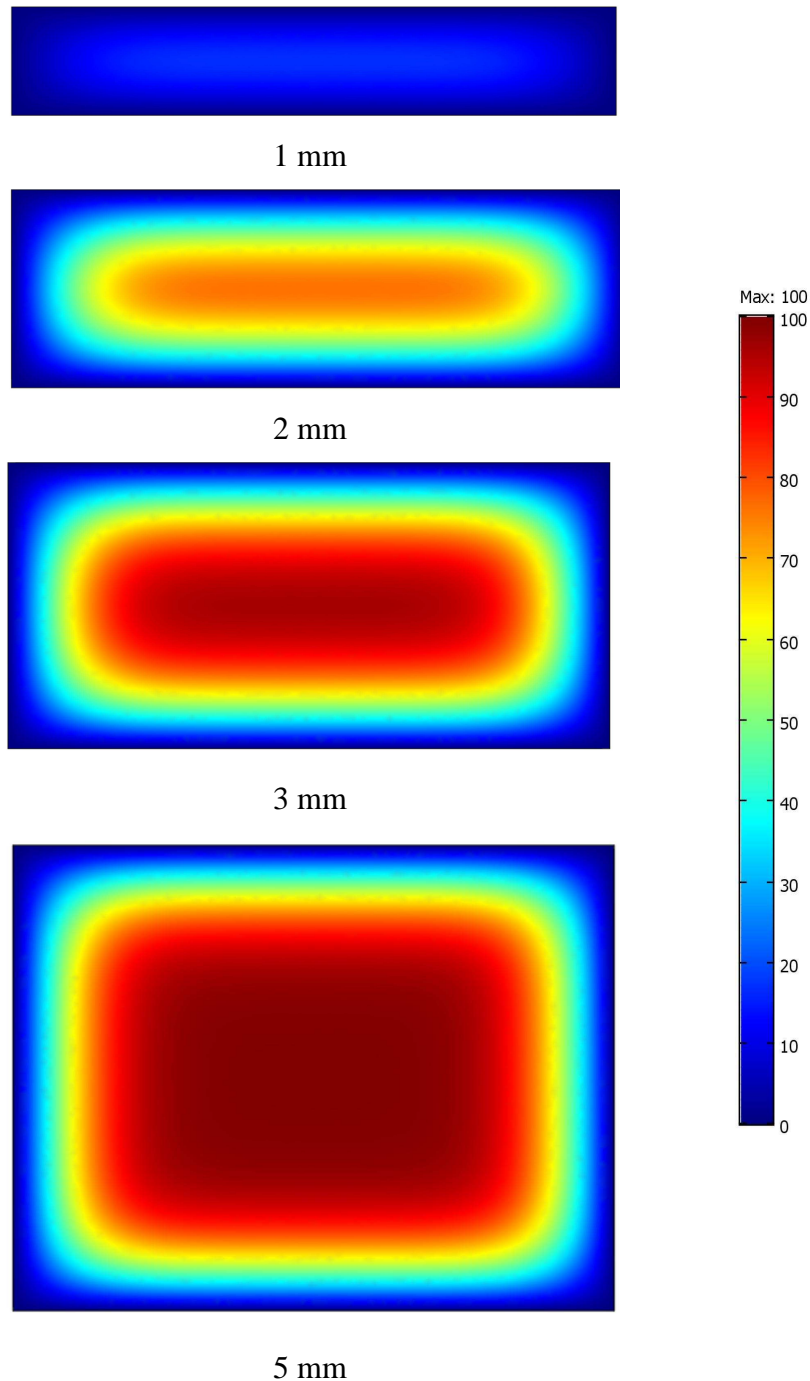


**Figure 4.19:** Contours of soluble binder content inside square samples with different thickness after 30 minutes solvent debinding.

#### 4.3.4.3 Comparison between 1D and 2D numerical simulations

**Figure 4.20** illustrates the distribution of the remaining soluble binder after 10 minutes solvent debinding inside a 0.92-mm-thick square sample using 1D and 2D numerical simulations, respectively. During water solvent debinding the water molecules dissolve the soluble binder by starting from the component surface, the water penetrates gradually into the moulded sample as shown in **Figure 4.20**. As the water diffuses into the component, it dissolves and extracts the soluble binder [AUZ11]. From this numerical simulation, one can determine the amount of the remaining soluble binder inside the whole sample at any time.

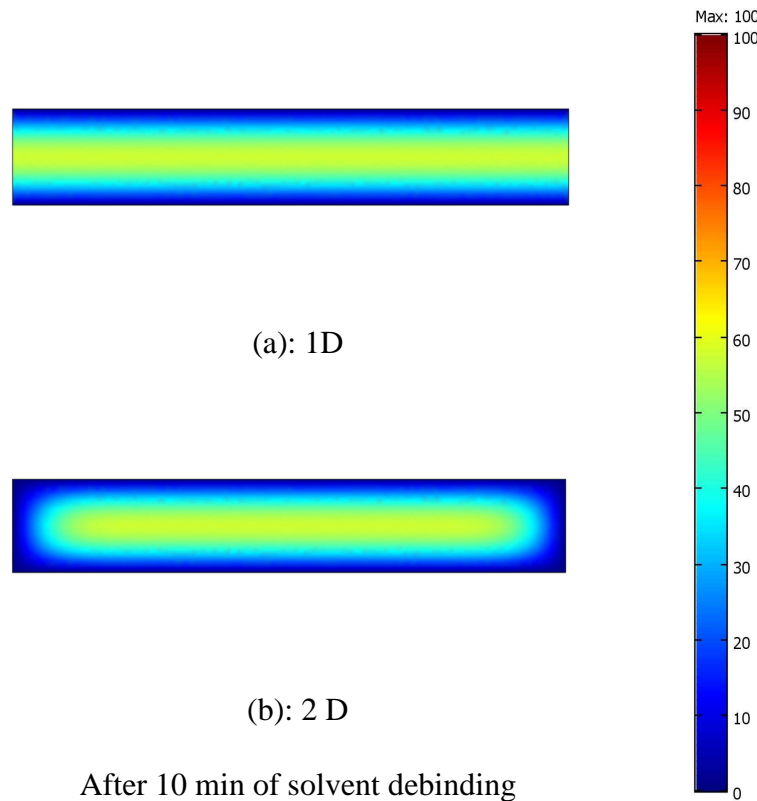


**Figure 4.20:** Contours of soluble binder content inside 0.92-mm-thick square sample after 10 minutes solvent debinding, (a) results for simulation 1D and (b) 2D.

In order to analyse the influence of width on the amount of remaining soluble binder, two tests have been conducted in 1D (y-direction) and 2D (both x and y-directions). **Figure 4.21** shows the evolution of remaining soluble binder amount over time inside a component having 0.92-mm-thick and 5.6 mm in width. It is clearly shown that the width of the component has a little effect on the solvent debinding

process in this study. One can conclude that the thickness plays a very important role in the water debinding process then the width one.

The 2D simulation is little faster than the 1D simulation. This is expected as the 1D simulation ignores lateral surfaces that soluble binder could escape from when compared with 2D simulation.

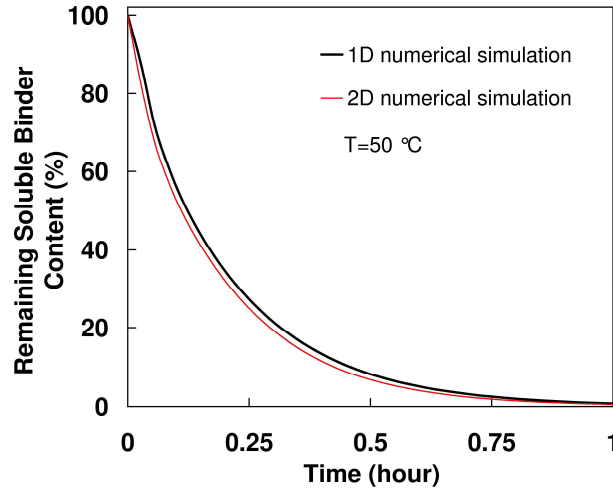


**Figure 4.21:** Binder remaining content inside 0.92-mm-thick square sample using 1D and 2D numerical simulations at 50°C

#### 4.4 Summary

In the first part of this chapter, numerical simulations have been carried out in thermal debinding of metallic components obtained by powder injection moulding of fine 316L stainless steel. A three-dimensional model of thermal debinding for which the component behaves as a porous media has been established. One can properly examine the distribution of remaining binder content, temperature and deformation in green components during thermal debinding process. It was shown that the remaining binder content is firstly eliminated at the component surface which means that the molten polypropylene starts to move from the center towards the external component surfaces. During thermal debinding, the total deformation of the PIM part is the sum of the deformations caused by polymer-content change and temperature change. During the increasing debinding-rate period, the total deformation is caused by temperature evolution and the entire specimen expands. During the high debinding-rate period, the deformation caused by polymer-content change dominates the total deformation and the entire specimen contracts.

In the second part, numerical simulation of water solvent debinding were carried out, the final amount of remaining soluble binder was slightly higher than the numerical value. This is due to a small amount of soluble binder which was blended into the nonsoluble binder during mixing process and could not be extracted during solvent debinding process. Almost no difference was shown between 1D and 2D numerical simulations results which explain that the component thickness plays a very important role in the water debinding process. An approximate model as a function of debinding temperature and component thickness has been established for PIM industries in order to select their solvent debinding conditions.

## Chapter 5: Experimental and Numerical Study of Sintering Process

---

### Contents

---

|  |            |
|--|------------|
| <b>5.1 Introduction.....</b>   | <b>116</b> |
| <b>5.2 Experimental investigation in sintering process.....</b>                          | <b>118</b> |
| 5.2.1 Materials .....  | 118        |
| 5.2.1.1 Powder properties.....   | 118        |
| 5.2.1.2 Binder properties .....  | 119        |
| 5.2.1.3 Samples preparation .....  | 120        |
| 5.2.2 Thermo-mechanical characterisation of W parts under H <sub>2</sub> atmosphere..... | 121        |
| 5.2.2.1 Dilatometric tests during sintering process.....                                 | 121        |
| 5.2.2.2 Beam bending tests during sintering process.....                                 | 124        |
| 5.2.3 Determination of sintering activation energy.....                                  | 126        |
| 5.2.3.1 Dorn's method.....   | 126        |
| 5.2.3.2 Constant heating rate method.....  | 127        |
| 5.2.4 Densification of tungsten components.....  | 128        |
| 5.2.5 Microstructure variation and grain growth.....                                     | 130        |
| 5.2.6 Variation of activation energy during sintering process.....                       | 132        |
| <b>5.3 Finite element modeling and identification of sintering parameters.....</b>       | <b>135</b> |
| 5.3.1 Constitutive model for sintering process.....                                      | 134        |
| 5.3.2 Identification of sintering parameters.....  | 138        |
| 5.3.2.1 Identification of material constants for W feedstocks.....                       | 138        |
| 5.3.2.2 Determination of sintering stress.....   | 142        |
| 5.3.2.3 Determination of uniaxial viscosity.....   | 143        |
| 5.3.2.3 Determination of activation energy for grain growth.....                         | 143        |
| <b>5.4 Numerical simulation results .....</b>  | <b>146</b> |
| 5.4.1 Material and process numerical implementation.....                                 | 146        |
| 5.4.2 Final shrinkages and relative densities of sintered bars.....                      | 148        |
| 5.4.3 Comparison between the simulation and experimental results .....                   | 151        |
| 5.4.3.1 Relative density.....  | 151        |
| 5.4.3.2 Final shrinkages.....  | 151        |
| <b>5.5 Summary.....</b>  | <b>153</b> |

---



## 5.1 Introduction

Sintering, as a final step of Metal Injection Moulding, which determines the final density and grain size, has an important influence on the mechanical and physical properties of the PIM components [GER 92]. In general, one gets a relative density of the sintered MIM components in the materials such as iron alloy, stainless steel, copper, ceramics, etc. is higher than 95% [GER 03]. However, this is hard to be achieved for pure tungsten (W), which has the highest melting temperature (3420°C) among the metals, at the sintering temperature below 1650°C [GER 92]. Owing to the very high fusion point, the consolidation of a conventional microcrystalline W powder grains is difficult and generally requires a temperature in excess of 1700°C through solid state sintering in electrical resistance sintering furnace under hydrogen atmosphere [AVI 10]. Low sintered density is an obstacle to the production of pure W components by MIM for applications concerned by high temperature such as electrodes of high intensity discharge lamps, plasma facing components for fusion reactors, furnace parts, etc.

Many efforts have been reported to improve the sinterability of W and reduce the sintering temperature. Hayden et al. [HAY 63] proposed to reduce the activation energy of sintering by addition of small amounts (<1 wt. %) of Group VIII transition metals. German et al. [GER 76] reported that the sintering temperature of W can be brought down from 2800 °C to 1400°C by using less than 1 wt. % addition of transition metals, such as palladium or nickel. Yu et al. [YU 11] investigated the influence of 0.4 wt. % Ni additives on the densification of MIM W-1.5 % Al<sub>2</sub>O<sub>3</sub> alloy. Ni has an important effect on promoting densification process, which largely reduces the sintering temperature, but the residual Ni element in sintered parts around 0.008 wt. % could be not allowed for some applications. Another important approach to activate sintering of W is through selection of nano-sized precursor W powder. However, such powder is expensive and prone to be contaminated [LIN 10]. Malewar et al. [MAL 07] reported that sintering temperature of nano-sized W produced by high energy mechanical milling can be decreased from the conventional temperature 2500°C to 1700°C. El-Atwani et al. [ATW 11] carried out sintering tests using fine grained, hard and ductile pure W powders for future fusion reactor applications. The bottom-up approach via powder consolidation by spark plasma sintering (SPS) was used at different temperature (1300-1800°C) and pressure (90-266 MPa) conditions.

Pure W powder, with an average particles size of about 1  $\mu\text{m}$  was sintered to high density, about 94% of theoretical density, with almost no grain growth at a temperature below 1400°C and an applied pressure up to 266 Mpa. Chanthapan et al. [CHA 12] carried out an experimental investigation using W powder (0.6-0.9 $\mu\text{m}$ ) sintered by field assisted sintering technology (FAST) in various processing conditions. The sample sintered with in-situ hydrogen ( $\text{H}_2$ ) reduction pretreatment and pulsed electric current during heating showed the lowest amount of oxygen. The maximum relative density achieved was 98.5% which is from the sample sintered at 2000°C, 85 Mpa for 30 min holding time. Recently, Wang et al. [WAN 10] reported that nanocrystalline W powder can be sintered to near-full density at a temperature as low as 1100 °C under  $\text{H}_2$  atmosphere without external pressure. Prabhu et al. [PRA 09] led an experimental investigation with another sintering heating mode, microwave sintering has been studied using as-received W and activated W powder. They conclude that the relative density of sintered part using as-received powder was 85 % and the one using activated powder was 93 %. Due to that MIM is a process for producing small parts in complex shapes, the innovative sintering approaches such as SPS, FAST and microwave sintering have not been applied for MIM in industry until now. Piotter et al. [PIO 08] carried out a comprehensive study on conventional sintering of W samples with a powder particle size of 2 $\mu\text{m}$  in dry  $\text{H}_2$  atmosphere at a temperature of > 2000°C. Thermal treatment resulted in a grain size of approximately 18  $\mu\text{m}$  and a final density of 95% as measured by He pycnometer. In order to reduce the grain size of the sintered W parts, one solution is using fine powder (e.g., the average particle size of 0.7  $\mu\text{m}$ ) and sintered at lower temperature (e.g., 1650°C) to reach a closed porosity necessary for the subsequent hot isostatic pressing (HIP) treatment. With the HIP cycle at 1600°C under 250 Mpa for 3h, the final MIM W parts can obtain a near full dense (relative density of 98.6-99%) and fine grain microstructure ( a grain size of approximately 5  $\mu\text{m}$ ) [ANT 11, ANT2 11]. Besides the application for near full dense parts, MIM has also been utilized to produce the porous W skeletons [SON 12]. In this case the relative coarse powders are crucial to the performance of the final parts.

In the present chapter, conventional sintering experiments in dilatometer have been used to investigate the densification behaviour of different components made of fine (0.4, 1.0 and 3.0 $\mu\text{m}$ ) and coarse (5.0, 6.0 and 7.0 $\mu\text{m}$ ) W powders which are

heated up to 1700 °C. The beam bending tests have been also carried out to measure the viscosity of the components during sintering process. The results reveal that the W components, made of fine powders 0.4 µm, are successfully manufactured with a relative density of 90-94% at the end of sintering process. The experimental tests were used to determine the different physical parameters of the viscoplastic constitutive law, these parameters are important for numerical simulation of sintering process. Comparison between numerical simulations results and experimental ones, in term of shrinkages and sintered densities, shows a good agreement. The finite element simulation has also proved to be fruitful for powder injection moulding process to predict final shrinkages and densities of W injection moulded components.

## 5.2 Experimental investigation in sintering process

### 5.2.1 Materials

#### 5.2.1.1 Powder properties

Fine and coarse W powders with various particle sizes (Xiamen Honglu, China) were used in this study. In order to obtain the powder with good flow ability for MIM, deagglomeration was carried out first via rod milling. For each type of W powder, 5 kg powder was put into a 5 liter polyurethane bottle, with 15kg W rods in diameter of 8 mm and a length of 10 mm. The powder was milled for 8 hours at a rotation speed approximately 28 rpm. **Figure 5.1-a** and **Figure 5.1-b** exhibit a scanning electron microscope (SEM) of the fine and coarse W powders, respectively. One can notice that most of particles show cuboidal morphology. Cumulative size in the range of 0.4-50 µm for fine powder and 7-70 µm for coarse powder has been determined using Malvern Mastersizer 2000, respectively. (See **Figure 5.1-c** and **Figure 5.1-d**).

**Table 5.1:** Chemical composition of the fine and coarse tungsten powders.

| Powder type | Chemical composition (ppm) |    |    |    |    |    |    |    |    |    |    |    |    |    |    |   |     |      |
|-------------|----------------------------|----|----|----|----|----|----|----|----|----|----|----|----|----|----|---|-----|------|
|             | K                          | Fe | Al | Si | As | Bi | Ca | Co | Cr | Cu | Mg | Mn | Mo | Ni | C  | S | O   | W    |
| Fine        | 15                         | 11 | 5  | 6  | 10 | 1  | 5  | 1  | 5  | 1  | 5  | 5  | 20 | 5  | 28 | 2 | 872 | bal. |
| Coarse      | 9                          | 16 | 5  | 6  | 10 | 1  | 5  | 1  | 9  | 1  | 5  | 5  | 20 | 5  | 5  | 2 | 184 | bal. |

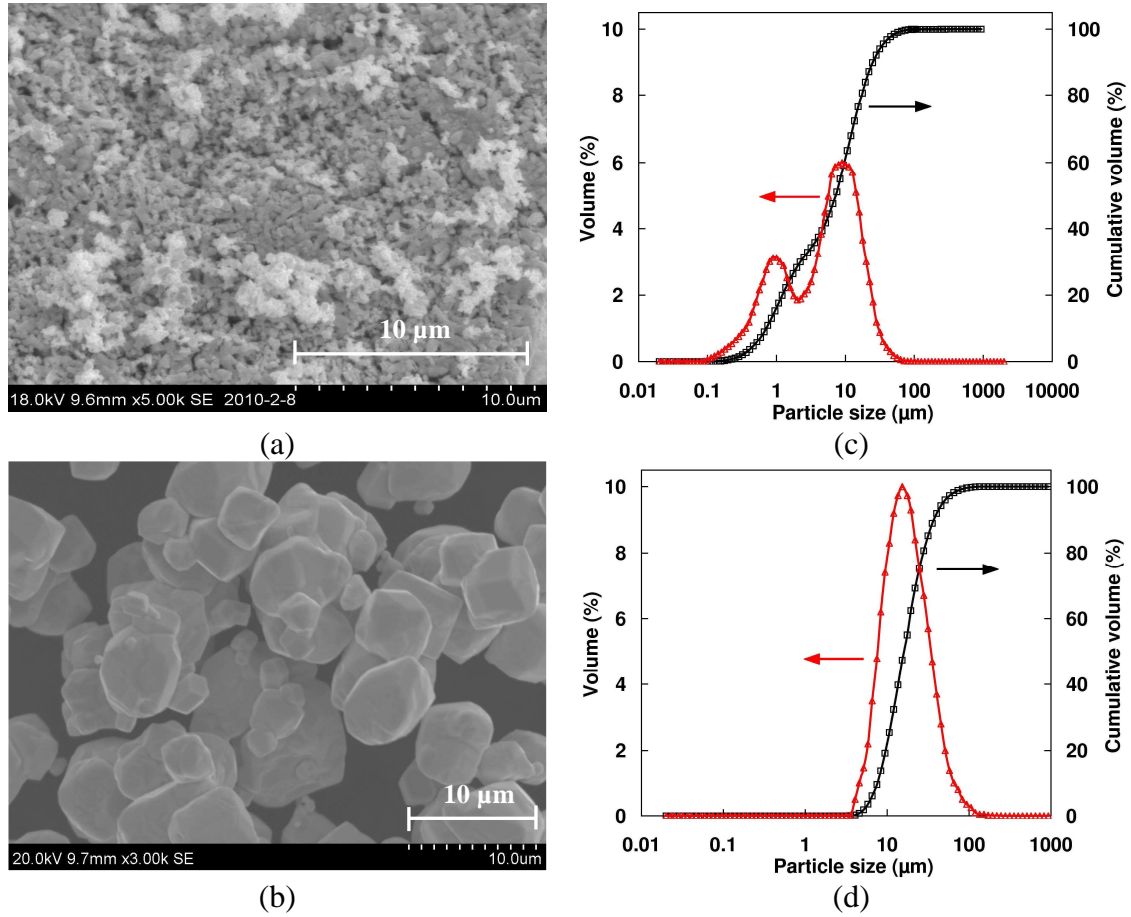


**Figure 5.1:** (a, b) SEM (secondary electron) image of fine (0.4μm) and coarse (7.0μm) W powders, (c) Particle size distribution of fine W powder (with cumulative size in the range of 0.4–50 μm) and (d) Particle size distribution of coarse W powder (with cumulative size in the range of 7–70 μm).

#### 5.2.1.2 Binder properties

A wax-polymer binder system was selected for MIM feedstock. The binder contains 51 w/o paraffin wax (PW), 30 w/o polypropylene (PP), 16 w/o polyethylene (PE) and 3 w/o stearic acid (SA). The critical solid loading (volumetric fraction of metal powder in the powder-binder mixture) was determined by torque rheometer. The mixing temperature of the chamber was set as 158 °C. The rotation speed for the screws was 60 rpm.

**Table 5.2:** Binder system components used in feedstock preparation.

| Binder System Components | Content (%) |
|--------------------------|-------------|
| Paraffin Wax (PW)        | 51          |
| Polypropylene (PP)       | 30          |
| Polyethylene (PE)        | 16          |
| Stearic Acid (SA).       | 3           |

### 5.2.1.3 Samples preparation

The standard wax-polymer binder system, in **Table 5.2**, was used for W MIM feedstock. The feedstock was injected to form bars in the dimension of 40×6×6 mm on an injection moulding equipment (Allrounder 360S, Arburg, Germany), (see **Figure 5.2-a**). Injection of the component was carried out with a set of optimized process parameters to minimise the phenomena of powder segregations and jetting [BAR 01].

The moulded bars underwent solvent debinding and thermal debinding sequentially. Solvent debinding was carried out in heptane at 37°C for 140 min, (see **Figure 5.2-b**). After this process, 50.7 wt. % binders were removed from the moulded components. The temperature profile employed in the thermal debinding was first at 450°C for 120 min at the heating rate of 1.5°C/min, followed by heating to 900°C at 2°C/min and holding for 30 min. The atmosphere for thermal debinding was nitrogen (N<sub>2</sub>), (see **Figure 5.2-c**). The slow heating rate aimed to avoid the appearance of eventual distortions and defects in debinding process. The temperature profile employed during the sintering step was first at 900°C at a heating rate of 10°C/min, followed by heating to 1700°C at 5°C/min and holding for 5 mins. Hydrogen (H<sub>2</sub>) atmosphere was used during sintering process, (see **Figure 5.2-d**).

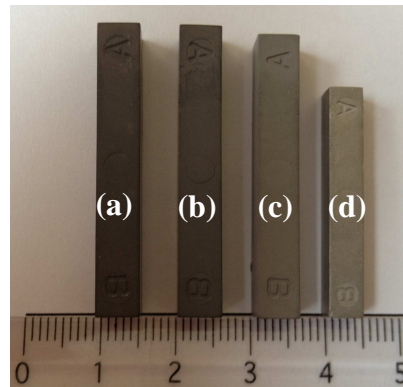


**Figure 5.2:** Tungsten components: (a) molded; (b) solvent debinded in heptane at 37°C for 140 min; (c) thermal debinded at 450 °C for 120 min with a heating rate of 1.5°C/min, followed by heating to 900 °C at 2 °C/min and holding for 30 min under N<sub>2</sub> atmosphere and (d) sintered at 1700°C under H<sub>2</sub> atmosphere.

The thermal debinded components were then presintered in the furnace under  $H_2$  atmosphere to obtain the holding strength necessary for dilatometric tests. For the samples with particle size of 0.4, 1.0 and 3.0  $\mu m$ , the presintering temperature was about 1100 °C and the holding time was 120 mins. For the other samples with coarse powder such as 5.0, 6.0 and 7.0  $\mu m$ , the higher presintering temperature as 1200 °C was employed due to the relatively poor sinterability of the powder. The heating rate was approximate 4°C/min.  $H_2$  atmosphere was used during presintering.

Relative densities of the presintered components are related in **Table 5.3**. Low relative densities after presintering step are due principally to the porosity left by departure of the binder.

**Table 5.3:** Relative density after presintering using coarse and fine tungsten powders under  $H_2$  with 4°C/min of heating rate and 120 min holding time.

| Particle size (um)               | 0.4  | 1.0  | 3.0  | 5.0  | 6.0  | 7.0  |
|----------------------------------|------|------|------|------|------|------|
| Initial solid loading (vol. %)   | 45.0 | 48.0 | 52.0 | 52.0 | 52.0 | 52.0 |
| Temperature of presintering (°C) | 1100 | 1100 | 1100 | 1200 | 1200 | 1200 |
| Density after presintering (%)   | 45.6 | 49.5 | 53.4 | 53.0 | 52.9 | 52.7 |

## 5.2.2 Thermo-mechanical characterisation of W components under $H_2$ atmosphere

The sintering process has been carried out using an automated Thermo-Mechanical Analyzer (TMA) provided by Setaram<sup>®</sup> with maximal temperature of 2400°C with only primary vacuum or air atmosphere. For security reasons related to the use of  $H_2$  as atmosphere, the present temperature test varies only from 25 to 1700°C. To maintain a  $H_2$  environment during sintering process, TMA setup permitted to generate hydrogen flow of excess of 20 mL/min. The same apparatus has been used to study the thermal debinding process, using DTA and TGA modules, of fine 316L stainless steel feedstocks [MAM 13].

### 5.2.2.1 Dilatometric tests during sintering process

The dilatometric tests were carried out to investigate the densification behaviour of the W components made from fine and coarse powders (see **Figure 5.3-a**). The initial length of the used components is  $l_0 = 12\text{ mm}$  (see **Figure 5.3-b**).

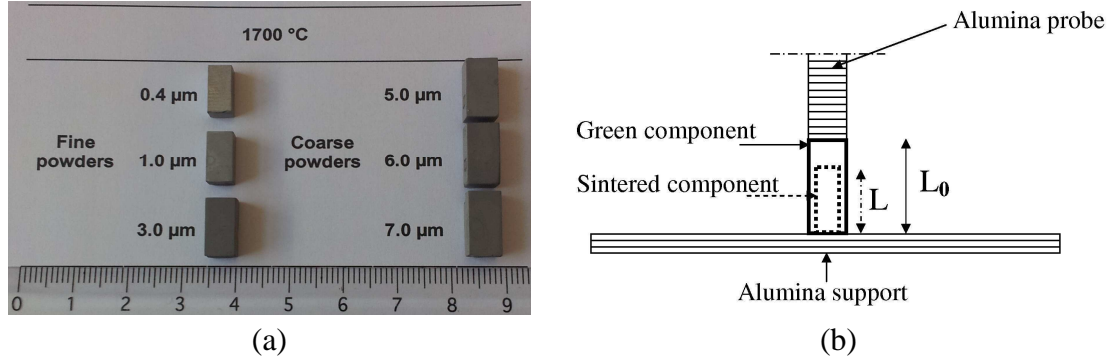


**Figure 5.3:** (a) Configurations of sintered components of fine and coarse W powders in dilatometer after sintering test at maximal temperature of 1700°C and H<sub>2</sub> atmosphere , (b) vertical dilatometer used in the experiments using Setaram<sup>®</sup> analyser.

Dilatometric tests enable the direct observation of the densification processes [AMI 10]. **Figure 5.4-a** and **Figure 5.4-b** show the measured shrinkage in the axial direction of W components as a function of temperature. Different grain sizes 0.4, 1.0, 3.0, 5.0, 6.0 and 7.0μm have been used in the present experimental investigation and all the components were heated up to 1700°C at 5 °C/min. Relatively low heating rate of 5°C/min allowed enough time for atomic diffusion. Nevertheless, very low heating rates could cause fast and sudden grain growth in the W material.

The shrinkage during sintering is determined as following:

$$\lambda = \frac{\Delta l}{l_0} = \frac{l - l_0}{l_0} \quad (5-1)$$

where  $\lambda$  is the shrinkage during sintering,  $\Delta l$  is the change in length,  $l_0$  is the original length of presintered components and  $l$  is the length at any time during sintering process.

The sintering shrinkages range from 0.93% for 7.0 μm to 19.87% for 0.4 μm. The temperature elastic strain for the apparent shrinkage of the components during sintering is in 1100°C for finer grain sized powders and 1290°C in case of coarser grain sized powders. There exist only elastic strains when the temperature is below it. It is true for the last cooling period to have only a linear thermal shrinkage from which one can estimate the linear thermal expansion coefficient. Except for the preheating and cooling period, the real process of sintering can be divided into three stages, the sintering begins in the initial stage, and then it subjects to the rapid shrinkage in the



intermediate stage, afterwards the shrinkage becomes much slower in the final stage to finish the sintering process [DAI 12].

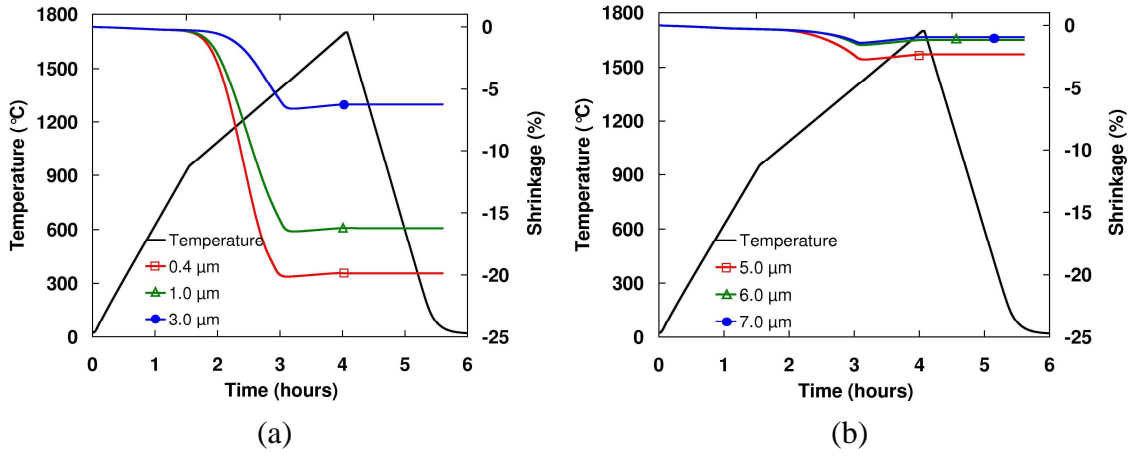


**Figure 5.4:** Evolution of shrinkage components vs. time for (a) fine W powders and (b) coarse W powders heated up to 1700°C using a heating rate of 5 °C/min and pure hydrogen atmosphere.

**Figure 5.5-a** and **Figure 5.5-b** show the evolution of shrinkage rates as a function of sintering temperature. Maximum shrinkage rates for the thermal cycles of fine and coarse W powders occur at the middle of the heating periods. The shrinkage rates values are ranged from 0.024 to 0.048 % min<sup>-1</sup> and from 0.098 to 0.288 % min<sup>-1</sup> for fine and coarse W powders, respectively. The increase in initial grain size gave rise to a decrease in the maximum shrinkage rate. One can conclude that shrinkage rates depend greatly on the initial grain size and fine powders are the most favorable for densification.

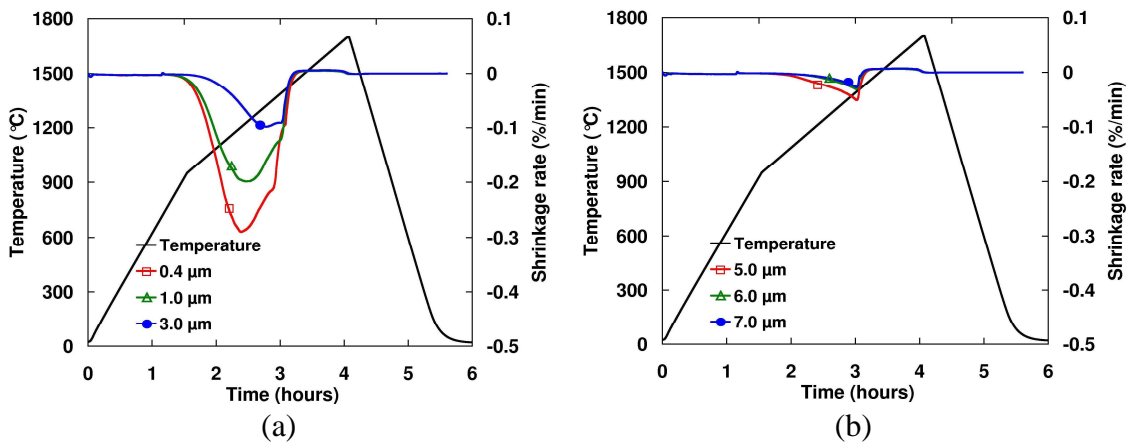


**Figure 5.5:** Evolution of shrinkage rates vs. time (a) fine W powders and (b) coarse W powders heated up to 1700°C using a heating rate of 5 °C/min.



### 5.2.2.2 Beam bending tests during sintering process

The beam bending tests during sintering process are used to determine the viscosity modulus of W parts at high temperature up to 1700°C during sintering, as shown in **(Figure 5.6-a)**. The beam bending test components are  $14.0 \pm 0.12$  mm in length,  $6.0 \pm 0.09$  mm in width and  $1.5 \pm 0.04$  mm in thickness. The beam bending span ( $L_s$ ) is chosen to be 12.0 mm with a support in alumina, as shown in **(Figure 5.6-b)**. The external load  $P$  at the centre of the component was 65g exerted by an alumina probe. The dilatometer tests showed that the apparent densification of fine and coarse W powders began at 1100 and 1290°C, respectively. So the beam bending tests were carried out in the dilatometer furnace using hydrogen atmosphere at the temperature ranged from 1100 to 1700°C with 5 minutes holding time and natural cooling was used in dilatometer furnace.

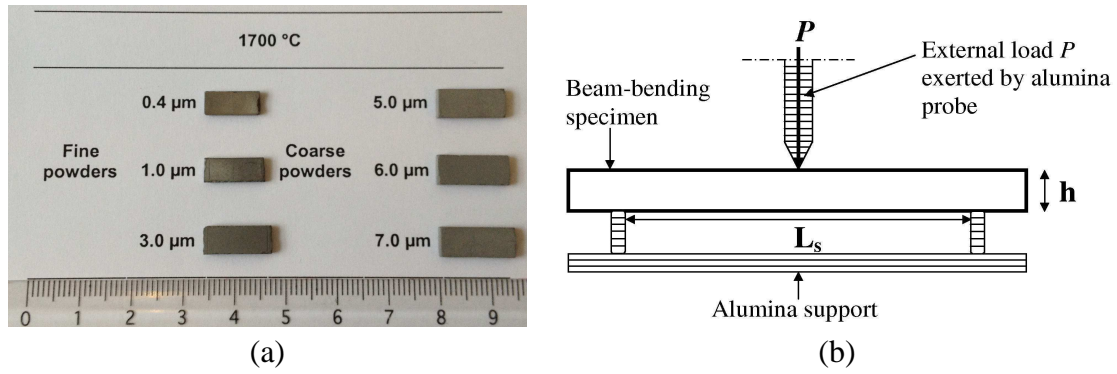


**Figure 5.6:** (a) Components configurations after beam bending tests at 1700°C and 100% hydrogen atmosphere for fine and coarse W powders, (b) vertical dilatometer used in the experiments using Setaram<sup>®</sup> analyser.

The components after beam bending tests are shown in **Figure 5.6-a**. Based on the measured deflection at the center position of the components, the deflection rate can be determined by the following expression:

$$\dot{\delta} = \frac{\Delta\delta}{\Delta t} = \Delta\delta \frac{\beta}{\Delta T} \quad (5-2)$$

where  $\dot{\delta}$  deflection rate,  $\Delta\delta$  is the change in deflection,  $\Delta T$  is the change in temperature and  $\beta$  is heating rate. The measured deflections for beam bending components of fine and coarse W powders are related in **Figure 5.7-a** and **Figure 5.7-b**, respectively. Along with the increasing of temperature, the deflections induced by

gravitational and external loads increase gradually after 1100°C because of the so called thermal softening effects.

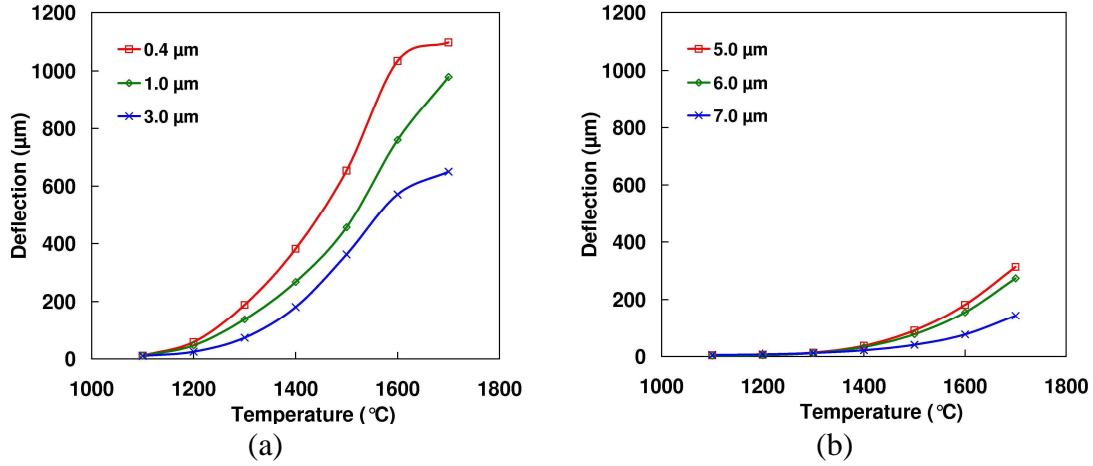


**Figure 5.7:** Deflections of W beam bending components vs. temperature during sintering with heating of 5°C/min in pure hydrogen atmosphere (a) fine grain sizes, (b) coarse grain sizes.

The obtained deflection rate curves, determined by eq. (5-2) of fine and coarse W powders, are shown in **Figure 5.8-a** and **Figure 5.8-b**, respectively. The rate of deflection of fine W powders represents a prominent decreasing for the heating stage from 1500 to 1700°C, as the rapid densification improves significantly the in situ strength in sintered components. One can conclude that when the sintering temperature becomes higher than 1500°C, the densification of fine W powders is almost finished.

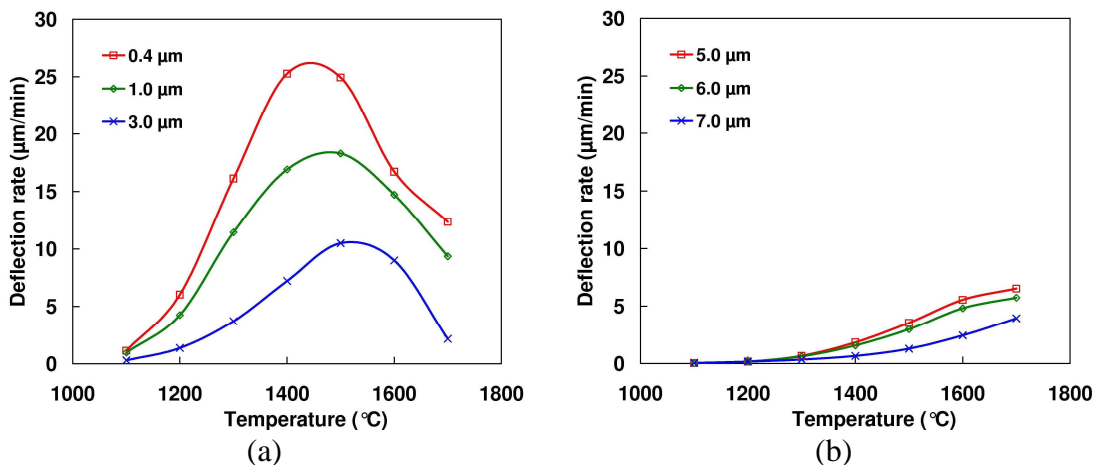


**Figure 5.8:** Deflection rates of W beam bending components vs. temperatures during sintering with heating of 5°C/min in pure hydrogen atmosphere, (a) fine grain sizes, (b) coarse grain sizes.

### 5.2.3 Determination of sintering activation energy

The objective of this estimation is to find out the sintering activation energy of coarse and fine W powders and to compare the calculated results by two methods.

#### 5.2.3.1 Dorn's method

This method, initially proposed by Dorn [DOR 57] for studying creep, gives a very fast and direct access to the measurement of sintering activation energy. The isothermal shrinkage rate  $v_1 = dy/dt$  is at first recorded at a temperature  $T_1$  for a sintering time  $t$ . Then, following a temperature increment made as quickly as possible, the same recording is made at a temperature  $T_2$ , a few tens degrees higher than  $T_1$ . The shrinkage rate in this interval is recorded to be  $v_2$ .

The experimental shrinkage curve obtained by dilatometric is generally in the form:

$$\Delta l/l_0 = \lambda = [K(T)t]^n \quad (5-3)$$

where  $l_0$  is the original length of the presintered component,  $K(T)$  is the Arrhenius constant,  $t$  is the time and  $n$  is a constant whose value depends on the sintering mechanism. If only the volume diffusion is operative  $n = 0.49$  [LAH 06], for grain boundary diffusion  $n = 0.33$  [LAH 06]. Equation (5-3) can also be written in the form:

$$\lambda^m = (\Delta l/l_0)^m = K(T)t \quad (5-4)$$

where  $m = 1/n$  and

$$K(T) = \left( AD_0 \Omega \gamma / G_c^{\psi k} \right) \left[ \exp(-Q/RT) / T \right] \quad (5-5)$$

where  $\gamma$  is the free surface energy,  $\Omega$  is the atomic volume,  $G_c$  is the size of the crystallite,  $k$  is the Boltzmann's constant,  $Q$  is the sintering activation energy,  $R$  is the universal gas constant,  $D_0$  is the pre-exponential term of the diffusion coefficient,  $m$ ,  $\psi$  and  $A$  are constants dependant on the geometric shape chosen for the particles. Equation (5-4) in differential form is:

$$d\lambda/dt = K(T)\lambda^{1-m}/m \quad (5-6)$$

Assuming the microstructural state remains unchanged during the temperature increment, one can get the following relation:

$$(\Delta l/l_0)_{\text{end step1}} = (\Delta l/l_0)_{\text{beginning step2}} \quad (5-7)$$

Implying this for the shrinkage rate, we get:

$$v_2/v_1 = (T_1/T_2) \exp[(-Q/R)(1/T_2 - 1/T_1)] \quad (5-8)$$

The equation for calculation of sintering activation energy, deduced from Equation (5-8) is of the form:

$$Q = [RT_2T_1/(T_2 - T_1)] \ln(T_2v_2/T_1v_1) \quad (5-9)$$

The assumption for this model is that the microstructural state remains unchanged during the temperature increment, which may not be true at high densification levels.

### 5.2.3.2 Constant heating rate method

This method, proposed by Wang and Raj [WAN 90] is very simple to formulate. Using Equations (5-4) and (5-5), the relative shrinkage rate could be written as:

$$d\lambda/dt = [k_0 f(\lambda) \exp(-Q/RT)] / G_c^{\psi_k} T \quad (5-10)$$

where  $f(\lambda) = \lambda^{1-m} / m$  and  $k_0 = AD_0\Omega\gamma$

In the constant heating rate method, where the constant heating rate  $\beta = dT/dt$  is 5, 10 and 20°C/min, the relative shrinkage rate may be written as:

$$d\lambda/dt = \beta(d\lambda/dT) \quad (5-11)$$

By substituting Equation (5-11) in equation (5-10) and taking logarithm on both sides, one can get the following equation:

$$\ln[T\beta(d\lambda/dT)] = -Q/RT + \ln k_0 - \ln G_c^{\psi_k} + \ln[f(\lambda)] \quad (5-12)$$

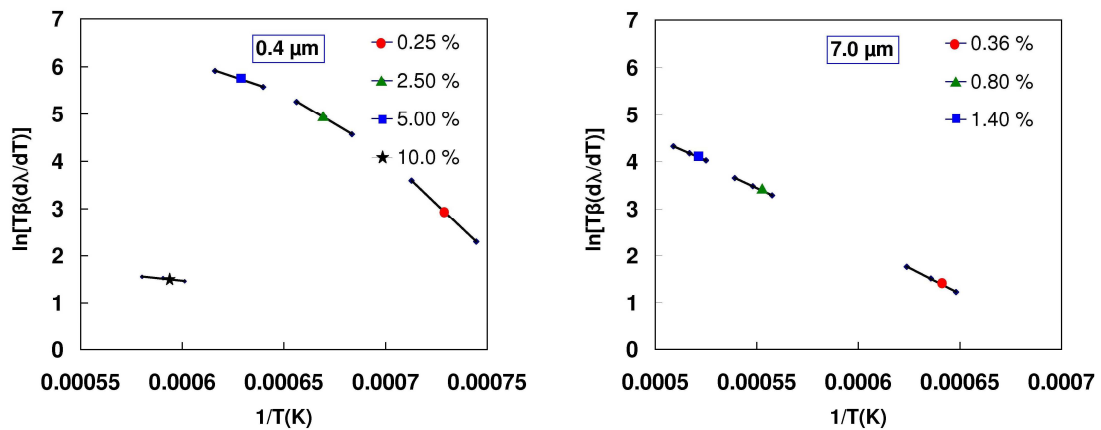


**Figure 5.9:** Sintering activation energy plots of  $\ln[T\beta(d\lambda/dT)]$  vs.  $1/T$  at different shrinkages and  $Q/R$  is the slope of the plot, (a) 0.4 μm, (b) 7.0 μm.

Plotting  $\ln[T\beta(d\lambda/dT)]$  as a function of  $1/T$  gives the value of  $Q/R$  as the slope of the plot (**Figure 5.9**), assuming other terms to be constant.

#### 5.2.4 Densification of tungsten components

The relative densities of W components, using fine and coarse powders sintered at various sintering temperatures (1500 and 1700°C) at a heating rate of 5 °C/min for 5 minutes holding time, are shown in **Figure 5.10**. The final density of the sintered components was measured by the pycnometer device. The sintered density generally increases with the sintering temperature for all components. However, the degree of densification is affected by the initial grain size of powders. There is a trend showing that the sintering temperature for densification of W shifts to a lower temperature as the grain size decreases. For example, components of 3.0 µm require a sintering temperature of 1700°C to achieve 69% in density, whereas components of 1.0 µm needs only 1500°C to achieve 69% in density. Thus, fine powders are an efficient way to sinter W components relative to coarse powders. In comparison with initial density, it also shown that a high sintering temperature does not improve the degree of densification of W components for coarse grain size. However, the relative density of W components significantly increases with increasing sintering temperature and decreasing grain size of powder.

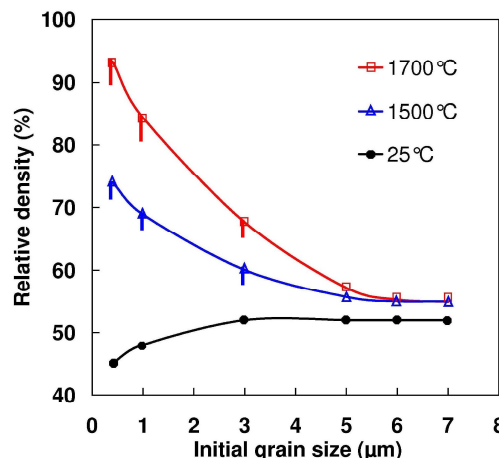


**Figure 5.10:** Final relative density of W vs. initial grain size before and after sintering process for components heated up to 1500 and 1700°C with 5°C/min for 5 minutes holding time under pure hydrogen atmosphere.

The fine W powder component with initial grain size of 0.4  $\mu\text{m}$  as related in **Figure 5.10**, obtains the best sintered density (90-94%) comparing to other components. This is due to larger surface area and fine W powder particles have large surface area than the coarse ones which will give maximum improvement in densification [KAN 05]. Large surface area for fine W powder increases energy reduction rate between particles and leads to a maximum improvement in final relative density.

**Table 5.4:** Shrinkages in different directions and final densities of the sintered components (using different grain size of tungsten powders).

|                                     |               |               |                |
|-------------------------------------|---------------|---------------|----------------|
| <b>0.4 <math>\mu\text{m}</math></b> | Length (mm)   | Width (mm)    | Thickness (mm) |
| Injected                            | 40.00         | 6.00          | 6.00           |
| Pre-densified                       | 37.79         | 5.64          | 5.63           |
| Densified                           | 30.12         | 4.53          | 4.52           |
| Shrinkage (%)                       | <b>24.7</b>   | <b>24.501</b> | <b>24.666</b>  |
| Density (%)                         | <b>90-94</b>  |               |                |
| <b>1.0 <math>\mu\text{m}</math></b> | Length (mm)   | Width (mm)    | Thickness (mm) |
| Injected                            | 40.00         | 6.00          | 6.00           |
| Pre-densified                       | 39.02         | 5.85          | 5.83           |
| Densified                           | 32.25         | 4.84          | 4.82           |
| Shrinkage (%)                       | <b>19.375</b> | <b>19.333</b> | <b>19.667</b>  |
| Density (%)                         | <b>82-85</b>  |               |                |
| <b>3.0 <math>\mu\text{m}</math></b> | Length (mm)   | Width (mm)    | Thickness (mm) |
| Injected                            | 40.00         | 6.00          | 6.00           |
| Pre-densified                       | 39.73         | 5.93          | 5.98           |
| Densified                           | 37.32         | 5.57          | 5.60           |
| Shrinkage (%)                       | <b>6.7</b>    | <b>7.167</b>  | <b>6.667</b>   |
| Density (%)                         | <b>65-67</b>  |               |                |
| <b>5.0 <math>\mu\text{m}</math></b> | Length (mm)   | Width (mm)    | Thickness (mm) |
| Injected                            | 40.00         | 6.00          | 6.00           |
| Pre-densified                       | 39.43         | 5.91          | 5.92           |
| Densified                           | 38.70         | 5.79          | 5.81           |
| Shrinkage (%)                       | <b>3.250</b>  | <b>3.500</b>  | <b>3.166</b>   |
| Density (%)                         | <b>55-56</b>  |               |                |
| <b>6.0 <math>\mu\text{m}</math></b> | Length (mm)   | Width (mm)    | Thickness (mm) |
| Injected                            | 40.00         | 6.00          | 6.00           |
| Pre-densified                       | 39.59         | 5.93          | 5.94           |
| Densified                           | 39.27         | 5.88          | 5.89           |
| Shrinkage (%)                       | <b>1.825</b>  | <b>2.000</b>  | <b>1.833</b>   |
| Density (%)                         | <b>54-55</b>  |               |                |

| <b>7.0 <math>\mu\text{m}</math></b> | Length (mm)  | Width (mm)   | Thickness (mm) |
|-------------------------------------|--------------|--------------|----------------|
| Injected                            | 40.00        | 6.00         | 6.00           |
| Pre-densified                       | 39.58        | 5.946        | 5.967          |
| Densified                           | 39.31        | 5.89         | 5.91           |
| Shrinkage (%)                       | <b>1.725</b> | <b>1.833</b> | <b>1.500</b>   |
| Density (%)                         | <b>54-55</b> |              |                |

The experimental results (shrinkage and relative density) are summarized in **Table 5.4**. The relative density of components has been determined using the following expressions:

$$\rho = \rho_{ap} / \rho_{th} \text{ where } \rho_{ap} = m/V_{ap} \text{ and } \rho_{th} = m/V_{py} \quad (5-13)$$

$\rho$ : is the relative density,  $\rho_{ap}$  is the apparent density,  $\rho_{th}$  is the theoretical density,  $m$ : is the mass the sample,  $V_{ap}$  is the apparent volume (surface  $\times$  depth) and  $V_{py}$  is the measured volume using the pycnometer. One can notice clearly in **Table 5.3** that the final shrinkage and density increase in values with decreasing the initial grain size of tungsten powders.

### 5.2.5 Microstructure change and grain growth

**Figure 5.11-a** shows the microstructure of the W powders prepared with initial grain size of  $0.4\mu\text{m}$ . All the samples have been sintered under pure hydrogen atmosphere up to  $1700^\circ\text{C}$  with  $5^\circ\text{C}/\text{min}$  using different holding times 5, 30, 60, 90 and 120 minutes, **Figure 5.11-b** to **Figure 5.11-f**. By increasing the holding time from 5 to 120 min, the final grain size of the samples increased from 4 to about  $27\mu\text{m}$ , which is related to the rearrangement of particles positions in order to form new contacts with each other. Afterwards, the sintering necks are formed at the contact area with elimination of the grain boundary area via grain growth diffusion process.

Another examination of the microstructure variation shows the existence of pores which also reduce in size by increasing holding time. One can clearly notice that these pores exist in the form of continuous open porosity when the holding time is about 5 minutes, **Figure 5.11-b**. When the holding time is ranged between 30 or 60 minutes, pores become smaller and are reduced to closed pores, indicating that the final density is almost reached, **Figure 5.11-c** and **Figure 5.11-d**.



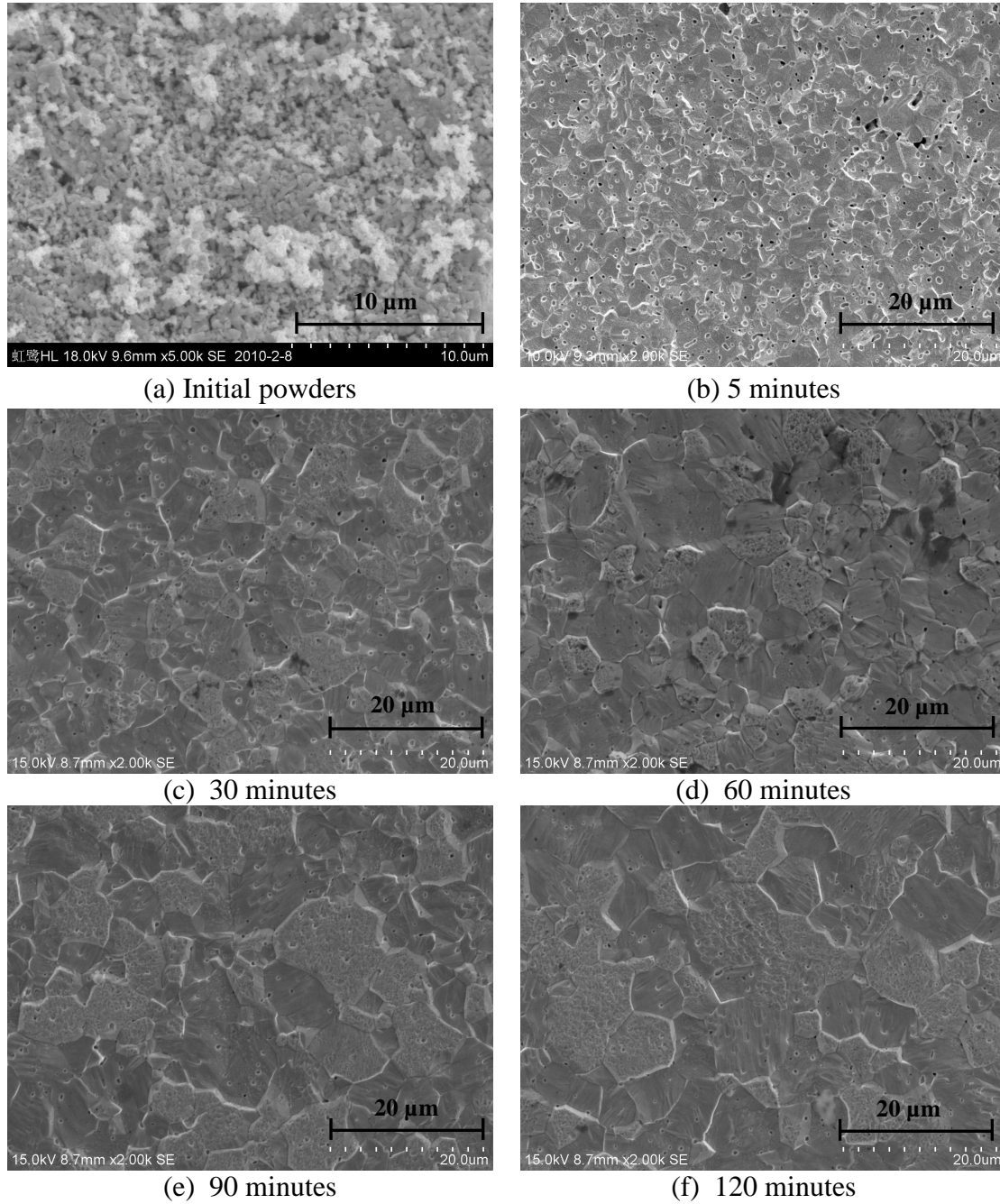


**Figure 5.11:** Microstructures variation of the sintered W samples after the thermal cycles of heating up to 1700 °C at 5 °C/min under pure hydrogen atmosphere for different holding time, (a) initial powders of 0.4μm, (b) 5, (c) 30, (d) 60, (e) 90 and (f) 120 minutes.

After 90 minutes **Figure 5.11-e**, closed pores undergo rapidly the densification by reducing its cross section and to be almost eliminated after 120 min when grain growth becomes a predominant phenomenon, **Figure 5.11-f**. One can conclude that



sintering process up to 1700°C of fine W powders requires a long holding time so that grain growth becomes the predominant phenomenon.

### 5.2.6 Variation of activation energy during sintering process

The main objective of this analysis is to find out the sintering kinetics and sintering activation energy of coarse and fine W powders and to compare the calculated results by the two methods.

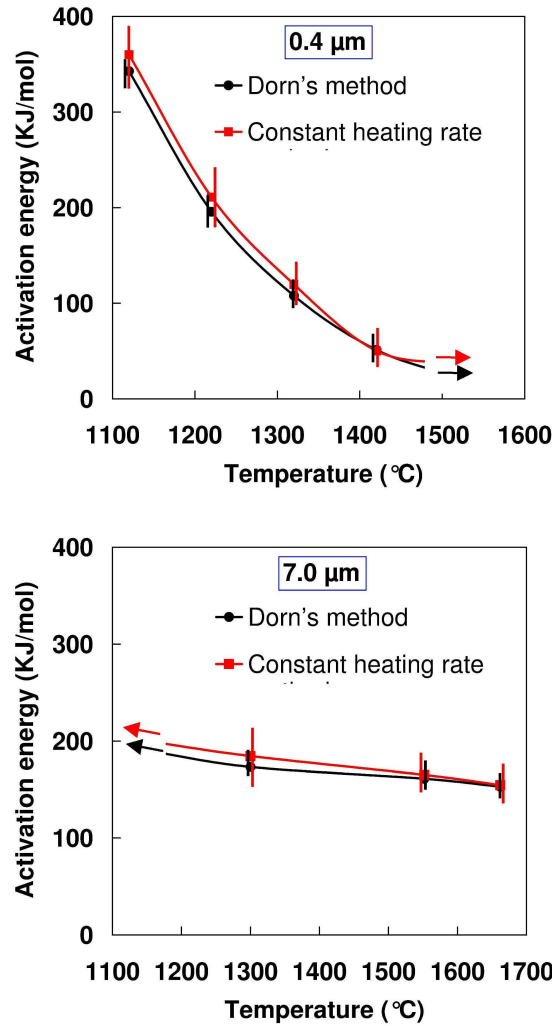


**Figure 5.12:** Change in sintering activation energy values with increasing temperature observed for Dorn's method and constant heating rate method, (a) 0.4 μm, (b) 7.0 μm using pure hydrogen atmosphere.

**Figure 5.12-a** and **Figure 5.12-b** show the apparent sintering activation energy dependencies evaluated for the sintering process at different temperatures, from 1100 to 1600°C under pure hydrogen atmosphere, for fine (0.4μm) and coarse (7.0 μm) W powders, respectively. In the related analysis, sintering activation energy

evolution obtained from Dorn's method and constant heating rate method for different powders indicate a proper correlation. For the constant heating rate method, the error is relatively large  $\pm 30$  kJ/mol. The results related to this investigation are in agreement with the sintering activation energy value of W powders; it is stated between 158.26 and 418.68 kJ/mol, depending on temperature, W quality and method of measurement [LAS 99]. Hayden and Brophy reported that the apparent sintering activation energy for boundary diffusion process is 378 kJ/mol. Small additions of Group VIII elements normally accelerate the interfacial transport process. Iridium, however, actually retards densification by the interfacial path with the result that volume self-diffusion of W possibly dominates the slower densification rate. For this process the apparent sintering activation energy is 558.6 kJ/mol [LAS 99, HAY 64]. Srivastav et al reported that the densification of W starts with diffusion along the grain boundaries and the corresponding sintering activation energy was about  $307 \pm 1$  kJ/mol<sup>-1</sup> at 1200°C [SRI 11].

The results given in **Figure 5.12-a**, covering a wide range of temperatures, show a decline in sintering activation energy at high temperatures. The same phenomena can be found in the literature (Liu et al [LIU 01] and Guillaume et al [GUI 07]). It is suggested that more than one densification mechanism is operative in the sintering experiments. Considering the decreasing activation energy trend in the present results with corresponding activation energies values, it is reasonable to deduce that the volume diffusion is not the dominant densification mechanism for the both type of W powders at low or high temperature because obtained sintering activation energies are more less then the one required for volume diffusion process.

At the beginning of sintering, the atom diffusion was difficult as a result of the long distance among particles in the components. So, the apparent value of sintering activation energy reflects this difficulty by having a high and nearly constant value, **Figure 5.12-b**. When the component densified further, more grain boundaries are formed, grain boundary diffusion will contribute to the densification of the specimen and sintering activation energy becomes less, **Figure 5.12-a**. One can conclude that the maximal required sintering activation energy, for grain boundary diffusion of the used W powders, is about  $80 \pm 20$  kJ/mol.

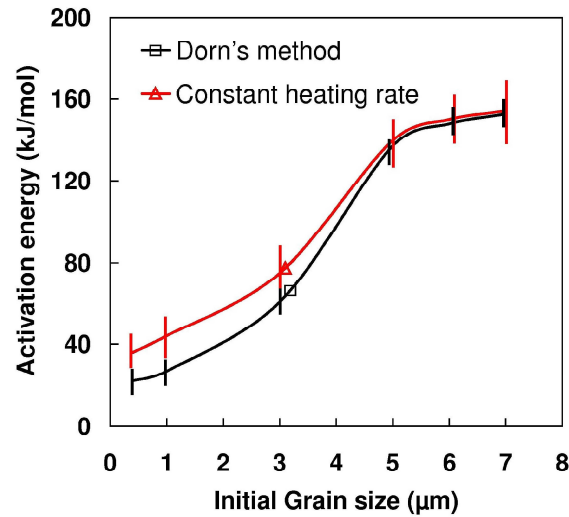


**Figure 5.13:** Sintering activation energy vs. initial grain size calculated based on constant heating rate and Dorn's method at 1500 °C using pure hydrogen atmosphere.

The sintering activation energy plotted as a function of initial grain size for W components shows a small difference in the calculated sintering activation energy corresponding to both methods. The apparent sintering activation energy for densification increases with increasing in initial grain size. It is duly noted that the sintering activation energy for densification is dependent on the used initial grain size. The sintering activation energy increases significantly when initial grain size ranges from 0.4 to 3 μm and then it is nearly constant with high relative values for coarse W powders (5.0 to 7.0 μm) as shown in **Figure 5.13**. High value of sintering activation energy indicates low thermal stability which causes a reduction in grain boundary mobility. An increase in the apparent sintering activation energy, for coarse W powders, beyond that for grain boundary diffusion indicates that a significant portion of the energy is being used to change the structure of the material without contributing to the densification process [BUT 11]. Therefore, fine W powders with initial grain size of 0.4 μm are the best ones to be sintered up to 1700°C under pure hydrogen atmosphere, as these powders are highly thermal stable comparing to other ones.

### 5.3 Finite element modeling and identification of sintering parameters

#### 5.3.1 Constitutive model for sintering process

In order to perform the sintering process using finite element method, several macroscopic models have been developed to predict the shrinkages and distortions of the components during sintering process. In these works, the sintering body is regarded globally as a compressible continuum even though it is composed of solid and pores. During sintering process, green components are usually elastic at room temperature and there exists an elastic to viscous transition region. The viscoplastic constitutive law in continuum mechanics can be used to describe this transition. Gasik et al. [GAS 00] described the total strain during sintering process with the following equation:

$$\dot{\boldsymbol{\varepsilon}} = \dot{\boldsymbol{\varepsilon}}_e + \dot{\boldsymbol{\varepsilon}}_{th} + \dot{\boldsymbol{\varepsilon}}_{vp} \quad (5-14)$$

where  $\dot{\boldsymbol{\varepsilon}}$  is the total strain rate,  $\dot{\boldsymbol{\varepsilon}}_e$  is the elastic strain rate,  $\dot{\boldsymbol{\varepsilon}}_{th}$  is the thermal strain rate and  $\dot{\boldsymbol{\varepsilon}}_{vp}$  is the viscoplastic strain rate. The elastic strain and thermal strain are due to the change in sintering temperature.

The elastic strain rate is assumed to be linear and isotropic. It can be expressed with the following Hooke's law:

$$\dot{\boldsymbol{\sigma}} = D_e \dot{\boldsymbol{\varepsilon}}_e \quad (5-15)$$

where  $D_e$  is elastic stiffness matrix for the isotropic materials.

The thermal strain  $\dot{\boldsymbol{\varepsilon}}_{th}$  is mainly due to thermal expansion that can be expressed as:

$$\dot{\boldsymbol{\varepsilon}}_{th} = \alpha \dot{T} I \quad (5-16)$$

where  $\alpha$  is the thermal expansion coefficient,  $\dot{T}$  is the incremental temperature rate and  $I$  is second order identity tensor. Based on the used dilatometric tests the constant  $\alpha$  is calculated around  $4.6 \times 10^{-6}$  m/m.K.

At high sintering temperature, viscoplastic strain is more dominant and overcome the elastic strain. The viscoplastic strain rate is given by the following equation [WAK 13] and [SON 06]:

$$\dot{\boldsymbol{\varepsilon}}_{vp} = \frac{\dot{\boldsymbol{\sigma}}}{2G_p} + \frac{\boldsymbol{\sigma}_m - \boldsymbol{\sigma}_s}{3K_p} I \quad (5-17)$$

where  $\dot{\varepsilon}_{vp}$  is the viscoplastic strain rate,  $\sigma'$  is the deviatoric stress tensor,  $\sigma_m = \text{tr}(\sigma)/3$  is the mean stress and  $\text{tr}(\sigma)$  is the stress tensor trace,  $I$  is second order identity tensor,  $G_p$  and  $K_p$  are respectively the shear and bulk viscosity of the porous material,  $\sigma_s$  is the sintering stress.  $G_p$ ,  $K_p$  and  $\sigma_s$  depend on the relative density, temperature and the microstructural factors such as grain and pore size. The following equation was proposed by Petersson et al. in order to calculate the sintering stress during liquid phase sintering for Tungsten Carbide Cobalt WC-Co with different grain size [PET 04]. This equation was also used in the modelling of solid state sintering for 316L stainless steel components [SON 06]:

$$\sigma_s = B\rho^C \quad (5-18)$$

where B and C are the material constants of sintering stress that should be identified.

Various models have been developed to determine  $G_p$ ,  $K_p$  and  $\sigma_s$  in the constitutive law. Kim et al. [KIM 03] and Gillia et al. [GIL 01] designed proper experiments to determine the viscosity modulus and sintering stress of Tungsten Carbide Cobalt WC-Co. The model assumed that the stress level of the sintering body is so low that the relationship between stress and strain rate tensor can be regarded as the linear one. The experiments of free sintering and uniaxial loading sintering of cylindrical specimens in dilatometer are employed to measure the vertical strain rate  $\dot{\varepsilon}_z^{vp}$  and  $\sigma_z$  the applied external stress on the specimen. The uniaxial viscosity  $\eta_p$  is determined by the following expression:

$$\eta_p = \frac{\dot{\varepsilon}_z^{vp}}{\sigma_z} \quad (5-19)$$

Bordia and Scherer [BOR 88] relate the Poisson ratio of the porous material to the relative density according to equation (5-19) and this relation has the appealing limit  $\nu_p = 0$  for  $\rho = 0$ .

$$\nu_p \approx \frac{1}{2} \sqrt{\frac{\rho}{3-2\rho}} \quad (5-20)$$

By the analogy with linear elastic theory, the shear and bulk viscosity modulus can be calculated using the following expressions [BOR 88]:

$$G_p = \frac{\eta_p}{2(1+\nu_p)} \quad (5-21)$$

$$K_p = \frac{\eta_p}{3(1-2\nu_p)} \quad (5-22)$$

For the solid state sintering of injection moulded parts in W powder, the grain boundary diffusion and bulk diffusion are the main mechanisms that contribute to the densification. The intermediate and final stages of nano-sized powders have similar densification behaviour to those of micrometer-sized powders, during which grain-boundary diffusion is the main mechanism of densification [WAN 12]. Based on the Coble's creep model proposed for grain boundary diffusion and the mechanics for porous materials, the expression for the uniaxial viscosity can be expressed as [SON 06]:

$$\eta_p = \frac{kTG^3\rho^2}{47.5V_a\delta_b D_{b0} \exp(-Q_b / RT)} \quad (5-23)$$

Equation (5-23) is suitable for describing the viscosity of the components during the isothermal sintering [WAN 12].

where  $T$  is the absolute temperature,  $G$  is grain size,  $k$  is Boltzmann's constant,  $V_a$  is the atomic volume,  $D_{b0}$  is the grain boundary diffusion frequency,  $R$  is gas constant,  $\delta_b$  is the thickness of grain boundary and  $Q_b$  is the activation energy for grain boundary diffusion. The material parameters such as  $V_a$ ,  $D_{b0}$ ,  $\delta_b$  and  $k$  are assumed to be constants during the entire sintering process.

The viscosity during the non-isothermal sintering can also be determined by the beam bending tests presented above. Based on the linear viscous–elastic analogy, the uniaxial viscosity is given by the following expression [SON 10].

$$\eta_p = \frac{1}{\dot{\delta}} \left( \frac{5\rho_0 g L_s^4}{32h^2} + \frac{PL_s^3}{4bh^3} \right) \quad (5-24)$$

where  $\eta_p$  is the uniaxial viscosity determined by the beam bending tests,  $\dot{\delta}$  is the deflection rate at the centre of the specimen,  $\rho$  is the initial relative density after presintering step,  $g$  is gravity acceleration,  $P$  is the external load,  $b$  and  $h$  are width and thickness of the component.

The relative density of the sintered component is calculated by the following expression:

$$\rho = \frac{\rho_0}{(1 + \lambda)^3} \quad (5-25)$$

where  $\rho_0$  is the initial relative density.

The interaction between the above equations is summarized in **Figure 5.14**. To identify the parameters B and C, the optimisation strategy is used. It regulates the parameters B and C in order to make the shrinkage curves of numerical simulation approach to the measured ones obtained by dilatometer tests. Then ABAQUS standard 6.10 is used as finite element solver. In order to achieve the constitutive law described above, subroutine UMAT is used and fully coupled with heat transfer.

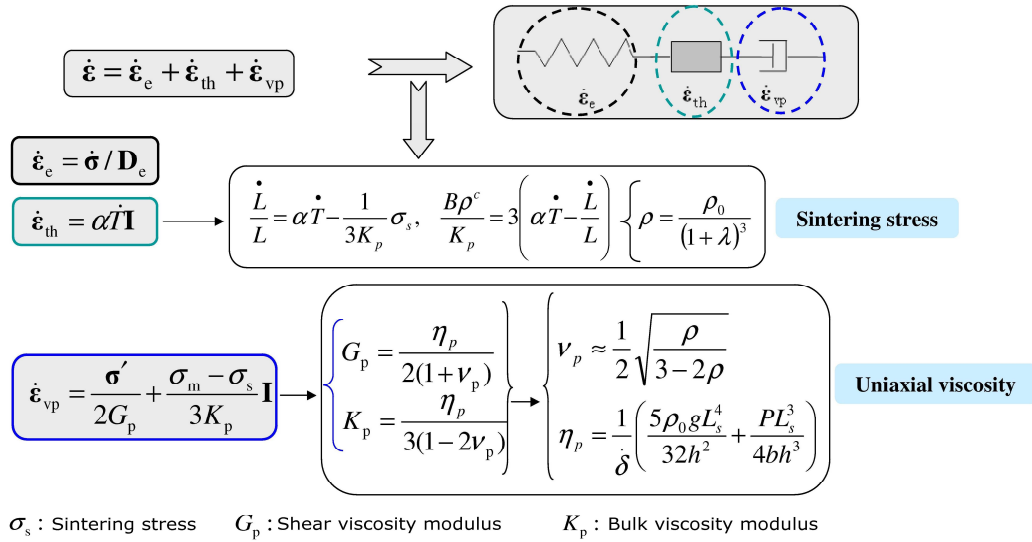


**Figure 5.14:** Thermo-elasto-viscoplastic constitutive model used for the sintering process.

### 5.3.2 Identification of sintering parameters

#### 5.3.2.1 Identification of material constants for W components

The following equation has been proposed to calculate the sintering stress during the sintering stage [SON 06]:

$$\frac{B\rho^C}{K_p} = 3 \left( \alpha \dot{T} - \frac{\dot{L}}{L} \right) \quad (5-26)$$

where  $\dot{L}$  is the dimensional change of the component,  $\alpha$  is the coefficient of thermal expansion and  $\dot{T}$  is the incremental temperature rate.

The strategy to identify the material constants using Matlab<sup>®</sup> platform consists in fitting the numerical uniaxial shrinkage curve according to equation (5-27) to the one obtained from the dilatometric tests. The inverse identification procedure [LAG 98], by the mean of the squared estimation error, has been used as related in the algorithm summarised in the following expression:

$$\begin{cases} \min G(x) \\ G(x) = \sum_{i=1}^n |\lambda^{\text{exp}}(T_i, x) - \lambda^{\text{num}}(T_i, x)|^2 \\ x = [B, C] \end{cases} \quad (5-27)$$

where  $G(x)$  is the mean residual squares of the tolerance objective function where  $i=1, \dots, n$  indicates different values of the sintering temperature;  $x$  stands for the set of material constants to be identified,  $\lambda^{\text{exp}}$  is the experimental uniaxial shrinkage obtained from the TMA test and  $\lambda^{\text{num}}$  is numerical uniaxial shrinkage obtained by using the optimization procedure. Nelder-Mead Simplex method has been employed to minimize the value of  $G(x)$  in our case.

Material constants should be determined properly and their determination for sintering model is important to obtain accurate results in numerical simulations by finite element methods. The evolution of uniaxial shrinkage obtained using the identified material constants with heating rate 5°C/min, for fine and coarse W powders, is related in **Figure 5.15**. One can notice that the global average error is about 4 %. The inverse method results are in a proper agreement with the experimental ones.



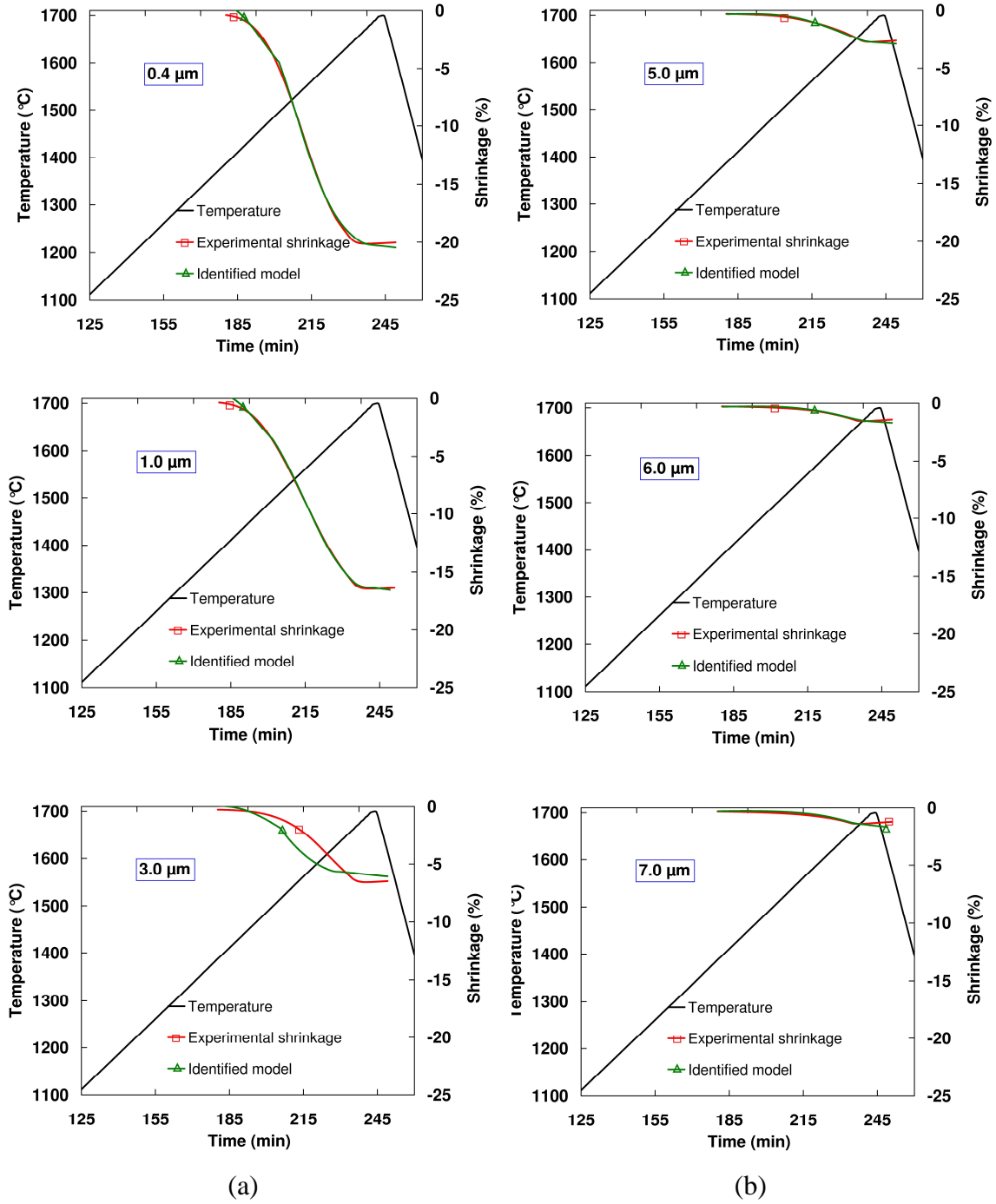


**Figure 5.15:** Evolution of uniaxial shrinkage versus sintering time, comparison between experimental and identified model results for: (a) fine W powders and (b) coarse W powders with heating rate eq. 5 °C/min in pure hydrogen atmosphere.

The identified material constants obtained for fine and coarse W powders are related in **Table 5.5**. Due to the different shrinkage rates during sintering stage, identification has been divided into two segments specified by critical relative density.

**Table 5.5:** Identified material constants for fine and coarse W powders with heating rate eq. 5 °C/min in hydrogen atmosphere.

|                       |                   |                      |       |                      |         |
|-----------------------|-------------------|----------------------|-------|----------------------|---------|
| Density               |                   | <0. 85               |       | >0. 85               |         |
| Material constants    |                   | $B_1 \times 10^{-3}$ | $C_1$ | $B_2 \times 10^{-3}$ | $C_2$   |
| Initial particle size | 0.4 $\mu\text{m}$ | 235.596              | 0.514 | 0.0331               | -73.597 |

|                       |                   |                      |       |                      |         |
|-----------------------|-------------------|----------------------|-------|----------------------|---------|
| Density               |                   | <0. 81               |       | >0. 81               |         |
| Material constants    |                   | $B_1 \times 10^{-3}$ | $C_1$ | $B_2 \times 10^{-3}$ | $C_2$   |
| Initial particle size | 1.0 $\mu\text{m}$ | 157.156              | 0.387 | 0.8307               | -29.819 |

|                       |                   |                      |         |                      |         |
|-----------------------|-------------------|----------------------|---------|----------------------|---------|
| Density               |                   | <0. 53               |         | >0. 53               |         |
| Material constants    |                   | $B_1 \times 10^{-3}$ | $C_1$   | $B_2 \times 10^{-3}$ | $C_2$   |
| Initial particle size | 3.0 $\mu\text{m}$ | 0.150                | -11.730 | 0.154                | -11.657 |

|                       |                   |                      |        |                      |         |
|-----------------------|-------------------|----------------------|--------|----------------------|---------|
| Density               |                   | <0. 53               |        | >0. 53               |         |
| Material constants    |                   | $B_1 \times 10^{-3}$ | $C_1$  | $B_2 \times 10^{-3}$ | $C_2$   |
| Initial particle size | 5.0 $\mu\text{m}$ | 0.164                | -5.419 | 0.010                | -15.550 |

|                       |                   |                      |        |                      |         |
|-----------------------|-------------------|----------------------|--------|----------------------|---------|
| Density               |                   | <0. 52               |        | >0. 52               |         |
| Material constants    |                   | $B_1 \times 10^{-3}$ | $C_1$  | $B_2 \times 10^{-3}$ | $C_2$   |
| Initial particle size | 6.0 $\mu\text{m}$ | 0.110                | -5.366 | 0.146                | -10.336 |

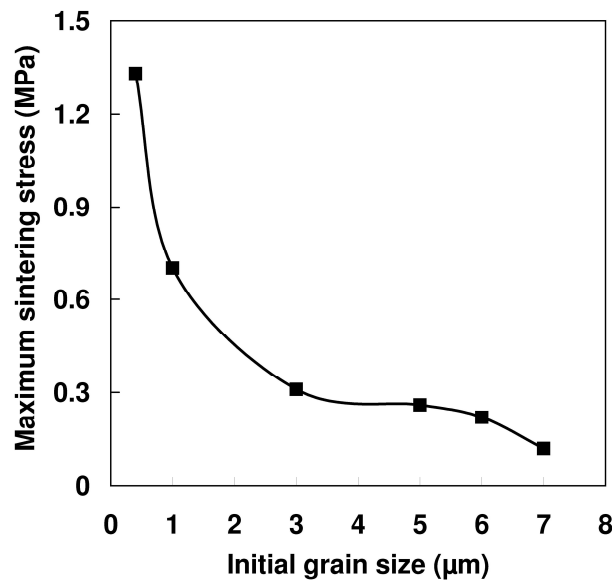
  

|                       |                   |                      |        |                      |         |
|-----------------------|-------------------|----------------------|--------|----------------------|---------|
| Density               |                   | <0. 52               |        | >0. 52               |         |
| Material constants    |                   | $B_1 \times 10^{-3}$ | $C_1$  | $B_2 \times 10^{-3}$ | $C_2$   |
| Initial particle size | 7.0 $\mu\text{m}$ | 0.080                | -5.366 | 0.150                | -11.181 |

### 5.3.2.2 Determination of maximum sintering stress

It is possible to plot the maximum sintering stress, using equation (5-17), as a function of initial grain size. The maximum sintering stress value decreases drastically from 1.33 to 0.31 Mpa for fine W powders (0.4-3.0  $\mu\text{m}$ ). For coarse tungsten powders (5.0-7.0  $\mu\text{m}$ ), the maximum sintering stress is relatively constant and ranges between 0.26 to 0.12 Mpa, **Figure 5.16**. One can conclude that the sintering stress is also sensitive to the initial grain size of powders.

For most materials, the maximum sintering stress values are often estimated to be 1 Mpa or below [PET 04] which is the case in the present study, **Figure 5.16**. The maximum sintering stresses obtained in the present investigation are higher than reported by Gillia et al. for Tungsten Carbide Cobalt WC-Co [GIL 01], where 0.08–0.2 MPa was determined. Also, sintering stress values between 0.8 and 0.4 MPa [VEN 86] for MgO doped alumina and between 0.1 and 0.4 MPa [DUC 89] for  $\text{SiO}_2$  were obtained. Values higher than 1 MPa are however not impossible and have for example been reported for alumina by Zuo et al. [ZUO 03] and by Cai et al. [CAI 97] for alumina and zirconia. The starting powder in these cases had smaller grain size which confirms the obtained results in the case of 0.4  $\mu\text{m}$ .



**Figure 5.16:** Maximum sintering stress plotted against initial grain size using pure hydrogen atmosphere.

### 5.3.2.3 Determination of uniaxial viscosity

**Figure 5.17** shows the uniaxial viscosity for the two materials with fine and coarse grain sizes, respectively. The uniaxial viscosity is derived from the data presented in **Figures 5.7** and **5.8**. The uniaxial viscosity shows a general trend with two main stages that are most distinct for the finer powder. When the sintering temperature ranges between 1100 and 1400°C, the uniaxial viscosity for fine powders decreases from 8 to 6 Pa.s, after which it becomes almost constant at 6 Pa.s, **Figure 5.17-a**. However, for the coarse powders, **Figure 5.17-b**, the uniaxial viscosity always decreases during the whole operation of sintering. The minimum uniaxial viscosity was obtained around 1300°C for finer tungsten powders and 1600°C for coarser ones. Decreasing in uniaxial viscosity can be explained that the density is still low, which is the case for coarse powders, **Figure 5.17-b**.

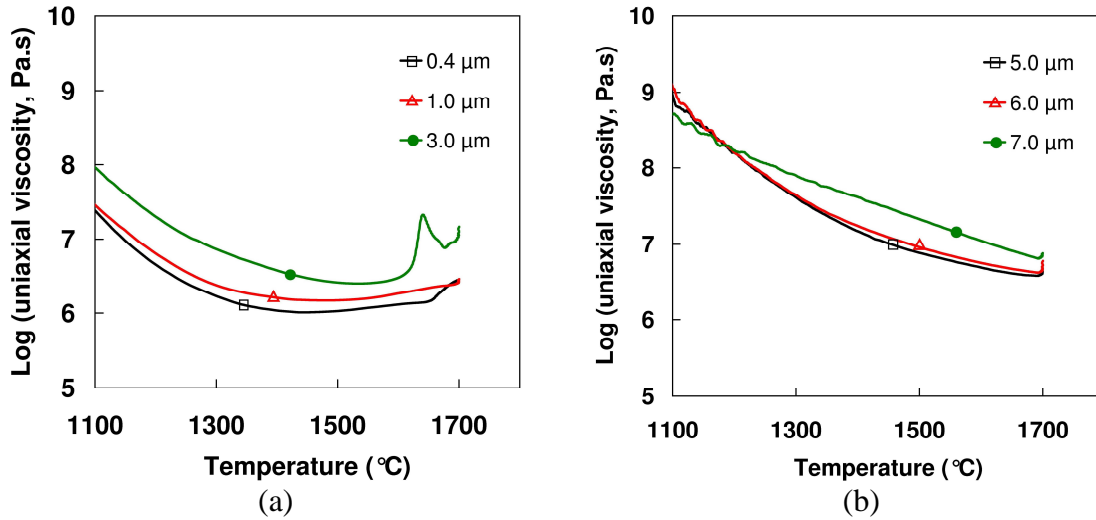


**Figure 5.17:** Determined uniaxial viscosity vs. sintering temperature, (a) fine powders, (b) coarse powders.

### 5.3.2.4 Determination of activation energy for grain growth

The grain growth behaviour for metal powders during the sintering is determined by the following equation [ZHA 05].

$$\begin{cases} G = G_0 + \frac{dG}{dt} \\ \frac{dG}{dt} = \frac{D_0 \exp(-Q_g/RT)}{G} \end{cases} \quad (5-28)$$

Where  $G$  is the final grain size,  $G_0$  is the initial grain size,  $Q_g$  is the activation energy for grain growth and  $D_0$  the pre-exponential term of the diffusion coefficient. Boonyongmaneerat obtained that the parameter  $D_0$  is in the range of  $0.95\text{--}1.00\ \mu\text{m}^2\ \text{s}^{-1}$  by the experiments for pure W powder compacts heated up to  $1725^\circ\text{C}$  [BOO 09].

For example, for finest powder one knows the initial grain size  $G_0 = 0.4\ \mu\text{m}$ . When the temperature is less than  $1200^\circ\text{C}$ , the activation energy for grain growth is chosen to be too high  $350\ \text{kJ/mol}$  (no grain growth). The objective is to determine the activation energy during the sintering process (temperature more than  $1200^\circ\text{C}$ ). This is possible because we know the final grain size  $G$  from the SEM images.

**Figures 5.18** plot the grain growth–sintering time curves of fine and coarse W powders. The sintering temperature varies from ambient temperature up to  $1700^\circ\text{C}$  for 5 minutes holding time and  $5^\circ\text{C/min}$  heating rate. The effect of initial grain size of W powders on sintering behaviour at final stage is also shown in these figures. It can be seen that powder with initial small grain size increases much more than the powder with initial coarse grain size. For example, for the coarse powder, the grain size increases from  $7.0\ \mu\text{m}$  to  $7.25\ \mu\text{m}$  as the temperature is increased from  $1200^\circ\text{C}$  to  $1700^\circ\text{C}$ , while the grain size increases from  $0.4\ \mu\text{m}$  to  $11.2\ \mu\text{m}$  indicating high grain growth for the fine powder in the same range of temperature which can explain also the high obtained density (90-94%) at the end of sintering process for this type of powder as presented previously in **Figure 5.10**. For experimental results using scanning electron microscope as shown in **Figure 5.18-a** and **Figure 5.18-b**, the final grain size of fine W powder ranges between  $8$  to  $11\ \mu\text{m}$  and  $7$  to  $8\ \mu\text{m}$  for the coarse one. The identification of the grain growth is based on equation (5-28) using Matlab platform and SEM images. The identified values of grain growth activation energy are related in **Table 5.6**.

**Table 5.6:** Identified values of grain growth activation energy.

| Initial grain size ( $\mu\text{m}$ )        | 0.4 | 1.0 | 3.0 | 5.0 | 6.0 | 7.0 |
|---|-----|-----|-----|-----|-----|-----|
| Activation energy for grain growth (kJ/mol) | 70  | 73  | 85  | 108 | 111 | 120 |

In a recent study by Beera et al. [BEE 13], grain size and density parameters have been investigated in SrO added Tungsten Bronze, same values of activation energies for sintering and grain growth have been obtained. However, for our case, different values are obtained.

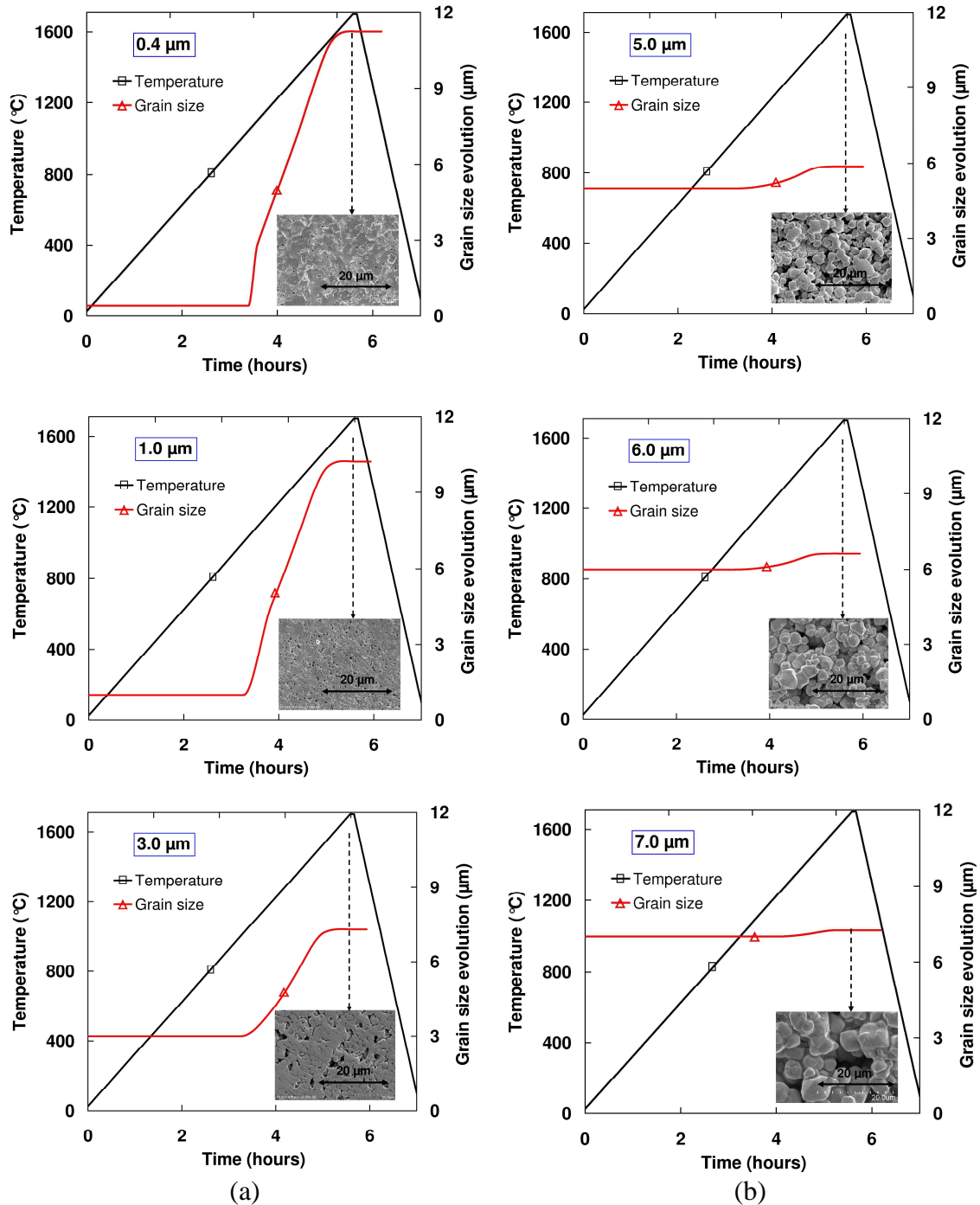


**Figure 5.18:** Grain growth during sintering process up to 1700 °C for 5min holding time and heating rate 5°C/min, (a) fine powders and (b) coarse powders.

## 5.4 Numerical simulation results

### 5.4.1 Material and process numerical implementation

The sintering process is investigated using numerical analysis for specimen obtained from injection with the fine and coarse W powders. The Abaqus finite element code is chosen for numerical simulation of the sintering process, as it provides the analysis of thermomechanics coupling. The thermal cycle employed for sintering was heating to 1700°C with 5°C/min and then holding for 5 minutes.

The ABAQUS<sup>®</sup> code for the sintering simulation is defined in an input file in association with a user-defined subroutine file, which is programmed in FORTRAN. The generation of the geometric model and the finite element mesh is done in the input file, followed by the definition of the material model. The viscoplastic model is referred to the user-defined subroutine, in which the strain rate during sintering process is defined. Several solution dependent state variables are also employed in the subroutine to update variables, such as sintering stress, viscosity, temperature and density. The initial conditions and boundary conditions are also defined in the input file. The same time increment (50 s) is used as it is in Solver. The material parameters and physical constants used in the present numerical simulations are related in **Table 5.7**.

The component geometry and the alumina support, used to create the model, are shown in **Figure 5.19-a**. Within ABAQUS, R3D4 (a four-node rigid element) and three-dimensional hexahedral C3D8R (Continuum, 3-D, 8-node, Reduced integration) have been set for the support and the component as the element type, respectively. The mesh of the sintered part and support are shown in **Figure 5.19-b**.

#### Initial conditions

The solution of the problem requires initial and boundary conditions. Initially, the temperature of the component is ( $T_0 = 1200^\circ\text{C}$ ), below this temperature sintering step can not take place. The initial density has been set with initial values corresponding to each feedstock.

$$\rho(x, y, z, 0) = \rho_0, \quad (x, y, z) \in \Omega \quad (5-29)$$

$$\sigma_s(x, y, z, 0) = 0.02\text{MPa}, \quad (x, y, z) \in \Omega \quad (5-30)$$

$$T(x, y, z, 0) = T_0 = 1200^\circ\text{C}, \quad (x, y, z) \in \Omega \quad (5-31)$$

### Boundary conditions

The boundary surface of the sintering component is divided into two parts, expressed as following:

$$\Gamma = \Gamma_c + \Gamma_f \quad (5-32)$$

where  $\Gamma$  is the total surfaces of the sintering component,  $\Gamma_c$  is the surfaces contacted with the support,  $\Gamma_f$  is the free surfaces exposed in the sintering atmosphere. Then the boundary conditions of force and displacement can be expressed as:

$$\vec{\sigma} \cdot \vec{n} = P_s, \quad (x, y, z) \in \Gamma_f \quad (5-33)$$

$$\vec{u} \cdot \vec{n} = 0, \quad (x, y, z) \in \Gamma_c \quad (5-34)$$

$$\tau = \sigma_f = \mu_f \cdot \sigma_n, \quad (x, y, z) \in \Gamma_c \quad (5-35)$$

where  $\vec{n}$  is the normal vector of the surface,  $\tau$  is shear stress,  $\sigma_f$  is distributed load of friction,  $P_s$  is the pressure of sintering atmosphere,  $\mu_f$  is the coefficient of the friction,  $\sigma_n$  is the normal stress of the contacted surfaces.

For thermal boundary conditions: the temperature of sintering component changes with the thermal cycle in the furnace as given in the following equation:

$$T = T_0 + \beta \cdot t, \quad (x, y, z) \in \Gamma \quad (5-36)$$

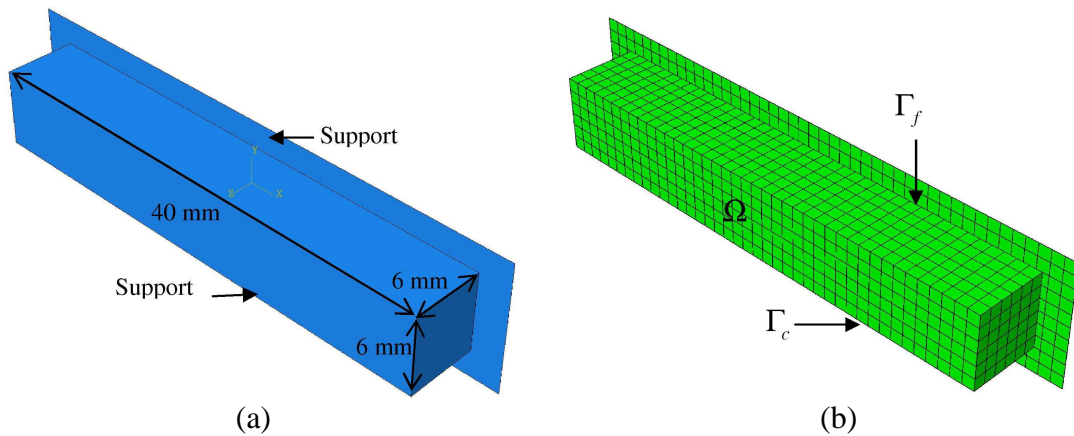


**Figure 5.19:** (a) Green component and the support plate before sintering, (b) finite element mesh of the assembly.



**Table 5.7:** Conditions for the numerical simulation of sintering process used for fine powder 0.4  $\mu\text{m}$ .

| Model parameters                                  |             | Value                    |
|---|-------------|--------------------------|
| Heating rate                                      | $\beta$     | 5°C/min                  |
| Maximal temperature                               | $T$         | 1700 °C                  |
| Initial relative density                          | $\phi$      | 0.45                     |
| Linear-expansion coefficient of powder skeleton   | $\alpha$    | 4.7x10 <sup>-6</sup> 1/K |
| Thermal conduction coefficient of powder skeleton | $\lambda_p$ | 117 W/m.K                |
| Density of powder skeleton                        | $\rho_p$    | 1930 kg/m <sup>3</sup>   |
| Poisson's ratio of the powder skeleton            | $\nu$       | 0.28                     |
| Young's modulus                                   | $E$         | 325 GPa                  |

#### 5.4.2 Final shrinkages and relative densities of sintered bars

The thermal cycle, employed for the present numerical simulation of sintering process, is heating up to 1700°C with heating rate of 5°C/min and then holding for 5min. The cylindrical coordinate system is used to present the simulation results. Centre of the part is set to be the origin of coordinate system. Initial homogeneous green relative densities of 45 and 52 % have been used in numerical simulation and correspond to W powders of 0.4 and (3.0, 7.0)  $\mu\text{m}$ , respectively. The final relative densities in three dimensions of the different sintered components using fine and coarse W powders are shown in **Figure 5.20**. It can be shown that the final relative densities are almost homogeneous for all types of powders with small variations estimated between 0.02 and 0.1%.

The final shrinkages of the sintered components of fine and coarse W powders are also shown in **Figure 5.21**. One can clearly notice that the sintering behaviour is sensitive to the initial grain size.

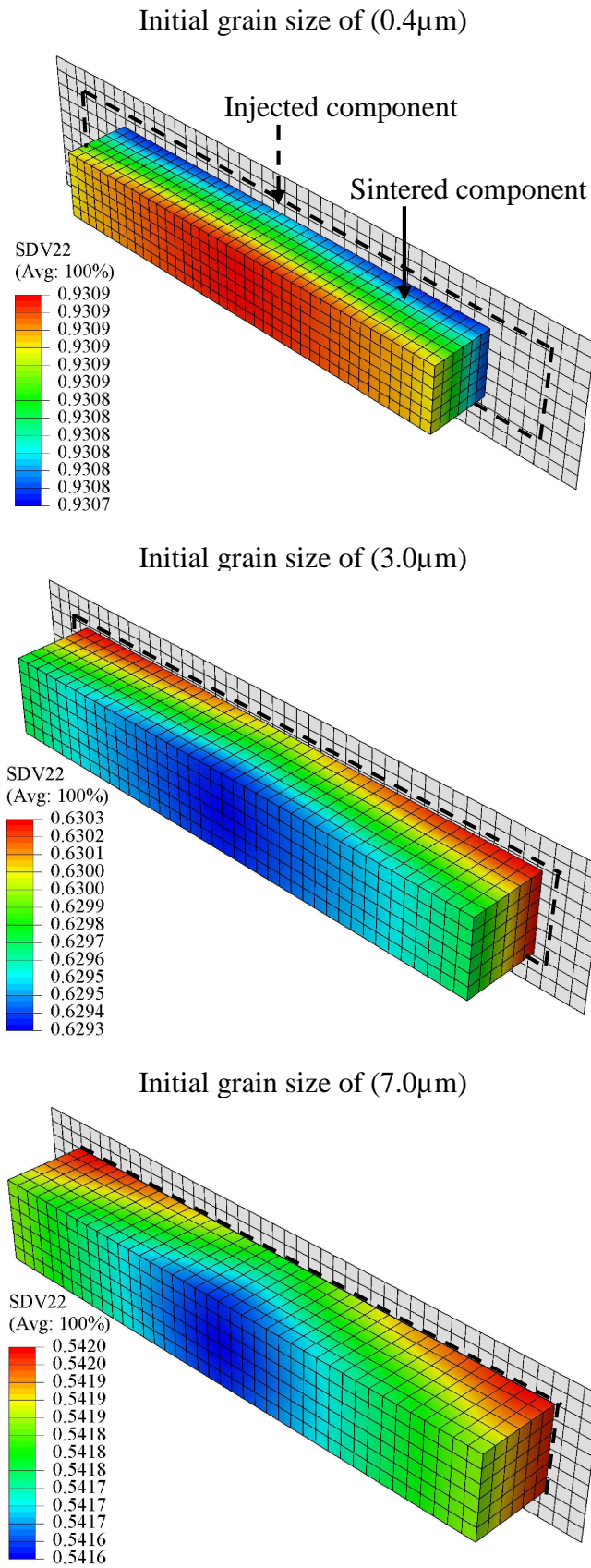


**Figure 5.20:** Numerical simulation results-final relative density values of sintered components at 1700 °C.

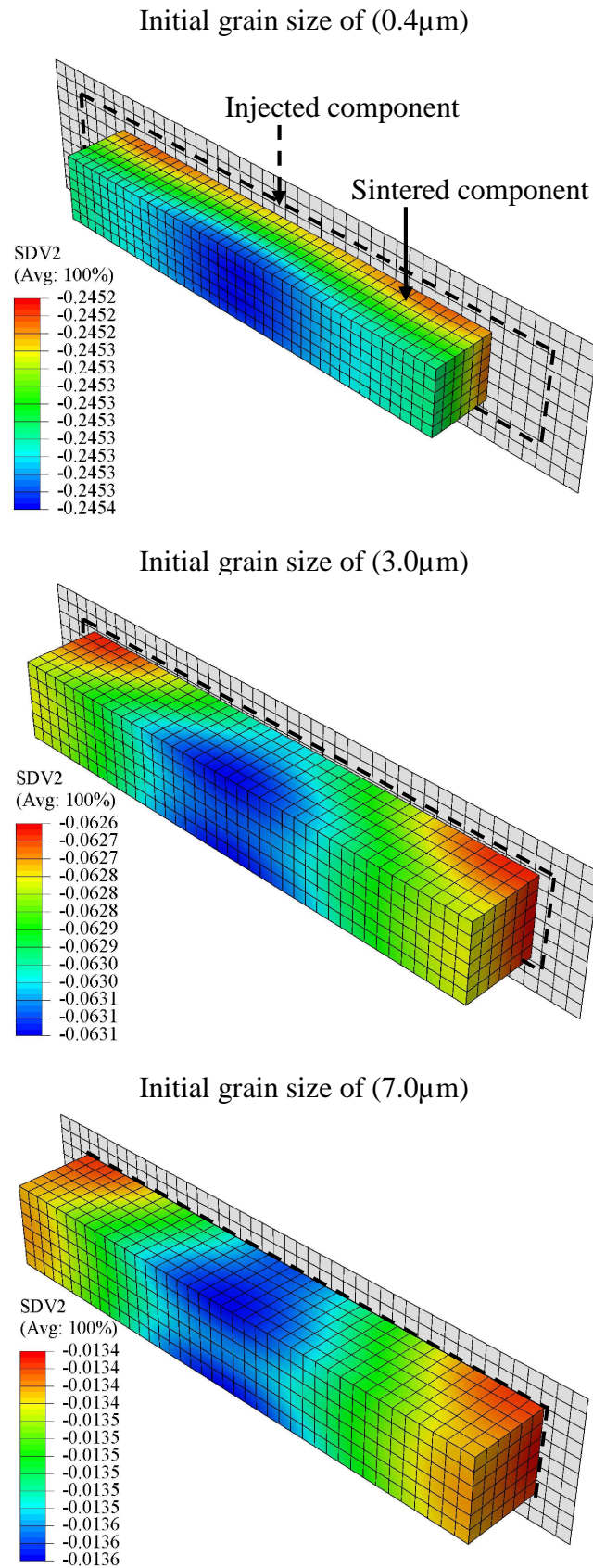


**Figure 5.21:** Numerical simulation results- shrinkage values of sintered components at 1700 °C.

### 5.4.3 Comparison between the simulation and experimental results

#### 5.4.3.1 Relative density

**Figure 5.22** relates a comparison between the experimental density and numerical one of tungsten components made from fine and coarse powders. The experimental and numerical densities are generally in agreement. However, for powder with  $3.0\ \mu\text{m}$ , the difference between the experimental value and numerical one is about 6 to 8%.

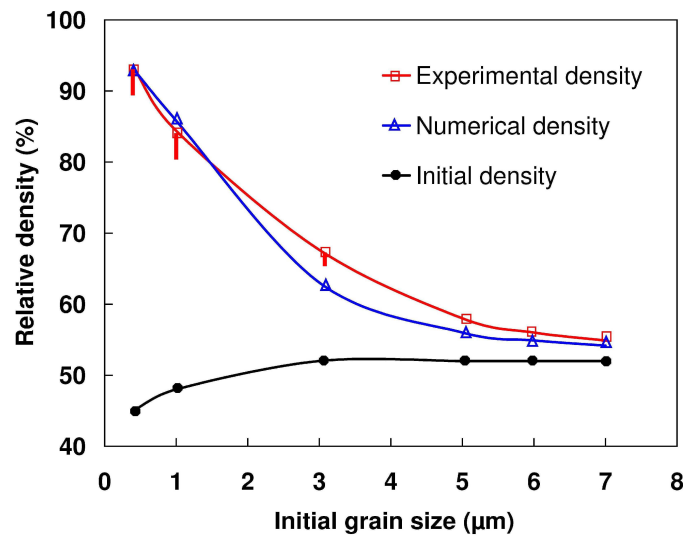


**Figure 5.22:** Comparison between the experimental and the numerical densities of tungsten components sintered at  $1700^{\circ}\text{C}$ .

#### 5.4.3.2 Final shrinkages

According to the **Figure 5.23**, one can notice that the experimental and numerical shrinkages are generally in agreement, especially for fine W powders with  $0.4$  to  $3.0\ \mu\text{m}$ . For coarse powders ( $5.0$  to  $7.0\ \mu\text{m}$ ), several experimental factors such as gravity, pores and friction between the support and the component could induce some errors and make the numerical simulation results different to the experimental ones.

One can also notice for both experimental numerical simulation results, isotropic shrinkages have been obtained after the sintering process. What ever the type of tungsten powder (fine or coarse), shrinkages are almost the same in all directions.

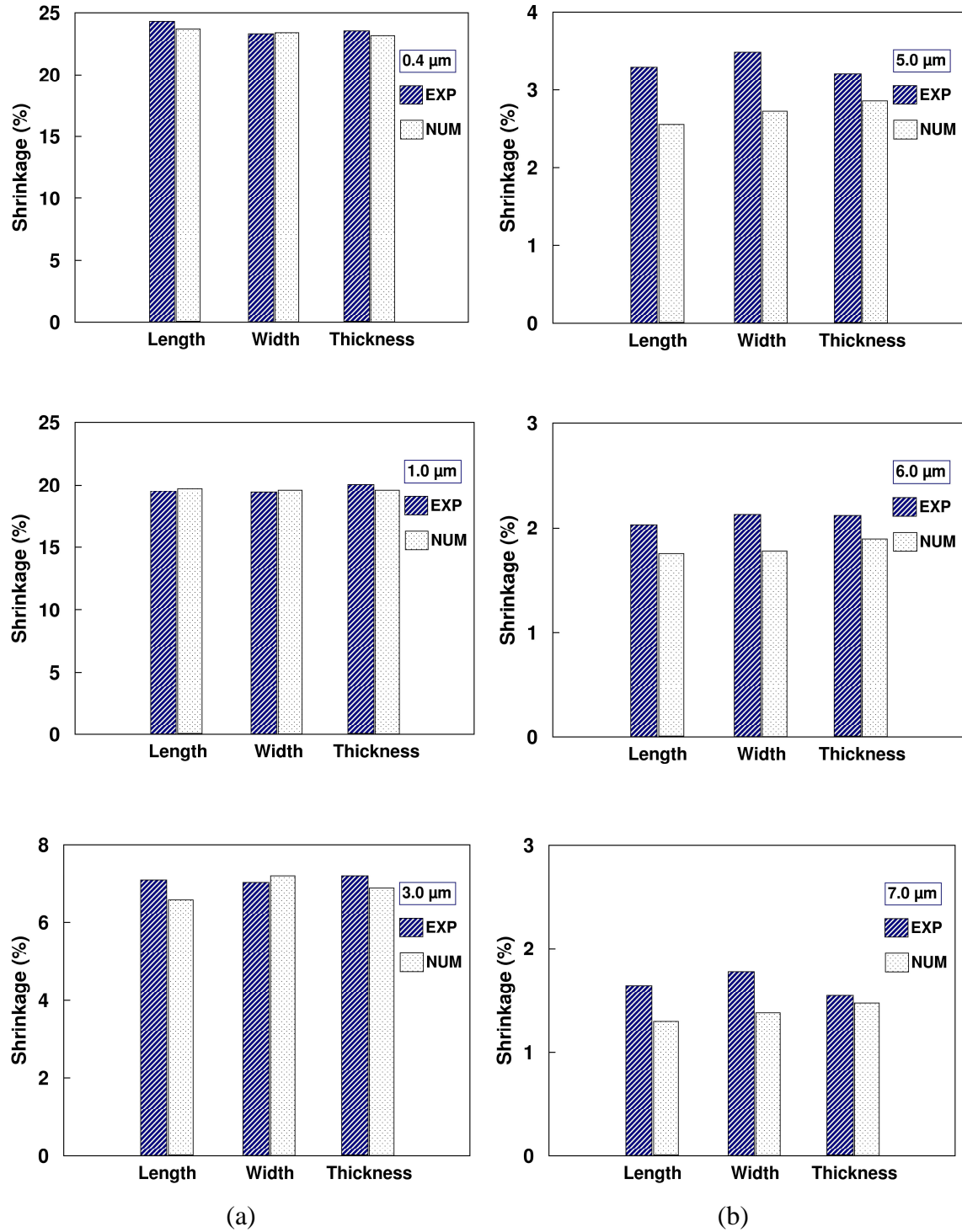


**Figure 5.23:** Comparison between the experimental and the numerical shrinkages: (a) fine W powders and (b) coarse W powders with heating rate eq. 5 °C/min.

## **5.5 Summary**

In this chapter, experimental investigations of sintering process for tungsten components have been carried out. Injection moulded components, using two types of tungsten powders (fine and coarse initial grain sizes), were sintered in hydrogen atmosphere up to 1700°C. The densification behaviour is sensitive to the initial grain size and the final density of tungsten components is almost reached in the case of fine powders 90-94%. However, the densification of coarse tungsten powders is never possible under the same conditions, height temperature is required for this type of powders >2000°C. The apparent sintering activation energy for densification increases drastically with increasing in initial grain size. It is duly noted that the sintering activation energy for densification is dependent on the used initial grain size.

The numerical simulation results showed that the shrinkage and density values are lower than the experimental ones. This difference in values, especially in the case of coarse powders, is due to several experimental factors such as gravity, pores and friction between the support and the component.

## Chapter 6: Conclusions and Perspectives

This work has been carried out by FEMTO-ST Laboratory in Besançon, France, tungsten components were provided by Xiamen Honglu Tungsten Molybdenum Industry in China. The present research focuses on the experimental investigations and numerical simulations of debinding and sintering processes using stainless steel 316L and tungsten components, respectively. The principal conclusions as well as lines of future work, for both processes, are summarized below.

### 6.1 Conclusions

Experimental investigations and numerical simulations related to thermal debinding have been carried out for metallic components obtained by powder injection moulding of fine 316L stainless steel.

In the first part, the degradation of the fine 316L stainless steel micro-powders mixed with a multi-component binder system has been studied through TGA and DTA analysis under an argon atmosphere. It has been clearly shown that the powder volume loading parameter has an effect on the thermal debinding behaviour. When the feedstock is highly loaded by powder, the high internal gas pressure would build-up significantly and lead to the formation of cracks and other defects as the case for feedstock loaded at 66%. The small value of activation energy obtained for the feedstock loaded at 62 % indicates that this feedstock is the one less sensitive to temperature (the well adapted for thermal debinding process). The values of the kinetic parameters that have been obtained by the Kissinger and Ozawa methods for different powder volume loadings indicated a proper correlation. One can also conclude that apparent activation energy for the pyrolysis of fine 316L stainless steel feedstocks is not similar for all conversion which indicates the existence of a complex multistep mechanism that occurs at the solid state. This means that the reaction mechanism is not the same in the whole degradation process and that activation energy is dependent on conversion and also powder volume loading.

In the second part dedicated to debinding, a three-dimensional model of thermal debinding for which the component behaves as a porous media has been established. The kinetic parameters  $A_1$  and  $A_2$  used for fine 316L feedstocks in the present model have been identified in order to fit the numerical remaining binder

content curve to the one obtained from the TGA tests. One can properly analyse the distribution of remaining binder content, temperature and deformation in green components during thermal debinding process.

It was shown that the remaining binder content is firstly eliminated at the component surface which means that the molten polypropylene starts to move from the center towards the external component surfaces. Also, the debinding numerical simulation results have clearly indicated that the debinding temperature evolution is progressively reached, which guarantees optimal debinding conditions. During thermal debinding, the total deformation of the PIM part is the sum of the deformations caused by polymer-content and temperature change. During the increasing debinding-rate period, the total deformation is caused by temperature evolution and the entire specimen expands. During the high debinding-rate period, the deformation caused by polymer-content change dominates the total deformation of the entire specimen, and the entire specimen contracts.

For the sintering investigation, tungsten components obtained by powder injection moulding, using fine and coarse initial grain sizes, have been sintered under pure hydrogen atmosphere up to 1700°C in order to simulate the sintering process. The effect of initial grain size on the dimensional changes of sintered components has been simulated using constitutive model and the main concluding remarks are as follows:

- The final relative density of tungsten powder components produced by powder injection moulding process depends mostly on the initial grain size of the used powders. The fine tungsten powder component with 0.4  $\mu\text{m}$  reached, at much reduced temperature 1700°C and much reduced holding time 5 min, the highest sintered density (90-94%) comparing to other powder components. This is due to the fact that fine W powder particles have large surface area than the coarse ones which gives maximum improvement in densification. Large surface area for fine W powder increases energy reduction rate between particles and leads to a maximum improvement in final relative density.
- Pure hydrogen atmosphere is the most suitable atmosphere for sintering where the W components may shrinkage up to 24% of the original size, depending mainly on the initial grain size of W powder. Vacuum and argon atmospheres are not suitable at all for W powders, maximal shrinkages of 11 and 15 % have respectively been obtained.



- The effect of sintering time on the microstructure, for fine W sintered components with initial grain size of 0.4  $\mu\text{m}$ , was investigated in this work. The SEM results indicated that the microstructures of the sintered components are not significantly influenced when holding time ranges between 60 and 120 min.
- The values of the sintering activation energies, obtained by Dorn's method and constant heating rate method, for W powders with different initial grain sizes indicated a proper correlation (for the constant heating rate method, the error is relatively large  $\pm 30$  kJ/mol). The activation energies for sintering of the fine and coarse W powders have been evaluated as 90 and 150 kJ/mol, respectively. High value of sintering activation energy indicates low thermal stability for coarse W powder which causes a reduction in grain boundary mobility and leads to poor sintered densities. Therefore, fine W powders with initial grain size of 0.4  $\mu\text{m}$  are the best ones to be sintered up to 1700°C under pure hydrogen atmosphere, as these powders are highly thermal stable comparing to other ones.
- Grain boundary diffusion has been identified as the dominant densification mechanism of the investigated W powders.
- The maximum sintering stress value decreases drastically from 1.33 to 0.31 Mpa for fine W powder (0.4-3.0  $\mu\text{m}$ ). For coarse tungsten powder (5.0-7.0  $\mu\text{m}$ ), the maximum sintering stress is relatively constant and ranges between 0.26 to 0.12 Mpa. One can conclude that the sintering stress is also sensitive to the initial grain size of powders.
- Using the present numerical simulation, one can properly analyse the final relative density and shrinkage distribution in injection moulded components during sintering process. The experimental shrinkages and relative densities of the sintered W components have been compared to the simulation results. Adequate comparisons are related for both types of powders. Nevertheless, for coarse powders 3.0 and 7.0  $\mu\text{m}$ , several experimental factors such as gravity, pores and friction between the support and the component could be the origin of errors which can make the numerical simulation results little different to the experimental ones.

## 6.2 Prospectives

### 6.2.1 Experimental prospectives

According to the experimental results, new investigations about new binder formulations for feedstocks preparation should be carried out, in order to overcome cracks during thermal debinding for components made with high powder volume loading as the case in our study (feedstock 66%). Also for the thermal debinding stage, other important processing parameters such as atmosphere and debinding cycle must be tested to take notice of their influence on the injected components during this crucial stage. One can also include the solvent debinding step to get an easy degradation during thermal debinding which might decrease the pressure gas inside the component during thermal debinding.

For sintering stage, bi-material component using different material will be sintered and examined with Scanning Electron Microscopy in order to understand the mechanical behaviour. One should also determine the physical parameters such as the friction coefficient, thermal conductivity and heat capacity of these materials. It will be also interesting to carry out thermal debinding and sintering tests for injection moulding components with complicated geometries to highlight the influence of component shape.

### 6.2.2 Prospectives for numerical simulation

For thermal debinding, the present model should be developed more to compute the remaining binder content for each polymer (PP+PW+SA). In fact, our model is not so efficient for real applications because we can not localize cracks and fractures in the debinded components made with high powder volume loading (feedstock 66%). Also, one should try to overcome the identification step in order to make the model more suitable for any used powders (copper, nickel, tungsten...etc).

In the case of sintering process, one should develop the numerical model by reducing the number of identified material parameters. It will be also interesting to include the thermal debinding step, just before the sintering one, in order to take into account the related shrinkages. Finally, numerical simulation of the sintering step for bi-material injection moulding components has to be also investigated by combining two material routines for the feedstocks having different mechanical and thermal characteristics such as Tungsten and Stainless or Copper.

## References

- [ABE 11] B. Abeln and S. J. Lombardo: Effects of a combined supercritical extraction/thermal cycle on binder removal cycle time, yield, and residual carbon of multilayer ceramic capacitors, *Journal of Ceramic Processing Research*, vol. 12, pp. 515-520, 2011.
- [ADA 07] J.M. Adames: Characterisation of polymeric binders for metal Injection moulding (MIM) process, PhD thesis, University of Akron, 2007.
- [AGG 07] G. Aggarwal, S.J. Par, I. Smid and R.M. German: Master Decomposition Curve for Binders Used in Powder Injection Molding, *Metallurgical and Materials Transactions A*, vol. 38, pp. 606-614, 2007.
- [AGG 06] G. Aggarwal, S.J. Park, and I. Smid: Development of niobium powder injection molding: Part I. Feedstock and injection molding, *International Journal of Refractory Metals and Hard Materials*, vol. 24, pp. 253-262, 2006.
- [AHA 09] X. Zhanga, W. Jongb, F. Pretoa: *J. Biomass and Bioenergy*, vol. 33, pp. 1435-1441, 2009.
- [AHN 08] S. Ahn, S.T. Chung, S.V. Atre, S.J. Park and R.M. German: Integrated filling, packing, and cooling CAE analysis of powder injection molding parts, *Powder Metallurgy*, vol. 51, pp. 318-326, 2008.
- [AHN 09] S. Ahn, S.J. Park, S. Lee, S.V. Atre and R.M. German: Effect of powders and binders on material properties and molding parameters in iron and stainless steel powder injection molding process, *Powder Technology*, vol. 193, pp. 162-169, 2009.
- [AMI 10] M. Aminzare, F. Golestani Fard, O. Guillon, M. Mazaheri and H.R. Rezaie: Sintering behavior of an ultrafine alumina powder shaped by pressure filtration and dry pressing, *Mate Sci Eng A*, vol. 527, pp. 3807-3812, 2010.
- [ANG 95] H. Angermann and Van der Biest: Binder removal in Powder Injection Molding, *Reviews in Particulate Materials*, vol. 3, pp. 35-69, 1995.
- [ANG 09] P.C. Angelo and R. Subramanian: *Powder Metallurgy Science, Technology and Applications*, August 2009.
- [ANT 11] S. Antusch, P. Norajitra, V. Piotter, H.J. Ritzhaupt-Kleissl, L. Spatafora: Powder Injection Molding – An innovative manufacturing method for He-cooled DEMO divertor components, *Fusion Engineering and Design*, vol. 86, pp. 1575-1578, 2011.
- [ANT2 11] S. Antusch, P. Norajitra, V. Piotter, H.J. Ritzhaupt-Kleissl: Powder Injection Molding for mass production of He-cooled divertor parts, *J. Nucl. Mater.*, vol. 417, pp. 533-535, 2011.
- [APMI 12] APMI International: *A Growth Industry Vital to Many Products*, June 2012.
- [ARO 05] Aroslav Blazek: Study of the reaction kinetics of the thermal degradation of polymer, PhD thesis, INP Toulouse, 2005.
- [ATT1 12] U.M. Attia and J.R. Alcock: Fabrication of hollow, 3D, micro-scale metallic structures by micro-powder injection moulding, *Journal of Materials Processing Technology*, vol. 212, pp. 2148-2153, 2012.

- [ATT2 12] U.M. Attia and J.R. Alcock: fabrication of ceramic micro-scale hollow components by micro-powder injection moulding, *Journal of the European Ceramic Society*, vol. 32, pp. 1199-1204, 2012.
- [ATW 11] O. El-Atwani, D.V. Quach, M. Efe, P. Cantwell, B. Heim, B. Schultz, E. Stach, J. Groza, JP. Allain: Ultrafine Grained Tungsten Prepared by Severe Plastic Deformation as Radiation Tolerant PFC Materials in Magnetic Fusion Devices, *Materials Science and Engineering A*, vol. 528, pp. 5670-5677, 2011.
- [AUZ11] D. Auzene, S. Roberjot: Investigations into water soluble binder systems for PIM, *PIM International*, vol.5, pp. 54-57, 2011.
- [AVI 10] M. Avijit, U. Anish and A. Dinesh: Effect of heating mode on sintering of tungsten, *Int J Refract Met Hard Mater*, vol. 28, pp. 597-600, 2010.
- [AYA 06] G. Ayad : Contribution à l'optimisation multi-physique du moulage par injection de poudres, Thèse de doctorat, Université de Franche-Comté, 2006.
- [AYA 04] G. Ayad, A. Lejeune, T.Barriere and J.C. Gelin: An optimization strategy for the determination of material and process parameters to avoid segregation defects during metal injection powder *Mat. Proc. and Design: Modeling, Simulation and Applications*, vol. 712, pp. 2120-2125, 2004.
- [BAL 05] P. Balaji: Metal injection molding. Report code: AVM049A, 2005
- [BAN 12] NP. Bansal, AR. Boccaccini, RK. Bordia and H. Camacho-Montes: *Sintering: Fundamentals and Practice, Ceramics and Composites Processing Methods*, First Edition. Edited by N P. Bansal and AR. Boccaccini. The American Ceramic Society. Published by John Wiley & Sons, Inc, 2012.
- [BAR 03] T. Barriere, B. Liu and J C. Gelin: Determination of the optimal process parameters in metal injection molding from experiments and numerical modeling, *J. Mater. Process Technol*, vol. 143-144, 636-644, 2003.
- [BAR 01] T. Barriere, J.C. Gelin and B. Liu: Experimental and numerical investigations on the properties and quality of parts produced by MIM, *Powder Metallurgy*, Ed. by Maney Publishing, vol. 3, pp. 228-234, 2001.
- [BAR 00] T. Barriere : Expérimentations, Modélisation et Simulation Numérique du Moulage par Injection de Poudres Métalliques, Thèse de doctorat, Université de Franche-Comté, 2000.
- [BAR 03] T. Barriere, B. Liu and J.C. Gelin: Determination of the optimal process parameters in metal injection molding from experiments and numerical modeling, *Journal of Materials Processing Technology*, vol. 143-144, pp 636–644, 2003.
- [BEE 75] W K. Beere: A unifying theory of the stability of penetrating liquid phases and sintering pores, *Acta Metall.*, vol. 23, pp. 131-138, 1975.
- [BEE 13] C.S. Beera, P.S.V. Subba Rao, B. Parvatheeswrararao, *Inter J of Eng Sci and Technol* 2013, 5: 272.
- [BEN 07] J.M. Benson and H.K. Chikwanda: Challenges of titanium metal injection moulding, 8th annual international RAPDASA conference, Tshwane University of Technology and Pilanesburg, South Africa; 7–9 November, 1–11, 2007.

- [BRI 12] J. Bricout: Fabrication du combustible nucléaire par injection: Etude de la formulation et du déliantage d'une pâte contenant des actinides, Ph.D thesis, University of Franche-Comté, 2012.
- [BER 01] S. Berg and O. Mars: Investigating the relationship between machinability Additives and machining parameter, *Advances in Powder Metallurgy and Particulate Materials*, compiled by W.B. Eisen and S. Kassam, Metal Powder Industries Federation, Princeton, NJ, part 6, pp. 50-55, 2001.
- [BER 10] O. Bergman and L. Nyborg: Evaluation of sintered properties of PM steels based on Cr and Cr-Mn prealloyed steel powders, *Powder Metallurgy Progress*, vol. 10, pp.1-19, 2010.
- [BOL 10] V. Boljanovic: Powder metallurgy, In *Metal Shaping Processes: Casting and Molding, Particulate Processing, Deformation Processes, Metal Removal*. Industrial Press Inc., ISBN 9780831 133801, New York, USA, pp. 75-106, 2010.
- [BOO 09] Y. Boonyongmaneerat: Effects of low-content activators on low-temperature sintering of tungsten, *J. Mater Process Technol*, vol. 209, pp. 4084-4087, 2009.
- [BOR 88] RK Bordia and G W. Scherer: On constrained sintering-I Constitutive model for a sintering body, *Acta Metall.*, vol. 36, pp. 2393-2397, 1988.
- [BUT 11] B. Butler, E. Klier, M. Kelly, M.Gallagher: Thermal stability of milled nanocrystalline tungsten powders, *Army Research Laboratory*; 2011.
- [CAO 92] M.Y. Cao, J.W. O'Connor: A New Water Soluble Solid Polymer Solution Binder for Powder Injection Molding, in *Advances in Powder Metallurgy*, American Powder Metallurgy Institute, Princeton, pp. 85–98, 1992.
- [CAL 05] J N. Calata: Densification behavior of ceramic and crystallisable glass materials constrained on a rigid substrate, Ph.D thesis, Blacksburg, Virginia, 2005.
- [CAI 97] P.Z. Cai, G.L. Messing and D.L. Green: Determination of the mechanical response of sintering compacts by cyclic loading dilatometry, *J. Am. Ceram. Soc.*, vol. 80, pp.445-452, 1997.
- [CFI 06] Starting a New Era in Catalytic Debinding of MIM Components, CFI-Ceramic Forum International, 2006.
- [CHA 12] S. Chanthapan, A. Kulkarni, J. Singh, C. Haines and D. Kapoor: Sintering of tungsten powder with and without tungsten carbide additive by field assisted sintering technology, *Int J Refract Met Hard Mater*, vol. 31, pp. 114-120, 2012.
- [CHE 99] C C. Chen and L W. Hourng: Numerical simulation of two-dimensional wick debinding in MIM by body fitted finite element method, *Powder Metallurgy*, vol. 42, pp. 313-319, 1999.
- [CHE 04] X. Chen, Y.C. Lam, Z.Y. Wang, K.W. Tan : Determination of phenomenological constants of shear-induced particle migration model, *Computational Materials Science*, vol. 30, pp. 223–229, 2004.
- [CHE 12] Z. Cheng, T Barriere, B. Liu, L. Baosheng and J.C. Gelin: A vectorial algorithm with finite element method for prediction of powder segregation in metal injection molding, *International Journal for Numerical Methods in Fluids*, vol. 70, pp. 1290-1304, 2012.

- [CLA 13] N. Clavier, R. Podor, G I N’Kou Boulala, J. Ravaux and N. Dacheux : Etude in situ du frittage d’oxydes de lanthanides et d’actinides par HT-MEBE, Colloque de la commission mixte « Poudres et Matériaux Frittés » de la SF2M et du GFC, pp.28, 2013.
- [COB 61] R L. Coble: Sintering crystalline solids. Intermediate and final state diffusions models, J. Appl. Phys., vol. 32, pp. 787 -792, 1961.
- [CON 13] Powder Injection Moulding International, Applications for MIM V: Consumer Products, 2013.
- [CRA 75] J. Crank: The mathematics of diffusion, 2nd ed., Clarendon Press, Oxford, UK, pp. 47–48, 1975.
- [DAI 12] S. Dai: J Mater Sci 2012;47:4579.
- [DAN 02] R L. Danley: New heat flux DSC measurement technique. Thermochim Acta, 395:201–208., 2002.
- [DJO 09] H. Djohari and J. J. Derby: Transport mechanisms and densification during sintering: II.Grain boundaries, Chemical Engineering Science, vol. 64, pp. 3810–3816, 2009.
- [DON 89] C. Dong and H K. Bowen: Hot-stage study of bubble formation during binder burnout, J. Am. Ceram. Soc., vol. 72, pp. 1082-1089, 1989.
- [DOR 57] J.E. Dorn: Creep and recovery, American Society for Metals, Cleveland, Ohio; 1957.
- [DUC 89] V.C. Ducamp, R. Raj: Shear and densification of glass powder compacts, J. Am. Ceram. Soc, vol. 72, pp. 798-804, 1989.
- [DUT 98] M. Dutilly : Modélisation du moulage par injection de poudre métallique, Thèse de doctorat, Université de Franche-Comté, 1998.
- [EDI 87] M.J. Edirisinghe and J.R. Evans: Rheology of ceramic injection moulding formulations, Br. Ceram. Trans. J., vol.86, pp. 18-22, 1987.
- [FAN 09] Y L. Fan, K S. Hwang, S H. Wu and Y C. Liao: Minimum amount of binder removal required during solvent debinding of Powder Injection-Molded compacts, Metall. Trans., vol. 40, pp.768-779, 2009.
- [FLY 66] J.H. Flynn, L.A.Wall, J. Res. Natl. Bur. Stand., A: Phys. Chem. Vol. 70A pp. 487, 1966.
- [FRE 45] J. Frenkel: Viscous flow of crystalline bodies under the action of surface tension, J. Phys. USSR, vol. 9, pp. 385-391, 1945.
- [FU 05] G. Fu, N.H. Loh, S.B. Tor, B.Y. Tay, Y. Murakoshi and R. Maeda: Injection molding, debinding and sintering of 316L stainless steel microstructures. Applied Physics A, vol. 81, pp. 495-500, 2005.
- [GAS 00] M. Gasik, Z. Baosheng: A constitutive model and FE simulation for the sintering process of powder compacts, Comp Mater Sci, vol.8, pp. 93-101, 2000.
- [GER 76] R.M. German and Z.A. Munir: Systematic trends in the chemically activated sintering of tungsten, High Temp Sci, vol.8, pp. 267-280, 1976.
- [GER 87] R.M German: Theory of thermal debinding, Int. Journal of Powder Metallurgy, vol.23, pp. 237-245, 1987.

- [GER 90] R.M. German, Powder Injection Molding, MPIF, Princeton, NJ, 1990.
- [GER 92] R M. German: Critical developments in tungsten heavy alloys. Princeton, NJ, USA; 1992.
- [GER 94] R.M. German, Powder Metallurgy Science,(Second Edition), Metal Powder Industries Federation, Princeton, NJ, ISBN: 1-878954-42-3, 1994.
- [GER2 94] R.M.German: Homogeneity Effects on Feedstock Viscosity in Powder Injection Molding, J. Am. Ceram. Soc., vol. 77, pp. 283-285, 1994.
- [GER 96] RM. German, 1996 Sintering Theory and Practice. John Wiley & Sons, Inc. USA.
- [GER 97] R.M. German and A. Bose: Injection Molding of Metals and Ceramics. Princeton, Metal Powder Industries Federation, Princeton, NJ, ISBN: 1-878-954-61-X, 413 pages, 1997.
- [GER 02] R M German: Computer modeling of sintering processes, Int. J. Powder Metall., vol. 38, pp. 48-66, 2002.
- [GER 03] R. M. German: User's Guide to Powder Injection Molding – Designs and Applications, Innovative Material Solutions, State College, PA, 320 pages, 2003. edition), Uchida Rokakuho Publishing, Tokyo, Japan, 472 pages, 1996.
- [GER 07] R.M. German: Global research and development in powder injection moulding, Powder Injection Moulding International, vol. 2, pp. 33-36, 2007.
- [GER 08] R.M. German: PIM breaks the \$1 bn barrier, Metal Powder Report, vol.63, pp. 8-10, 2008.
- [GIA 11] Global Industry Analysts: Metal and Ceramic Injection Molding, Inc., San Jose, USA, 2011.
- [GIL 01] O. Gillia, C. Gosserond, D. Bouvard: Viscosity of WC-Co compacts during sintering, Acta Mater, vol. 49, pp. 1413-1420, 2001.
- [GON 12] J. González-Gutiérrez, G. Beulke Stringari and I. Emri: Powder Injection Molding of Metal and Ceramic Parts, Some Critical Issues for Injection Molding, Dr. Jian Wang (Ed.), ISBN: 978-953-51-0297-7, pp. 65-88, 2012.
- [GUI 07] B.G. Guillaume and G. Christian: Apparent Activation Energy for the Densification of a Commercially Available Granulated Zirconia Powder, J Am Ceram Soc, vol.90, pp. 1246-1250, 2007.
- [HAI 98] P J. Haines, M. Reading and F W. Wilburn: Differential thermal analysis and differential scanning calorimetry. In Brown ME, editor. (ed): Handbook of Thermal Analysis and Calorimetry, vol 1 The Netherlands: Elsevier Science BV; 279–361, 1998.
- [HAJ 09] S. S. Hajimirsadeghi, M B. Teimouri, M. Rahimi-Nasrabadi and S. Dehghanpour: Non-isothermal kinetic study of the thermal decomposition N-{bis[benzyl(methyl) amino] phosphory}-2,2 dichloacetarmide and N-{bis[dibenzyl amino]phosphory l}2,2-dichloraacetamide, J Therm Anal Calorim, vol. 98, pp.463-468, 2009.
- [HAU 11] B. Hausnerová, “Powder injection moulding- An alternative processing method for automotive items”, New Trends and Developments in Automotive System Engineering, InTech Publishers, Rijeka, Croatia, 129, 2011.



- [HAY 63] H.W. Hayden and J.H. Brophy: The activated sintering of tungsten with Group VIII elements. *J Electrochem Soc*, vol. 110, pp. 805-810, 1963.
- [HAY 64] H.W. Hayden, J.H. Brophy: Low-temperature sintering of pure tungsten and tungsten-iridium, *J Less-Common Metals*, vol.6, pp. 214-218, 1964.
- [HEA 04] D.F. Heaney, R. Zauner, C. Binet, K. Cowan and J. Piemme: Variability of powder characteristics and their effect on dimensional variability of powder injection moulded components. *J. Powder Metallurgy*, vol. 47, pp.145-150, 2004.
- [HOS 06] W F. Hosford, *Material Science*, Cambridge University Press, 2006.
- [HOW 05] K.S. However, G.J. Shu and H.J. Lee: Solvent Debinding Behavior of Powder Injection Molded Components Prepared from Powders with Different Particle Sizes, *Metallurgical and materials transactions A*, vol. 36, pp 161-167, 2005.
- [HU 00] SC. Hu and KS. Hwang: Dilatometric analysis of thermal debinding of injection moulded iron compacts, *Powder Metallurgy*, vol. 43, pp. 239-244, 2000.
- [HWA 02] C.J. Hwang, And T.H. Kwon: Polymer Engineering and Science, A full 3D finite element analysis of the powder injection molding filling process including slip phenomena, *Polymer Engineering and Science*, vol. 42, pp. 33-50, 2002.
- [IMB 08] M. Imbaby, K. Jiang and I. Chang: Soft lithography and powder metallurgy for fabrication of micro stainless steel machine parts, *J. Mater. Lett*, vol.62, pp.4213-4216, 2008.
- [JAN 08] B. Jankovic: Kinetic analysis of the nonisothermal decomposition of potassium metabisulfite using the model-fitting and isoconversional (model-free) methods, *Chemical Engineering Journal* vol. 139, pp. 128-135, 2008.
- [JAR 08] T. Jardiel, M.E. Sotomayor, B. Levenfeld, and A. Várez: Optimization of the Processing of 8-YSZ Powder by Powder Injection Molding for SOFC Electrolytes, *International Journal of Applied Ceramic Technology*, vol.5, pp.574-581, 2008.
- [JEN 08] M. Jenni, L. Schimmer, R. Zauner, J. Stampfl and J. Morris: Quantitative study of powder binder separation of feedstocks, *Powder Injection Moulding International*, vol. 2, pp. 50-55, 2008.
- [JOC 09] E. Jochen and B. Dirk: Product specification-polyMIM@Cu999, Germany, 2009.
- [JOH 63] D L. Johnson and I B. Cutler: Diffusion sintering I. initial stage sintering models and their application to shrinkage of powder compacts, *J. Am. Ceram. Soc.*, vol. 46, pp. 541-545, 1963.
- [JOH 70] D L. Johnson: A general model for the intermediate stage of sintering, *J. Am. Ceram. Soc.*, vol. 53, pp. 574-577, 1970.
- [JOR 08] H.R.C. DA SILVA JORGE: Compounding and processing of water soluble binder for Powder Injection Moulding. Ph.D thesis, Universidade do Minho, 2008.
- [KAN 04] S-J L. Kang and Y I. Kang: Sintering kinetics at final stage sintering: model calculation and map construction. *Acta Mater.*, vol. 52, pp. 4573-4578, 2004.
- [KAN 05] S.J.L. Kang *Sintering: densification, grain growth and microstructure*. Elsevier Butterworth-Heinemann.UK, 2005.



- [KAR 04] C. Karatas, A. Kocer, H.I. Unal and S. Saritas: Rheological properties of feedstocks prepared with steatite powder and polyethylene-based thermoplastic, *Journal of Materials Processing Technology*, vol.152, pp.77-83, 2004.
- [KLA 07] E. Klar and P. Samal: *Powder Metallurgy Stainless Steels: Processing, Microstructures, and Properties*, ASM International®, 2007.
- [KOH 07] I. Kohsari, S M. Pourmortazavi and S S. Hajimirsadeghi: Non-isothermal kinetic study of the thermal decomposition of diaminoglyoxime and diaminofurazan, *J. Therm. Anal. Calorim*, vol. 89 543-546, 2007.
- [KON 10] X. Kong, T. Barriere, J C. Gelin and C. Quinard: Investigations on sintering of 316L stainless steel powders and identification of physical parameters from coupling experiments and finite element simulations, *Int. J. Powder Metall.*, vol.46, pp. 61-72, 2010.
- [KON 11] X. Kong: Development and characterization of polymer-metallic powder feedstocks for micro-injection molding, Ph.D thesis, University of Franche-Comté, 2011.
- [KON 11] X. Kong: Development and characterization of polymer-metallic powder feedstocks for micro-injection molding, Ph.D thesis, University of Franche-Comté, 2011.
- [KON 12] X. Kong, T. Barriere and G.C. Gelin: Determination of critical and optimal powder loadings for 316L fine stainless steel feedstocks for micro-powder injection molding, *Journal of Materials Processing Technology*, vol. 212, pp. 2173-2182, 2012.
- [KOW 97] S J. Kowalski, G. Musielak and A. Rybicki: Response of dried materials on drying conditions, *Int. J. Heat Mass Transfer*, vol. 40, pp.1217-1226, 1997.
- [KIM 00] W I. Kim, S D. Kim, S B. Lee and I K. Hong: Kinetic characterisation of thermal degradation process for commercial rubbers, *Journal of Industrial and Engineering Chemistry*, vol. 6, pp. 348-355, 2000.
- [KIM 03] H.G. Kim, O. Gillia, D. Bouvard: A phenomenological constitutive model for the sintering of alumina powder, *J. Euro Ceram Soc*, vol. 23, pp. 1675-1685, 2003.
- [KIN 13] Kinetics- Metal Injection Moulding, available from: <http://www.kinetics.com>, accessed on 3 March 2013.
- [KIS 57] H E. Kissinger: Reaction kinetics in differential thermal analysis, *J. Analyt. Chem.*, vol. 29, pp.1702-1706, 1957.
- [KRA 04] T. Kraft and H. Riedel: Numerical simulation of solid state sintering: model and application, *J. Eur. Ceram. Soc.*, vol. 24, pp. 345-361, 2004.
- [KUT 04] T R G. Kutty, K B. Khan, P V. Hegde, J. Banerjee, A K. Sengupta, S. Majumdar and H S. Kamath: Development of a master sintering curve for ThO<sub>2</sub>, *Journal of Nuclear Materials*, vol. 327, pp. 211-219, 2004.
- [LAG 98] J.C. Lagarias, J.A. Reeds, M.Wright, P.E. Wright: Convergence properties of the Nelder-Mead simplex method in low dimensions, *SIAM J Optim*, vol.9, pp. 112-147, 1998.

- [LAH 06] D. Lahiri, S.V. Ramana Rao, G.V.S. Hemantha Rao and R. K. Srivastava: Study on Sintering Kinetics and Activation Energy of UO<sub>2</sub> Pellets using Three Different Methods, Vol. 357, pp. 88-96, 2006.
- [LAM 03] O. Lam, D. Bellet, M. Di Michiel and D. Bouvard: In situ microtomography investigation of metal powder compacts during sintering, Nuclear Instruments and Methods in Physics Research B, vol. 200, pp.287-294, 2003.
- [LAS 99] E. Lassne, Schubert W.D. Tungsten: Properties, Chemistry, Technology of the Element, Alloys, and Chemical Compounds; Kluwer Academic and Plenum Publishers: New York, 1999.
- [LEW 96] J A. Lewis, M A. Galler and D P. Bentz: Computer simulations of binder removal from 2-D and 3-D model particulate bodies, J. Am. Ceram. Soc., vol. 79, pp. 1377–1388, 1996.
- [LI 03] Y. Li, S. Liu, X Qu and B. Huang: Thermal debinding processing of 316L stainless steel powder injection molding compacts, Journal of Materials Processing Technology, vol., pp. 65-69, 2003.
- [LI 07] Y. Li, L. Li, and K.A. Khalil: Effect of powder loading on metal injection molding stainless steels, Journal of Materials Processing Technology, vol. 183, pp. 432-439, 2007.
- [LIN 98] H.K. Lin and K.S. Hwang: In situ dimensional changes of powder injection-molded compacts during solvent debinding, Acta Materialia, vol. 46, pp. 4303-4309, 1998.
- [LIN 05] T L. Lin and L W. Houring: Investigation of wick debinding in metal injection molding: numerical simulations by the random walk approach and experiments, Advanced Powder Technology., vol. 16, pp. 495 -515, 2005.
- [LIN 10] Y.J. Lin and K.S. Hwang: Swelling of Copper Powders during Sintering of Heat Pipes in Hydrogen-Containing Atmospheres, Mater Trans, vol. 51, pp.2251-2258, 2010.
- [LIU 00] FJ. Liu, K.S. Chou: Determining critical ceramic powder volume concentration from viscosity measurements, Ceramics International, vol. 26 pp. 159-164, 2000.
- [LIU 01] Z.Y. Liu, N.H. Loh, S.B. Tor, K.A. Khor, Y. Murakoshi and R. Maeda: Binder system for micropowder injection molding, Materials Letters, vol. 48, pp. 31–38, 2001.
- [LIU 01] Z.Y. Liu, N.H. Loh, K.A. Khor, and S.B. Tor: Sintering activation energy of powder injection molded 316 L stainless steel, Scr. Mater, vol. 44, pp. 1131-1137, 2001.
- [LIU 03] Z.Y. Liu, N.H. Loh, S.B. Tor and K.A. Khor: Characterization of powder injection molding feedstock, Materials Characterization, vol. 49, pp.313-320, 2003.
- [LIU 07] L. Liu, N.H. Loh, B.Y. Tay, S.B. Tor, Y. Murakoshi and R. Maeda: Effects of thermal debinding on surface roughness in micro powder injection molding, Materials Letters, vol. 61, pp. 809-812, 2007.
- [MAC 84] J.W. MacBeth: Ceramic Engine Components Reduce Wear, Friction, Ceramic Industry, vol.7, pp. 33-45, 1984.  
22 March 2013.

- [MAD 95] D.S. Madan and A. Fitzgibbon: Shelf Life of MnS Powder and MnS Containing Mixes, *Advances in Powder Metallurgy and Particulate Materials*, compiled by M. Phillips and J. Porter, Metal Powder Industries Federation, Princeton, NJ, 1995, part 8, pp.177-182.
- [MAD 13] Metal Injection Moulding, available from: <http://www.made-in-china.com>, accessed on 3 March 2013.
- [MAL 07] R. Malewar, K.S. Kumar, B.S. Murty, B. Sarma, S.K. Pabi: On sinterability of nanostructured W produced by high-energy ball milling, *Journal of Materials Research*, vol. 22, pp. 1200-1206, 2007.
- [MAM 11] B. Mamen, T. Barriere and J.C. Gelin: Study of the thermal decomposition for different feedstocks powder injection moulding, *Euro PM2011*, vol. 3 pp. 235-241, 2011.
- [MAM 12] B. Mamen, T. Barriere and G.C. Gelin: Solvent debinding process in Powder Injection Molding: experiments and numerical simulations, *Steel research international*, pp. 783-786, 2012.
- [MAM 13] B.Mamen, T.Barriere and J-C.Gelin: Investigations on thermal debinding process of 316L stainless steel powders and identification of kinetic parameters from coupling experiments and finite element simulations, *Powder technology*, vol. 235 pp. 192–202, 2013.
- [MAS 89] S. Masia, P D. Calvert, W E. Rhine and H K. Brown: Effect of oxides on binder burnout during ceramics processing, *J. Matl. Sci.*, vol. 24, pp.1907-1912, 1989.
- [MAS 06] H. Masuda, K. Higashitani and H. Yoshida: *Powder Technology Handbook*, third edition, published by Taylor and Francis Group, LLC, pp. 213, 2006.
- [MAT 13] Powder Injection Moulding, available <http://materiaux.ecam.fr>, accessed on 3 March 2013.
- [MIC 12] MICRO manufacturing: <http://www.micromanufacturing.com>, accessed on.
- [MIL 85] P. Mills: Non-Newtonian behaviour of flocculated suspensions. *J Phys Lett.*, vol. 46, pp. 301–309, 1985.
- [MOH 11] U L Mohsin, D. Lager, C. Gierl, W. Hohenauer and H. Danninger: Simulation and optimisation for thermal debinding of copper MIM parts using thermokinetic analysis, *Powder Metallurgy*, vol. 54, pp. 30-35, 2011.
- [MOR 10] O. Morteza and M. Omid: Microwave versus conventional sintering: A review of fundamentals, advantages and applications, *Journal of Alloys and Compounds*, vol. 494, pp. 175-189, 2010.
- [MUS 96] G. Musielak: Internal stresses caused by outflow of moisture and phase change inside dried material, *Drying Technol.*, vol. 14, pp. 289-306, 1996.
- [MUT 89] B.C. Mutsuddy: Equipment selection for injection moulding, *Ceram. Bull*, vol. 10, pp. 1796-1802, 1989.
- [MUT 95] B.C. Mutsuddy and R.G. Ford, *Ceramic Injection Molding*, New York, NY: Chapman & Hall, 1995.
- [NAG 06] B.S. Nagendra Parashar and R.K Mittal: *Elements of Manufacturing Processes*, May 2006.

- [NAS 04] R S. Nasar, M. Cerqueira, E. Longo and J A. Varela: Sintering mechanisms of  $\text{ZrO}_2$  MgO with addition of  $\text{TiO}_2$  and CuO, *Ceramics International*, vol. 30, pp. 571-577, 2004.
- [OLE 98] E A. Olevsky: Theory of sintering: from discrete to continuum, *Materials Science & Engineering R*, vol. 23, pp.41-99, 1998.
- [OLI 05] R.V.B. Oliveira, V. Soldi, M.C. Fredeland and A.T.N. Pires: Ceramic injection molding: influence of specimen dimensions and temperature on solvent debinding kinetics, *Journal of Materials Processing Technology*, vol. 60, pp. 213-220, 2005.
- [ONB 10] V.P. Onbattuvelli, S. Vallury, T. McCabe, S.J. Park and S.V. Atre: Properties of SiC and AlN feedstocks for the powder injection moulding of thermal management devices, *PIM International*, vol. 4, pp. 64-70, 2010.
- [ONB 13] P.P. Onbattuvelli, R.K. Enneti, S.J. Park and S.V. Atre: The effects of nanoparticle addition on binder removal from injection molded aluminum nitride, *International Journal of Refractory Metals and Hard Materials*, vol. 36, pp. 77-84, 2013.
- [OSS 08] T.A. Osswald, L-S. Turng and P. Gramann: *Injection Molding Handbook*, Carl Hanser Verlag, Munich 2008, Germany.
- [OZA 65] T. Ozawa: A new method of analyzing thermogravimetric data. *Bull Chem Soc Jpn*, vol.38, pp. 1881–1886, 1965.
- [PAS 02] S. Pascoli, P.A.P. Wendhausen, and M.C. Fredel: Keeping to Form in the Powder Business, *Met. Powder Rep.*, vol. 57, pp. 32–37, 2002.
- [PAR 09] S J. Park, Y. Wu, D.F. Heaney, X. Zou, G. Gai and R.M. German: Rheological and thermal debinding behaviors in titanium powder Injection Molding, *J. Metall. Trans.*, vol. 40A, pp. 215-222, 2009.
- [PET 04] A. Petersson and J. Ågren: Constitutive behaviour of WC–Co materials with different grain size sintered under load, *Acta Mater.*, vol. 52, pp. 1847–1858, 2004.
- [PIO 08] V. Piottter, B. Zeep, P. Norajitra, R. Ruprechtb, A. Wethc and J. Hausselta: Development of a powder Metallurgy process for tungsten components, *Fusion Engineering and Design*, vol. 83, pp. 1517-1520, 2008.
- [PIO 12] V. Piottter, E. Honza, A. Klein, T. Mueller, K. Plewa: *Micro Precision Parts produced by Powder Injection Molding*, Karlsruhe Institute of Technology (KIT) and Institute for Applied Materials (IAM-WPT), Germany, 2012.
- [POO 10] G. Pooria, T M. Tahereh and R. Bijan: Differential Scanning Calorimetry Techniques: Applications in Biology and Nanoscience, *J. Biomol Tech.*, vol.21, pp.167-193, 2010.
- [POU 07] S M. Pourmortazavi, I. Kohsari, M B. Teimouri and S S. Hajimirsadeghi: Thermal behaviour kinetic study of dihydroglyoxime and dichloroglyxime, *J. Mater. Lett*, vol. 61, pp. 4670-4673, 2007.
- [PRI 00] D M. Price, D J. Hourston and F. Dumont: Thermogravimetry of Polymers, *Encyclopedia of Analytical Chemistry* R.A. Meyers (Ed.), John Wiley & Sons Ltd, Chichester, pp. 8094-8105, 2000.

- [PRA 09] G. Prabhu, A. Charkraborty, and B. Sarma: Microwave sintering of tungsten, *Int J. Refract Hard Met*, vol. 27, pp. 545–548, 2009.
- [PAR 09] S J. Park, Y. Wu, D F. Heaney, X. Zou, G. Gai and R M. German: Rheological and thermal debinding behaviors in titanium powder Injection Molding, *J. Metall. Trans.*, vol. 40A, pp. 215-222, 2009.
- [QUI 08] C. Quinard : Experimentation, modélisation et simulation dans le domaine de l'élaboration de micro-composants injectés à partir de poudres, Ph.D. Thesis, University of Franche-Comté, 2008.
- [QUI 09] C. Quinard, T. Barriere and J C. Gelin: Development and property identification of 316L stainless steel feedstock for PIM and micro-PIM, *J. Powder Technol.*, vol.190, pp. 123-128, 2009.
- [QUI 11] C. Quinard, J. Song, T. Barriere and J C. Gelin: Elaboration of PIM feedstocks with 316L fine stainless steel powders for the processing micro-components, *Powder Technology*, vol. 208, pp. 383-389, 2011.
- [RAF 12] M. Rafi Raza, F. Ahmad, M A. Omar and R M. German: Effects of cooling rate on mechanical properties and corrosion resistance of vacuum sintered powder injection molded 316L stainless steel, *J. Mater. Process. Technol.*, vol. 212, pp.164-170, 2012.
- [RAJ 12] J. Rajabia, N. Muhamada, A.B. Sulong, A. Fayyaza and A. Wahia: Advantages and Limitations of Using Nano Sized Powders for Powder Injection Molding Process, vol. 59 pp. 137-140, 2012.
- [RIC 05] V B. Ricardo, S. Valdir, F. Marcio and P. Alfredo: Ceramic injection moulding: Influence of specimen dimensions and temperature on solvent debinding kinetics, *Journal of Materials Processing Technology*, vol. 160, pp. 213-220, 2005.
- [RIV 11] T. Rivera: Advances in Ceramics - Synthesis and Characterization, Processing and Specific Applications, chapter 6, Edited by Costas Sikalidis, 2011.
- [SAC 11] RM. Sachanandani and S J. Lombardo: Effect of green body size and heating rate on failure during thermal debinding and on the debinding cycle time, *Journal of Ceramic Processing Research*, vol. 12, pp. 115-121, 2011.
- [SAN 97] H. Sanderow, J. Spirko and R. Corrente: The Machinability of P/M Materials as Determined by Drilling Tests, *Advances in Powder Metallurgy and Particulate Materials*, compiled by R.A. McKotch and R. Webb, Metal Powder Industries Federation, Princeton, NJ, part 15, pp. 125-143, 1997.
- [SAN 05] M.A. Santos, A.M. Maliska, A.N. Llein, W. Ristow and J.L.R. Muzart: Debinding of injected parts using an abnormal glow discharge, *Materials Science and Engineering A*, vol. 407, pp. 71-76, 2005.
- [SCH 00] G. Schlieper: Technical Coordinator, Metal Injection Molding, EPMA, 1, 2000.
- [SEG 04] P. Budrugaec and E. Segal: On the nonlinear isoconversional procedures to evaluate the activation energy of nonisothermal reactions in solids, *Int. J. Chem. Kinet.*, vol. 36, pp. 87-93, 2004.
- [SOM 08] I M., Somasundram, A. Cendrowicz, D I. Wilson and M L. Johns: Phenomenological study and modelling of wick debinding. *Chemical Engineering Science*, vol.63, pp.3802-3809, 2008.

- [SON 06] J. Song, J.C. Gelin, T.Barriere and B. Liu: Experiments and numerical modelling of solid state sintering for 316L stainless steel components, *J. Mater Process Technol*, vol. 177, pp. 352-355, 2006.
- [SON 07] J. Song: Experiments, modelling and numerical simulation of the sintering process for metallic or ceramic powders, Ph.D thesis, University of Franche-Comté, 2007.
- [SON 10] J. Song, T. Barriere, B. Liu, J.C. Gelin and G. Michel: Experimental and numerical analysis on sintering behaviours of injection moulded components in 316L stainless steel powders, *Powder Metallurgy*, vol. 53, pp. 295-304, 2010.
- [SON 12] J. Song, M. Ouyang, Y. Yu, Z. Zhuang: World Congress and Exhibition of Powder Metallurgy, vol. 14, 2012.
- [SOT 10] M.E. Sotomayor, A. Varez, and B. Levenfeld: Influence of powder particle size distribution on rheological properties of 316L powder injection moulding feedstocks, *Powder Technology*, vol. 200, pp. 30–36, 2010.
- [SHE 02] Y. Shengjie, Y C. lam, S.C.M Yu and K C. Tam: Thermal debinding modeling of mass transport and deformation in powder-injection molding compact, *J. Metall. Trans.*, vol. 33B, pp. 477- 488, 2002.
- [SHI 02] Z. Shi, Z.X. Guo, and J.H. Song, A diffusion-controlled kinetic model for inder burnout in a powder compact, *J. Acta Mater*, vol.50, 1937-1950, 2002.
- [SHI 04] Z. Shi and Z X. Guo: Kinetic modelling of binder removal in powder-based compacts, *Materials Science and Engineering*, vol. 365, pp.129-135, 2004.
- [SHI 06] G. Shibo, Q. Xuanhui, H. Xinbo, Z.Ting and D. Bohuave D: Powder injection molding of Ti–6Al–4V alloy, *Journal of Materials Processing Technology*, vol. 173, pp.310-314, 2006.
- [SRI 11] Ajeet K. Srivastav, M. Sankaranarayana and B. S. Murty: Initial-stage sintering kinetics of nanocrystalline tungsten, *Metall. Mater. Trans. A.*, vol. 42, pp. 3863-3866, 2011.
- [SUA 04] M.E.V.S. Suárez-Iha, J.A.F.F. Rocco, J.E.S. Lima, A.G. Frutuoso, K. Iha, M. Ionashiro and J. R. Matos, TG studies of a composite solid rocket propellant based on HTPB-binder, *J. Therm. Anal. Calorim.*, vol. 77, pp. 803-813, 2004.
- [SUP 00] R. Supati, N.H. Loh, K.A. Khor and S.B. Tor: Mixing and characterization of feedstock for powder injection molding, *Materials Letters*, vol. 46, pp.109-114, 2000.
- [SUR 03] P. Suri, S.V. Atre, R.M. German, J.P. de Souza: Effect of mixing on the rheology and particle characteristics of tungsten based powder injection molding feedstock. *Materials Science and Engineering A*, vol. 356, pp. 337-344, 2003.
- [TAS 11] M. Tassilo and L. Reinhard: Current status of ceramic injection moulding, ebookbrowse edition, pages 17, 2011.
- [TOM 11] V. Tomasic, I. Brnardic, H. Jenei, V. Kosar, and S. Zrnècvić: Combustion of Active Carbon as a Model Carbon Material: Comparison of Non-catalytic and Catalytic Oxidation, *J. Chem. Biochem. Eng. Q*, vol. 25, pp. 283-287, 2011.



- [TOR 11] J.M. Torralba, J. Hidalgo and A. Jimenez-Morales: Powder injection moulding, Processing of small parts of complex shape, Proceedings of ICIT&MPT 2011 8<sup>th</sup> International Conference on Industrial Tools and Material Processing Technologies, ISBN 9789616692021, Ljubljana, Slovenia, pp. 53-58 October 2-5, 2011.
- [TRU 97] M. Trunec and J. Cihlár: Removal of Thermoplastic Binders from Ceramic Green Bodies, *Journal Ceramics-Silikáty*, vol.41, pp.67-80, 1997.
- [TRU 02] M. Trunec and J. Cihlar: Thermal removal of multicomponent binder from ceramic injection mouldings, *Journal of the European Ceramic Society*, vol. 22, pp. 2231- 2241. 2002.
- [VEN 86] K.R Venkatachari and R. Raj : Shear deformation and densification of powder compacts, *J. Am. Ceram. Soc.*, vol.69, pp. 499-506, 1986.
- [VER1 94] R. Vetter, M J. Sanders, I. Majewska-Glabus, L Z. Zhuang and J. Duszczyk: Wick-Debinding in Powder Injection Molding, *International Journal of Powder*, vol. 30, pp. 115-124, 1994.
- [VER2 94] R. Vetter, W R V. Horninge, P J. Vervoort, I Majewskaglabus, L Z. Zhuang and J. Duszczyk: Square-root wick debinding model for powder injection-molding, *Powder Metallurgy*, vol. 37, pp. 265-271, 1994.
- [UPA 97] G. S. Upadhyaya 1997: Powder metallurgy technology, Cambridge International Science Publishing, First published August 2002, pp. 70-71.
- [WAK 13] F. Wakai: Mechanics of viscous sintering on the micro- and macro-scale, *Acta Materialia*, vol.61, pp. 239–247, 2013.
- [WAN 90] J. Wang and R. Raj: Estimate of the activation energies for boundary diffusion from rate-controlled sintering of pure alumina, and alumina doped with zirconia or titania. *J. Am. Ceram. So.c*, vol. 73, pp.1172-1175, 1990.
- [WAN 10] H. Wang, Z. Zak Fang, KS. Hwang, H. Zhang, D. Siddle: Sinterability of Nanocrystalline Tungsten Powder. ” *Int. J. Refrac. Met. Hard Mater*, vol. 28, pp. 312-316, 2010.
- [WAN 12] H. Wang and Z.Z Fang: Kinetic Analysis of Densification Behavior of Nano-sized Tungsten Powder, *J. Am Ceram Soc*, vol. 95, pp. 2458–2464, 2012.
- [WAS 06] G S. Was, S. Teyseyre and Z. Jiao: Corrosion of Austenitic alloys in supercritical water, *Corrosion Reviews*, vol. 62, pp. 989-1005, 2006.
- [YAK 00] AO. Yakimov and T W. Coyle: A statistical analysis of the factors affecting thermal debinding in powder injection molded parts, *Journal of Materials Science Letters*, vol. 19, pp. 2255-2257, 2000.
- [YAN 99] X.M. Yang and R.J. Petcavich: Powder and binder systems for use in metal and ceramic powder injection molding, United States Patent 5,977, 230, 1999.
- [YAN 02] W.W. Yang, K.Y. Yang and M.H. Hon: Effects of PEG molecular weights on rheological behavior of alumina injection molding feedstocks, *Materials Chemistry and Physics*, vol.78, pp.416-424, 2002.
- [YAN 03] W.W. Yang, K.Y Yang, M.C. Wang and M.H. Hong: Solvent debinding mechanism for alumina injection molded compacts with water-soluble binders, *Ceramic International*, vol. 29, pp. 745-756, 2003.

- [YU 11] Y. Yu, J. Song, J. Liu, Z. Zhuang: Proceedings of the Eighth International Conference on Tungsten and Hard materials, vol. 18, 2011.
- [ZAU 04] R. Zauner, C. Binet, D. F. Heaney, and J. Piemme: Variability of feedstock viscosity and its correlation with dimensional variability of green powder injection moulded components, Powder Metallurgy, vol. 47, pp 1-6, 2004.
- [ZHA 05] R. Zhang: Numerical simulation of solid-state sintering of metal powder compact dominated by grain boundary diffusion, PhD thesis, The Pennsylvania State University, USA; 2005.
- [ZHA 09] X. Zhanga, W. Jongb and F. Pretoa: Estimating kinetic parameters in TGA using B-spline smoothing and the Friedman method. J. Biomass and Bioenergy, vol. 33, pp. 1435–1441, 2009.
- [ZLA 08] B.S. Zlatkov, E. Griesmayer, H. Loibl, O.S. Aleksic, H. Danninger, C. Gierl and L.S. Lukic: Recent Advances in PIM Technology I. Science of Sintering, vol. 40, pp. 79-88, 2008.
- [ZIE 77] O C. Zienkiewicz: The Finite Element Method-3rd Edition, McGraw Hill, London, 787 pages, 1977.
- [ZOR 02] J.E. Zorazi, C.A. Perottoni and J.A.H. Da Jornada: Hard-skin development during binder removal from  $\text{Al}_2\text{O}_3$ -based green ceramic bodies, Journal of Materials Science, vol.37, pp. 1801-1807, 2002.
- [ZUO 03] R. Zuo, E. Aulbach and J. Rodel: Experimental determination of sintering stresses and sintering viscosities, Acta Materialia, vol. 51, pp. 4563-4574, 2003.
- [ZUO 04] R. Zuo, J. Rödel: Temperature dependence of constitutive behaviour for solid-state sintering of alumina, Acta Mater, vol. 52, pp. 3059-3067, 2004.